

Nanoscale physical properties of polymer thin films for energy applications

Matteo Sanviti

Supervisors:

Prof. Angel Alegría

Dr. Daniel E. Martínez-Tong

Index

Resumen	iii
Outline of the thesis	ix
1 Theoretical background	1
1.1 Macromolecules	3
1.2 Physical properties of polymers	4
1.2.1 The glass transition.....	4
1.2.2 Crystallinity	5
1.2.3 Mechanical properties of polymers	8
1.2.4 Dielectric properties of polymers	12
1.2.5 Relaxation in polymers.....	15
1.3 Polymers for electronics	19
1.4 Polymer blends	22
2 Materials and methods.....	29
2.1 Materials	31
2.2 Sample Preparation	34
2.3 Experimental methods	36
2.3.1 Atomic Force Microscopy (AFM)	36
2.3.2 Broadband Dielectric Spectroscopy (BDS).....	46
3 Dielectric characterization of PEO semicrystalline thin films	51
3.1 Introduction.....	53
3.2 BDS characterization of PEO thin films.....	56
3.2.1 Heterogeneity in supported PEO melt.....	58
3.2.2 Melting of PEO thin films	62
3.3 Imaging the heterogeneous transport properties in PEO by nano-Dielectric Spectroscopy	68
3.3.1 A model for <i>n</i> DS	68

3.3.2 Modelling the loss factor of the AFM system capacitor	75
3.3.3 Charges dynamics in PEO complex nanostructure	81
3.4 Summary	88
4 Fabrication and nanoscale properties of tailored PEDOT:PSS nanostructures	89
4.1 Introduction.....	91
4.2 Fabrication and local properties of PEDOT:PSS nanostructures	93
4.2.1 PEDOT:PSS nanospheres	93
4.2.2 Surface nanostructuring of PEDOT:PSS thin films	101
4.3 Summary	113
5 PEDOT:PSS/PEO blend thin films: mechanical and electrical properties at the nanoscale	115
5.1 Introduction.....	117
5.2 Topography	118
5.3 Internal structure and phase separation.....	121
5.4 Mechanical properties.....	124
5.5 Electrical properties	126
5.6 Influence of molecular weight on morphology and structure	128
5.7 Influence of molecular weight on mechanical and electrical properties.....	132
5.8 Summary	137
6 Conclusions	139
6.1 Final remarks	141
6.2 Perspectives	144
Appendix	145
List of publications	151
References.....	153

Resumen

Los componentes clásicamente utilizados en la fabricación de dispositivos electrónicos para la producción de energía y su almacenamiento, son principalmente derivados inorgánicos de materias primas minerales. Su cada vez más escasa disponibilidad, acompañada por el alto impacto ambiental tanto por los métodos de extracción como de refinamiento, utilizados constituyen un tema de fundamental importancia en el sector energético. Para enfrentar el problema, a lo largo de los años se han diseñado varios materiales conductores de base orgánica, que han proporcionado una alternativa sintética a los conductores inorgánicos. Entre estos, los compuestos macromoleculares destacan por sus procesabilidad y propiedades estructurales. Las macromoléculas se conocen comúnmente como polímeros, que se utilizan en una amplia gama de aplicaciones por sus propiedades físicas convenientes. Ciñéndonos a las aplicaciones energéticas, entre los materiales poliméricos más recientes en circulación podemos distinguir varios ejemplos de polímeros intrínsecamente conductores, tanto iónicos como electrónicos. Los polímeros conductores de iones, como los de electrones, han atraído atención considerable debido a sus buena estabilidad química y propiedades mecánicas u ópticas. Esta clase de compuestos constituyen materiales avanzados que pueden presentar nanoestructuras supramoleculares complejas, las cuales determinan su comportamiento tanto en volumen, cuanto bajo las condiciones de funcionamiento del dispositivo correspondiente donde en muchos casos el material está nanoestructurado. Por esta misma razón, hoy en día el desarrollo de materiales poliméricos avanzados se beneficia de forma importante de la investigación básica y aplicada de nanoestructuras poliméricas.

En esta tesis se presenta el estudio de algunos polímeros nanoestructurados con aplicaciones energéticas. Como objetivo general, se busca aclarar la relación entre una conformación supramolecular dada y las propiedades físicas resultantes. Por un lado, la tesis se enfoca en la caracterización de los procesos de polarización y desplazamiento iónico en un material semicristalino con aplicaciones en almacenamiento de energía. Por otro lado, se estudiaron las propiedades mecánicas y eléctricas de un polímero intrínsecamente conductor, tanto en algunas nanoestructuras inducidas mediante diversos tratamientos, como en sus mezclas con el material semicristalino previamente mencionado. Este estudio se realizó sobre muestras en configuración de película delgada, en vista de sus posibles implementaciones en dispositivos electrónicos multicapa para aplicaciones energéticas. En concreto, nos enfocamos en la caracterización de dos polímeros: óxido de polietileno (PEO), un conductor iónico semicristalino utilizado para electrolitos sólidos, y el poli(3,4-etilendioxitiofeno)-poli(estireno

sulfonato) (PEDOT:PSS), un conductor electrónico comúnmente empleado en células solares y dispositivos electrónicos.

Primero, discutimos las propiedades dieléctricas de PEO en estado sólido y fundido a través de un estudio empleando espectroscopía dieléctrica de banda ancha (BDS). Este estudio nos ha permitido entender la cinética que gobierna la transición sólido-líquido, la dinámica del fundido y el papel que juega la heterogeneidad debida a la presencia de interfases.

La caracterización BDS de muestras altamente conductoras como el PEO suele verse obstaculizada por los fenómenos de polarización que tienen lugar a las interfaces de los electrodos que constituyen la muestra. Para evitar tal polarización interfacial, empleamos muestras con un grosor extremadamente bajo (< 100 nm); en esta situación, los efectos parásitos disminuyen ya que la fuerza dieléctrica de la polarización baja al disminuir el espacio entre los electrodos. Al seguir esta estrategia, pudimos abordar la transición de fusión siguiendo la constante dieléctrica del material bajo investigación durante la rampas de calentamiento y enfriamiento. Aquí, mostramos que la transición de sólido a líquido está acompañada por la presencia de un proceso atribuido al polímero fundido. Para obtener más información sobre cómo interviene este proceso en la relajación del líquido formado, realizamos otra serie de experimentos manteniendo las capas delgadas de polímero a una temperatura adecuada en el régimen de fusión, es decir, entre el inicio y el final de la transición. Este procedimiento nos permitió monitorear in situ el proceso de fusión. Al ocurrir de la transición sólido-líquido coincide la formación de una fase más móvil, y esto puede ser observado experimentalmente por la constante dieléctrica, que es, por lo tanto, una prueba del desarrollo de la fase líquida durante la fusión.

Asimismo, este estudio también proporciona información sobre la polarización dieléctrica inducida por cargas en las interfaces de materiales semicristalinos, mostrando la función que tiene la cristalinidad del polímero sobre la evolución de la movilidad iónica a temperaturas inferiores al punto de fusión. Con la intención de visualizar la disposición de las fases involucradas en los fenómenos de polarización interfacial, se empleó la caracterización nano-dieléctrica de las películas acoplando el concepto BDS con la microscopía de fuerza atómica (AFM). De tal manera se realizaron experimentos de espectroscopía nano-dieléctrica (*n*DS). La configuración y las condiciones de funcionamiento del experimento son descritas en detalle a través de un modelo que permite interpretar la señal de salida del microscopio, presentando la discusión teórica completa y su validación mediante datos experimentales. El modelo desarrollado implementa algunos principios desde aproximaciones preexistentes, esta vez teniendo en cuenta efectos locales del entorno de la punta a la distorsión del campo eléctrico

en la proximidad de la muestra. Además, se describe el factor de pérdida del movimiento del cantiléver bajo las condiciones experimentales y se relaciona este a la constante dieléctrica de la muestra investigada, presentando una herramienta fundamental para el estudio de las propiedades dieléctricas por AFM. Basándonos en este modelo, reportamos una descripción sobre la disposición de los canales de transporte de iones y la orientación preferencial de la polarización interfacial en las películas delgadas semicristalinas a partir de la caracterización obtenida mediante *n*DS-AFM. El estudio reveló una mayor conductividad iónica en proximidad de las áreas amorfas, las cuales conllevan a la vez una mayor contribución de los fenómenos de polarización.

Siempre bajo confinamiento en película delgada, estudiamos el material conductor orgánico PEDOT:PSS, que también exhibe su propia nanoestructura intrínseca. Para mejorar o modificar las propiedades de las películas delgadas obtenidas a partir del producto comercial, utilizamos dos técnicas de nanoestructuración: reprecipitación y *solvent vapor annealing* (SVA). El protocolo de reprecipitación propuesto permitió obtener nanoesferas poliméricas conductoras, mientras que mediante SVA fue posible modificar selectivamente la superficie de las películas tanto en su morfología como su conductividad. Las nanoestructuras obtenidas estuvieron compuestas por varias fases y caracterizadas por diferentes propiedades mecánicas y/o eléctricas. Para abordar las características composicionales y las propiedades físicas correspondientes a cada elemento que constituye las películas delgadas nanoestructuradas, se presenta y discute un estudio detallado de los estudios nanomecánicos y nanoeléctricos realizadas mediante AFM.

Las nanoesferas obtenidas por reprecipitación presentan un diámetro de 120 nm, conservando buenas propiedades mecánicas, ópticas y eléctricas. Sin embargo, la caracterización nanomecánica reveló un arreglo diferente de las fases de PSS y PEDOT respecto al precursor comercial, enseñando un enriquecimiento de PEDOT a la superficie de las nanoesferas. Por otro lado, a igual grosor de la película delgada, la investigación nanoeléctrica atribuye una conductividad más baja a las nanoesferas en comparación con el producto comercial. Debido a la disposición menos empaquetada de sus granos conductores, la conductividad de PEDOT:PSS, en dirección perpendicular al plano de su confinamiento monodimensional, baja al disminuir del grosor de este. Por lo tanto, los resultados designan una influencia más efectiva del confinamiento 1D sobre la conductividad eléctrica de las nanoesferas.

Pasando a las superficies modificadas por SVA, los resultados muestran que PEDOT:PSS expuesto a vapores de tetrahidrofurano bajo condiciones controladas resulta en una mayor movilidad de las cadenas de polímero, la cual permite una segregación vertical de PEDOT:PSS en el volumen de la película delgada, desde un estado granular hacia una capa superficial de unos pocos nanómetros (≈ 30 nm). Mediante un experimento de nanoindentación, sumado a mediciones nanoeléctricas, se pudo evaluar la disposición de la fase superior y su penetración en el volumen de la película. La naturaleza química del estrato superficial se estudió mediante pruebas nanomecánicas y mediante mediciones topológicas después de enjuague en solución acuosa. Los resultados enseñan que la capa superficial obtenida se dispone como un fino recubrimiento discontinuo de PEDOT neutro en cima de la película delgada, la cual mantiene las propiedades originales de PEDOT:PSS en el volumen de abajo de esa.

Para concluir nuestro estudio sobre los polímeros investigados, presentamos la caracterización de mezclas PEDOT:PSS/PEO. Las películas delgadas obtenidas a partir de estas mezclas poliméricas se investigaron variando la concentración de los dos componentes en toda la gama de composiciones. La separación de fases y la cristalización se han estudiado a diferentes escalas mediante la combinación de AFM y Grazing Incidence Wide Angle X-ray Scattering (GIWAXS). A partir de la caracterización de los compuestos, se pudieron observar en detalle varias disposiciones de los dos polímeros en las películas delgadas obtenidas a partir de estas mezclas, lo que reveló su influencia recíproca en determinar las propiedades finales.

El estudio sobre la topología de las varias mezclas analizadas enseña la típica conformación superficial esperada en el caso de películas obtenidas desde los componentes puros. A través de pruebas AFM y GIWAXS comprobamos una mayor cristalinidad al aumentar el contenido de PEO, mientras una evidente separación de fase se notó en aquellas muestras con un contenido de PEO igual o superior al 40%, que coincide con la concentración límite para una homogénea dispersión de PEDOT:PSS en la matriz PEO. Además, pudimos estimar las propiedades nanomecánicas y nanoeléctricas cuantitativamente a través de AFM y finalmente poner de manifiesto la dependencia de las propiedades físicas de las películas delgadas con su composición y estructura, tanto en la micro escala como en la nano escala. Al variar de la composición, logramos diferentes capacidades de recubrimiento, propiedades mecánicas y conductividad eléctrica. Los análisis nanomecánicos permitieron atribuir la naturaleza composicional de las fases registradas. Estas, en conjunto con los perfiles topológicos, permitieron identificar la preferencial disposición de PEO en capas ultra delgadas en muestras a concentraciones intermedias.

Las pruebas nanoeléctricas atribuyeron una conductividad creciente al aumentar de la concentración de PEDOT:PSS, tal y como esperado. Además, dependiendo del peso molecular del PEO, la respuesta eléctrica de las películas delgadas de las mezclas resultantes muestra algunas diferencias, las cuales se traducen en distintas conductividades eléctricas. En particular, una mayor conductividad fue registrada por PEO con pesos moleculares más elevados, lo cual en este caso es consecuencia de una favorecida segregación de dominios conductores al aumentar del peso molecular mismo.

El estudio presentado muestra nuevas alternativas para abordar la caracterización microscópica de las propiedades físicas en películas delgadas de polímeros a través de la investigación de materiales nanoestructurados. Las herramientas introducidas no solo sirvieron para una coherente descripción de los sistemas desarrollados en nuestro trabajo, sino se proponen como medios útiles a la caracterización de cualquier otra nanoestructura polimérica y non. Los materiales estudiados representan unos recursos cuyas implementación en ámbito energético se sigue investigando desde hace años. En este sentido, nuestro trabajo solo aporta algunas estrategias para el estudio y la modificación de sus nanoestructura con el intento de ampliar sus posibles empleos en los campos tecnológicos que les concierne. Sin embargo, nuestra caracterización a la micro y nano escala demuestra la naturaleza compleja de estos materiales, señalando la importancia que una nanoestructura específica dispone en el determinar las propiedades físicas de estos.

Outline of the thesis

Polymeric materials, commonly known as plastics, compose an enormous variety of products that scale the widest range of properties and applications, leading their scientific development to be one of the protagonists in the progress of facilities and accessories used in our daily life. However, to give a precise definition of plastic it is not always an easy task, as this terminology can space several different meanings depending on context and topics. Nevertheless, these materials share a series of characteristic properties: polymeric materials have a low specific weight per gram and, in many cases, they can also show good mechanical properties and flexibility. Also, they can often be solution processed and they usually have a low cost, providing a direct integration to industrial manufacturing. With the continuous development of new fabrication techniques and analysis instrumentation, the investigation and modification of these materials has been broadly carried out during the past few decades.

Polymers consist of large molecules, *i.e.*, macromolecules characterized by the multiple repetition of one or more species of atoms or groups of atoms (constitutional repeating units) linked each other in amounts sufficient to provide a set of properties that do not vary markedly with the addition of one or a few of the constitutional repeating units. In addition to the most commonly used polymers, as commodity polymers and engineering polymers, nowadays there is an increasing interest in the advanced polymeric materials, which can exhibit complex supramolecular nanostructures determining their specific behavior in bulk or under the operating conditions of the corresponding devices. Particularly important is the case when the polymeric material is used in the form of a thin film, as for instance in most of the applications in the electronic devices industry. This geometry gives rise to large interfaces, with air and/or substrate, impacting in many cases the resulting material properties.

In this thesis, we present the study of nanostructured polymers thin films with energy applications. The principal aim is to provide insights into the possible link between the supramolecular conformation and the resulting physical properties. To relate the effect of the nanostructural arrangement on the resulting properties, we focused on the impact that nanoconfinement could have on the behavior of several solid phases in thin film configuration, for which we investigated dielectric properties, charges displacement, and mechanical response. Hence, the work focuses on nano -dielectric, -electric, and -mechanical studies of polymer thin films. The characterization of these nanostructured polymers was mainly carried out by means of Atomic Force Microscopy (AFM). In addition, Broadband Dielectric Spectroscopy (BDS)

and Grazing-Incidence Wide-Angle X-Ray Scattering (GIWAXS) were also been used in the specific case of semicrystalline polymer thin films.

To facilitate the presentation of the results in a logical manner we have organized the different chapters as follows:

In chapter 1, we provide a general background on the main characteristics and properties of macromolecules, followed by an introduction on the effect of nanoconfinement in polymers.

In chapter 2, we present the polymers we have considered along this thesis work and the experimental methods and protocols followed in the contest of the several studies.

In chapter 3, we start presenting results on thin films of the well-known polymer poly(ethylene oxide), concerning the dielectric relaxation phenomena as obtained respectively by means of BDS and by the electric forces detected using a AFM-based approach.

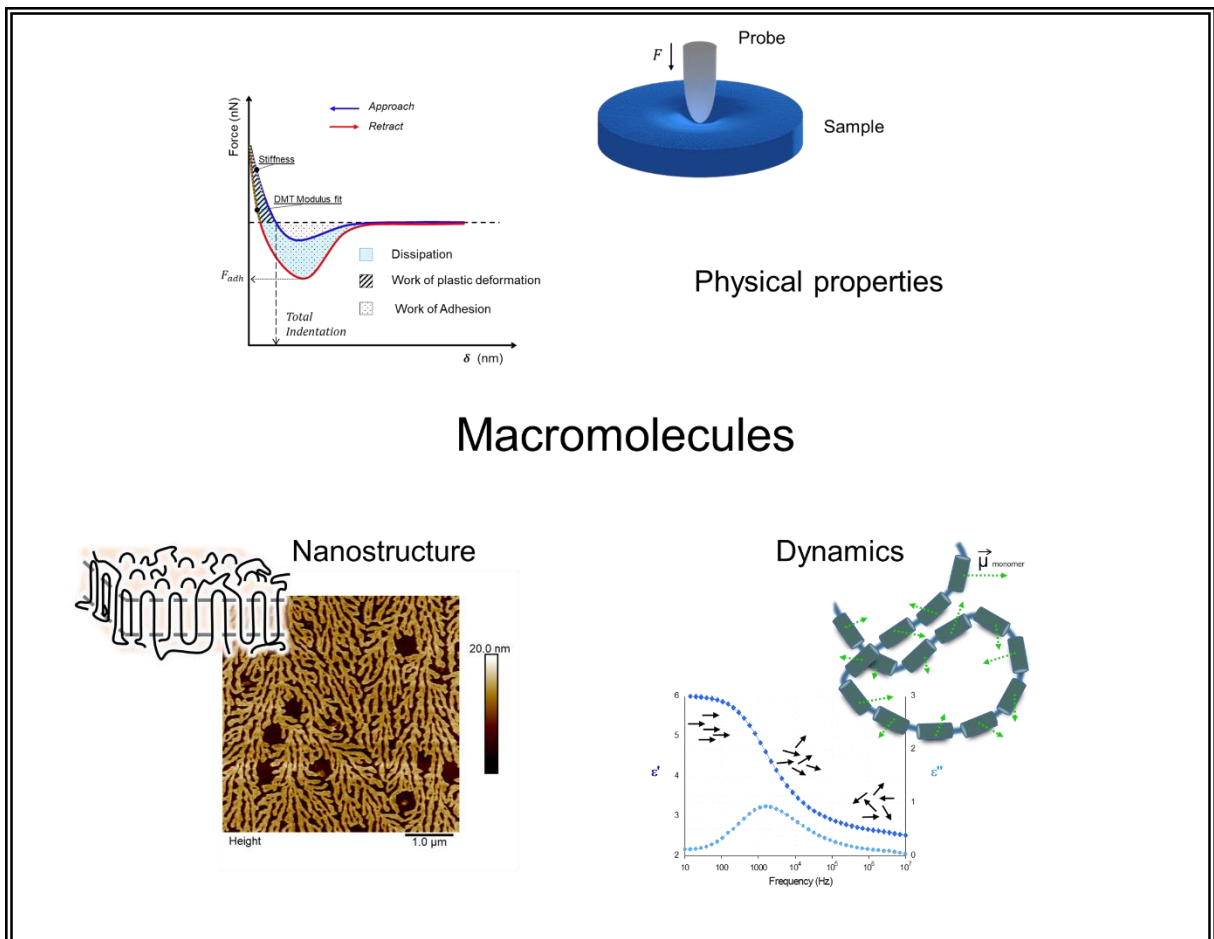
In chapter 4, we focused on the quantitative nanoscale study of the intrinsically conductive polymer poly(3,4-ethylenedioxythiophene):poly(styrene sulfonate) (PEDOT:PSS) through the investigation of some induced nanostructures obtained by reprecipitation and solvent vapor annealing methods.

In chapter 5, the blends resulting from the mixture of the two discussed polymers are studied, giving insights into the complex disposition of the new formed phases. Major attention was given to the impact of such arrangement onto the final nano-mechanical and nano-electrical properties.

The final conclusions and outlook of this thesis work are presented in chapter 6.

Chapter 1

Theoretical background



1.1 Macromolecules

The unique properties of polymers derive from their enormous molecular mass. This can vary for the different chains constituting the material, as they usually present different sizes. The most used units to indicate the molar mass distribution are the *number average* (M_n) and the *weight average* (M_w), defined as follows:

$$M_n = \frac{\sum_i N_i M_i}{\sum_i N_i} = \sum_i n_i M_i \quad (1.1)$$

$$M_w = \frac{\sum_i N_i M_i^2}{\sum_i N_i M_i} = \frac{\sum_i W_i M_i}{\sum_i W_i} = \sum_i w_i M_i \quad (1.2)$$

where N_i is the number of molecules of molar mass M_i , n_i the numerical fraction of those molecules, W_i the mass of molecules with molar mass M_i , and w_i the mass fraction of those. The standard deviation of the molar mass distribution ($\bar{\sigma}$), related to the ratio $\frac{M_w}{M_n}$ (*polydispersity* - *PDI*), can be expressed as: $\bar{\sigma} = M_n \sqrt{\frac{M_w}{M_n} - 1}$. A system of a given number of macromolecular chains constitutes a perfectly *monodisperse* polymer if $M_n = M_w$, resulting in a $PDI = 1$. This situation is generally not observed for any of the known synthetic or natural polymers, where $M_n < M_w$.

The chains size and its distribution have a direct impact on the final features and behavior of the polymer, being it a key factor affecting all those intrinsic physical aspects that characterize these functional materials, including rheological, mechanical, optical, and thermodynamic properties^{1,2}. An example is reported in Figure 1.1, where we can see how the molecular weight importantly affects the melting point of poly(ethylene).

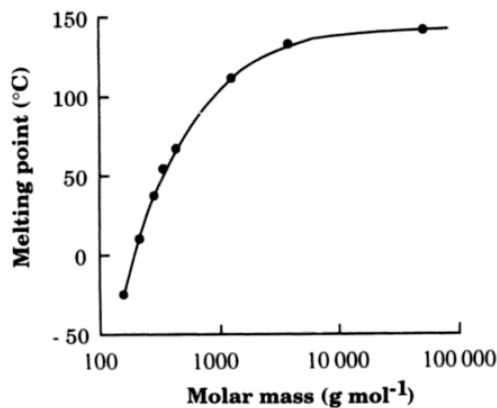


Figure 1.1. The dependence of the Melting Point (lower temperature for the material to undergo a transition between solid and melt) of poly(ethylene) respect its molar mass. Image taken from *Polymer Physics* (GEDDE U.L.F., 1995), drawn after data collected by Boyd and Phillips (1993)³.

1.2 Physical properties of polymers

Both in natural and in synthetic materials we can count a huge amount of polymers, differing from each other in chemical structures, physical features, and/or formulations ⁴. For this reason, the discussion of their properties in absolute terms is almost impossible as they can present an extended variety of the matter states. Nevertheless, one can observe the recurrence of some peculiar phase transitions or molecular dynamics which are characteristics of macromolecules ³. Taken into account the previous assumptions, the following paragraph reports a brief summary of those physical aspects retained useful for the comprehension of the intrinsic properties of polymers.

1.2.1 The glass transition

In the most general scenario, among the wide family of polymeric materials, many examples present, in a certain range of temperature, the physical state of glass. A *glass* is a non-crystalline solid. Glasses show the disordered and irregular structure typical of liquids, not allowing brownian motions or significant molecular displacements, resulting in a freezing-in of the molecules dynamics. A liquid melt or a rubber becomes a glass when it solidifies lowering down its temperature without crystallization ⁵. This phenomenon is commonly defined as *glass transition*. The glass transition is a pseudo second-order transition in which a supercooled melt yields, on cooling, a glassy structure. It is not a *true* thermodynamic phase transition due to the absence of discontinuity points in any of the derivatives of the free energy ⁶, hence it conserves a kinetic character ⁷. The temperature at which the glass transition occurs is the *glass-transition temperature* (T_g) ⁸. The kinetic aspect of this transition can be appreciated by observing the T_g shift in accord with the cooling rate, as the faster the liquid goes out of the equilibrium the highest the T_g results to be ⁹.

Among the most common techniques used to evaluate experimentally the T_g of a polymer we find calorimetric methods ⁹. For example, by Differential Scanning Calorimetry (DSC) it is possible to follow first or second order transitions in the studied material by measuring the difference in Heat Flow between one sample and a standard, both heated at the same heating rate. The results of the DSC analysis on a sample of poly(vinyl acetate) (PVAc) is presented in Figure 1.2(a), where is visible the pseudo second order transition, associated to the glass transition, as a vertical inflection of the heat flow in proximity of the T_g .

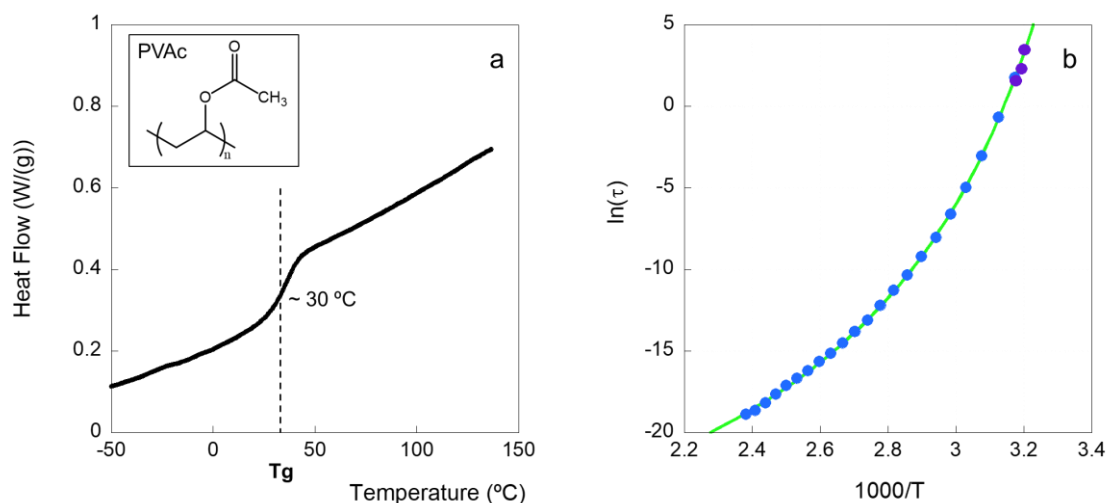


Figure 1.2. a) PVAc mid density ($M_w = 140$ g/mL; $T_g \approx 30^\circ$ C) thermogram obtained experimentally by DSC. b) trend of τ associated to the glass transition in PVAc mid density as a function of T. The data were experimentally acquired in our laboratories by BDS (blue dots) and Modulated-DSC (purple dots). VFT fit (eq. 1.3) plotted as a green line.

The segmental motions responsible of the change from the liquid (or rubbery) state to the glassy state, and the other way around, are connected to a relaxation time (τ), that is the time characterizing spontaneous fluctuations of polymer segments¹⁰. The relaxation times associated to such dynamics range between low values ($\tau < 10^1$ s) at $T > T_g$ to relatively high ($\tau \gg 10^2$ s) at $T < T_g$. The τ related to the glass transition usually follows a Vogel-Fulcher-Tammann (VFT) equation (eq. 1.3)¹¹ and it is called *segmental relaxation time* (τ_α). The typical dependence of τ_α with temperature is shown in Figure 1.2(b).

$$\ln(\tau) = \ln(\tau_0) + \frac{T_0 D}{T - T_0} \quad (1.3)$$

τ_0 is the high temperature limit of the time constant, T_0 the Vogel temperature, and D a constant.

1.2.2 Crystallinity

The glass transition concerns disordered systems and constitutes a fundamental background for better understanding the rubbery or the glassy state of polymeric materials. However, these aspects alone do not fully describe all the conformations adopted by polymers as, in some cases, they allow a certain degree of order which can lead, as an example, to the

formation of crystals¹². For kinetic reasons, the formation of an ideal crystal from a highly entangled and disorderly coiled melt, *i.e.*, a polymer melt, is highly improbable. For this reason, polymers are almost never 100% crystalline then, we call those allowing any crystallinity degree “semicrystalline” materials¹³. The intrinsic chemical regularity of the macromolecules, meaning their degree of periodicity in the repetition of a compositional unit, both in composition and symmetry, is the dominant factor that determines if a polymer can crystallize or not. For example, defects and end-groups constituting different chemical centers respect to the repeating units favor disorder, consequently lowering the degree of crystallinity¹⁴. In a similar way, for those polymers presenting stereocenters, the stereoregularity generally allows a higher crystalline degree^{15,16}.

The crystalline unit cell of a polymer crystal is composed of atoms of different chains, these chains densely stuck together in their rigid elongated conformation giving a hierarchical structure in such a way as to result in their lowest conformational energy. The conformation adopted by the single chain varies with the chemical nature of the polymer itself¹⁶. As an example, in Figure 1.3 we reported the typical repeating units along a segment of crystallized chain in the case of high-density poly(ethylene) (HDPE) and isotactic poly(propylene) (iPP)¹⁷.

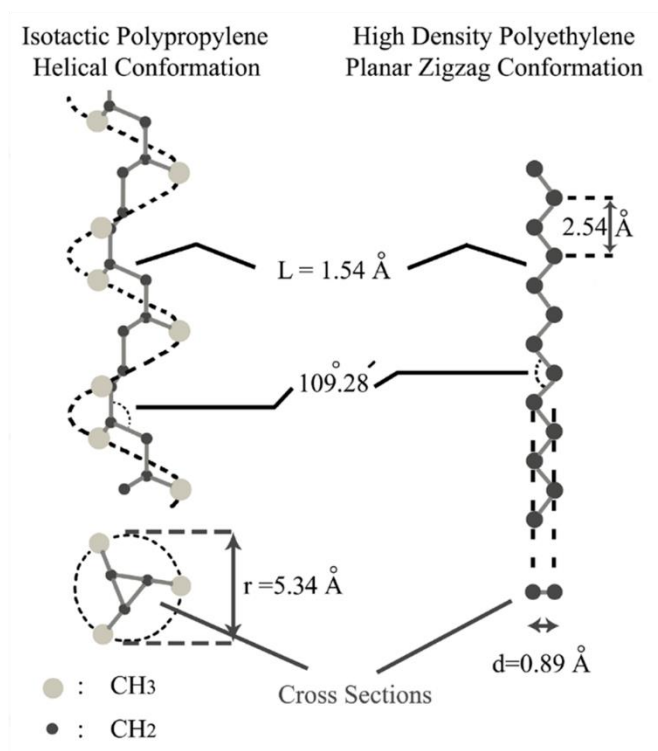


Figure 1.3. Arrangement of the atoms in high-density poly(ethylene) (HDPE) and isotactic poly(propylene) (iPP) molecules along a segment of crystallized chain. Image taken from the work of Nejabat G. R¹⁷.

Figure 1.4 shows the crystals nucleation growth typical of polymers. The crystalline portion of the bulk material locates usually in domains named “crystalline lamellae”. Each lamella is a nanometric thin sheet (usually between 10 and 20 nm) composed of packed macromolecular chains organized perpendicularly to the two flat parallel facets constituting the interface¹⁸. The chains fold at the interfaces providing multiple crystalline segments in loops that can repeat adjacently or more irregular, as schematically sketched in Figure 1.4(a,b). Then, the amorphous portion of a semicrystalline polymer locates at the interface of the crystalline lamellae, where the chains cannot adopt any ordered structure¹⁹. Molecular bridges are features commonly formed in these regions, where multiple lamellae share the same polymer chains through amorphous branches²⁰. Due to their peculiar growth from the liquid, the crystalline lamellae dispose in characteristic superstructures. At the very beginning of the crystallization, small nuclei form from the liquid state (Figure 1.4(1)) from which the crystalline lamellae start growing radially (Figure 1.4(2)) to finally generate rounded microscopic objects, either called “spherulites” (Figure 1.4(3)). A spherulite size can vary over a large range. Based on the initial arrangement of the crystalline nuclei and their development, the spherulites arrange among the vacant free volume with typical patterns, one of them drawn in Figure 1.4(4)).

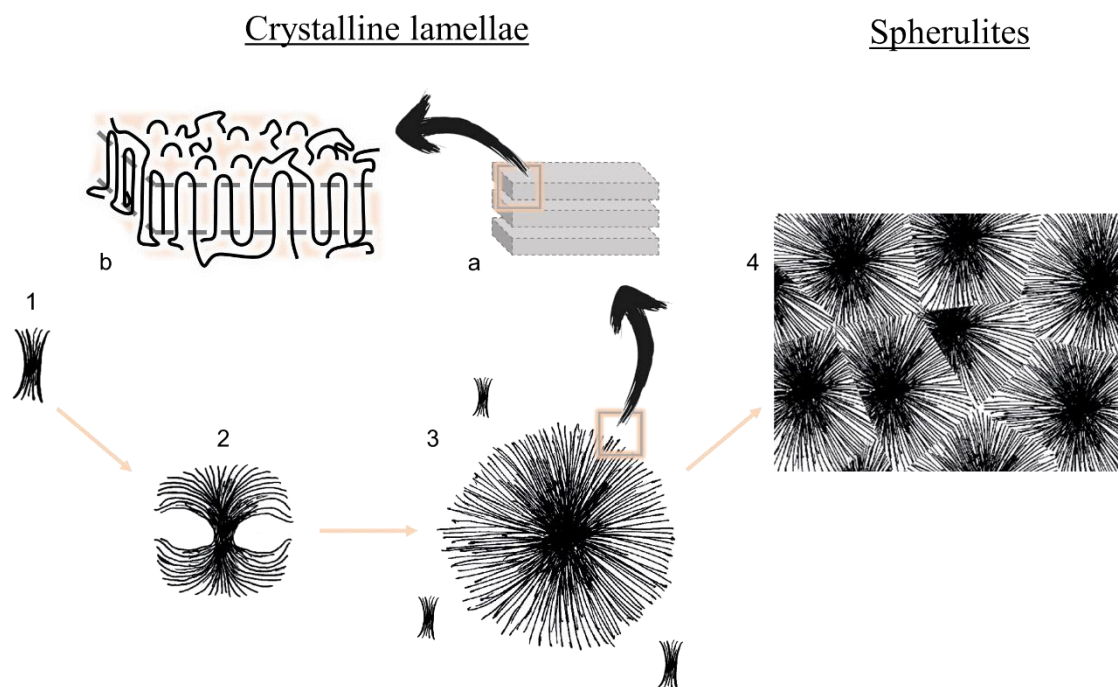


Figure 1.4. Growth and spatial configuration of semicrystalline polymers. At first, small nuclei appear among the melt (1), on which thereafter the crystalline lamellae start growing radially (2) to finally form spherulites (3). The spherulites can aggregate in suprastructures accordingly to the volume they can fill (4).

Semicrystalline polymers obey to the Bragg's law (eq. 1.4). As the dimensions of such semicrystalline objects is in the range of the X-Ray radiation, X-Ray scattering methods allow determining the crystallinity degree and long range ordering. According to the Bragg's law:

$$n\lambda = 2d \sin(\theta) \quad (1.4)$$

where λ is the wavelength of the diffracted light, n the diffraction order, d the spacing between the lattice planes of the crystal, and 2θ the scattering angle. For example, in a *Wide Angle X-Ray Scattering* experiment (WAXS) one preferential scattering angle, characteristic for the unit crystal cell, return a defined peak in intensity of scattering, while any amorphous contribution would appear as part of a broad hump covering a wide range of diffraction angles ¹⁶.

1.2.3 Mechanical properties of polymers

As previously mentioned, a convenient feature of polymers is their extremely versatile mechanical response for unit of weight which, among others, constitutes one of the most critical factors determining their impressive technological impact ²¹.

We can describe and compare the mechanical properties of different objects by several attributes, one of the most used is the Young's modulus (E) ²². The value of E is intrinsic of a material, in the Hooke's law it is expressed as:

$$E = \frac{\sigma}{\epsilon} \quad (1.5)$$

$$\sigma = \frac{F}{A} \quad (1.6)$$

where σ is the stress resulting as the value of force (F) applied to the body per unit of area (A), and ϵ is the strain, meaning the deformation (δ) per deflection unit. Considering an initial length l_0 , for a longitudinal stretch follows:

$$\epsilon = \frac{\delta}{l_0} \quad (1.7)$$

Another unit relevant to describe the mechanical response of polymers is the *stiffness* (k), which gives information about the elasticity. k is defined as the force divided by the deformation ²².

$$k = \frac{F}{\delta} \quad (1.8)$$

The Young's modulus does not only vary for materials presenting different chemical structure, but it is also influenced by changes in phase ²³, hydration state ^{24,25}, and other factors

²⁶. For this reason, it is normally temperature dependent ²². In polymers, we have a marked change in modulus between the rubbery state and the glassy state, *i.e.*, in the proximity of T_g . Moreover, the modulus drops down when the plastic melts, meaning that we expect a drastic change near the melting point (T_m) for those polymers that allow a melting transition before undergoing degradation. Interestingly, the crystallinity degree of a polymer has a direct impact over the elastic modulus because the crystalline objects constitute physical branches providing a more rigid lattice for a bulk material. For this reason, in a semicrystalline polymer the modulus does not change as much as in an amorphous one at the T_g , and a more defined melt transition is obtained due to the fusion of the crystalline domains at a specific T_m , as sketched in Figure 1.5 ²⁷.

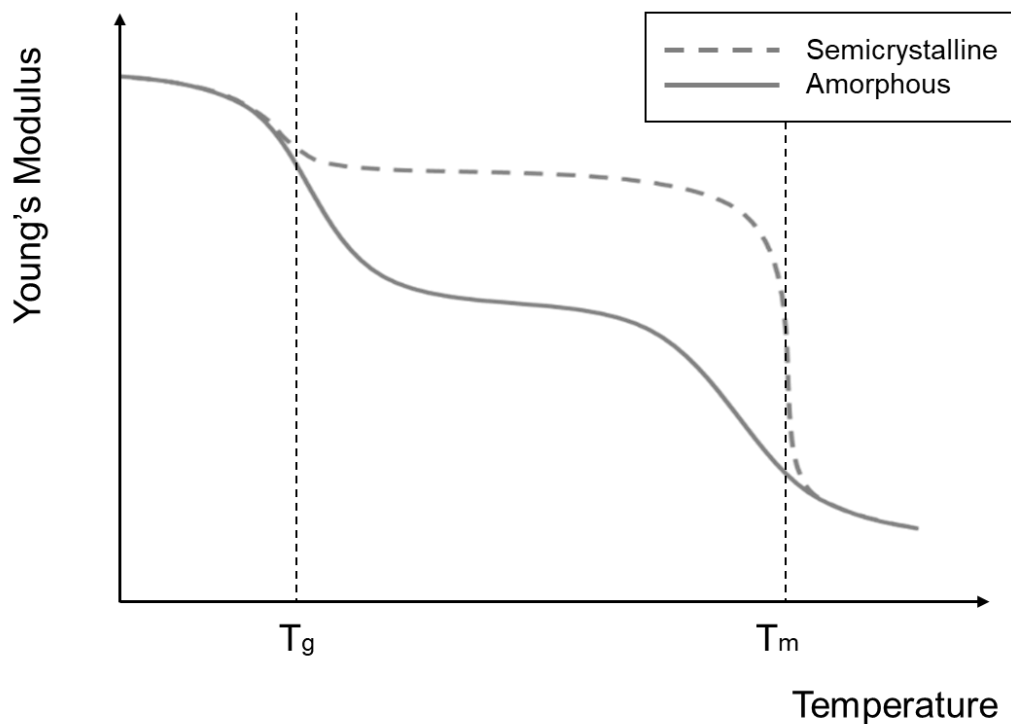


Figure 1.5. Young's modulus in logarithmic scale respect to the temperature for a generic polymer ²⁸.

The most usual way to evaluate the Young's modulus of a material is analyzing the stress-strain curve obtained by elongation, compression, or torsional analysis to directly deriving E from eq. 1.5 ²⁹. Alternatively, it is possible to take advantage of an indenter for indentation experiments by means of several approaches differing each other for indenter shape, indenter dimensions, and environment. These kinds of techniques use a force applied to a sharp probe in order to induce a partially plastic partially elastic deformation on the analyzed material, this provides the so-called *Force-distance Curve* (FC) useful for the quantitative evaluation of the mechanical properties ³⁰. In this field, probes possessing a size of the order of the

nanometers, or few tens of nanometers, enable performing nano-indentation experiments, which come particularly useful for the study of small material volumes and thin films³¹. When this principles are coupled to Atomic Force Microscopy (AFM), we are even able to determine such properties by imaging the mechanical response of submicrometer objects, obtaining information about complex surfaces composed of different micro- and nano- domains presenting heterogeneous mechanical phases, as further deepen in section 2.3.1³². To contextualize, we reported in Figure 1.6 the scheme of a FC as obtained by an AFM probe.

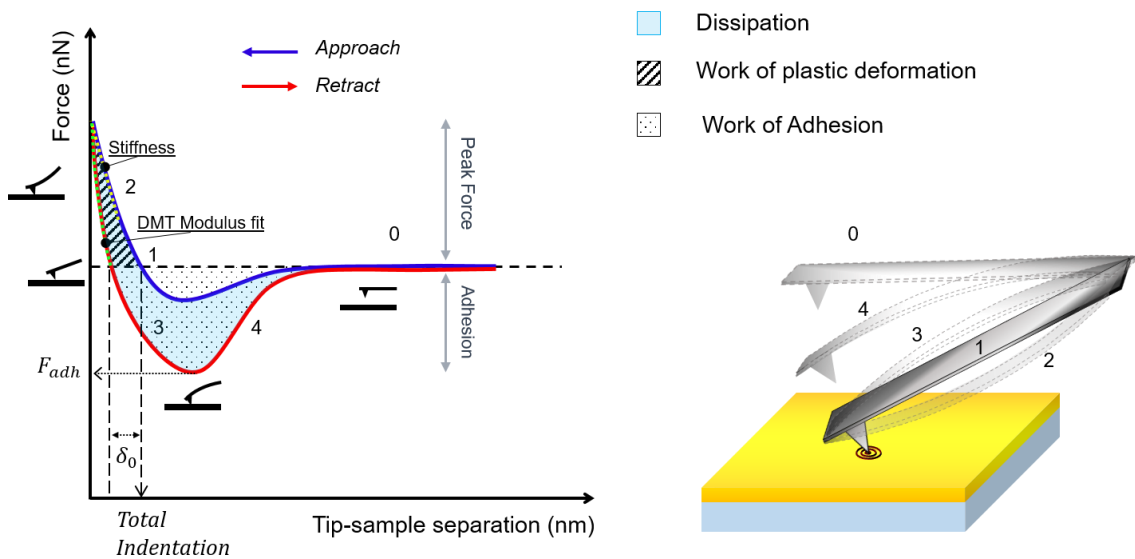


Figure 1.6. Aspect of a Force-distance Curve, neglecting any contribution arising from the *ringing mode* (see section 2.3.1), where F_{adh} is the Adhesion Force and δ_0 the sample plastic deformation.

By nanomechanical analysis we can count a lot of mechanical information stored in a single FC, such as the adhesion force (F_{adh}), the plastic deformation, the dissipation, the work of adhesion, or the work of plastic deformation, and also the Young's modulus³³. To have quantitative estimations of the E it is fundamental to model the contact between the tip and the sample. In this context, Sneddon and Hertz provided two different models for the evaluation of the tip-sample contact area (Figure 1.7)³⁴.

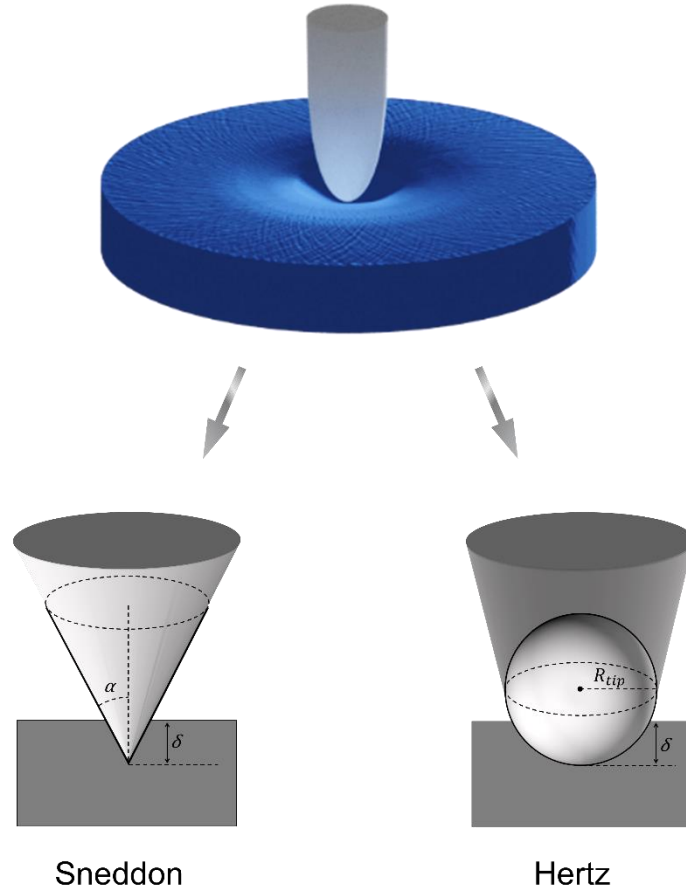


Figure 1.7. Scheme of the tip shape model for two different approximations in an indentation experiment.

$$F = \frac{2}{\pi} \frac{E}{(1-\nu^2)} \tan(\alpha) \delta^2 \quad (1.9); \quad F = \frac{4}{3} \frac{E}{(1-\nu^2)} \sqrt{R_{tip}} \delta^3 \quad (1.10)$$

The relationship between the applied force F and the indentation depth δ is given by eq. 1.9 for the Sneddon model and by eq. 1.10 for the Hertzian model, being α the cone angle (in the Sneddon approximation), R_{tip} the tip radius (in the Hertz approximation), and ν the Poisson's ratio. According to the Hertzian model, the contact area s can be calculated by eq. 1.11 (being a the contact radius) as follows.

$$s = \pi a^2 = \pi \left(\frac{R_{tip} F}{E} \right)^{\frac{2}{3}} \quad (1.11)$$

The model used in our calculations to derive the mechanical modulus from an FC is the Derjaguin-Müller-Toporov (DMT), that is an extension of the Hertz model which takes into account the adhesion force between the contacting bodies³⁵. In the DMT model, the adhesion

forces are considered as a force offset ³⁶. From the simplified DMT model, one can get the relation between force and indentation as:

$$F - F_{adh} = \frac{4}{3} \frac{E}{(1-\nu^2)} \sqrt{R_{tip}} \delta^3 \quad (1.12)$$

1.2.4 Dielectric properties of polymers

Polymers are mostly known to be good electrical insulators having in most of the cases high resistivity, therefore presenting the capability to hinder a current flow. These sorts of materials are also known as “dielectrics”. In this context, the dielectric properties of polymers are not only of fundamental importance in the world of electronics and electrical engineering ³⁷, but they can unveil the intrinsic molecular or charges dynamics specific of the material, also yielding valuable information upon the polymer structure ³⁸. In this section, an introduction to some basic concepts of electrostatics will be provided, and it then will be presented their implementation in describing relaxation phenomena in polymers.

Elements of electrostatics

The study of the interaction of electric fields with matter and its distribution in the free space for stationary (or slow-moving) electric charges concerns that branch of physics known as “electrostatics” ³⁹. The principles of electrostatics are well described by Maxwell’s equations and Coulomb’s laws. One of the most discussed issues in this field is brought by the charge distribution in molecules and its impact on the properties and dynamics of matter. For example, molecular features such as “dipoles”, possessing a purely electrostatic character, are of fundamental relevance to describe natural phenomena. An electric dipole is the framework resultant from any separation of positive and negative charges in the considered portion of the space; here, the dipole moment ($\vec{\mu}$) is the related system’s polarity magnitude. In the simplest scenario of 2 charges respectively positive and negative, with electric charge respectively $+q$ and $-q$, separated by a distance \vec{d} (Figure 1.8 (a)), the dipole moment vector corresponds to $\vec{\mu}_{(q1_q2)} = q \vec{d}$. Extending this definition to a volume V for a continuous distribution of charges ($\rho(r)$) we obtain:

$$\vec{\mu}(r) = \int_V \rho(r) (\vec{r} - \vec{r}') d^3\vec{r}' \quad (1.13)$$

where \vec{r} is the reference position and $d^3\vec{r}'$ the infinitesimal volume fraction.

Even though not every molecular system possesses a dipole moment, we can count a big amount of them that generate dipoles, a few of those are represented in Figure 1.8 (b,c,d).

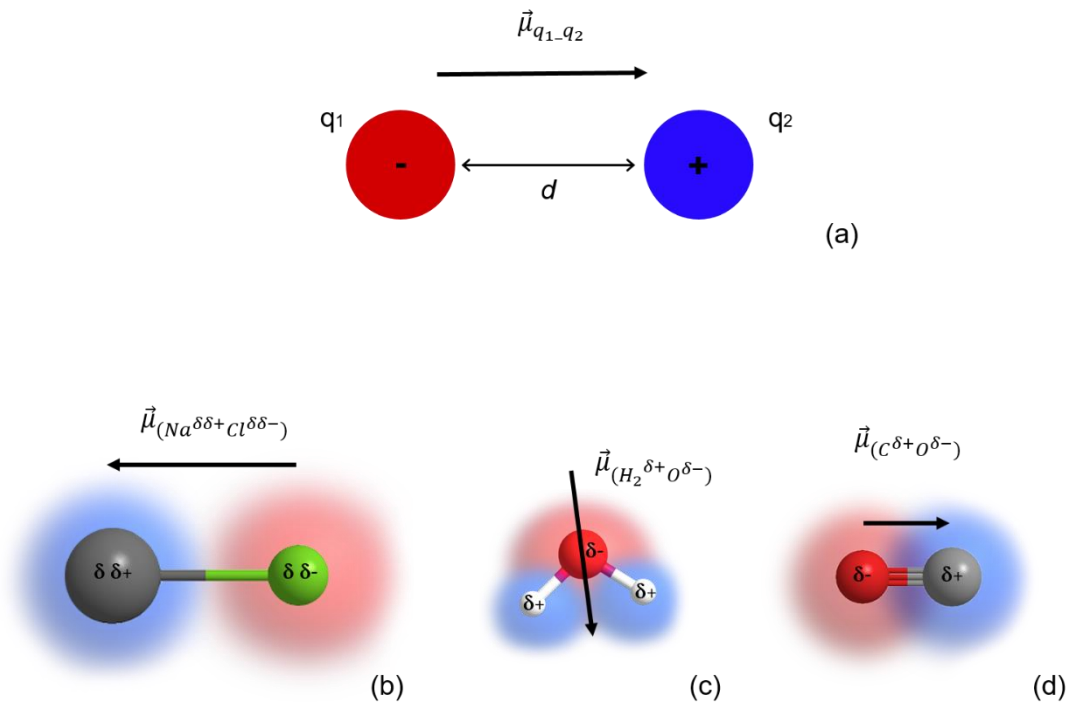


Figure 1.8. a) Schematic representation of a dipole generated from two charges $+q$ and $-q$ separated by a distance d . Below: schematic representation of dipoles in NaCl (b), H₂O (c), and CO (d).

Considering a volume V containing N elements with dipole moment $\vec{\mu}$, it is possible to evaluate the macroscopic polarization \vec{P} from eq. 1.14, which can be reformulated as eq. 1.15 for every element of the volume uniaxially oriented by an electric field \vec{E} .

$$\vec{P} = \frac{1}{V} \sum_{i=1}^N \vec{\mu}_i \quad (1.14)$$

$$\vec{P} = \frac{N}{V} \langle \vec{\mu} \rangle \quad (1.15)$$

There are two main polarization mechanisms, i) induced polarization, in which the presence of the external electric field is at the origin of the electrical dipole moments, and ii) orientational polarization, that arises from the reorientation of existing (molecular) dipoles, provoked by the external electric field. As a first approach to quantitatively evaluate the orientational polarization \vec{P}_{OR} for a set of molecules with dipole moment $\vec{\mu}$, we assume some conditions: (i) the dipoles do not interact with each other, and (ii) the electric field \vec{E}_{Local} at the location of the dipole is not being affected by the dipole itself and it is equal to the outer electric field. Under these requirements, the mean value of the permanent dipole moment is only

affected by thermal fluctuations against the electric field axis, which can be expressed by a Boltzmann distribution considering the interaction energy for the dipole with the electric field as $\vec{\mu} \cdot \vec{E} = \mu E \cos(\theta)$ (with θ the angle between the two vectors):

$$\langle \vec{\mu} \rangle = \frac{\int_{4\pi} \vec{\mu} e^{\left(\frac{\vec{\mu} \cdot \vec{E}}{k_B T}\right)} d\Omega}{\int_{4\pi} e^{\left(\frac{\vec{\mu} \cdot \vec{E}}{k_B T}\right)} d\Omega} \quad (1.16)$$

where $e^{\left(\frac{\vec{\mu} \cdot \vec{E}}{k_B T}\right)} d\Omega$ is the probability to have the dipole vector oriented between Ω and $\Omega + d\Omega$ in the space angle, k_B the Boltzmann constant, and T the temperature. Eq. 1.16 can be simplified by approximating the interaction energy of the dipole with the electric field to be weak compared to the thermal energy⁴⁰. By this approximation, we obtain eq. 1.17.

$$\langle \vec{\mu} \rangle = \frac{\mu^2}{3k_B T} \vec{E} \quad (1.17)$$

Combining eq. 1.15 and 1.17 finally leads to eq. 1.18.

$$\vec{P} = \frac{N}{V} \frac{\mu^2}{3k_B T} \vec{E} \quad (1.18)$$

The polarization \vec{P} describes the dielectric displacement originating in the material as a consequence of an applied external electric field. Considering the dielectric displacement defined as $\vec{D} = \epsilon_s \epsilon_0 \vec{E}$ ($\vec{D}_0 = \epsilon_0 \vec{E}$) for small electric field strength, the polarization can be expressed as:

$$\vec{P} = \vec{D} - \vec{D}_0 = (\epsilon_s - 1)\epsilon_0 \vec{E} \quad (1.19)$$

where ϵ_0 is the permittivity of vacuum ($8.854 \times 10^{-12} \text{ V}^{-1} \text{ m}^{-1}$) while ϵ_s is the static relative permittivity of the material.

Introducing the contribution \vec{P}_∞ to the relation presented in eq. 1.18, and obtaining $\vec{P}_s = \frac{N}{V} \frac{\mu^2}{3k_B T} \vec{E} + \vec{P}_\infty$, we are finally able to link the dielectric permittivity to the permanent dipole moment as:

$$\epsilon_s - \epsilon_\infty = \frac{N}{V} \frac{\mu^2}{3k_B T} \quad (1.20)$$

where ϵ_∞ accounts exclusively for the induced polarization mechanism: $\vec{P}_\infty = (\epsilon_\infty - 1)\epsilon_0 \vec{E}$.

1.2.5 Relaxation in polymers

Relaxation phenomena occur when the perturbation of a system gives rise to a time dependence in some of the system properties. For instance, mechanical relaxation occurs when, after applying an instantaneous stress, the deformation varies with time until reaching a new equilibrium value^{41,42}. In the case of dielectric relaxation, the dielectric permittivity is time dependent. Thus, in general relaxation deals with the response of the sample to the applied perturbations. A particular case of general interest is that where the response of the sample to the applied perturbation is just proportional to the strength of the perturbation itself (linear response). In this situation the fluctuation-dissipation theorem states⁴⁰:

“The response of a system at the thermodynamic equilibrium to a small applied disturbance is the same as its response to a spontaneous fluctuation”

By considering the dielectric relaxation, for an applied electric field on a dielectric material with a certain polarizability, we can schematically assume its polarization response in time as represented in Figure 1.9.

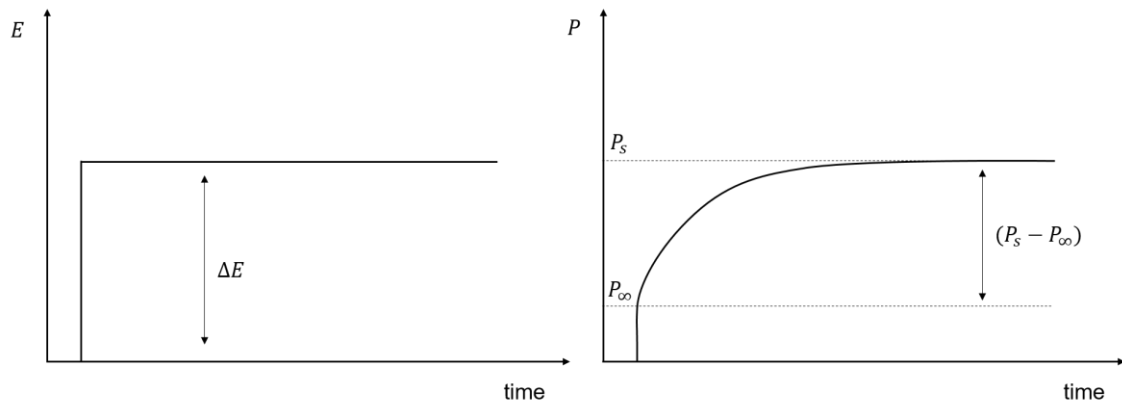


Figure 1.9. Representation of the polarization P resulting in a dielectric material from an applied electric field E in time.

Introducing a normalized *Creep Function* $\Phi(t) = (1 - e^{-\frac{t}{\tau_D}})$, with τ_D defined as the time constant characteristic for the polarization process, it is possible to express $P(t)$ as a function of P_s and P_∞ as :

$$P(t) = P_\infty + (P_s - P_\infty)\Phi(t) = P_\infty + (P_s - P_\infty)(1 - e^{-\frac{t}{\tau_D}}) \quad (1.21)$$

This time dependence of the polarization implies a time dependent dielectric permittivity $\varepsilon(t)$. This can always be expressed as a complex dielectric permittivity in the frequency domain by a simple Fourier transformation:

$$\varepsilon^*(\omega) = \varepsilon'(\omega) - i\varepsilon''(\omega) = \varepsilon_\infty - \int_0^\infty \frac{d\varepsilon(t)}{dt} e^{-i\omega t} d\omega \quad (1.22)$$

From eq. 1.21 and 1.22, the corresponding model to describe the relaxation in terms of dielectric constant in function of the frequency is obtained:

$$\varepsilon^*(\omega) = \varepsilon_\infty + \frac{\varepsilon_s - \varepsilon_\infty}{1 + i\omega\tau_D} \quad (1.23)$$

Eq. 1.21 and 1.23 describe the so-called *Debye model* for a generic dielectric relaxation⁴⁰. In this model the real part is given as: $\varepsilon'(\omega) = \varepsilon_\infty + \frac{(\varepsilon_s - \varepsilon_\infty)}{1 + (\omega\tau_D)^2}$ and the imaginary part as: $\varepsilon''(\omega) = (\varepsilon_s - \varepsilon_\infty) \frac{\omega\tau_D}{1 + (\omega\tau_D)^2}$.

Thus, the imaginary part shows a peak (the loss peak) with a maximum at $\omega_{MAX} = 1/\tau_D$ and width 1.14 decades, whereas the real part shows a step increase when the frequency is reduced through ω_{MAX} .

The *Debye* relaxation is the simplest case that one can face analyzing the dielectric function $\varepsilon^*(\omega)$ and it is normally rare in usual systems, where the measured dielectric functions are much broader in frequency than predicted by it and, in many cases, asymmetric. For this reason, several empiric model functions were proposed taking advantage of shape parameters. Here we report the three most used examples: the Havriliak-Negami (eq. 1.24) setting α and β as shape parameters with $0 < \alpha, \alpha\beta \leq 1$, and the two particular Cole-Cole (eq. 1.25), and Cole-Davidson (eq. 2.26).

$$\varepsilon^*(\omega) = \varepsilon_\infty + \frac{\varepsilon_s - \varepsilon_\infty}{(1 + (i\omega\tau_{HN})^\alpha)^\beta} \quad (1.24)$$

$$\varepsilon^*(\omega) = \varepsilon_\infty + \frac{\varepsilon_s - \varepsilon_\infty}{1 + (i\omega\tau_{CC})^\alpha} \quad (1.25)$$

$$\varepsilon^*(\omega) = \varepsilon_\infty + \frac{\varepsilon_s - \varepsilon_\infty}{(1 + i\omega\tau_{CD})^\beta} \quad (1.26)$$

With $\frac{1}{\tau_p} = \frac{1}{\tau_{model}} \left(\sin\left(\frac{\alpha\pi}{2+2\beta}\right)^{\frac{1}{\alpha}} \left(\frac{\alpha\beta\pi}{2+2\beta}\right)^{\frac{1}{\alpha}} \right)$ for τ_p being the characteristic relaxation time of the considered polarization mechanism which corresponds to the reciprocal of the angular frequency at the maximum of $\varepsilon''(\omega)$. As we can observe in Figure 1.10, the Havriliak-Negami model fits very well the dielectric data of PVAc.

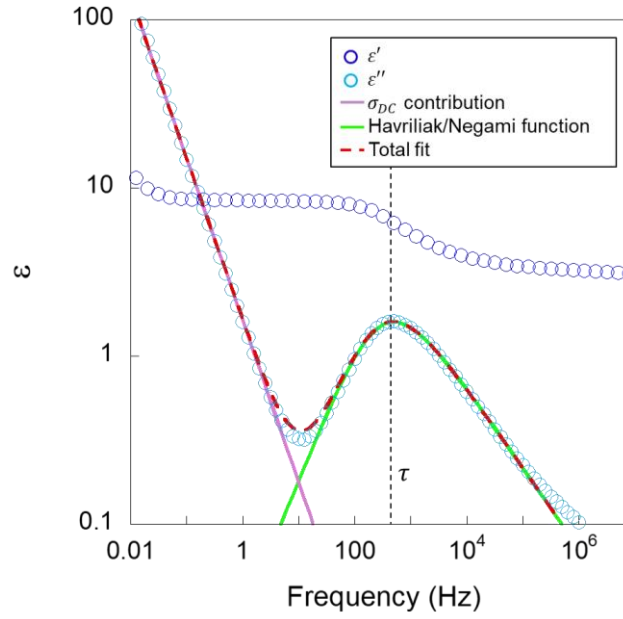


Figure 1.10. BDS spectrum of PVAc at 70° C.

It is worth to be mentioned that the fluctuation of mobile charge carriers also affects the dielectric function as conductivity and permittivity are linked.

$$\sigma^*(\omega) = \sigma'(\omega) + i\sigma''(\omega) = i\omega\varepsilon_0\varepsilon^*(\omega) \quad (1.27)$$

The movement of parasitic electric charges at low frequency, like the fast frequency independent displacement of ionic impurities able to generate important D.C. conductivity contributions to the dielectric function, significantly alters the dielectric response of the material. As an example of this, we can distinguish the pronounced conductivity contribution in the dielectric spectra of PVAc at 70° C in the low frequency range (Figure 1.10). In this case, the measured permittivity should be described as:

$$\varepsilon^*(\omega) = \varepsilon_\infty + \frac{\varepsilon_s - \varepsilon_\infty}{(1 + (i\omega\tau_{HN})^\alpha)^\beta} + \frac{\sigma^*(\omega)}{i\omega\varepsilon_0} \quad (1.28)$$

Different models have been proposed to allow a proper description of the dielectric function considering conductivity contributions in the low frequency range, here we mention two of them: the Jonscher empirical model (eq. 1.29) and the free energy barrier model proposed by Dyre (eq. 1.30).

$$\sigma'(\omega) = \sigma_{DC}(1 + (\omega\tau_j)^s) \quad (1.29)$$

$$\sigma^*(\omega) = \sigma_{DC} \left(\frac{i\omega\tau_e}{\ln(1+i\omega\tau_e)} \right) \quad (1.30)$$

Where σ_{DC} is the d.c. conductivity contribution, τ_j and τ_e are time constants, and s a power law parameter with boundaries: $0 < s \leq 1$.

1.3 Polymers for electronics

The technological development of organic conducting materials has been a challenging research topic in the past decades. Due to their unique structural properties, polymers have revealed to be particularly promising in the engineering of such materials^{43,44}. In fact, even though most of the polymer materials are good insulators, we find several exceptions of particular technological interest in the field of organic conducting materials.

Nowadays, we count with a great number of commercial polymers with many different properties and electrical conductivity is no exception. As electrical conduction may occur through the movement of either electrons or ions, we distinguish between “polyelectrolytes” (ion conduction), “conducting” (ohmic conduction) and “semiconducting” (low non-ohmic conduction) polymers. Some of the main chemical structures of these materials are summarized in Figures 1.11 and 1.12. Their main applications in nano- and micro- devices include: Supercapacitors⁴⁵, Organic Thin Film Transistors (OTFTs)⁴⁶, Organic Solar Cells (OSCs)⁴⁷, and Light Emitting Diodes (OLED)⁴⁸, among several others⁴³.

Semiconducting polymers (Figure 1.11 (b,d and f)) are characterized by conjugated or partially conjugated π -orbitals that extend all over the single chains, giving a conductive band separated in energy by a defined potential from the valence band. Electron conducting polymers (Figure 1.11 (a, c and e)) can be obtained from a semiconducting oxidized precursor: the oxidation brings to the compound electronic vacancies that tend to be filled by neighbor groups, this allows to reduce the band gap between the conductive and non-conductive states of the system⁴⁹ and for an applied ΔV the vacancies can now move along the chains generating a current. This phenomenon is known as “hopping conduction” and it implies localized electrons discrete jumps across an energy barrier from one site to another⁵⁰. In this regime, an electron can overcome the energy barrier by two different paths: step over it or tunneling through. The relative importance of these two mechanisms depends on the shape of the barrier and the availability of thermal energy⁵¹. Contrary to metallic ordered conducting media, in a hopping conduction regime the conductivity increases by increasing temperature⁵² according to the Variable Range Hopping (VRH) model expressed by eq. 1.31.

$$\sigma(T) = \sigma_0 e^{\left(\frac{-T_0}{T}\right)^\beta} \quad (1.31)$$

T_0 and σ_0 are constants, while β varies depending on the considered model; in the most known Mott VRH model, $\beta = \frac{1}{d+1}$ where $d = 1, 2$ or 3 for 1, 2 or 3 dimensional conduction respectively⁵³.

Often, an inert charge carrier is necessary to balance the charges of the conductive polymer when its oxidized form is a radical ion. Organic materials resulting from coupled ions and electrons conductors are known as mixed ionic-electronic conductors (OMIECs), both anionic and electronic transports contribute to the electrical response of OMIECs devices⁵⁴, which find their application in multiple fields, spacing from electronics to health technology⁵⁵.

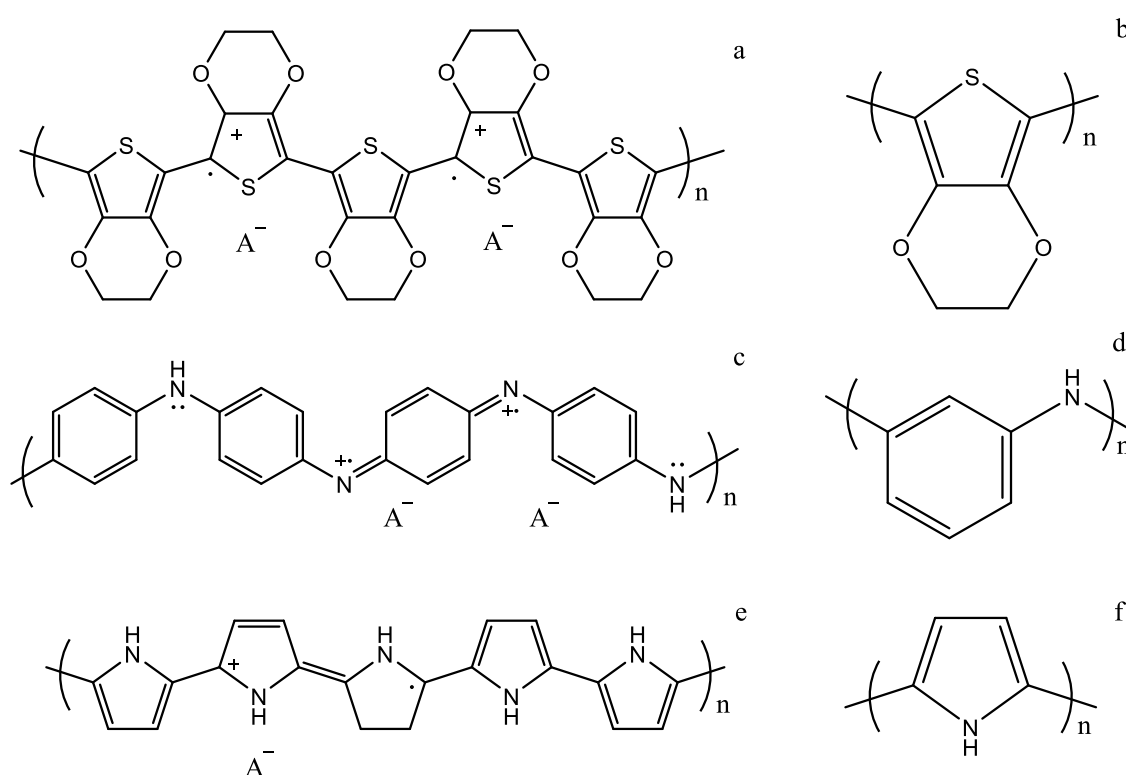


Figure 1.11. Chemical structure of important semiconducting (b,d,f) and conducting polymers (a,c,e). a) oxidized (benzoid) poly(3,4-ethylenedioxythiophene) (PEDOT); b) PEDOT; c) oxidized Polyaniline (PANI); d) PANI; e) oxidized Polypyrrole (PPy); f) PPy.

Among the conducting polymers, poly(3,4-ethylenedioxythiophene) complexed with poly(styrene sulfonate) (PEDOT:PSS, Figure 1.11 (a) for $A^- = PSS$) is perhaps one of the most studied ones. Originally patented in 1991 as “Baytron”, PEDOT:PSS presents good processability, high electrical conductivity, optimal optical transparency in the visible region when processed as thin films, high thermal stability and good mechanical flexibility⁵⁶. PEDOT:PSS is the most widely used polymeric material for fabricating the existing photovoltaics (PVs), displays, transistors and various sensing electronics⁵⁷.

Finally, polymer electrolytes (Figure 1.12 (a-d)) cannot transport electrons or vacancies, but ions. Macromolecules containing electronegative atoms can coordinate metallic cations by coulombic interaction, it permits them to dissolve different types of salts giving mobility to the dissolved ions inside the polymeric matrix ⁵⁸. This class of materials is mostly employed as Solid Polymer Electrolytes (SPE), leading to applications in batteries ⁵⁹. The main SPE matrixes are obtained from monomers containing oxygen or halide atoms, including poly ethers, poly alcohols, poly esters and poly halides (Figure 1.12).

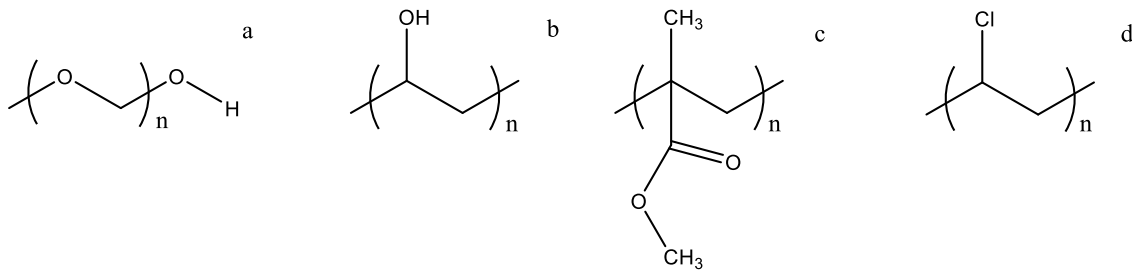


Figure 1.12. Chemical structure of polymer electrolytes. a) poly(ethylene oxide) (PEO); b) poly(vinyl alcohol) (PVA); c) poly(methyl methacrylate) (PMMA); d) poly(vinyl chloride) (PVC).

The ionic conductivity of an electrolyte can be determined by the number density (n) of the charges (q) and by the ionic mobility (μ_q) by following the Einstein relation (eq. 1.33) ⁶⁰:

$$\sigma = \sum_i n_i q_i \mu_{q_i} \quad (1.32)$$

$$\mu_q = \frac{Dq}{k_B T} \quad (1.33)$$

$$\mu_q \propto \frac{1}{\tau_s} \propto \omega_s \quad (1.34)$$

where D is the ions' diffusivity, which can be estimated as a function of a characteristic relaxation time τ_s . Several models, such as VFT-like, Dynamic Bond Percolation (DBP) ⁶⁰, the Random Barrier Model (RBM) ⁶¹, and others ^{62,63}, were developed through the years to predict the ion mobility and diffusivity from experimental data.

1.4 Polymer blends

Multicomponent polymer mixtures have been widely employed and studied in materials engineering among several different fields of application as they constitute an effective way to tune the final materials characteristics or to achieve new ones ^{64,65}. The benefits coming from blending polymers are several, such as providing materials with the desired properties and/or with improved performance at the lowest price ^{64,66}. In the easiest approximation, polymer blends divide in two types: miscible and immiscible. Ideally, miscible blends do not present any phase separation between the elements constituting the blends, while immiscible blends show multiple phases each containing purely one of the elements constituting the system. However, this first approximation does not give a comprehensive esteem of real systems, where partial miscibility might be observed. For this reason, we also distinguish partially miscible blends. The physical properties of the blend strongly depend on its miscibility degree, which in turn depends on its chemical and compositional nature ⁶⁵. In thermodynamic terms, as schematically sketched in Figure 1.13, considered ΔG_m the Gibbs free energy of mixing for a binary blend composed of elements 1 and 2, we define it as completely miscible if the relations in eq. 1.35 and 1.36 are satisfied for every possible value of ϕ , being $0 \leq \phi \leq 1$ the volume fraction of one of the two elements.

$$\Delta G_m < 0 \quad (1.35)$$

$$\frac{\partial^2 \Delta G_m}{\partial \phi^2} > 0 \quad (1.36)$$

If the system never satisfies these conditions, the blend will be completely immiscible, conserving two phases respectively pure in component 1 and in component 2 at every concentration of those. For the intermediate situation (partially miscible blends), a certain concentration threshold of solubility for one element into the other, or for both elements into each other, is observed. This can lead to the formation of multiple phases composed of miscible blends. In Figure 1.13, we reported the conditions in terms of ΔG_m describing polymer blends miscibility and the expected impact of it on the molecular dynamics of the obtained material.

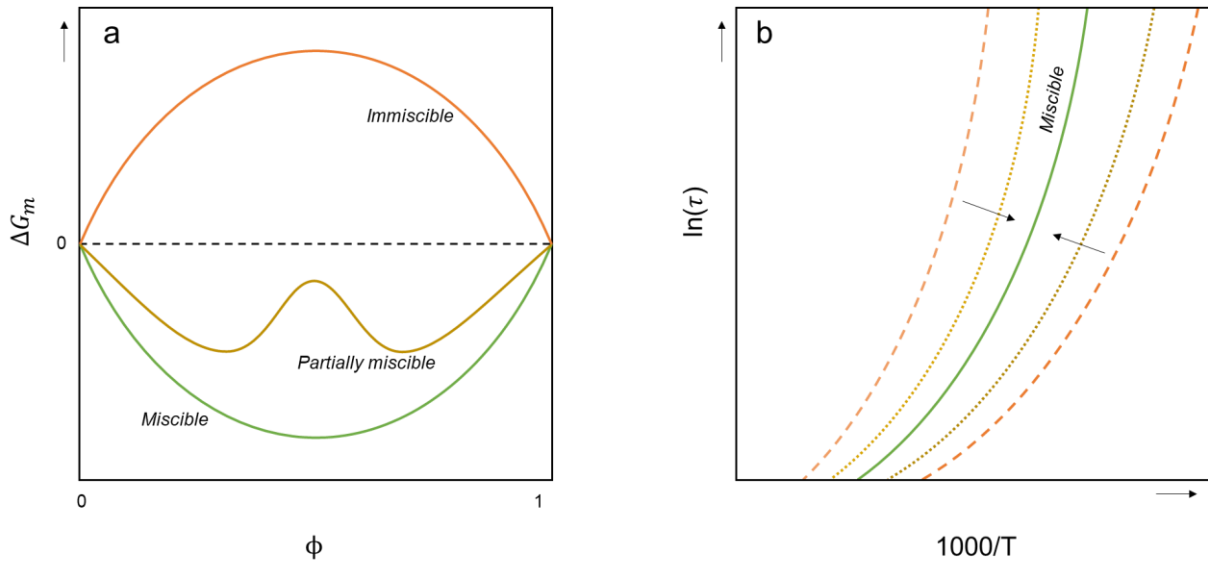


Figure 1.13. ΔG_m in function of ϕ and segmental relaxation dynamics for different cases of di-component polymer blends.

The properties of polymer blends are strictly related to their morphology thus, the characterization of the microscopic arrangement of the different phases that they might present constitutes an important tool to better understand their macroscopic physical aspects⁶⁷. In this context, several microscopy techniques have been employed through the years to get access to important information such as degree of miscibility and the type of phase separation. Among them, we can find optical microscopy (POM), confocal microscopy, transmission electron microscopy (TEM), scanning electron microscopy (SEM), or AFM⁶⁵. Thanks to such characterization techniques, it has been observed that polymer blends can in some cases provide well defined nanostructures, making the design of such compounds an interesting starting point to obtain nanostructured materials⁶⁸.

1.5 Nanostructured materials

Nanostructured materials are composed of building units with at least one of their dimensions at a length scale ranging from tens to few nanometers. The great scientific interest around these systems arises from their unique properties, intimately connected to their patterns at the nano-scale⁶⁹. We find in nature several examples of nanostructures, such as the complex architectures built by biological systems both in cellular frames and extracellular tissues⁷⁰. All these structures form as consequence of self-assembly processes, *i.e.*, an ordered aggregation of matter that is spontaneous in the given environmental conditions. Among the big variety of self-assembled nanostructures observed in synthetic polymers, one of the most known is the already introduced supramolecular aggregation of the lamellae in semicrystalline polymers (section 1.2.2).

A nanostructured material presents by definition one or more of its constitutional units confined in a certain geometrical shape. In other words, nanostructured materials are composed of nanoconfined elements. The nanoconfinement effects on the glassy dynamics of polymers have been broadly studied for several systems^{71,72}. In particular, it was observed that the increased freedom (compared to the bulk) of the surficial segmental motions would importantly reduce the T_g for a polymer confined in a geometry which maximizes its exposed surface to air (“soft” nanoconfinement). On the other hand, if the nanoconfinement is “hard” (for the interface of the nanoconfined object being adsorbed on another material) the T_g increases^{73,74}. In the scene of structural changes induced by confinement in polymeric materials, crystallinity does not make exception: depending on the nanometric block geometry and dimension, one nanoconfined semicrystalline polymer can significantly differ in temperature of crystallization and melting respect to the bulk material as long as in its crystallinity degree^{75,76}.

The structural and functional behavior of a nanostructured material is strongly affected by its arrangement at the nanoscale, which makes crucial to have control over the disposition and morphology of the repeating patterns for the given nanostructure. For this reason, several nanostructuring techniques have been developed through the years to effectively tune or artificially induce a certain nanostructure on a target material, such as laser irradiation methods⁷⁷, electrospinning, solvent displacement⁷⁸ or solvent induced methods⁷⁹. In this thesis we present the study of different polymer nanostructures that we obtained in thin film configuration. Thereafter, in order to provide a general idea of what kind of confinement they represent, in the following lines we describe the main expected features from polymer thin films.

Polymer thin films

Polymer thin films are polymeric layers having a thickness ranging from fractions of micrometers to few nanometers. Their most common fabrication strategy is spin coating, but other methods, such as dip coating, solvent casting, or inject printing, are also employed. The application fields are several, ranging from biomedical to electronics, which explains their big technological impact in recent years. Thin films can be modelled as a 1D confinement where the geometrical shape parameter is the thickness of the film itself. Due to the extremely low thickness, thin films use to be supported on a substrate and the interaction at the interface with it is not of secondary importance regarding the formation of the film and its final conformation and properties. The strength of this interaction drives important aspects as homogeneity and intrinsic molecular dynamics. For strong interactions, the adhesion forces at the interface with the substrate lead to the formation of a first adsorbed thin layer on which the film grows, in this case homogeneous coatings are obtained even for extremely low values of thickness. Vice versa, repulsive interactions between the sample and the substrate disfavor the formation of ultra-thin films and often promote “dewetting”, which is the phenomenon occurring when a continuous thin polymer film breaks up due to the instability of the film conformational geometry⁸⁰. To describe the stability of a film at a thickness $h > h_0$ (being h_0 the minimum film thickness), we can say as follows. By taking a polymer solution/melt on a substrate and introducing the interface potential between the two equal to φ , it is possible to describe the system as stable, metastable, or unstable assuming the occurrence of dewetting when the second derivative of φ respect to the thickness is negative, as shown in Figure 1.14(a).

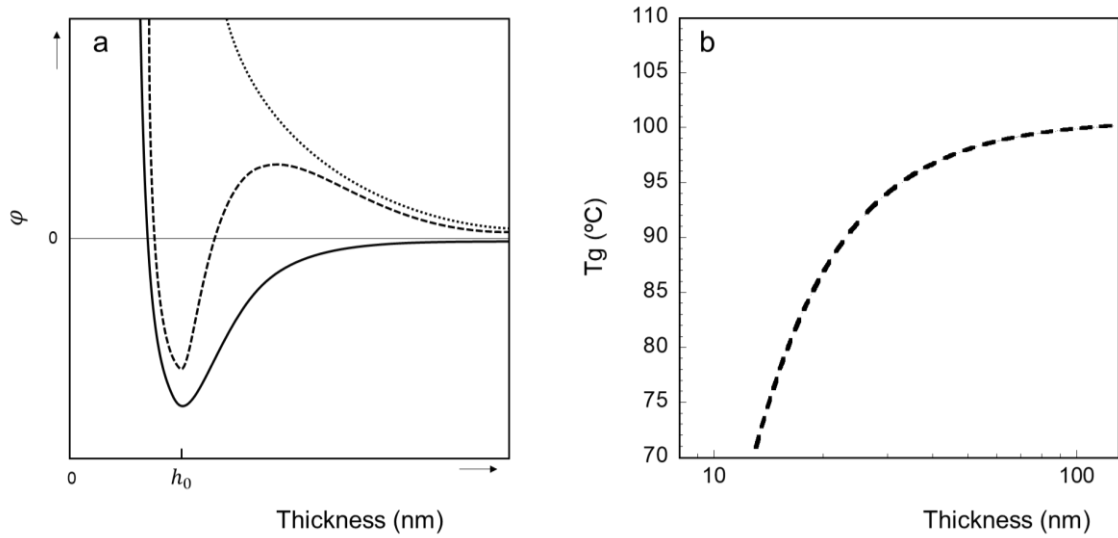


Figure 1.14. a) Sketch of the effective interface potential φ as a function of film thickness for stable (dotted line), unstable (solid line), and metastable (dashed line) films; b) Values of T_g for PS thin films in function of thickness as predicted by the Keddie's model ⁸¹.

The adsorbed layer between the polymer and the surface gives a hard confinement contribution to the film ⁸². By the recent advances in the topic ⁸³, we know that the adsorption/desorption depends on temperature usually following an Arrhenius activated process with energy comparable to the segmental mobility. The adsorption/desorption kinetics respect the annealing time can be expressed by a logarithmic growth which continues until reaching an equilibrium plateau ⁸⁴.

In supported polymer thin films, the fraction of material open to the atmosphere respect with the bulk one is maximized, but at the same time the layer adsorbed on the substrate provides a constrained interface, hence both hard and soft confinements play a significant role in such geometry ^{82,85}. In this scenario, changes in T_g can be expressed as a function of thickness (h) through empirical relations. As an example, eq. 1.37 enables estimating the T_g introducing a characteristic length α and a free parameter δ ⁸¹.

$$T_g(h) = T_{g,bulk} \left(1 - \left(\frac{\alpha}{h} \right)^\delta \right) \quad (1.37)$$

Beside these physical aspects, the thin film geometry also affects the capability of a polymer to crystallize, having in most of the cases direct impact on the degree and the layout of crystallinity ⁸⁶. It was observed that the transition between two and three dimensional spherulites can be induced by thickness reduction. This constitutes the first and simplest example of semicrystalline materials behavior in 1D confinement ⁸⁷. Moreover, in polymer thin

films the lamellae growth can undergo a preferential orientation due to interactions with the substrate. Strong interactions hinder the flow of the melt promoting a vertical stuck of the rigid chain segments during crystallization for extremely low thicknesses⁸⁸, as schematized in Figure 1.15(a). This is the case of PEO, that can orient its crystalline frontiers preferentially in-plane in such allocation, preserving a dendrimer-like morphology in dewetted or partially dewetted configurations (Figure 1.15(b))⁸⁹.

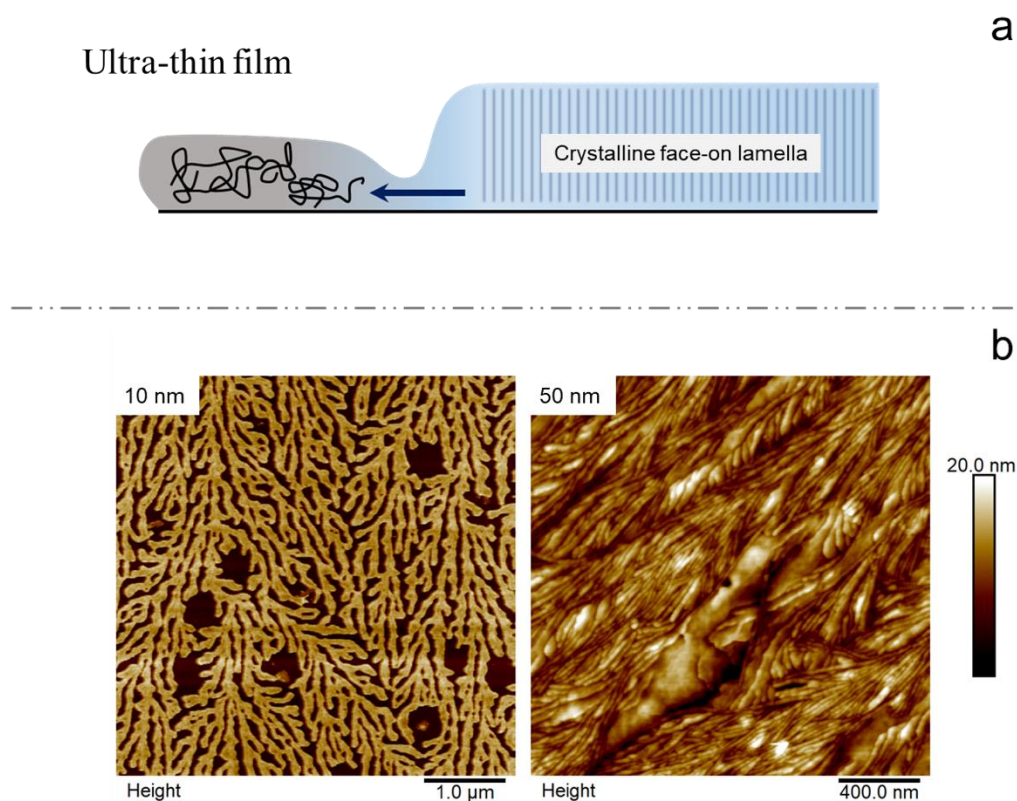
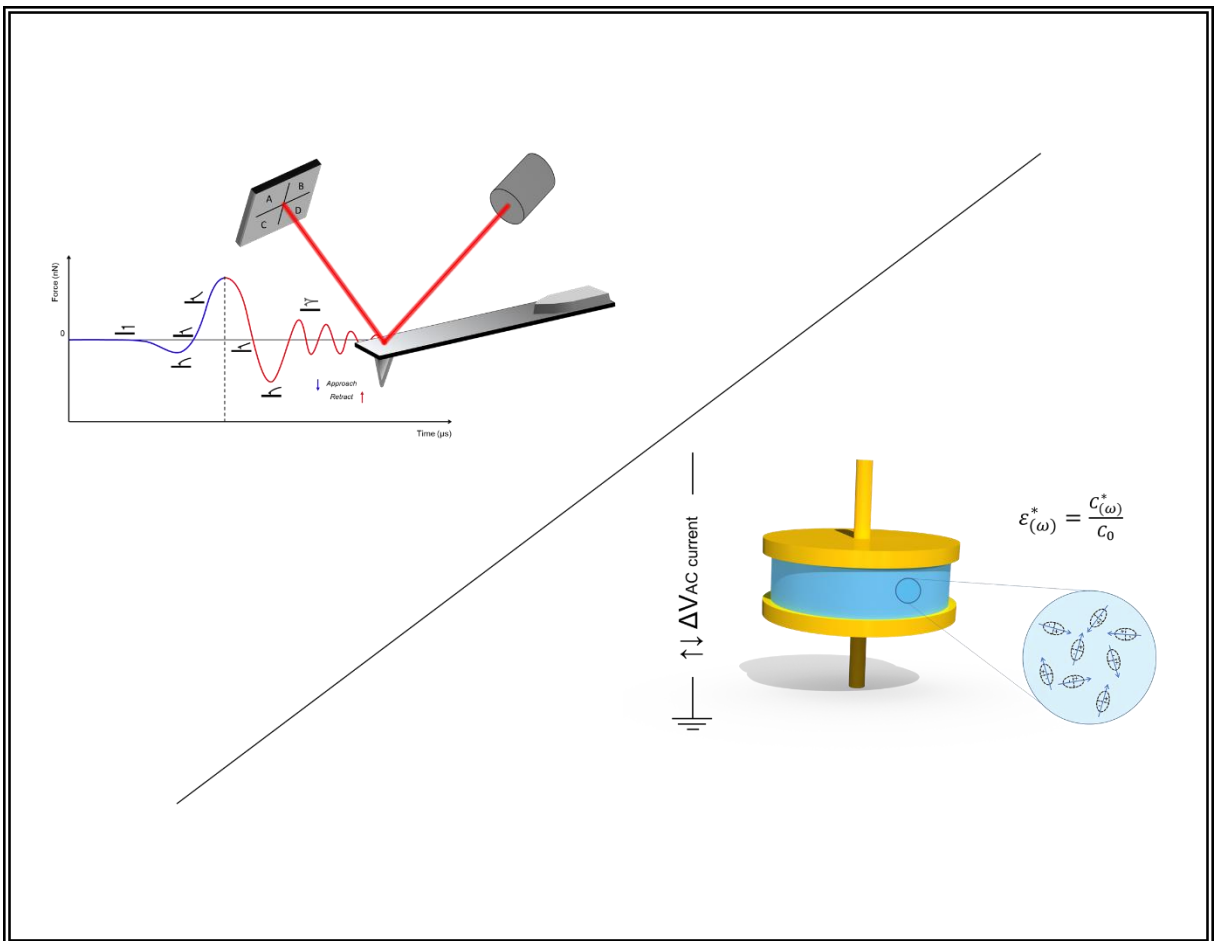


Figure 1.15. a) scheme of the crystallization process from melt of a polymer ultra-thin film. b) AFM images of PEO thin film respectively with thickness of 10nm and 50 nm.

Along with phase transitions, thickness-induced variation of intrinsic physical properties, such as viscoelasticity or conductivity are not rare^{90,91}. At this respect, the nature of the confinement effects on the physical properties of polymer thin films is not always easy to measure. The current challenges in understanding the involved interphases and their complex dynamics mostly consist in the necessity of developing fast and robust strategies to investigate the nanoscopic features characterizing these kinds of systems⁹².

Chapter 2

Materials and methods



2.1 Materials

Poly(ethylene oxide)

Poly(ethylene oxide) (PEO), also known as poly(ethylene glycol) (PEG), is a polymeric compound usually synthesized starting from ethylene oxide, which finds several applications both in industry and medicine⁹³. Due to the high ionic conductivity of this material, PEO is also employed as solid polymer electrolyte (SPE) in its doped state^{94,95}; being the most used doping agent for this kind of systems Li⁺ based salts⁹⁴. PEO T_g is around -50° C, but it is not easily detectable by traditional calorimetric techniques⁹⁶, due to its relatively high crystalline degree. In fact, PEO has a high crystalline degree at room temperature with usual values of T_m and T_c respectively ~60° C and ~50° C (Figure 2.1).

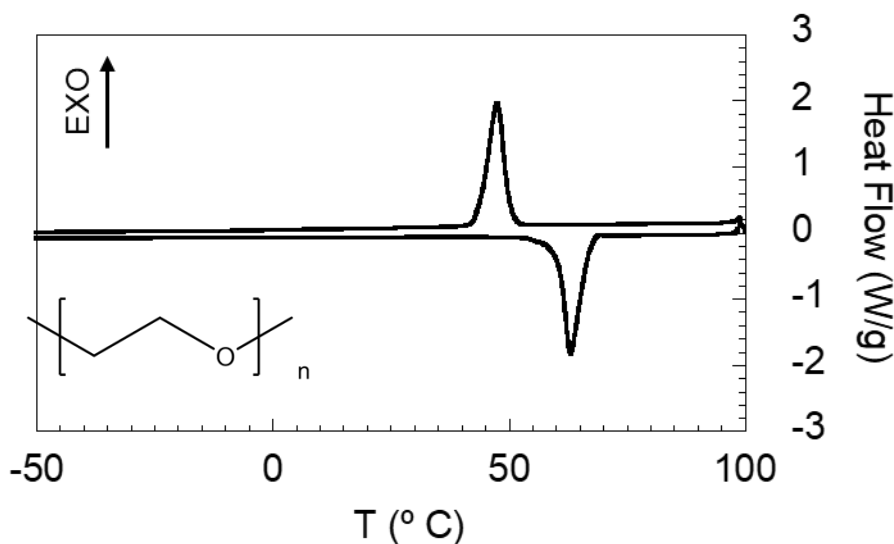


Figure 2.1. Crystallization and melting of PEO as observed by the heat flow per gram respect to the temperature, respectively associated to an endothermic and an exothermic first order transitions. DSC results for PEO^{35kDa} (cooling corresponds to positive heat flow and heating to negative heat flow values).

The physical properties of this polymer, such as mechanical properties, ion conductivity and viscosity, or the crystallinity degree, strongly depend on the molecular weight⁹⁷. For the work presented in this thesis, PEO with different molecular weights was purchased from Sigma Aldrich and used as received (200 kDa: product #181994; 100 kDa: product #181986; 35 kDa: product #94646).

Poly(3,4-ethylenedioxythiophene) poly(styrene sulfonate) (PEDOT:PSS)

PEDOT:PSS is an intrinsically conducting polymer composed of partially oxidized PEDOT⁺ chains coordinated to PSS⁻ to balance the positive charges. Commercial PEDOT:PSS is usually synthesized from EDOT monomer in presence of PSS through electrochemical polymerization in water providing water-based dispersions presenting different electrical conductivities depending on the PEDOT to PSS ratio, which is characteristic of every formulation⁹⁸. The aqueous product obtained from the synthesis is composed of PEDOT:PSS (insoluble) and un-coordinated PSS (soluble), being this in excess with respect to PEDOT⁽ⁿ⁺⁾. The coulombic interactions between the positively charged PEDOT segments and the negative PSS side groups lead the system's stability, which makes of fundamental importance the ratio between the two in the resulting material^{99,100}. Commercial PEDOT:PSS is usually available as a water dispersion composed of highly conducting nanoparticles dispersed in a dilute water solution of PSS. In fact, the electric conductivity mechanism and the macroscopic properties of this material are strongly related to its nanostructured nature¹⁰¹. The radius of the nanoparticles can range between 30 and 500 nm depending on the synthesis conditions¹⁰².

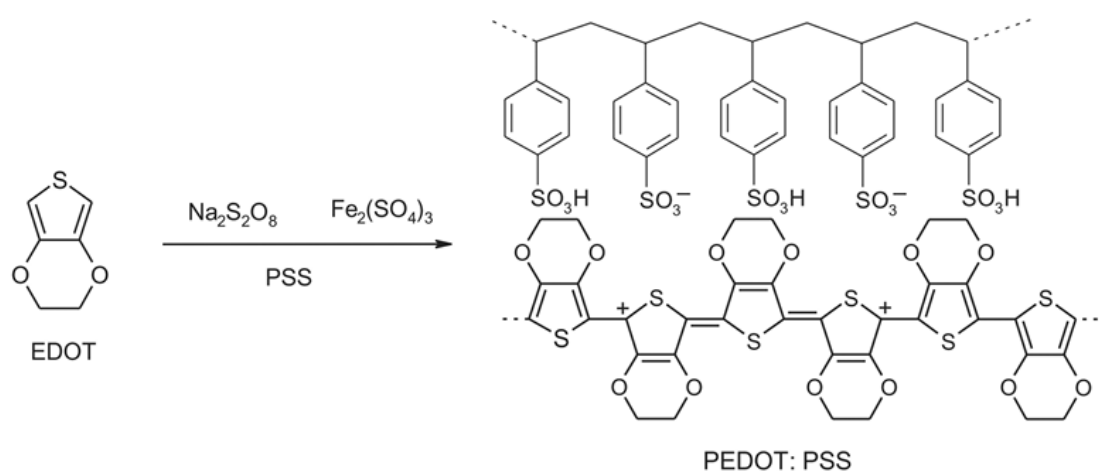


Figure 2.2. Scheme of PEDOT:PSS polymerization. Reprinted from Ref⁹⁹.

In this work, highly conductive grade PEDOT:PSS, used for the study of pristine and nanostructured thin films, was purchased from Sigma Aldrich (product #655201), with a nominal conductivity > 200 S/cm. PEDOT:PSS with lower conductivity, used for PEDOT:PSS/PEO blends, was purchased from Ossila Ltd (Heraeus ClevisTM AI 4083). For both the commercial solutions, we found mean particles' size value of ≈ 50 nm as discussed later in the thesis.

Other materials

Poly(vinyl acetate) (PVAc) and Poly(methyl methacrylate) (PMMA) are viscoelastic materials, solid at room temperature, obtained by the polymerization of their respectively starting monomers vinyl acetate and methyl methacrylate (MMA) ¹⁰³. The most known application of PVAc is for adhesives as it is used in emulsion for many commercial glues ¹⁰⁴, while PMMA is broadly employed as inorganic glass, due to its high impact strength, lightweight, shatter-resistance, and favorable processing conditions ¹⁰⁵.

In the work presented in this thesis we used PVAc (Mw = 100 kDa, Tg = 43 °C, Sigma-Aldrich: product number 189 480) and PMMA (Mw = 120 kDa, Tg = 103 °C, Sigma-Aldrich: product number 182230).

Substrates

Different substrates can be used for the preparation of polymeric thin films. In this work, we used Silicon (Si) Wafers and glass-coated Indium Thin Oxide (ITO, Ossila, product #S111) as substrates for the thin film preparation. Two different types of Si Wafers were employed: semiconductive (regular, Ted Pella Inc., product number: 16008) and conductive (Arsenic n-doped, resistivity ~ 0.001 Ωcm).

Normally, a thin layer of Silicon Oxide (SiOx) always develops on the surface of Si, with a usual thickness of a few nm. This hydrophilic layer tends to lower the coatability of the substrate by polar solutions. For this reason, “piranha solution” (H₂SO₄:H₂O₂(35_wt% in water)=3:2 – vol/vol) was used to rinse the wafers before the deposition of the thin polymer layer for those sample spin coated from aqueous solutions.

Other substrates, such as Gold coated Silicon wafer (Au, Sigma-Aldrich, product number: 643262) and SiOx (Ted Pella Inc., product number: 21620-55), were used as received.

For the dielectric study of polymer thin films, we took advantage of an Aluminum (Al) layer to deposit those samples that needed highly conducting substrates in the characterization step. The geometry of these samples and their characteristics are described in section 2.3.2.

2.2 Sample Preparation

Preparation of polymer thin films

In thin film preparation, coating techniques allow obtaining very thin sheets of polymers from a diluted solution directly cast or spin coated onto a substrate. In this work, these two deposition techniques were used to obtain regular and continuous polymer thin films. A scheme of such techniques is sketched in Figure 2.3 and shortly explained below. For the spin coating we used a spin coater purchased from Ossila (product code: L2001A3-E461-UK).

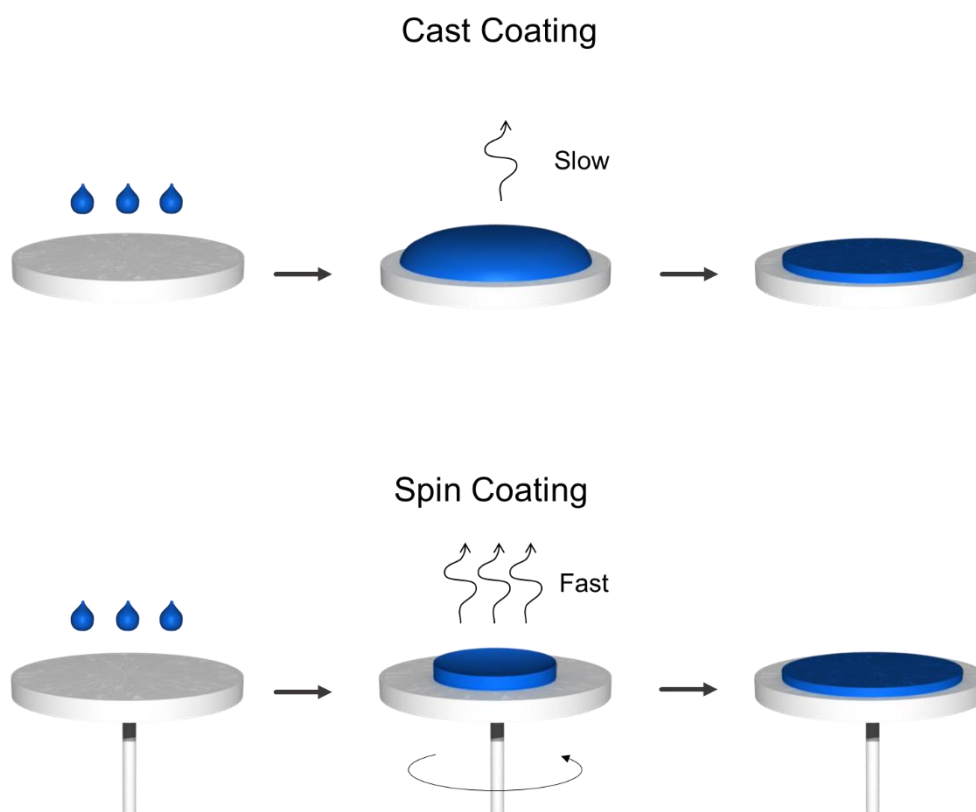


Figure 2.3. Scheme of cast and spin coating. The rounded disks represent the substrate while the blue features indicate a generic polymer solution developing the final thin film.

- In cast coating, a drop of polymer solution is poured on top of the substrate. The sample is then left in air at room temperature to allow slow evaporation of the solvent under an upside down funnel to avoid dust contamination.
- In spin coating a drop of polymer solution is poured on top of the substrate, the substrate is fixed onto a plate that starts rotating immediately after the drop deposition. The rotation makes the drop flow covering all the substrate and allows the correct

evaporation of the solvent. For the preparation of the polymer thin films discussed in this work, we selected a rotation speed of 3000 rotations per minute for a total time of 1 to 2 minutes.

Nanostructuring techniques

To induce the desired nanostructure onto PEDOT:PSS thin films, described in details in chapter 4, we used two protocols:

➤ Reprecipitation

We were able to fabricate polymer nanospheres by the so called “reprecipitation method”, which is a common route to prepare polymer nanospheres of different chemical natures⁷⁸. The reprecipitation method is a solvent-displacement technique that relies on crashing out hydrophobic polymer chains in solution by displacing a solvent with a non-solvent, generally water¹⁰⁶. The polymer solvent and the non-solvent must be miscible with each other. The reprecipitation method can be resumed as follows.

By using a syringe, a known volume of a polymer solution is injected into a known volume of non-solvent. The immiscibility of the polymer in the non-solvent, and fluid dynamic given by the injection, make possible the aggregation of the polymer in sphere shaped nanoparticles, resulting in a final colloidal dispersion. The selection of the correct solvent/non-solvent couple, their relative ratio, and the polymer solution concentration, are the main parameters affecting the nanospheres’ dimensions and stability. If the solvent has a lower boiling point than the counter solvent, the latter can be easily separated by evaporation. In the opposite case, the solvent can be also separated by dialysis¹⁰⁷.

➤ Solvent Vapor annealing (SVA)

SVA is a widely used technique for the nanostructure modification or reorganization of polymer films. This technique consists of exposing the film to a solvent vapor saturated atmosphere for a certain amount of time¹⁰⁸. The impact of the nanostructuring technique on the sample depends on the polymer nature, the selected solvent, and the time of annealing.

For SVA, we used a glass desiccator (inner diameter = 150 mm) saturated with THF vapors. This chamber was prepared by leaving a pure volume of THF (20 mL) free to evaporate inside it. The solvent was replaced as many times as required until it preserved its volume without further evaporation. The polymer pristine thin films were subjected to solvent vapors at different times. After solvent exposure, the films were left again in high vacuum, overnight and at room temperature, to allow evaporation of the residual solvent.

2.3 Experimental methods

2.3.1 Atomic Force Microscopy (AFM)

Microscopic methods constitute a powerful tool to investigate the structure of polymeric systems on multiple length scales, helping the investigation of the disposition of complex compositional and topological features also giving visual feedback of the micro- and nano-domains composing the material of interest ¹⁰⁹. Among these methods, AFM distinguishes for its versatility and relatively fast data acquisition ¹¹⁰. The working principle of AFM is shown in Figure 2.4: the electronics control the vertical z -position of the probe respect to the sample, which enables having a desired deflection of the cantilever; then the probe is shifted all along the interested surface portion by the piezoelectric scanner in the x - y plane and the photodiode converts in electric signal the bending of the cantilever (that depends on the tip-surface interactions) for each pixel of the resulting image.

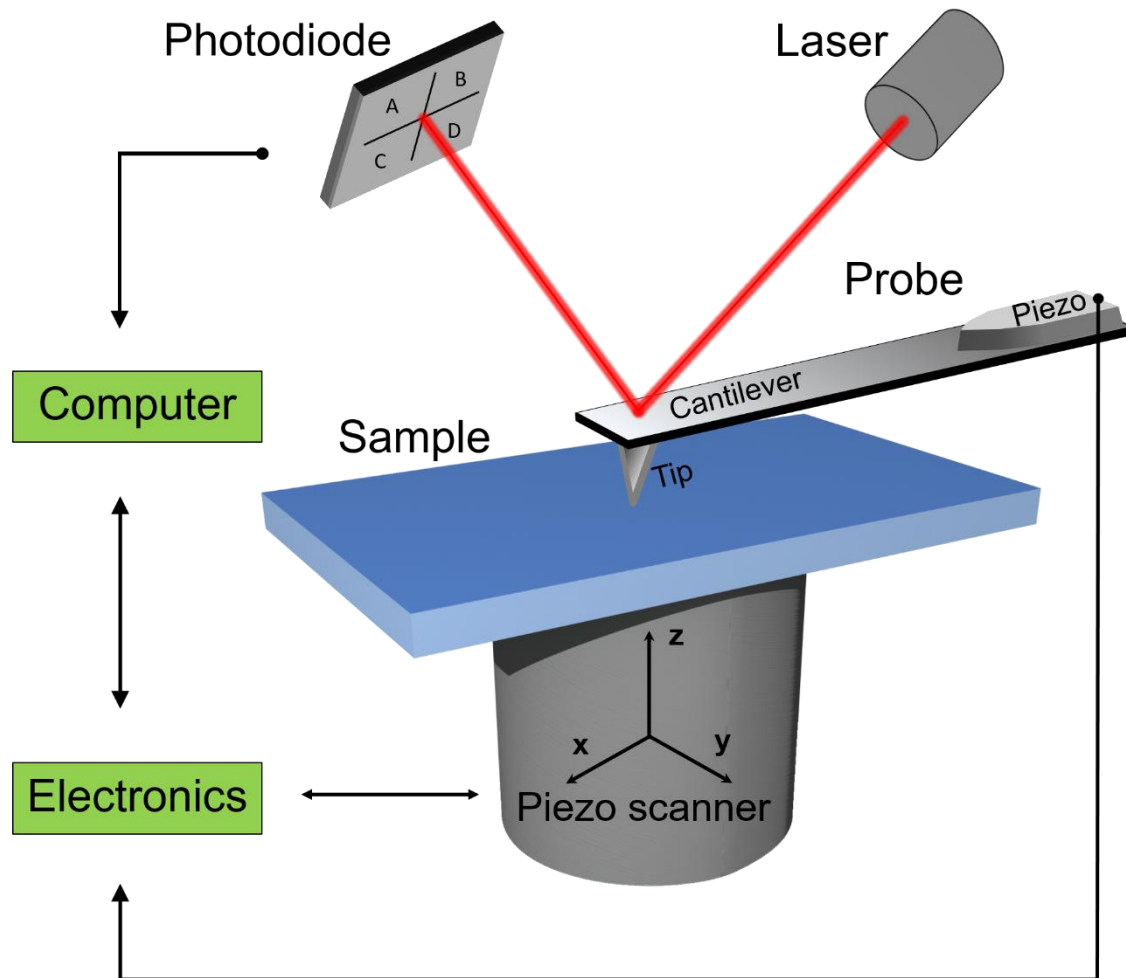


Figure 2.4. Scheme of the AFM setup.

The working conditions of an AFM significantly vary from an operational mode to another. In the following lines we are introducing the imaging acquisition methods employed in the work presented by the thesis.

Operation modes:

Contact mode. In contact mode, the system scans the sample at a fixed deflection setpoint of the cantilever. In these conditions, the force applied by the tip to the sample is maintained constant for the entire acquisition. To ensure that, the electronics correct the voltage sent to the piezo scanner after every scanned point. The feedback of the system to the topological arrangement of the sample, evaluated from the cantilever following the height profile, provides the final image¹¹¹. The adjustment of this acquisition technique deals with the “deflection setpoint”, but other parameters such as “scan rate” and “samples per line” are also important, as they define the velocity with which the tip brushes the surface and the acquisition time. The

feedback loop which determines the z-adjustment of the piezo scanner is controlled by the Proportional-Integral-Derivative control: PID gains. A correct modulation of the proportional, integral, and derivative gains determines the right compromise between a good signal to noise ratio and an accurate estimation of the height at every scanned point. PID, scan rate and samples per lines parameters play an important role in every AFM operation mode, even if the acquisition time per line varies from one mode to another. Depending on the topography features of the sample, high deflection setpoints may be required to have a good tip-sample interaction in order to obtain good image resolution; this fact is particularly problematic when the sample is soft and more prone to be damaged, which might give artifacts in the final image. Moreover, soft or adhesive samples can easily contaminate the tip in these operating conditions.

Intermitted contact mode. In Intermitted contact mode, or tapping mode (TM), the tip is vibrating at a frequency near to the cantilever resonance frequency (f_0 , generally around 10^5 Hz) and brought close enough to the surface to interact with the sample (intermittent contact)¹¹¹. The oscillation is kept at a fixed amplitude by the system that adjusts the *z-position* of the probe respect to the sample and gives the topography profile. The main parameters that the user must take into account for such operation mode are the “Amplitude Setpoint” (that drives the strength of the tip-sample contact interaction) and the “reference frequency” at which the cantilever is operating (that strongly affects the accuracy of the experiment). The Amplitude Setpoint is the target amplitude of the cantilever oscillation set *during the scan*, this is lower than the drive amplitude (which is the amplitude of the *free oscillation in air* for the same applied excitation to the lever, set at 500 mV for all our experiments) in order to allow an effective tip-sample interaction. The reference frequency varies with the cantilever f_0 (that needs to be calibrated at the very beginning of the experiment), it is generally selected at lower frequency respect to the f_0 , as the resonance frequency in proximity of the sample is generally lower. A scheme of the TM operation is shown in Figure 2.5.

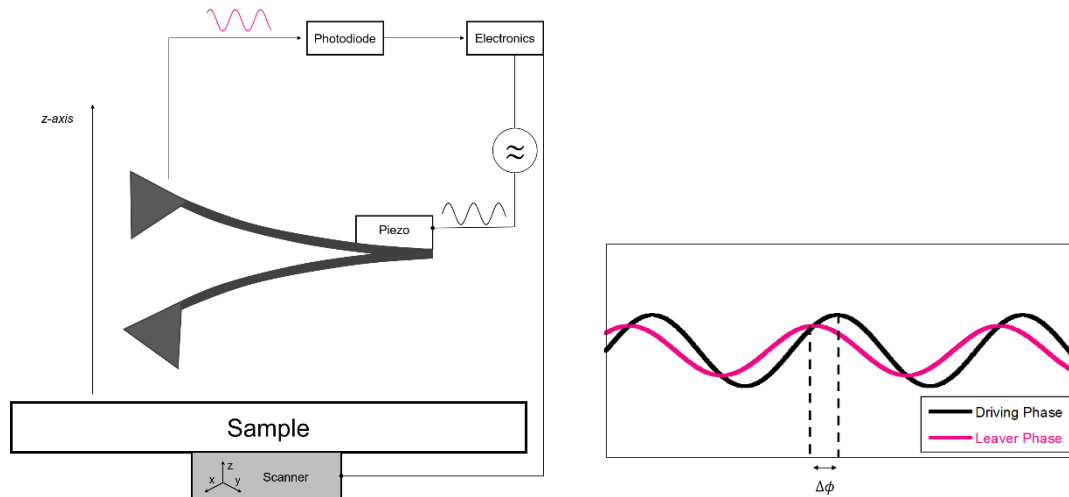


Figure 2.5. Scheme of the AFM operation in TM.

An interesting feature of this operation mode is the possibility to analyze the phase of the outgoing signal respect to the driving excitation. In this analysis, the resulting phase shift ($\Delta\phi$) is registered for every pixel, returning a phase image that can provide information about the mechanical response of the studied material ¹¹². More specifically, the resonance frequency of the cantilever shifts when the interaction between it and the analyzed surface changes. This shift will be to lower frequencies for attractive forces or to higher frequencies for repulsive ones. A higher phase shift represents a stronger interaction of the tip with the substrate, which can be ascribed to zones on the sample with different mechanical properties. Height and phase images are acquired simultaneously.

Peak Force Tapping mode. Another AFM imaging method is *force volume*, which defines a series of AFM operation modes able to store force-distance data at every scanned spot. Peak Force Tapping (PFT) is a force volume protocol introduced by Bruker that uses the peak in force gained from the acquired FCs to control the feedback loop and to give the height output ¹¹¹.

PFT presents a fundamental difference with respect to ordinary Tapping Mode: it works with a stationary cantilever whereas the sample tip distance varies through the z -movement of the scanner at a frequency far from f_0 (usually between 1 kHz and 4 kHz), in such a way to neglect any dynamics noise arising from a resonant object. In our work, we acquired PFT images with a drive frequency of 2 kHz. PFT allows better control over the forces acting between the tip and the sample, giving the possibility to register and analyze them ¹¹³. Ideally speaking, we can imagine the behavior of the cantilever as represented in Figure 2.6 where is

shown a scheme of the force acting on the sample during a single cycle of tip-sample interaction in the range of interest.

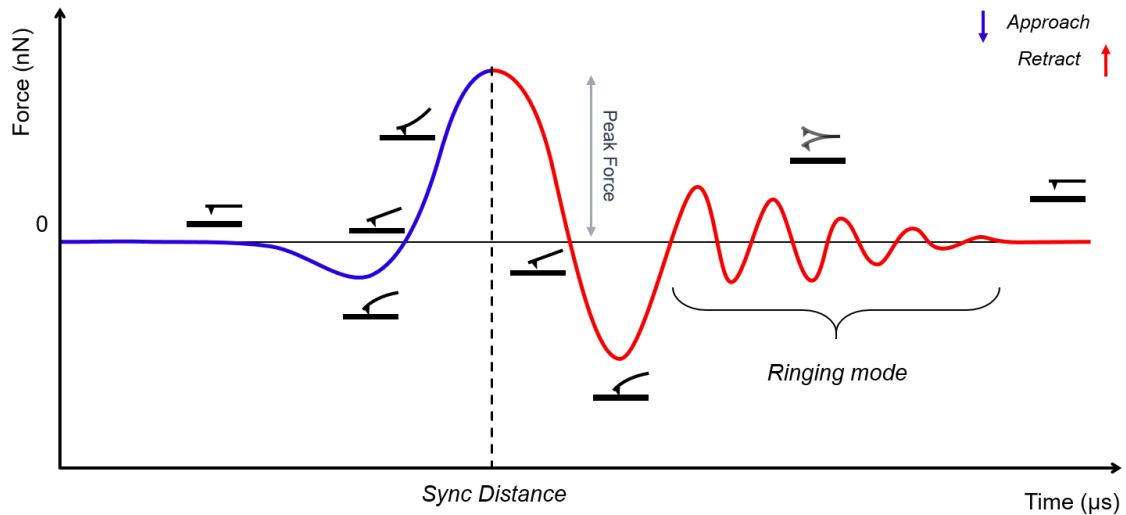


Figure 2.6. Force vs time in PFT operation mode.

The “PFT amplitude” is the maximum cantilever deflection during the scan and it is an important parameter to take into account as it highly affects the feedback accuracy from the height channel along with the experiment. The selected PFT amplitude for our experiments was 100 nm. The most important parameter regulating the experimental operation in PFT is the “Peak Force Setpoint”. This is the maximum force applied by the tip to the sample (similarly to the “Amplitude Setpoint” for TM) and it must be properly chosen by the user to avoid sample/tip damaging or tip contamination. Higher Peak Force Setpoints provide higher precision in the topological investigation of approximatively non-deformable surfaces. Normally, harder samples allow choosing higher Peak Force Setpoints (always taking care not to damage the tip). The “Sync Distance” is a time constant at which the z -piezo is at its lowest traveling position during PF-QNM imaging (see below), and it is fundamental in order to obtain quantitative values^{113,114}. It is shown in Figure 2.6 as the time in proximity of the dotted line. The Sync Distance is the point when the maximum force is achieved and it is fundamental to properly set the limit between trace and retract (which are the lines respectively blue and red in Figure 2.6). This parameter was evaluated using a hard sample as reference (sapphire) and left constant during the set of experiments.

Image processing:

The software used for the image processing in this work was Nanoscope Analysis 1.9 (baseline adjustment, surface roughness, thickness evaluation) and ImageJ (maps composition, nanoparticles analysis).

Baseline adjustment. Due to small plane inclinations always present in the samples/substrates, the AFM rough images normally result bow shaped or tilted respect to the uniform surface that the user may expect. For this reason, before the image analysis is usually necessary to correct the baseline approximating the plane to a polynomial function (first order or higher).

Surface roughness. From the topography images, the mean surface roughness (R_a) was calculated as $R_a = N^{-1} \sum_{i=1}^N |z_i - z_0|$, where N is the total number of pixels in the image, $|z_i - z_0|$ the average height value at the i -th pixel of the image, from the mean plane (z_0).

Maps composition. By using a software analysis on images from different channels (such as modulus and height) it is possible to obtain a compound image where the portion of one channel, deriving from pixels presenting a property value (in the color scale) above a certain threshold, is overlying on the other channel image. In this way, it is possible to highlight portions of the surface topography presenting the physical property of interest. We made use of ImageJ software for such image processing.

Nanoparticles analysis. The size of a set of nanoparticles in a sample can be estimated by AFM by acquiring several images of the film and evaluating the mean value of the imaged objects. This operation can be also done by using a software analyzer able to recognize the desired object shape giving selectively the size distribution of for a considered picture. For this kind of measurements we used ImageJ software. An example of this image analysis is reported in Figure 2.7 where several nanospheres of PEDOT:PSS are counted and analyzed by the software.

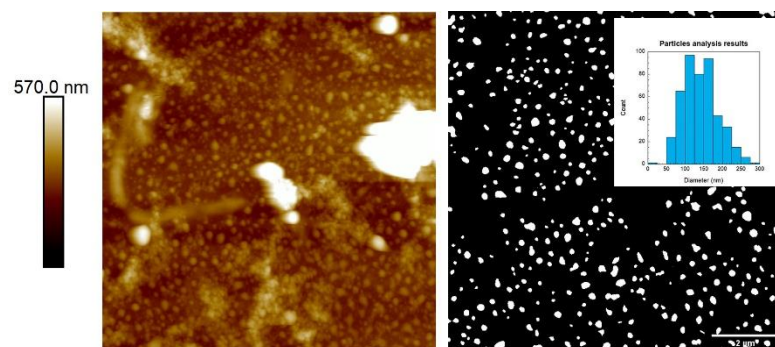


Figure 2.7. AFM height image of PEDOT:PSS nanospheres deposited on ITO glass with the corresponding particles' size analysis. Scale of the images reported below (right) in the black and white picture.

Thickness evaluation. We evaluated the thin films' thickness via AFM. By scratching the surface using sharp tweezers we induced a cut on the film then, with the help of the optical microscope, the tip was brought in proximity to the cut edge and approached to the sample surface as usual. The film thickness evaluation was performed in TM and we measured the height between the sample/substrate step as reported in Figure 2.8.

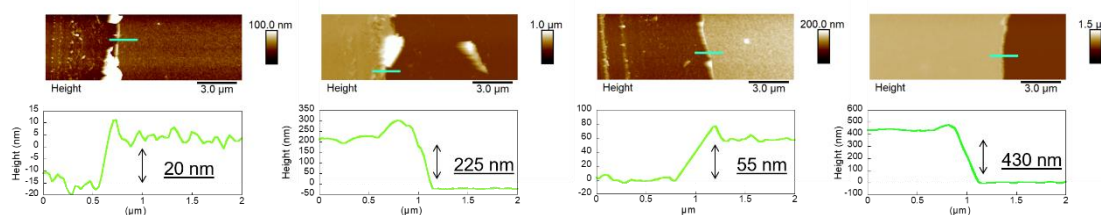


Figure 2.8. Cross section height evaluation of PEDOT:PSS thin films at different thicknesses deposited on ITO glass.

Quantitative Nanomechanical Analysis (QNM)

In general, AFM does not only provide information about the topography, but also data related to tip-sample interactions during the scan which, with the appropriate model, can be extrapolated in terms of forces to quantitatively evaluate the mechanical properties of the sample with quite good spatial resolution³⁵. This concept constitutes the basis of Quantitative NanoMechanical analysis (QNM) operation, able to uncover the disposition of features with different mechanical response and to address them quantitative values in Young's modulus, Stiffness, or Adhesion³². All these parameters are obtainable from Force-distance Curves (FC) that the instrument acquires at every tip-sample interaction cycle. QNM works in PFT mode, and it needs a proper calibration of the tip spring constant and of the "Deflection Sensitivity" parameter in order to obtain reliable FCs from the signal acquired during the PFT experiment.

In our work, for Peak Force-QNM (PF-QNM) measurements the system was calibrated following recent literature reports^{115–117}. For the calibration of the probe, we followed a strict protocol to ensure coherence between each set of experiment. The cantilevers' spring constant was calculated using Sader's method. This calibration approach uses the resonance frequency, the quality factor and the geometrical attributes of the cantilever to derive its spring constant^{118,119}. The quality factor is the ratio of energy stored to energy lost in one radian of a cycle of oscillation and is calculated by the system during the resonance frequency calibration. The Deflection Sensitivity, which is the ratio between the applied force and the resultant z -separation of the probe while the cantilever bends in contact with a hard surface, was calibrated by performing a linear FC against a sapphire standard (1 Hz, Z -ramp = 200 nm, trigger threshold = 0.2 V). The Deflection Sensitivity was verified before and during PF-QNM operation, using the same sapphire sample (PeakForce frequency = 2 kHz, PeakForce amplitude = 100 nm, PeakForce setpoint = 0.2 V), allowing a maximum 10% deviation between the PF-QNM and force-distance results. Immediately afterward, the "Sync Distance" parameter was evaluated using the sapphire sample. The obtained value was fixed during all PF-QNM measurements. Furthermore, we calibrated the tip radius by using a poly(styrene) (PS, standard reference: Bruker, PeakForce QNM Sample Kit) sample with known $E_{PS} = 3\text{GPa}$ following eq. 1.12.

By PF-QNM, it was possible to obtain both maps with mechanical contrast and local mechanical properties. We must clarify that the geometry of polymer nanostructures might influence a proper quantification of mechanical properties by PF-QNM maps alone, as reported recently¹²⁰. Also, problems as topography crosstalk and the influence of the sinusoidal excitation of the piezo scanner during mapping³² might affect a precise quantification of mechanical properties by PF-QNM maps. For this reason, the information gained from local nanoindentation experiments provide the possibility to have a more precise evaluation of quantitative properties. This fact does not exclude the extremely useful level of details obtainable in terms of nanomechanical mapping from the PF-QNM images.

Conductive-AFM (C-AFM)

By C-AFM one can acquire conductivity maps by scanning the sample surface under a constant bias between the tip and the sample. With the same setup, we can also measure the electrical conductivity of the sample in a chosen spot of its surface by performing local experiments. The AFM setup for this kind of experiments requires a conducting substrate, where the polymer thin film is deposited on top, and a conductive AFM tip both connected to

the circuit. We performed the C-AFM experiments in Contact Mode. The electrical conductivity was measured by local I-V curves. In C-AFM experiments it is required a precise control of the forces between probe and sample to perform a proper surface scanning without scratching, while at the same time allowing good electrical contact¹²¹. In this way, we calibrated the probes to allow force control, in a similar way to the mechanical calibration. We obtained the cantilevers' spring constant by Sader's method and calibrated the deflection sensitivity against a Sapphire standard, as detailed before. The local experiments were performed by the acquisition of current-voltage curves (I-V curves) on particular areas of the surface. At this point, a DC voltage ramp was sent to the sample (S_{BIAS}), at 1 Hz rate. For each sample, the corresponding I-V curve was acquired. We calculated the conductance of the films by determining the slope of the curves via a fitting to a linear function, and obtained the resistance as its reciprocal value. From the conductance measurements, was possible to estimate the samples' conductivity (σ) as:

$$\sigma = \frac{C \cdot h}{s} \quad (2.1)$$

Where h is the sample thickness, C the conductance, and s the tip-sample contact area^{33,122,123}. In our work, the contact area was calculated using the Hertz contact mechanics approximation (eq. 1.11)¹²⁴.

Nano-Dielectric Spectroscopy (*nDS*)

AFM also provides the possibility to map the electrostatic forces acting between the tip and the sample. In this context, Electrostatic Force Microscopy (EFM) is based on the electrical force (F_e) resulting from the interaction of a conductive AFM probe with charged and/or polarizable entities in the material¹²⁵. The AFM operation consists of a two steps *line-by-line* scan. The first one consists of a PFT or a TM height scan, where zero voltage is sent during the profile acquisition. The second step actuates in "lift mode", where the tip is maintained at a fixed distance far away from the surface without any mechanical excitation. During the lift mode, the tip and the sample are connected to an electrical circuit and a sinusoidal electric bias is applied to the tip. The voltage amplitude (V_0) and the frequency (f_e) of the electrical field between the tip and the sample in lift mode are selected by the user. Given the sinusoidal voltage $V(t)$ with a frequency $f_e = \frac{\omega_e}{2\pi}$, by modeling the probe-sample system as a capacitor with capacitance C , it is possible to evaluate the electrical force resulting from an electrostatic potential energy W (described by eq. 2.3) as:

$$V_0 = V_0 \sin(\omega_e t) \quad (2.2)$$

$$W = \frac{1}{2} CV^2 \quad (2.3)$$

$$F_e = \frac{\partial W}{\partial z} \quad (2.4)$$

$$F_e(t) = \frac{1}{2} \frac{\partial C}{\partial z} (V_s + V_0 \sin(\omega_e t))^2 \quad (2.5)$$

V_s is the surface potential and gives information about the charge accumulation at the surface interphase resulting from the applied electric field. As our study focuses on the dielectric properties of the investigated materials, which are related to the capacitance, we made use of the second harmonic of the cantilever motion, that is not influenced by V_s . The relation between the capacitance and the electrostatic force in the second harmonic of the cantilever oscillation, which allows measuring the nano-dielectric properties of the sample, is then expressed as follows.

$$F_{2\omega_e}(t) = -\frac{1}{4} \frac{\partial C}{\partial z} V_0^2 \cos(2\omega_e t) \quad (2.6)$$

For an applied frequency ω_e much lower than the resonant frequency of the cantilever, the resulting force (related to the deflection of the cantilever itself) oscillates at twice the applied frequency (out of phase from the applied voltage). However, if some dissipative electrical interaction takes place as, for example, a dielectric relaxation, there will be a change in phase. This change in phase as a function of ω_e allows detecting the dielectric relaxation phenomena with a lateral resolution in the nanoscale range^{126–128}.

Equipment

The AFM measurements were carried out in a Multimode AFM equipped with Nanoscope V electronics and the Signal Access Module III (Bruker), running Nanoscope 8.15 software (Build R3Sr8.103795). For the nanodielectric characterization, the system was coupled with the external lock-in amplifier SR-865A.

The morphology and mechanical studies were conducted using AFM probes Tap300Al-G and Tap150Al-G probes by BudgetSensors (spring constant k respectively ≈ 20 N/m and ≈ 3 N/m, $R \approx 10$ nm, $H \approx 15$ μ m, $W \approx 30$ μ m, $L \approx 125$ μ m, resonance frequency f_0 respectively 300 kHz and 150 kHz).

C-AFM measurements were carried out using conductive probes (DDESP-FM-10, Bruker, conductive diamond coating, $k \approx 6$ N/m $R \approx 100$ nm, $H \approx 3$ μm , $W \approx 30$ μm , $L \approx 225$ μm , $f_0 = 105$ kHz; SCM-PIT-V2, Bruker, conductive PtIr coating, $k \approx 6$ N/m $R \approx 25$ nm, $H \approx 13$ μm , $W \approx 30$ μm , $L \approx 225$ μm , $f_0 = 75$ kHz). In this case, the samples were deposited on ITO substrates that were later on connected to the AFM sample holder using silver conductive paint (RS components, product #189-3593). For the C-AFM characterization, we used a deflection setpoint of 50-75 nN of normal force. The current signal was detected by the current amplifier (Extended TUNA application module) at a 100 nA/V of maximum sensitivity.

The *n*DS characterization of the lower molecular weight sample was carried out by using a SCM_PIT_V2 probe, the model validation as long as the high molecular weight sample with HQ:DPE-XSC11 (μmasch , conductive Pt coating, $k \approx 7$ N/m $R \approx 50$ nm, $H \approx 15$ μm , $W \approx 30$ μm , $L \approx 125$ μm , $f_0 = 155$ kHz).

2.3.2 Broadband Dielectric Spectroscopy (BDS)

Broadband Dielectric Spectroscopy (BDS) is a powerful tool to experimentally evaluate the $\varepsilon^*(\omega)$ and obtain information about the relaxation processes that occur in a frequency window approximately between 10^{-3} Hz and 10^9 Hz, range where ions' and dipoles' fluctuations are normally contributing to the polarizations that might occur. The principles of BDS are briefly explained in the following section.

Experimental setup

To evaluate the complex dielectric function in the analyzed samples, we made use of a broadband dielectric spectrometer. The impedance of the sample was measured in a parallel plate capacitor in an impedance analyzer by applying a sine wave electric potential. The scheme of the sample cell is shown in Figure 2.9. The permittivity is then obtained from the measured complex capacitance $C^*(f)$ through $Z^*(f)$ as:

$$\varepsilon^*(f) = C^*(f) \frac{d}{A\varepsilon_0} \quad (2.7)$$

Where d is the distance between plates, A the electrode area, and $C^*(f) = -\frac{i}{2\pi f} Z^*(f)$.

area, and $C^*(f) = -\frac{i}{2\pi f} Z^*(f)$.

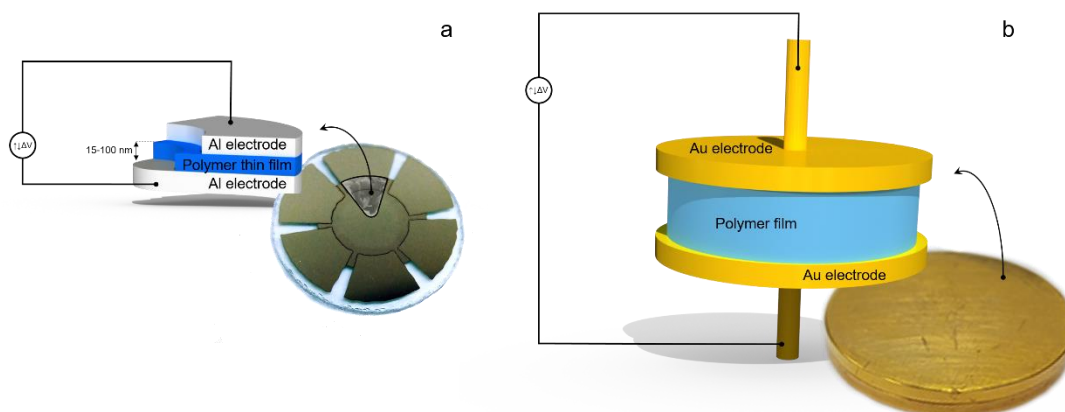


Figure 2.9. Scheme of the sample sandwiched in different electrodes geometries: a) thin film spin coated on a layer of Al obtained by Physical Vapor Deposition and sandwiched with a second Al layer deposited on top of it in the same conditions, b) sample film between two gold plated electrodes, obtained by compressing at Temperature > melting Temperature using a Teflon spacer.

In this work, we used two different sample geometries for the BDS measurements. For measurements on “thick” samples (0.1 mm), we adopted a capacitor configuration constitute of two gold plated electrodes with diameter of 20 mm, and a sheet of our sample in between with thickness ≈ 0.5 mm. In this case the measurements were performed with the equipment Novocontrol high-resolution dielectric analyzer (alpha-A analyzer). For measuring the dielectric function of thin films the sample was deposited from Toluene solutions at different concentrations over Al (Sigma-Aldrich, purity >99.9%) round electrodes previously deposited by Physical Vapor Deposition (PVD) on a glass substrate, the upper Al electrodes were also deposited by PVD directly on the samples. The PVD was carried out by means of Tectra Mini-Coater equipment. The area of the obtained capacitors was evaluated by ImageJ software from images acquired through a magnifying glass, giving a usual value of ~ 7 mm². The thickness of the thin films was evaluated through eq. 2.7 at $T=30^\circ$ C and $f=10^5$ Hz considering a value of ϵ_∞ for PEO = 2.75. For the BDS characterization of thin films nanocapacitors, we employed a Solartron Analytical equipment.

2.3.3 Other complementary methods

Differential Scanning Calorimetry (DSC).

The principles of the technique consist in measuring simultaneously the temperature of a reference standard and the sample, from which is derived the heat flow passing through the

sample from the rate of temperature change for a given amount of heat. DSC provides information about the heat flow in the material as a function of temperature, in a range of temperatures as wide as the equipment allows (usually between -100 °C and 500 °C) as long as the sample does not degrade ¹²⁹.

In the presented work, DSC was used for monitoring the glass transition and the melting/crystallization phenomena of the polymers investigated. DSC measurements were carried out on approximately 5 mg of samples using a Q2000 TA instruments. A liquid nitrogen cooling system (LNCS) was used with a 25 mL/min helium flow rate. Measurements were performed by placing the samples into aluminum pans.

Conductivity measurements

A widely employed technique to measure the conductivity and the resistance of polymer films is *four-point probe* analysis (FPP). This technique relies on four probes at a known distance one each other. A known current generated by a DC power supply passes through the two external probes, while the other two probes measure the voltage difference induced in the conducting specimen. By this technique is possible to obtain Current-Voltage curves, which provide quantitative information about the conductivity of the studied film ¹³⁰.

Surface electrical conductivity measurements were conducted on thin films with a four-point probe apparatus (Ossila, T2001A3), with a probe spacing of 1.27 mm, a set current range of 20 mA, and target current 5 mA.

Grazing-Incidence Wide-Angle X-ray Scattering (GIWAXS)

Grazing-Incidence Wide-Angle X-ray Scattering (GIWAXS) takes advantage of the Wide-Angle X-ray Scattering (WAXS) principles to give insights into the surface nanostructure of the sample. In GIWAXS, an X-ray beam is sent to the sample surface with a characteristic incidence angle α_i . The detector collects the resulting horizontal (r) and vertical (z) scattered elements: these determine the components of the scattering vector, providing information about the orientation of the scattering planes at the sample surface. With such information, a precise map of the crystalline cell are obtained for a perfectly ordered monocrystal, while in polymer samples can be achieved important insights into the orientation, disposition, and conformation of the crystalline lamellae or nanostructured surfaces ¹³¹.

Grazing-Incidence Wide-Angle X-ray Scattering (GIWAXS) was carried out in collaboration with Dr. Mari Cruz García-Gutiérrez (Instituto de Estructura de la Materia, IEM-CSIC, Serrano 121, 28006 Madrid, Spain) at ALBA synchrotron, BL-11 (NCD-SWEET), whose group was engaged in both acquiring and processing the GIWAXS data. The X-ray beam wavelength was set at $\lambda = 0.1$ nm ($E = 12.4$ keV). GIWAXS patterns were collected by a LX255-HS 2D (Rayonix) area detector, placed at 14.6 cm from the sample. Set-up parameters were calibrated using Cr_2O_3 . Reduction of GIWAX images was accomplished by using available MatLab software^{132,133}.

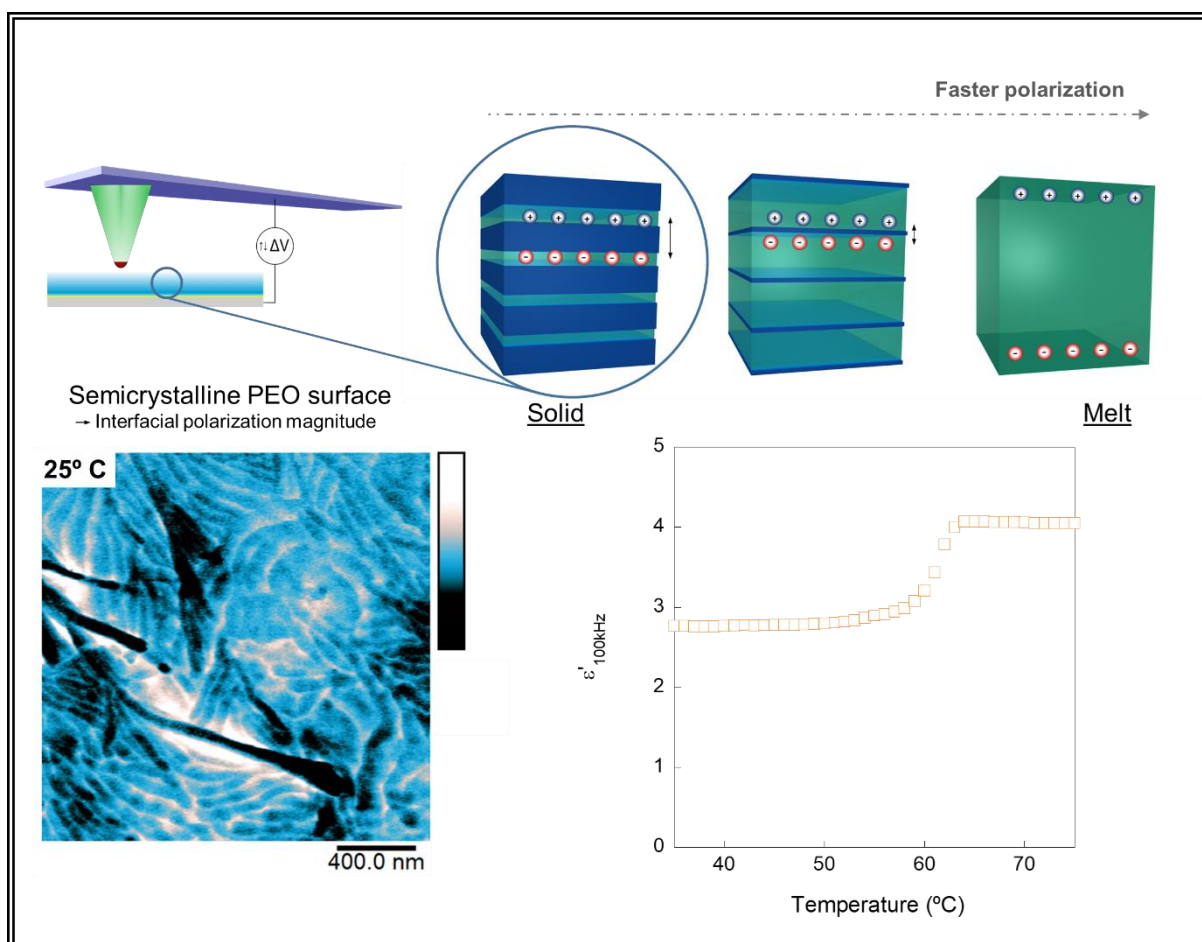
UV-Visible absorption and DLS

By UV-Visible (UV-Vis) absorption and Dynamic Light Scattering (DLS) we identified the oxidation state and the size of PEDOT:PSS nanospheres, as explained in details in chapter 4 (section 4.2.1).

UV-Vis spectra were recorded on an Agilent 8453A apparatus using a quartz cuvette, at room conditions. The DLS measurements were carried out at 25 °C in a Zetasizer Nano-ZS apparatus, using disposable glass cuvettes.

Chapter 3

Dielectric characterization of PEO semicrystalline thin films



3.1 Introduction

The dielectric characterization of highly conducting samples is often obstructed by polarization processes which mask many (usually every) molecular contributions in the low frequency range of the spectra. The most common polarization, often considered as a purely parasitic one, is the so called Electrode Polarization (EP). It arises from accumulated charges at the interface of each functioning electrode; if the oscillation time of the electric field allows to these to move through the entire body of the sample, the charges can dispose against the electric field opposing a dielectric strength relatively high with respect to any structural relaxation that may occur in the material¹³⁴. But EP itself is not necessarily an undesired parasitic contribution for the sake of the information obtainable in BDS. In fact, it can be used to study the *free ion density* and *diffusivity* of ion-conducting specimens, giving access to several intrinsic characteristics of these samples^{135–137}; this is because the EP is promoted in highly conducting systems, as the most the charge carriers can move the more likely polarization effects are induced.

In semicrystalline media, a second fundamental polarization effect must be considered in the BDS analysis: the Maxwell-Wagner-Sillars relaxation (MWS). The MWS relaxation is an interfacial polarization process occurring at the interface of the crystalline lamellae, thereafter in the amorphous fraction of the polymer, as a consequence of the trapping of free charge carriers (such as ions) in between them. This relaxation takes place due to the different dielectric properties of the crystalline and amorphous fractions, which generates a heterogeneous medium composed of microdomains with different permittivities/conductivities and regularly spaced by a thickness given by the lamellae geometry. One can take advantage of such interfacial polarization to study the crystallinity of the system and to experimentally provide evidences of the complex interface disposed by a semicrystalline object^{138,139}.

EP and MWS are intimately connected as both relaxations are driven by the ion diffusivity in the body under the given conditions. As an example of that, we report in Figure 3.1 the dielectric spectra of a sample of PEO both in solid and melt state. As we can observe, the huge contribution of EP would mask any other eventual relaxation. In a sample of solid state PEO, both EP and MWS are observed. The MWS is always faster than the EP as the migration of an ion among the single lamella is faster rather than for the entire capacitor. In melt state PEO, the conductivity significantly increases suggesting a promoted ion mobility in the liquid with respect to the solid. For this reason, a detailed description of the system in terms of

molecular dynamics results hindered by the intense polarization phenomena dominating the BDS signal.

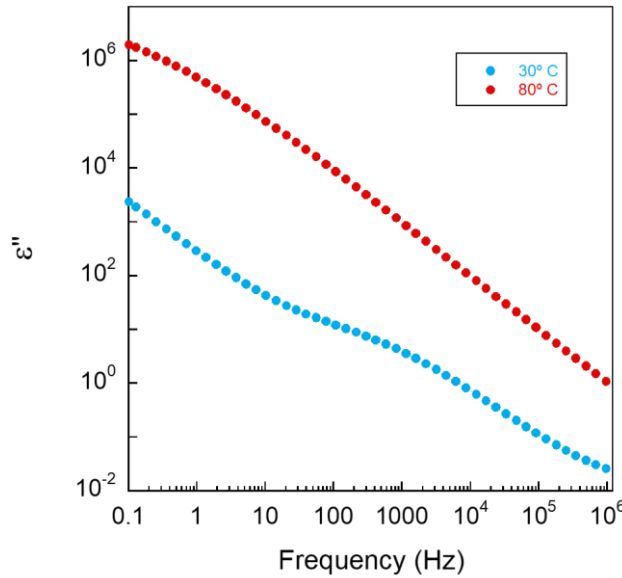


Figure 3.1. BDS results at 30° C and 80° C for a sample of PEO with a thickness of 0.1 mm.

The intensity of an interfacial polarization, such as EP, depends on the thickness of the sample. For example, modeling EP as a Debye relaxation the following relations are valid ⁶⁰:

$$\Delta\varepsilon_{EP} = \left(\frac{D}{2l_D} - 1\right) \varepsilon_{\infty} \quad (3.1)$$

$$\tau_{EP} = \left(\frac{D}{2l_D}\right) \frac{\varepsilon_s \varepsilon_0}{\sigma_0} \quad (3.2)$$

To an interfacial relaxation is generally attributed a Debye length (l_D) that indicates the effective spacing of the electrical double layer. As it may be deduced from relation 3.1, one strategy to reduce this polarization contribution is to reduce the thickness (D) down the l_D of the investigated sample, in such a way to minimize those effects considered parasitic in our analysis.

In the first section of this chapter, we are going to present an in depth dielectric characterization of semicrystalline polymeric systems taking advantage of PEO ultra-thin films. As we will see, the thin film geometry allows to separate the polarization contributions to structural relaxations in the BDS spectra. In such a way we were able to follow the intrinsic dynamics at the melt state, adsorption/desorption kinetics at the electrode interface, as long as the crystallization/melting process in the studied system. In the second section, we will present the imaging of the heterogeneous dielectric behavior of PEO thin films at the nanoscale by

AFM in Electrostatic Force Microscopy (EFM) to visually show the complex conductivity paths in semicrystalline materials. A detailed modeling of the EFM apparatus and operation comes along in section 3.3.

3.2 BDS characterization of PEO thin films

In Figure 3.2 (a) are shown the BDS spectra in ϵ'' vs frequency of a PEO ultra-thin film with thickness ≈ 20 nm acquired in heating ramp. Also, in Figure 3.2(b), a graphical representation of $\epsilon'_{(100\text{ kHz})}$ against temperature displays how the dielectric constant changes during the ramp. Knowing that the change from solid to liquid state strongly affects the value of ϵ'_{∞} ¹⁴⁰, we can by Figure 3.2(b) give an estimation of the real T_m by considering the transition to occur at the onset of the plotted curve. The T_m of the commented sample was estimated to be between 60° C and 65° C. The T_c was similarly evaluated from a cooling ramp and found to be ≈ 50 °C. Interestingly, we observed a peak in the ϵ'' spectra for $T > T_m$. We will now on refer to the relaxation associated to such signal as μ -. The μ -process observed for $T > T_m$ cannot be associated to segmental mobility, which at this temperature is expected to be more than one million times faster, then it must be related to another relaxation process occurring in such conditions in PEO¹⁴¹. Moreover, as the intensity of this slow process increases as the melting progresses, we attribute this relaxation mechanism to the newly formed polymer melt.

The dynamics of polymeric melts are governed by the flow of macromolecules constantly disentangling and entangling each other that, in a non-equilibrated system, respond to temperature dependent regimes to which is possible to ascribe an Arrhenius trend thereafter an activation energy¹⁴². We commonly refer to this molecular process as “SAP” (Slow Arrhenius Process). The SAP is then related to the flow of the polymer chains and its activation energy matches with the activation energy of the flow⁸³. In a semicrystalline body, where the system can be described by a “frozen” lattice of crystalline domains hindering the shear of macromolecules, the volume fraction of the domains that can relax as a consequence of the SAP is extremely low and localized in the amorphous part. For this reason, a sample of pure PEO under heating shows a clear signal associated with the SAP in the dielectric spectra only after the fusion of the crystals. This evidence can be experimentally appreciated by BDS, but only for samples with extremely low thickness, being the signal normally masked by polarization phenomena in thicker ones (see section 3.1).

As the intensity of the μ -process increases as the melting progresses, we attribute this relaxation mechanism to the newly formed polymer melt. Knowing that, we can claim that the data confirm our previous considerations, showing a clear peak (associated with the SAP of PEO) specifically at the melt state.

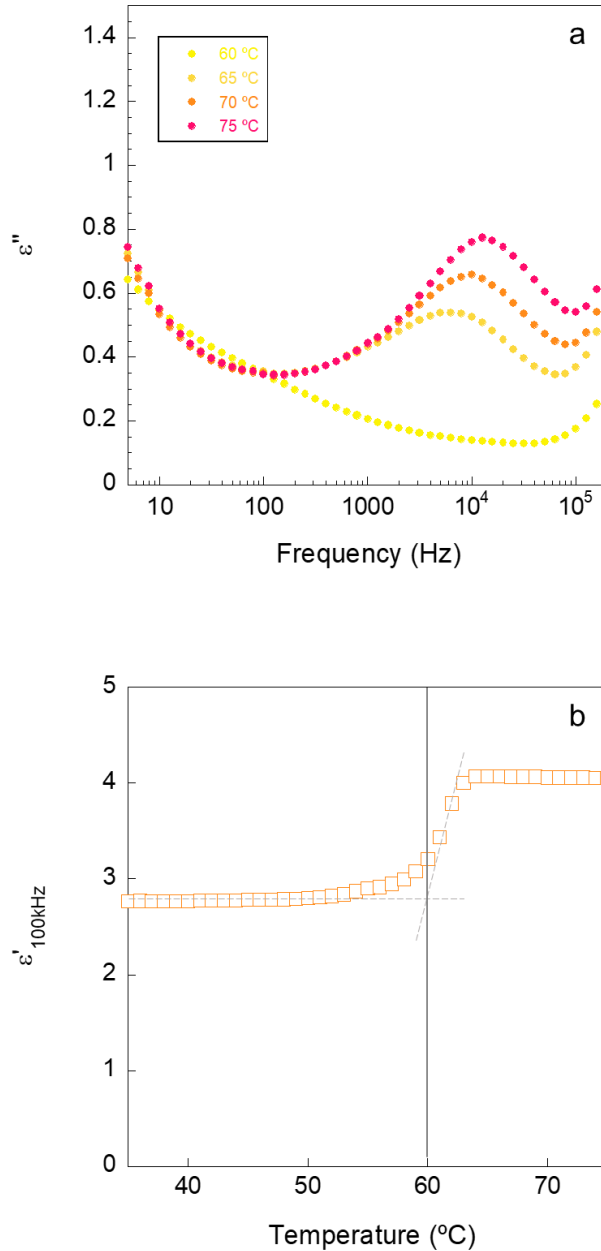


Figure 3.2. Dielectric spectra of PEO ultra-thin film (thickness ≈ 20 nm) at different temperatures for a 1 °C/minute heating ramp.

Being the μ -process ascribable to the melt dynamics, it is possible to take advantage of it to follow the formation/fusion of crystals in time, providing more insights into the kinetics governing crystallization processes in semicrystalline polymers. Nevertheless, this is not the only information that we could gain from the dielectric signature in PEO ultra-thin films. In fact, the analysis also revealed slow and weak changes of the peak position in isothermal conditions, not related to the formation of a liquid phase. As we will see, the peak shift with annealing time is linked to a changed chains conformation in the volume unit.

3.2.1 Heterogeneity in supported PEO melt

To gain more information on the μ -process, we performed another set of experiments by holding the thin polymer films at a suitable temperature in the melting regime. This procedure permitted us to monitor *in situ* the entanglement dynamics in the melt. The annealing experiments on PEO thin film were performed at 65° C, a heating/cooling cycle (in the same conditions of the dynamic analysis) was performed after annealing. To compare the dynamic analysis and the isothermal one on two different samples of PEO, each measuring ≈ 20 nm of thickness, the μ -process from the entire dielectric dataset was approximated to an Havriliak-Negami function with α and β parameters respectively fixed at 0.75 and 1. The fitting results obtained namely τ and $\Delta\varepsilon$, are reported in Figure 3.3.

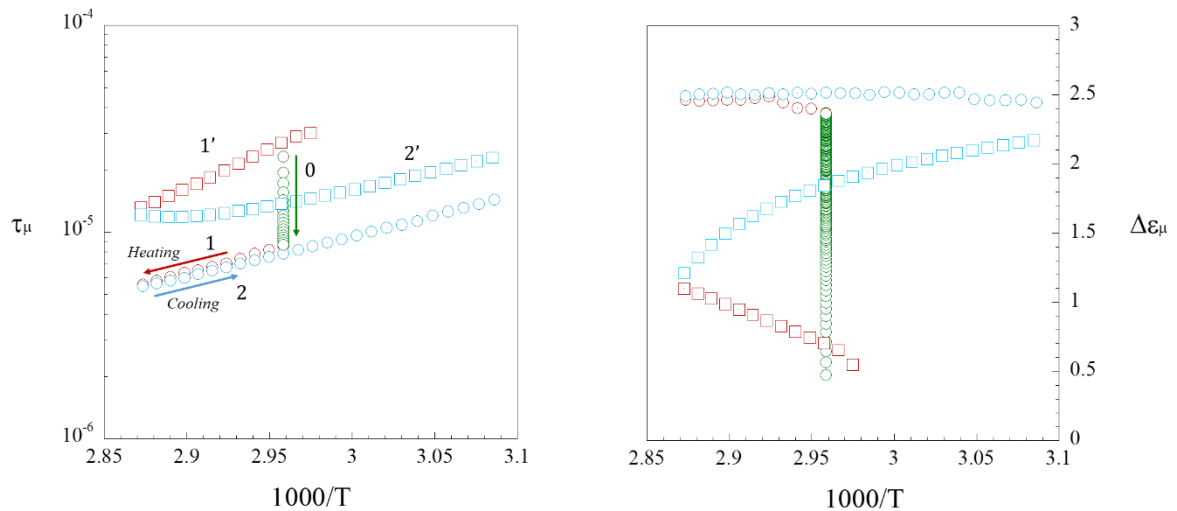


Figure 3.3. Values of τ_μ and $\Delta\varepsilon_\mu$ in logarithmic scale against $1000/T$ (Temperature in °K) for two samples of PEO thin films each possessing thickness ≈ 20 nm. Data plotted as squares refer to a single heating (red: 1') and cooling (light blue: 2') cycle on a fresh sample; data plotted as circles refer to one heating (red: 1) and cooling (light blue: 2) cycle on a sample annealed at 65° C for 48 h in isothermal conditions (green: 0).

As we can observe from the τ values respect temperature, the sample undergoes hysteresis for a first dynamic scan during the heating/cooling cycle, showing quite different values between the heating and the cooling ramp (indicated as squares in the graph from Figure 3.3). This fact suggests a non-equilibrium state of the polymer melt under investigation. By assuming the liquid to have an Arrhenius-like behavior ($E_a = R \partial \ln \tau / \partial (T^{-1})$) and fitting the latest data in cooling ramp (considering the system in this range to be close to its equilibrium state), we obtain an E_a value of 36 kJ/mol. If we now consider data from the isothermal analysis

(indicated as green circles in the graph from Figure 3.3), we can clearly recognize an equilibration of τ_μ with time toward lower values. Moreover, the hysteresis between heating and cooling disappears after the annealing, indicating a different state of the now stable liquid. By fitting the data from the cycle after the annealing, an E_a of 38 kJ/mol was estimated, matching the previous value and confirming that the system goes toward equilibration with the annealing time. Moreover, the E_a of the μ -process matches with the flow activation energy of PEO (≈ 38 kJ/mol from rheological analysis¹⁴¹), as one should expect from a SAP⁸³.

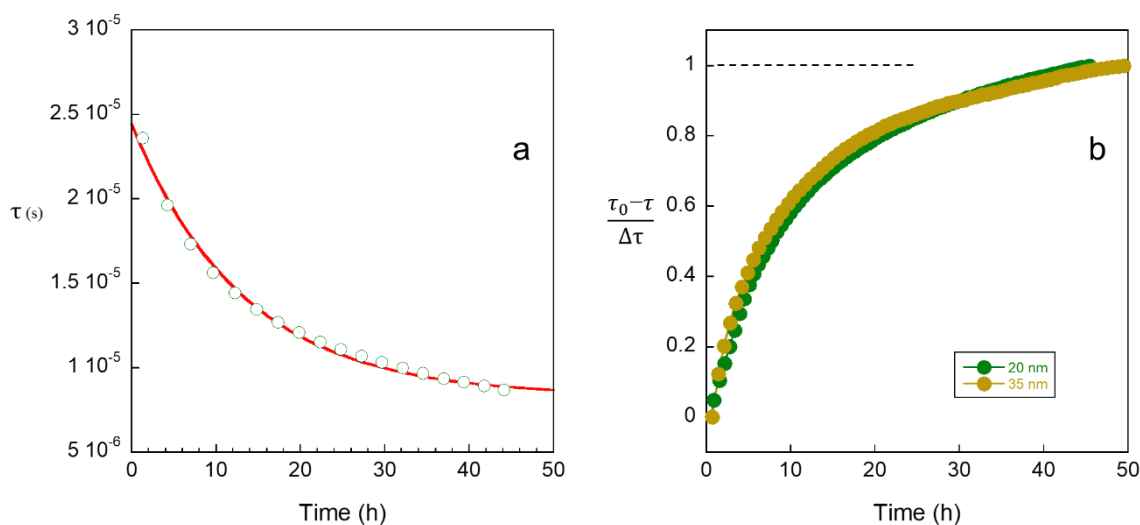


Figure 3.4. a) values of τ_μ against time in isothermal conditions at 65° C for one sample of PEO thin film with thickness ≈ 20 nm. In red: fit to an exponential decay curve. b) Normalized values of τ vs time from isothermals on samples with two different thicknesses, respectively 20 nm and 35 nm. τ_0 identifies the relaxation time corresponding to the infinity annealing limit of isothermal. We set 45 hours as the infinite time of isothermal.

The reason behind changes in τ_μ with time can not be connected to the progressive formation of the liquid because this would alter the magnitude *only*, so then the dielectric strength, of the μ -process due to the evolution of the crystal/melt volume fraction during fusion. In fact, for a shift in relaxation time a different dynamics of the molecular motion would be expected. These considerations lead us to the conclusion that a change in the liquid properties themselves should happen to justify such outcomes. At first instance, a difference in the adsorbed fraction of PEO chains at the surface of the Al electrodes during the annealing could explain such a behavior. The fact that desorption of polymer chains is promoted at higher temperatures is in line with this idea¹⁴³. The increased mobility related to the desorption of the previously partially adsorbed PEO at the surface could indeed fasten up the melt dynamics¹⁴⁴. This hypothesis stands while the kinetics of the process is unrelated to the crystals fusion and,

more important, unchanged for different samples' thicknesses⁸⁴. By focusing on Figure 3.4(b), we can notice how the equilibration kinetics agree with this idea, showing no change with thickness.

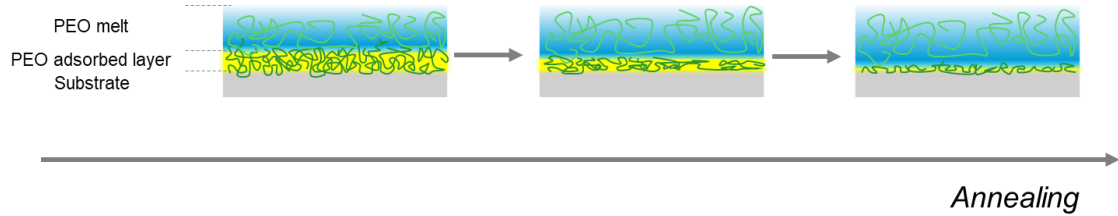


Figure 3.5. Scheme of the equilibration of the polymer adsorbed interface at the Al electrode.

On the other hand, knowing that different molecular conformations may change the rheological properties of the thin film, the results do not exclude a difference in the entanglement disposition of PEO chains at $T > T_m$, which is also in line with other previously reported works^{145,146}. Following this idea, the decrease in relaxation time, connected to the increased mobility of the melt molecules, would be then related to an increased reentanglement rate⁸³. This behavior finds explanation in the intrinsic nature of polymer melts obtained from semicrystalline precursors, where the resulting liquid phase can present a long-living heterogeneous character¹⁴⁷. Figure 3.4(a) shows the values of τ_μ annealed in isothermal conditions at 65° C. Here, the decay of τ_μ to a fixed and lower value reveals the kinetics of the melt: after the fusion point, the new formed *heterogeneous liquid* (having higher molecular mobility¹⁴⁸) tends to equilibrate with time toward the formation of a more stable phase for longer annealing periods¹⁴⁹ (Figure 3.6).

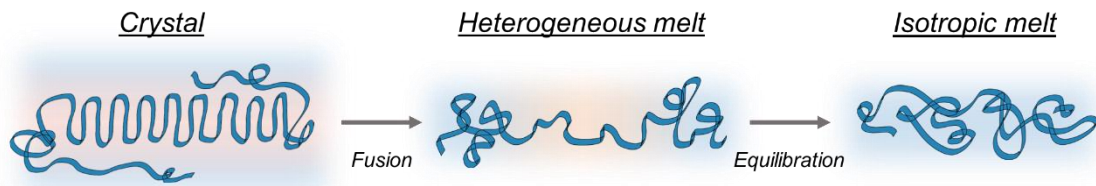


Figure 3.6. Schematic representation of the formation and equilibration of a heterogeneous liquid from a semicrystalline precursor.

To present another evidence of the entanglement evolution for $T > T_m$ in the heterogeneous media, we acquired the BDS spectra on a sample of PEO subjected to multiple heating/cooling cycles. The temperature in the cooling step was lowered below the crystallization temperature in every cycle. The analyzed sample presented a thickness of ≈ 35 nm, which is higher than the first case we presented. The τ_μ values of the sample were found to

be higher respect to the lower thickness example; as we will see in the next paragraphs (section 3.2.2), the increase of τ_μ with thickness is generally observed and connected to the nature of the relaxation itself.

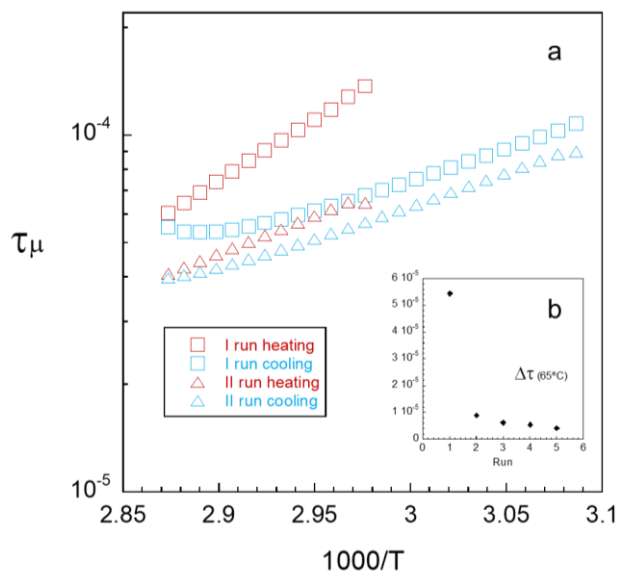


Figure 3.7. a) values of τ_μ in logarithmic scale against $1000/T$ (Temperature in $^\circ\text{K}$) of PEO thin films with thickness ≈ 35 nm during two consecutive heating/cooling cycles; b) $\Delta\tau_\mu$ at 65°C between the heating and cooling step for five consecutive heating/cooling cycles.

As we can observe in Figure 3.7(a), the melting and recrystallization of the polymer do not affect the trend of the relaxation time with temperature. This evidence can be appreciated by following the two series of data displayed by light blue squares and red triangles, revealing once again that the shift in τ_μ position with time is unrelated to any crystallization or melting dynamics. The peak displacement with temperature in the heating step follows the dynamics of the final points from the previous cooling, demonstrating entanglement retention due to *memory effect* of the new melt obtained from the recrystallized material^{150,151}. The results shown in Figure 3.7(a) envisage a smaller hysteresis in the second cycle compared to the first one. These findings point out the impact of the thermal history on the properties of the resulting phase, for which a higher level of heterogeneity is observed in liquids obtained by melting freshly spin-coated films rather than slowly cooled ($0.1^\circ\text{C}/\text{min}$) samples. The melt equilibration after annealing is further proven by following the hysteresis magnitude after several heating/cooling cycles (Figure 3.7(b)), where at every annealing step the value of $\Delta\tau_\mu$ between heating and cooling (at 65°C , for each cycle) keeps lowering down.

All these considerations are not in conflict with our first hypothesis which ascribes the hysteresis phenomenon to the desorption of PEO at the Al interface. In fact, under this

circumstance, the evidence accounting the superposition of the τ_μ vs $1000/T$ slope from the second heating and the first cooling is justified by a the freezing-in of the adsorbed layer as a consequence of crystallization. Under these conditions, in the second cycle the system recovers the desorption kinetics once it accesses the melt state again. As a consequence, we cannot discard one hypothesis or another, these concerning heterogeneous liquid and adsorbed interfaces.

Our study highlights the complexity of the studied system and the several factors one must take into consideration during the analysis of the dynamics in semicrystalline systems. On the other hand, they open the possibility to take advantage of these concepts to follow *in situ* the complex dynamics of such heterogeneous liquids.

3.2.2 Melting of PEO thin films

The melting of polymers is usually conceived as a first order transition where the material undergoes a strong change in elastic modulus and density due to the fusion of its crystalline domains. The mechanism of melting and crystallization of polymeric materials has been argument of debate since several decades due to the complexity given by their semicrystalline nature (see section 1.2.2), for which it is not possible to adopt any model involving an infinitely repeating unit cell for the entire bulk like in standard crystalline media¹⁵². Moreover, the growth and fusion of the crystalline lamellae can develop following different paths, complicating even more the understanding of such dynamics¹⁵³. To follow *in situ* the melting of semicrystalline polymers, we focused the attention on the previously discussed samples of PEO thin films. In particular, we monitored the evolution of the melt dynamics to elucidate any contribution of the progressing fusion of the crystals by BDS taking advantage of the μ -process both in dynamic and isothermal conditions. More specifically, from the isothermal analysis, we were able to recognize the evolution of the μ -peak with time. Changes in $\Delta\epsilon_\mu$ derive from the increment of the liquid fraction per unit of volume. This is directly ascribable to the progressive fusion of the crystalline nuclei providing direct visualization of the melting of these crystalline objects. The complex component of the dielectric constant vs frequency for different annealing times is plotted in Figure 3.8(a).

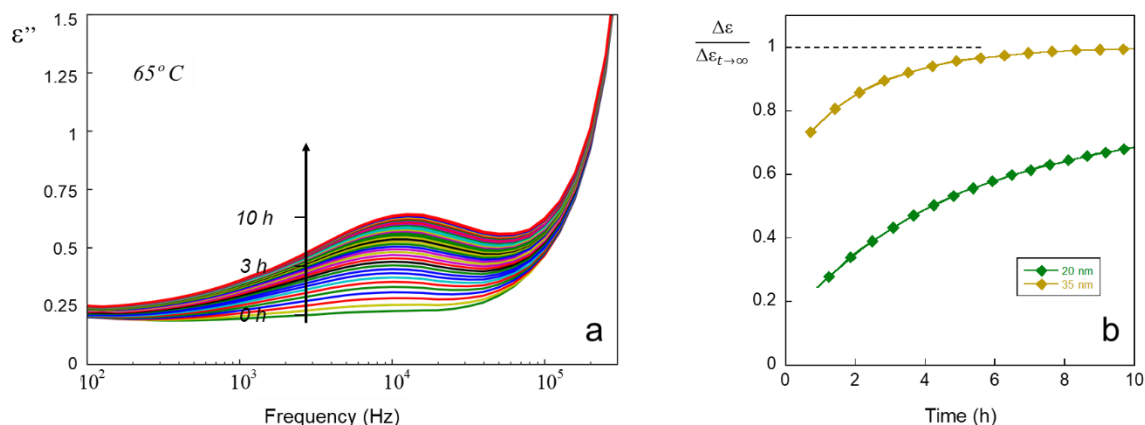


Figure 3.8. a) BDS spectra in ϵ'' vs frequency for PEO thin film (thickness ≈ 20 nm) in isothermal conditions at 65°C ; b) Normalized values of $\Delta\epsilon_\mu$ vs time from the fits on the data from isothermal on samples with two different thicknesses, respectively 20 nm and 35 nm. We set 45 hours as the infinite time of isothermal ($t \rightarrow \infty$).

As we can observe, the peak position slightly changes for an annealing time up to 10 h. This small change in τ_μ is explained by taking into account the presence of multiple phases in the melt, which constitute a heterogeneous media slowly equilibrating with time toward the isotropic state, as discussed in section 3.2.1. On the other hand, the trend of the dielectric strength with time at 65°C (Figure 3.8(b)) shows the fusion of the crystals. At time zero $\Delta\epsilon_\mu$ is extremely low due to the limitation of the dipoles fluctuation given by the crystalline lattice. As the isothermal proceeds, $\Delta\epsilon_\mu$ rises as a consequence of the fusion of the crystals; the maximum rate of fusion, connected to the maximum value in the sigmoidal slope¹⁵⁴, is not so evident from the curves because the system at 65°C is already partially fused, or it quickly fuses at the initial steps of the isothermal. The kinetics shown by the dielectric strength evolution with the annealing time agrees with a nucleation-growth phase transition, being this the usual mechanism driving the polymer crystal melting¹⁵⁵. The curves describing the dielectric strength ascribable to the μ -process in isothermal conditions for different thicknesses reveal the impact of confinement on the crystals' fusion kinetics. We remember that, for higher confinement of PEO, its crystallinity and crystallization/fusion rate can suffer important changes; an increased fusion time is expected for highly constrained semicrystalline polymer films thereafter, samples with lower thickness need more time for the crystalline domains to fully fuse¹⁵⁶. This evidence is experimentally observed by the data presented in Figure 3.8(b), where the melting kinetics of the thinner sample is slower respect to the thicker one.

By analyzing the properties of melt PEO it was possible to discuss several aspects of polymer melting, but more information about the state of the system in solid, or even in the

earlier stages of solid-liquid transition, still lacks deeper insights. To provide a comprehensive description of the studied system, we decided to investigate any other eventual relaxation phenomena related to the crystallinity of PEO by expanding the analysis on a broader range of temperature, now considering also $T < T_m$.

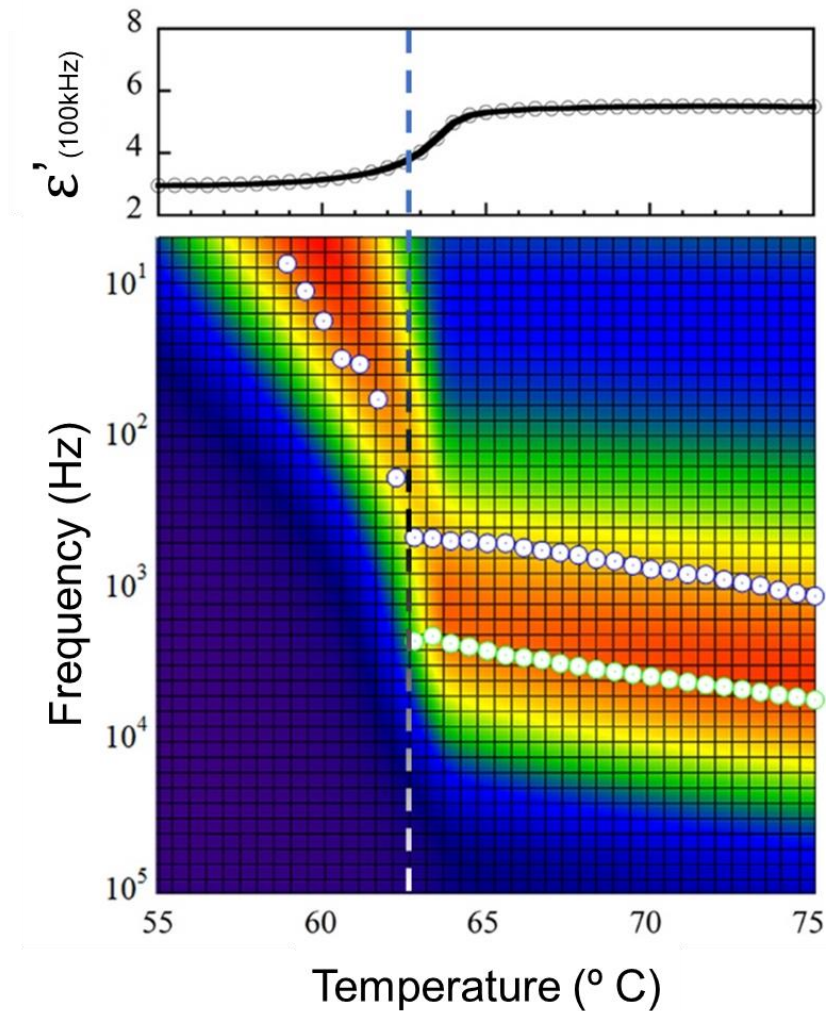





Figure 3.9. Dielectric characterization of 35 nm thick PEO thin film. Similarly to Figure 3.2(b), values of ϵ' at 10^5 Hz were plotted against temperature to recognize the solid-liquid transition. At the bottom: 3D plot of ϵ'' vs frequency vs temperature between 55°C and 75°C on a heating ramp at 1°C/min. Color map scale: 0.0  5.0; peaks ascribable to the MW- and μ -process are labeled in the chart respectively as  and .

In Figure 3.9 we report the BDS spectra of a 35 nm thick PEO film through a 3D plot where frequency and ϵ'' are plotted over the temperature window of interest. As we can observe in the 3D plot a second peak appears at $T > 55^\circ\text{C}$. This signal does not disappear above the melt temperature, as we can observe from the dielectric signatures of the sample at $T > T_m$ from Figure 3.9. We will now on refer to this signal as “MW”. The position of the latter peak below

T_m is extremely sensitive to temperature, shifting rapidly toward higher frequencies until reaching completely different dynamics after the melting point. In the melt, the evolution of the MW signal with temperature follows the dynamics of the μ -process. To better understand the nature of the MW signal, we acquired BDS data on several samples with different thicknesses (results in figure 3.10).

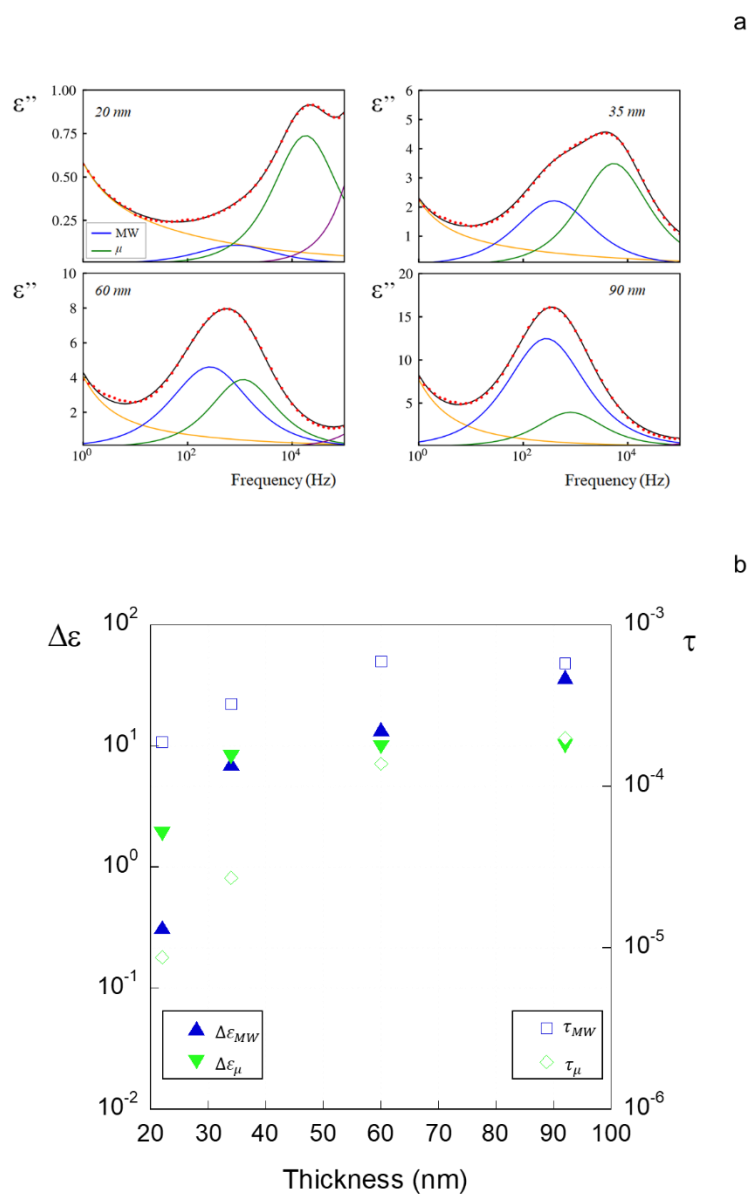


Figure 3.10. At the top: BDS spectra of PEO samples with different thicknesses at 65° C after 48 h annealing. At the bottom: results obtained from the fit on the spectra plotted as τ and $\Delta\epsilon$ respect the samples' thickness.

As we can observe from the obtained results, the MW-process (at lower frequency respect to the μ -process) shows up by increasing the thickness. By extrapolating the relaxation times corresponding to the peaks in function of thickness and fitting the two series of data to a power law, we obtain a factor of 2.3 for the μ -process and a factor of 0.83 for the MW-process. The

values obtained in τ_{MW} and $\Delta\epsilon_{MW}$ put in comparison with τ_{μ} and $\Delta\epsilon_{\mu}$, for a set of samples at 65° C, are plotted in Figure 3.10(b). The fact that the MW signal appears by increasing the thickness, and its relatively high dielectric strength in thick samples, suggests the nature of such relaxation itself, which we envisage to be associated with interfacial polarization.

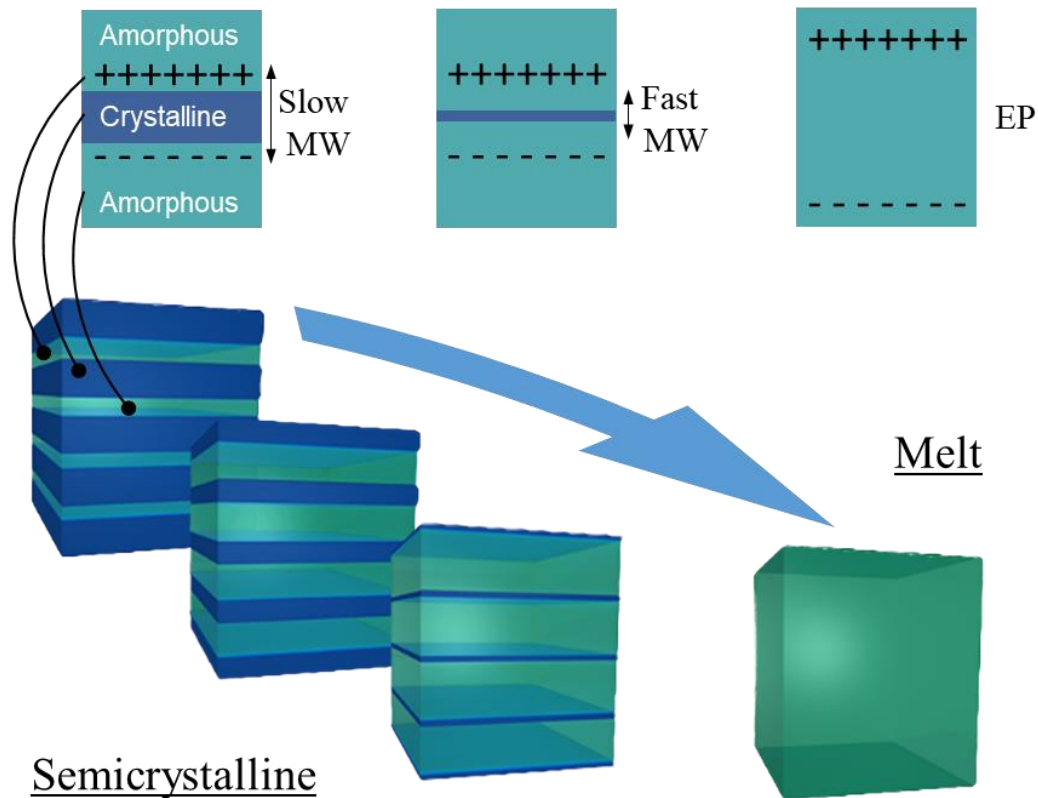


Figure 3.11. Scheme of interfacial polarizations occurring in PEO under an applied electric potential at the melting point.

By knowing that EP relaxations are highly correlated to the chains dynamics of the medium^{135,157}, the MW signal for $T > T_m$ must be related to the interfacial polarization between the two electrodes due to its evident correlation with μ . On the other hand, the different evolution of the peak position below the T_m seems to address to the MW interfacial polarization a different nature in solid state, where it is associated to a way faster kinetics. For this reason, we ascribe the MW-process below the T_m to the interfacial polarization between semicrystalline objects (MWS relaxation) that rapidly fuse in proximity of the melting point. With the progressive fusion of the crystals, the MW-process fastens up due to the lower lamellae number and thickness¹³⁹, shifting the values of the peak maximum toward higher frequencies by the proceeding of the lamellar fusion. Resuming, we attribute the peak MW at $T < T_m$ to interfacial

polarization taking place at the lamellar interphase (MWS-like) which develops towards an electrode polarization once the polymer finds its melt state.

To summarize, in the work presented by this first section we systematically investigated the melting process in PEO semicrystalline thin films via BDS. By monitoring the real part of permittivity at high frequency as a function of temperature in the heating ramp, we were able to identify the T_m under the applied heating rate. By the acquisition of the dielectric spectra, it was possible to identify a relaxation process as a peak in ϵ'' sharing the same activation energy that the melt flow and addressed as μ -process. The molecular origin of such process was ascribed to the SAP, moreover, the μ -process occurs in the liquid only, giving the possibility to introduce an experimental methodology to investigate the kinetics involved in the solid/liquid transition of the polymer. The strong hysteresis exhibited by the μ -process between the first heating and the first cooling attests to a heterogeneous metastable character of the supported melt, which equilibrates towards equilibrium with annealing time. The heterogeneity of the melt can be attributed either to the layer adsorbed at the electrode interface or to the characteristics of the liquid itself. Finally, by increasing the thickness of the sample a second peak was detected. The MW-process, ascribed to interfacial polarization, increases by increasing the thickness of the sample and follows the dynamics of the SAP in the melt state. From the acquired set of data, we envisage that the MW-process evolves from a MWS polarization toward EP along with the fusion of the crystalline objects in proximity of the solid/liquid transition.

3.3 Imaging the heterogeneous transport properties in PEO by nano-Dielectric Spectroscopy

In the past few decades, the growing interest in soft matter and advanced materials have driven an equally big necessity of having more effective microscopy techniques in order to get access to the compositional characteristics of complex micro- or nano- structures. In this respect, a series of methods that enable the unveiling of structural and compositional elements of a surface were developed by means of Atomic Force Microscopy (AFM)¹⁵⁸. For example, Peak-Force Quantitative Nanomechanical Mapping (PF-QNM) (see section 2.3.1), Scanning Kelvin Probe Microscopy (KPFM), which is able to map a surface's work function¹⁵⁹, and infrared related AFM methods (IR-AFM), which are capable to relate the infrared absorption fingerprints to the surface composition¹⁶⁰.

In the previous section, we demonstrated the effectiveness of broadband dielectric spectroscopy (BDS) in studying the dynamics and charge mobility of PEO thin films. Nevertheless, by only relying on the classical BDS experiment, the influence of the nanostructure boundaries and interfaces on the dielectric signature cannot be directly assessed, thus becoming a model-dependent aftermath. In fact, in section 3.2 we did not focus on the special arrangement of the involved phases at the solid state, nor on how this affects the ion mobility in the semicrystalline medium. As already reported in previous other works^{161,162}, a promising solution to register the dielectric signature of the PEO complex nanostructured surface is the use of Electrostatic Force Microscopy (EFM) in the alternated current regime. Following this idea, in this chapter we present a study aiming to get insight into ion transport in PEO through *n*DS taking advantage of the EFM setup. Here, we are exposing a detailed model of the *n*DS with the aim of demonstrating the consistency of the experimental observations that we are going to discuss concerning the ion conductivity in the semicrystalline polymer.

3.3.1 A model for *n*DS

In EFM, the lack of an appropriate model to directly link the AFM signal to the complex dielectric constant still constitutes an important applicability limitation of the technique. The existing models are derived by considering purely conducting substrates. In the case of

dielectric samples, under the assumption of small film thicknesses, they are mostly arranging the discussion without taking into account the possibility of more complex electrostatic interactions occurrence between the probe and the surface^{163,164} such as, as we will see, the heterogeneity of the electric field in proximity of the tip due to electrostatic charge accumulation. To provide a more consistent correlation between the signal in output from the AFM and the local dielectric properties of a generic substrate, we elaborated a model of the system starting from the probe-sample geometry and integrating previously adopted strategies with a systematic study of the experimental setup.

In a local *n*DS experiment (non-scanning) the tip is lifted at a certain distance (z) from the surface and a sinusoidal voltage (V) is sent to the circuit where the upper electrode is the AFM probe and the bottom one is a flat grounded conducting substrate on which lays the sample thin film (see section 2.3.1). As exhaustively explained in the upcoming section, the resulting motion of the cantilever is well described by the damped harmonic oscillator. The electrical force F_e driving the oscillation, experimentally measured by the photodiode, provides information about the probe-sample capacitance (eq. 2.6). The shape of the probe constitutes a complex geometry, so it is convenient to model the probe-sample-capacitor as a sum of contributions coming from different bodies of easier interpretation: the *cantilever*⁽ⁱ⁾, the *cone*⁽ⁱⁱ⁾, and the *apex*⁽ⁱⁱⁱ⁾ separately (see Figure 3.12, eq. 3.3). By firstly considering the simpler case, for a purely conductive substrate the following relations were proposed.

$$F_{e(2\omega_e)Tot} = -\frac{1}{4}V_0^2 \cos(2\omega_e t) \left(\sum_i \frac{\partial C_i}{\partial z} \right) \quad (3.3)$$

- (i) The apex contribution comes from its analytical expression, as read in eq. 3.4, derived for a spherical capacitor of radius R attached at the end of the cone of angle θ (see Fig. 3.11)¹⁶⁵.

$$\frac{\partial C_{apex}}{\partial z} = 2\pi\epsilon_0 \frac{R^2(1-\sin(\theta))}{(z+R(1-\sin(\theta)))} \quad (3.4)$$

- (ii) The cantilever of length L , width W , and tilt angle (respect the sample plane) α , is modeled as a plate. Then, we approximate the cantilever-sample capacitor to the plates geometry with an extra-factor that takes into account the distortion of the electric field due to border effects (BE)^{166,167} (eq. 3.5).

$$\frac{\partial C_{cantilever}}{\partial z} = \pi\epsilon_0 (BE) \left(\frac{1}{\pi} \right) \left(\frac{LW}{(z+H)^2} \right) \left(\frac{1}{1+\frac{L}{z+H} \tan(\alpha_{tilt})} \right) \quad (3.5)$$

- (iii) The geometry of the cone portion is given by the tip apex radius R , the cone height H and the cone angle θ . The conical contribution to the force, expressed in eq. 3.6, is calculated by integration over the force acting on the interested portion of the cone ¹⁶⁷.

$$\frac{\partial C_{cone}}{\partial z} = \frac{2\pi\epsilon_0}{\left(\ln\left(\tan\left(\frac{\theta}{2}\right)\right)\right)^2} \left(\ln\left(\frac{H}{z+R(1-\sin(\theta))}\right) - 1 + \left(\frac{R \frac{\cos^2(\theta)}{\sin(\theta)}}{z+R(1-\sin(\theta))}\right) \right) \quad (3.6)$$

A similar approach was followed by Hudlet et al. (without considering the cantilever contribution) ¹⁶⁵ and by Law et al. (without considering BE) ¹⁶⁷ to resolve the force resulting from a purely conducting grounded substrate. In their works, the authors proved the good consistency of the model by verifying experimentally the results obtained on Si wafer. More recently, the model was extended for the description of the force in presence of a thin dielectric layer, opening the possibility to get quantitative information about the dielectric properties of a sample in thin film geometry ¹⁶⁴. Respect to the relations already seen for conducting substrates, the model equations normally used to determine the local dielectric constant add an effective extra distance to z depending on the thickness (h) and on the relative permittivity of the dielectric layer (ϵ) as : $z \rightarrow z + \frac{h}{\epsilon}$, in such a way to relate values of F_e to ϵ ^{163,164}. It is important to underline that such assumption is an approximation valid for $\frac{h}{\epsilon} \ll R$, that to say for effective thicknesses small enough to not distort the electric field due to polarization effects. The validity of the model was experimentally studied by *Miccio et al.* on PVAc thin films ¹²⁵.

In Figure 3.13(a), we report the data in $F_{e(2\omega)}$ as a function of z acquired on a SiOx thin film with thickness 200 nm and on a *perfect* conductor (Au), respectively. In the same chart, the solid curves show the calculations performed by modelling the probe geometry parameters of the tip (see Table 3.1) following eq. 3.4,3.5, and 3.6. As observed from the results, the model describes well the behavior in the proximity of metals (Au), but it fails at short tip-sample distances in the presence of a dielectric (SiOx). In particular, by strictly considering the above presented equations and assuming a uniform electric field in the dielectric layer, we found that the measured force at short distances increases faster than expected in the presence of a dielectric of significant thickness. This occurs because the extra polarization charges accumulated at the surface of the sample generate a contribution which affects the total force. Then, considering this evidence, an extra term will be needed to describe the system for

dielectric films when the condition $\frac{h}{\varepsilon} \ll R$ does not apply. Therefore, in eq. 3.3 we should consider four distinct contributions:

$$\sum_i \frac{\partial C_i}{\partial z} = \frac{\partial C_{\text{excess}}}{\partial z} + \frac{\partial C_{\text{apex}}}{\partial z} + \frac{\partial C_{\text{cone}}}{\partial z} + \frac{\partial C_{\text{cantilever}}}{\partial z} \quad (3.7)$$

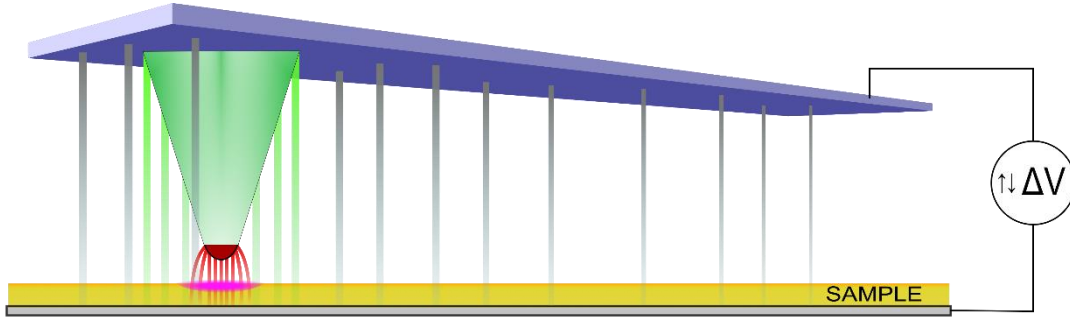


Figure 3.12. Scheme of the probe-sample capacitor. The colored lines are a visual representation of the electric field shape characteristic for the separated contributions to the total capacitor. Grey: *cantilever*; green: *cone*; red: *apex*; pink: *excess* from the partially charged surface potential.

As we expect the extra charges to accumulate near the apex, the excess term shall involve the apex force component. To model excess force, we considered that the surface charge density generated by a point charge close to a dielectric surface and that close to a conductor plane are different just by a factor $\frac{\varepsilon - 1}{\varepsilon + 1}$ ^{168,169}. Moreover, this excess term should vanish for $\frac{h}{\varepsilon} \ll R$ and therefore we introduce an exponential decay for this limit. Following these ideas, the evaluation of the excess force leads to:

$$\frac{\partial C_{\text{excess}}}{\partial z} = \left(1 - e^{-\frac{h}{R\varepsilon}}\right) \left(\frac{\varepsilon - 1}{\varepsilon + 1}\right) \frac{\partial C_{\text{apex}}}{\partial z} \quad (3.8)$$

In Figure 3.13(b) we show the comparison of the experimental results on PVAc and SiOx films ($h = 110$ nm and $h = 200$ nm, respectively) and the curves evaluated using the above presented approach. In both cases, we obtained a good agreement using the typical values of ε for PVAc ($\varepsilon = 3$) and SiOx ($\varepsilon = 3.9$). The calculations were performed starting from the characteristic parameters of the used probe (typical values reported in Table 3.1). Values of cantilever length L , cantilever width W , and cone height H were provided by the supplier. The cantilever tilt angle α_{tilt} is the orientation of the probe holder respect with the sample surface, estimated to be ≈ 30 - 35° . The border effects BE , cone angle θ , and tip radius R were left as free parameters in the fitting of the results on the conducting substrate. These parameters were fixed for all the calculations related to the same probe. By changing the AFM probe, only a small deviation

results from different specimen of the same type. The deflection sensitivity of the photodiode was also left as a free parameter. As the deflection sensitivity usually undergoes small changes with time due to laser misalignment from an experiment to another, it was not strictly fixed even under the usage of the same tip, thus, it does not present one typical value. For this reason, we did not report this parameter in Table 3.1.

Probe: HQ_DPE_XSC11			
R	Tip radius	~ 40 [§]	nm
θ	cone angle	~ 20 [§]	°
H	cone length	15 ⁺	μm
W	cantilever width	30 ⁺	μm
L	cantilever length	150 ⁺	μm
α_{tilt}	cantilever tilt angle	~ 30 [*]	°
BE	border effect	2-7 [§]	/
f_0	resonance frequency	150 [*]	Hz
K	spring constant	7 [*]	N/m

Table 3.1. Parameters of the tip used for the validation of the model. (*) Nominal values provided by the probe supplier. (+) Determined from SEM images of the probe. (§) Determined by experiments on a bare conducting substrate ($R^2=0.986$).

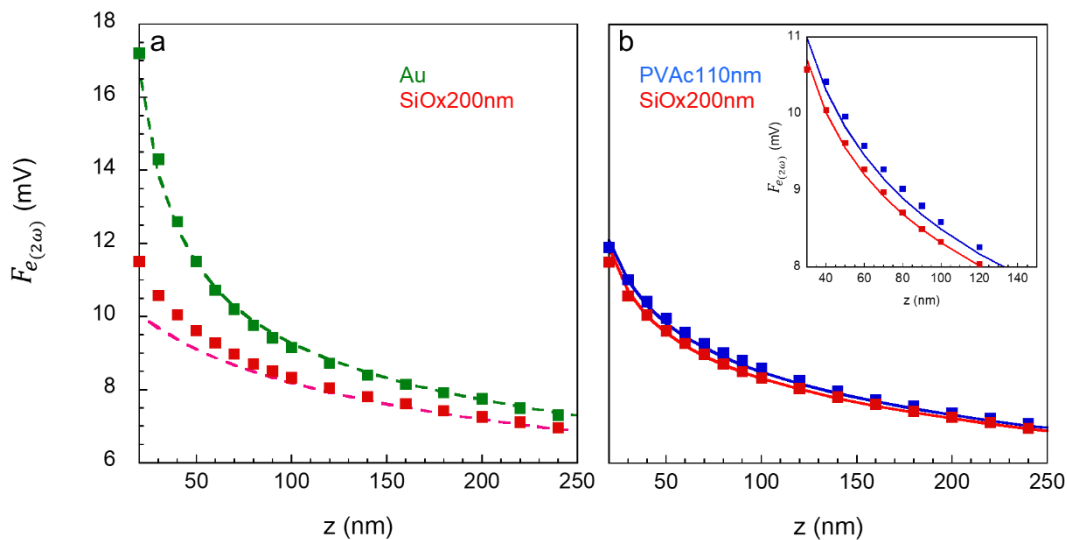


Figure 3.13. Results for a local n DS experiment on different substrates plotted as $F_{e(z,\omega)}$ against z . The experimental parameters are shown in upper table 3.1. The continuous lines represent the predictions from the model without (dashed lines, a) and with (solid lines, b) the excess contribution to the total electrostatic force.

Based on our previous discussion, the postulations so far advanced forward a good understanding of the forces acting on the probe in the conditions given by the *nDS* experiment. On the other hand, what we are mostly interested in a broadband dielectric characterization is the information related to matter dynamics or, in other words, the information bounded to the dielectric losses of the material where generally a frequency dependent dielectric permittivity is present. Thus, it is important to note that in the above expressions $\varepsilon = \varepsilon(\omega_e)$, since F_e is determined using an electrical field varying at frequency ω_e . It follows that, for non-uniform dielectric films, distinct ε values should be considered for the different contributions of cantilever, cone, and apex. However, for the contributions related to the tip apex, the local values $\varepsilon_{loc}(\omega_e)$ corresponding to a small area below the apex would be of relevance¹²⁶.

Before starting modeling the different contributions to the dielectric loss of a generic sample, we need first of all to access that information from the experimental data resulting from *nDS*. For a fixed frequency, in the case of a film where some dielectric relaxation occurs, the oscillating electrical force will have two components each connected either with the real or with the imaginary part of the capacitances appearing in eq. 3.3 ($C^*=C'-iC''$). The one related with the real part would drive the cantilever motion (with amplitude $F_{e,driv} \propto \frac{\partial C'}{\partial z}$) whereas the other one would correspond to a friction-like force since it will act out of phase (with amplitude $F_{e,frict} \propto \frac{\partial C''}{\partial z}$). Note that the loss tangent relates both C' with C'' and $F_{e,driv}$ with $F_{e,frict}$, as:

$$\tan(\delta) = \frac{C''}{C'} = \frac{F_{e,frict}}{F_{e,driv}} \rightarrow F_{e,frict} = F_{e,driv} \tan(\delta).$$

Assuming the probe motion during the local *nDS* experiment to be described by an harmonic oscillation $x(t) \approx A_0 \sin(\omega t + \varphi)$, any eventual shift in phase (φ) between the oscillation of the probe and the sinusoidal exciting electric field at frequencies far below the resonant frequency ω_0 will be related to the dissipative forces acting on the probe. Finding the connection between the dielectric losses of the dielectric film and such dissipative forces, would therefore allow relating the complex dielectric permittivity of the film to the phase shift registered by *nDS*¹⁷⁰.

Let's write the equation of motion for the AFM probe under these circumstances:

$$\frac{F_{driv} \sin(\omega t)}{m} = \omega_0^2 x + \frac{F_{driv}}{m} \tan(\delta) \cos(\omega t) + \ddot{x}(t) = \omega_0^2 A_{driv} \sin(\omega t) \quad (3.9)$$

Being the resonance frequency $\omega_0 = \left(\frac{k}{m}\right)^{\frac{1}{2}}$ with m representing the mass and k the elastic constant of the probe, respectively. A_{driv} represents the amplitude of the probe oscillation in

the zero-frequency limit and without friction ($\delta = 0$). For the sinusoidal AFM probe oscillation, the above equation can be rewritten as:

$$-\frac{\omega^2}{\omega_0^2} \sin(\omega t + \varphi) + \frac{A_{driv}}{A_0} \tan(\delta) \cos(\omega t) + \sin(\omega t + \varphi) = \frac{A_{driv}}{A_0} \sin(\omega t) \quad (3.10)$$

If the AFM probe motion is approximately represented by that of a damped harmonic oscillator, with a frictional force $F_{frict} = -\lambda \dot{x}(t)$, the corresponding equation would read as:

$$-\frac{\omega^2}{\omega_0^2} \sin(\omega t + \varphi) + \frac{\omega}{\omega_0^2} \frac{\lambda}{m} \cos(\omega t + \varphi) + \sin(\omega t + \varphi) = \frac{A_{driv}}{A_0} \sin(\omega t) \quad (3.11)$$

from which we obtain:

$$\tan(\varphi) = -\frac{\omega \lambda}{(\omega_0^2 - \omega^2)m} \text{ and } \frac{1}{A_0} = \left((\omega_0^2 - \omega^2)^2 + \left(\frac{\omega \lambda}{m} \right)^2 \right)^{\frac{1}{2}}.$$

It follows that direct comparison of the two eq. 3.10 and 3.11 for $\varphi \approx 0$ yields to:

$\rightarrow \lambda \approx \frac{m \omega_0^2 A_{driv}}{\omega A_0} \tan(\delta)$. Considering now a real AFM probe moving with a given friction term λ_0 , the *n*DS equation of motion in terms of a damped harmonic oscillator equation would include an effective friction term: $\lambda_{eff} \approx \lambda_0 + \frac{m \omega^2 A_{driv}}{\omega A_0} \tan(\delta)$, which can be rewritten as:

$$\lambda_{eff} \approx \lambda_0 + \frac{m \omega_0^2 A_{driv}}{\omega} \left((\omega_0^2 - \omega^2)^2 + \left(\frac{\omega \lambda}{m} \right)^2 \right)^{\frac{1}{2}} \tan(\delta).$$

Using this effective friction, the motion of the AFM probe during the *n*DS experimental conditions would correspond to:

$$\tan(\varphi_{eff}) \approx -\frac{\omega \lambda_0}{(\omega_0^2 - \omega^2)m} - \left(1 + \frac{\omega^2 \lambda_0^2}{m^2 (\omega_0^2 - \omega^2)^2} \right)^{\frac{1}{2}} \tan(\delta).$$

Since $\tan(\varphi_0) = -\frac{\omega \lambda_0}{(\omega_0^2 - \omega^2)m}$ we finally obtain:

$$\tan(\varphi_0) - \tan(\varphi_{eff}) \approx \left(1 + \tan^2(\varphi_0) \right)^{\frac{1}{2}} \tan(\delta)$$

$$\tan(\delta) \approx \frac{\tan(\varphi_0) - \tan(\varphi_{eff})}{\left(1 + \tan^2(\varphi_0) \right)^{\frac{1}{2}}} \quad (3.12)$$

Eq. 3.12 allows obtaining the phase angle δ , characteristic of the capacitor formed by the AFM probe and the dielectric film on a metallic substrate, as a function of the phase of the oscillating AFM probe as determined on a reference loss-free surface, φ_0 , and on the dielectric

film under investigation, φ_{eff} . For low values of the phase shifts eq. 3.12 can be further simplified as:

$$\delta \approx \varphi_0 - \varphi_{eff} \quad (3.13)$$

According to eq. 3.13, one can directly estimate the dielectric loss of the material under investigation by simply calibrating the system with a reference substrate, where the latter must present no dielectric losses in the interested frequency window. δ will be given by the difference of the phases registered on the dielectric sample and a reference background.

3.3.2 Modelling the loss factor of the AFM system capacitor

To seek a connection between the loss factor of the AFM system capacitor and the dielectric properties of the film, we want now to expand the discussion in order to model the term δ . We can describe the probe-sample system as an air-filled capacitor as that resulting in the case of a conducting surface with capacitance C_A , in series with the sample capacitor of thickness h and complex dielectric permittivity ε^* . The complex sample capacitance of the dielectric film can be expressed as $C_S^* = C_0(\varepsilon' - i\varepsilon'')$, where C_0 is the capacitance of a dielectric film of permittivity 1 (air capacitor), also known as geometrical capacitance. In this case, the relation $\frac{1}{C^*} \approx \frac{1}{C_0\varepsilon^*} + \frac{1}{C_A}$ applies, which can be transformed in:

$$C^* \approx \frac{C_{A(z)} C_S^*}{C_{A(z)} + C_S^*} = \frac{C_0 \varepsilon^*}{1 + \frac{C_0}{C_A} \varepsilon^*} \quad (3.14)$$

Alternatively, introducing the complex dielectric modulus $M^* = \frac{1}{\varepsilon^*}$ it follows $\left(\frac{1}{C^*}\right)' \approx \frac{M'}{C_0} + \frac{1}{C_A}$ and $\left(\frac{1}{C^*}\right)'' \approx \frac{M''}{C_0}$. Thereafter, $\tan(\delta)$ is given as:

$$\tan(\delta) = \frac{\left(\frac{1}{C^*}\right)''}{\left(\frac{1}{C^*}\right)'} \approx \frac{M''}{\frac{C_0}{C_A} + M'} \quad (3.15)$$

These approximations provide the link between the dielectric properties of the film and the loss factor of the AFM capacitor. Eq. 3.15 already provides some empirical outputs: for very thin films $\left(\frac{C_0}{C_A} \gg 1\right)$, $\tan \delta \rightarrow 0 \propto M''$; vice versa $\left(\frac{C_0}{C_A} \ll 1\right)$: $\tan \delta \approx \frac{M''}{M'}$.

To provide the solution for a general case, we now need to evaluate the term $\tan(\delta)$ for every component (*cantilever, cone, apex, and excess*).

For the *excess* contribution coming from the surface in proximity to the apex, we have not a serial combination of sample and air capacitances and eq. 3.15 does not apply. Contrary, $\tan(\delta)$ can be calculated directly from the expression of the full capacitance: $C_{excess} \propto \frac{\varepsilon^* - 1}{\varepsilon^* + 1}$ as:

$$\tan(\delta) = \frac{2M''}{(1-M')^2 - M''^2} \approx \frac{2\varepsilon''}{\varepsilon'^2 - 1}.$$

In the case of *cantilever*, *cone*, and *apex* calculations, it is convenient to consider the above equations for a virtual dielectric film of permittivity 1. Under the previous approximations, the capacitance can be calculated as a serial system that must coincide with the capacitance calculated at a distance $z + h$ from a metallic surface:

$$\frac{1}{C_0} + \frac{1}{C_A(z)} \approx \frac{1}{C_{tot}} = \frac{1}{C_A(z+h)}$$

By using this approximation, we can calculate $\frac{C_0}{C_A}$ as:

$$\frac{C_0}{C_A} \approx \left(\frac{C_A(z)}{C_A(z+h)} - 1 \right)^{-1} \quad (3.16)$$

without any reference to the dielectric material other than the film thickness.

Now let's proceed with the evaluation of eq. 3.16 for each of the contributions to the total AFM probe system capacitance. Adopting the plate geometry for the cantilever contribution, it is possible to estimate $C_{A_{cantilever}}$ ¹⁶⁶ as:

$$C_{A_{cantilever}}(z) \propto \left(H + \frac{L}{2 \sin(\alpha_{tilt})} + z \right)^{-1} \quad (3.17)$$

Thus, from eq. 3.16 we obtain: $\left(\frac{C_0}{C_A} \right)_{cant} \approx \left(H + \frac{L}{2 \sin(\alpha_{tilt})} + z \right) / h$.

For the capacitance of a cone portion there is not a general expression, but it exists for a metallic cone portion perpendicular to a conducting plane when the cone vertices meet the plane itself¹⁶⁵. A geometrical representation of such situation is provided in Figure 3.14.

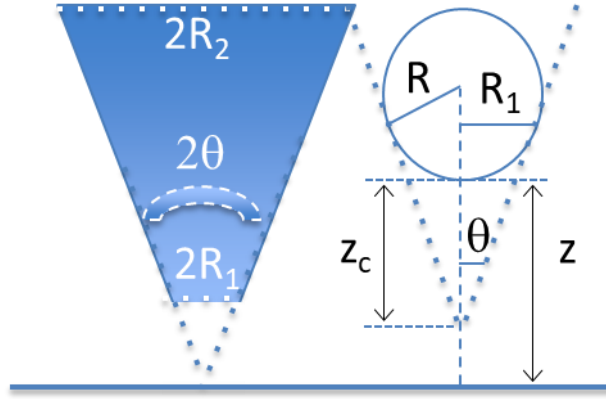


Figure 3.14. Scheme of the cone geometry.

In this case:
$$C_{cone} = \frac{2\pi\epsilon_0(R_2 - R_1)}{\ln\left(\frac{1}{\tan\left(\frac{\theta}{2}\right)}\right)}$$

For the cone representing the tip of the AFM probe, $R_2 \approx H \tan(\theta)$, $R_1 = R \cos(\theta)$ and $z_c = R \left(\frac{1}{\sin(\theta)} - 1\right)$. Therefore, the cone tip capacitance at this distance from the conducting substrate is given by:

$$C_{A_{cone}}(z = z_c) \approx \frac{2\pi\epsilon_0(H \tan(\theta) - R \cos(\theta))}{\ln\left(\frac{1}{\tan\left(\frac{\theta}{2}\right)}\right)} \quad (3.18)$$

The cone capacitance for other tip positions can be calculated approximately by means a first order expansion around z_c as: $C_{A_{cone}}(z) \approx C_{A_{cone}}(z = z_c) - \frac{\partial C_{cone}}{\partial z}(z_c - z)$.

where the coefficient $\frac{\partial C_{cone}}{\partial z}$ is given by the equation of the force contribution from the cone (eq. 3.6) evaluated at $z = z_c$. In this way we obtain:

$$\left(\frac{C_0}{C_A}\right)_{cone} \approx \frac{C_{A_{cone}}(z=z_c)}{\left(\frac{\partial C_{cone}}{\partial z} - h - z + z_c\right) h}$$

For the conventional apex contribution, the analytical expression of the capacitance is given by¹⁷¹:

$$C_{A_{apex}}(z) = 2\pi\epsilon_0 R \ln\left(1 + R \left(\frac{1 - \sin(\theta)}{z}\right)\right) \quad (3.19)$$

which, when used in eq. 3.16, results in:

$$\left(\frac{C_0}{C_A}\right)_{\text{apex}} \approx \left[\frac{\ln\left(1 + R\left(\frac{1 - \sin(\theta)}{z}\right)\right)}{\ln\left(1 + R\left(\frac{1 - \sin(\theta)}{z + h}\right)\right)} - 1 \right]^{-1}$$

Finally, using each term $\tan(\delta)_i$ (with $i = \text{cantilever, cone, apex, excess}$) in eq. 3.15, the total $\tan(\delta)$ can be directly obtained as:

$$\tan(\delta) = \frac{\sum_i (\tan(\delta)_i \frac{\partial C_i}{\partial z})}{\sum_i \left(\frac{\partial C_i}{\partial z}\right)} \quad (3.20)$$

where $\frac{\partial C_i}{\partial z}$ have to be calculated according with eq. 3.4, 3.5, 3.6 and 3.8.

Model Validation

To validate the model, we acquired the n DS spectra on a thin film of PMMA ($h = 120$ nm) deposited on a Si wafer for three different z tip-sample distances, respectively 100 nm, 30 nm, and 20 nm. The sample was prepared by spin coating from a solution with concentration of the polymer in Toluene equal to 20 mg/mL. PMMA was selected among other polymers as a standard substrate because it presents a prominent β -relaxation at room temperature in the frequency range accessible to the technique. Moreover, due to the relatively high stiffness of PMMA, errors arising from adhesion or plastic deformation during the acquisition of the force curve needed to estimate the tip-sample distance are minimized, providing the possibility to have higher accuracy in the calculation of z , also preventing the possibility of tip contamination

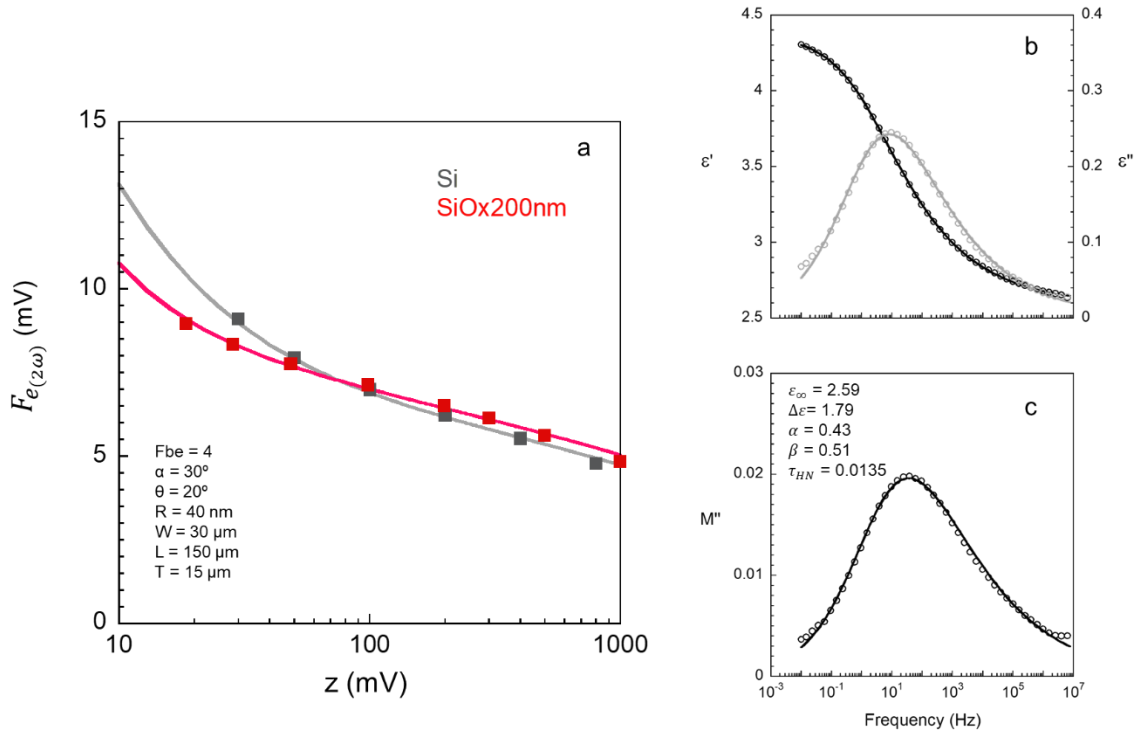


Figure 3.15. a) Results for a local n DS experiment on Si and SiOx plotted as $F_{e(z,\omega)}$ against z in logarithmic scale, experimental point (squares) and fit results (solid lines). b,c) BDS results (circles) and respectively HN fitting (solid lines) at 28° C on PMMA in ϵ^* (b) and M'' (c).

Before proceeding with the calculation of the n DS spectra from the model, the parameters of the tip were adjusted by fitting the data of the electrical force as a function of z obtained on two standards, SiOx ($h = 200$ nm) and Si, with the same tip and setup employed during the n DS experiment on PMMA. The results of the analysis are shown in Figure 3.15(a) where, to better appreciate the fittings, a logarithmic scale was used to plot z values.

The spectra at 28° C of the bulk sample were obtained by BDS and shown in Figure 3.15(b,c). We selected this conditions in order to start our calculations from data acquired at T slightly higher than room temperature, this because the local temperature at the AFM tip-sample region during the n DS experiment can be higher compared to the surrounding atmosphere due to the heating caused by the laser beam or other factors. By fitting the dielectric function to the Havriliak-Negami model (eq. 1.28), we quantified a value of $\tau_{\beta_{PMMA}}^{HN} = 1.35 \times 10^{-2}$ s and $\Delta\epsilon_{\beta_{PMMA}} = 1.79$. The same values obtained by BDS of $\epsilon'(f)$ and $M^*(f)$ were used to calculate the expected n DS response on the PMMA thin film at different z -distances by means of eq. 3.20. Finally, we compared the expected values of δ from the model respect to the experimental data. Figure 3.16 shows the experimental data (discrete points) and the values of δ calculated following the model equations (solid lines) in the same plot. As we can observe, the

superposition of the calculations with the experimental results is accurate, demonstrating the good consistency of the proposed model for the case of PMMA.

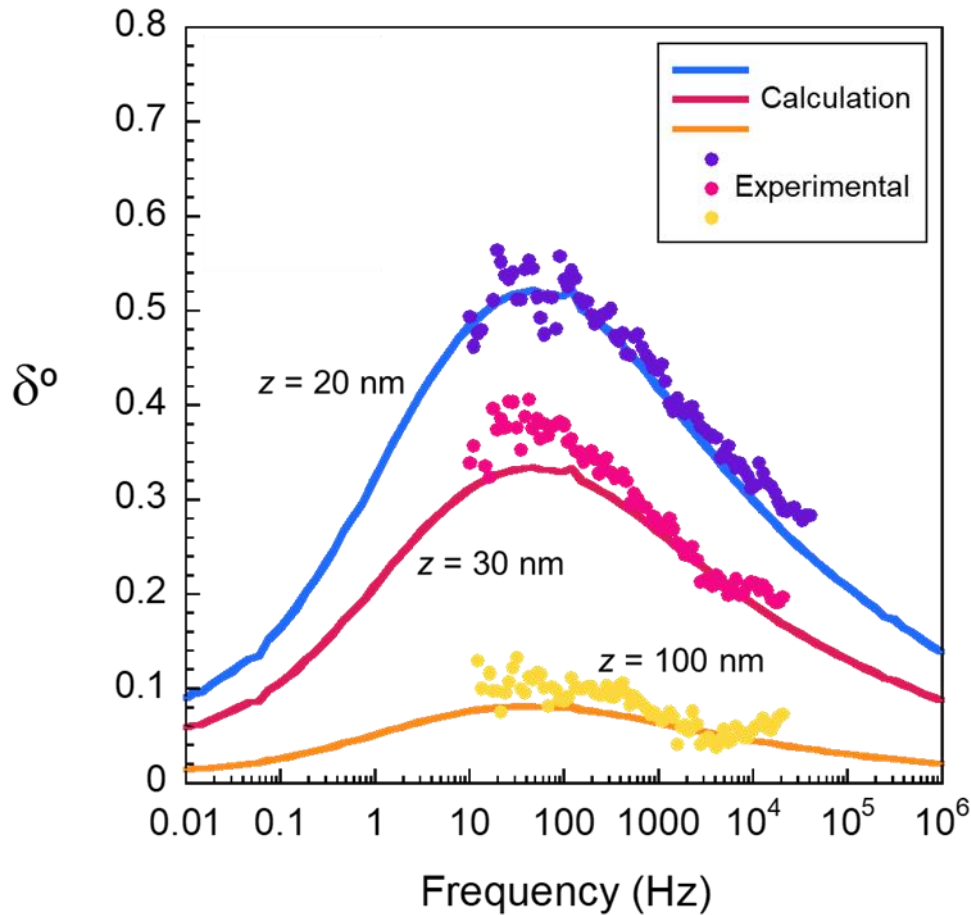


Figure 3.16. Experimental n DS results on PMMA expressed as δ vs frequency for different z -distances (discrete points) and relative predictions from the model equations (solid lines).

As disposed by the obtained results, the peak in δ for all the explored z -distances fairly matches the maximum obtained in M'' by the BDS investigation of the bulk material. This evidence remarkably proves the intimate connection between the imaginary part of the dielectric modulus and the n DS local response of a material. By taking advantage of such result, it is now possible to make predictions on the dielectric signatures from an n DS spectra economizing any over-theoretical postulations, which would come particularly useful in those samples of higher adhesion forces where the z -distance is often hard to esteem or control. To conclude, the advantages of the proposed method are mainly arising from its power of systematic description of the electrical forces and electrical losses acting at the tip-sample interface, which opens the possibility to have a better prediction of what kind of response a

sample could have in *n*DS just starting from its bulk BDS features. At the same time, the model constitutes a step forward in understanding the physical meaning of δ .

3.3.3 Charges dynamics in PEO complex nanostructure

To study the arrangement of the crystalline lamellae and their impact on the dielectric properties of the semicrystalline polymer under investigation, we performed *n*DS AFM studies of PEO spin-casted on a Si wafer substrate. In the first instance, we used a lower molecular weight precursor obtaining isolated aggregates of the order of microns (or fractions of microns). The *n*DS characterization of the lower molecular weight sample was carried out using SCM_PIT_V2 probe (R: 25 nm, H: 2.8 μ m, W: 35 μ m, L: 225, f_0 : 75 kHz, k: 3 N/m). Due to the lower viscosity of solutions obtained from low molecular weights, samples of PEO prepared by spin coating from a diluted solution forms more likely dewetted-like microdomains, giving the possibility to better distinguish singular lamellae or stack of a known number of lamellae on the substrate. Keeping this in mind, we prepared a sample of PEO with a molecular weight of $M_w = 35$ kDa from a 2.5 mg/mL concentrated solution in THF following the standard procedure (see section 2.2). The resulting topography is presented in Figure 3.17(a). Here, we can distinguish the flat surface of the Si wafer substrate ($R_a < 1$ nm) on which PEO microdomains grew independently as isolated aggregates, spaced one another several hundreds of nanometers (> 400 nm). As expected for PEO ultra-thin films (see section 1.5), the disposition of the lamellae with respect to the substrate surface is preferentially flat-on, displaying no edge-on domains in the portion of sample surface captured by the image. The height of the obtained aggregates ranges between 20 and 60 nm with a number of lamellae constituting every separated object between 1 and 4. Thanks to the convenient morphology of such sample it was possible not only to image, but also to separately probe the dielectric response of areas with a known disposition and number of lamellae. Moreover, the substrate is easily discernible at the surface of the sample, opening the possibility to compare the results with the Si dielectric reference all at once in the same environment. Figure 3.17(b) shows the phase shift δ from the second harmonic of the cantilever respect to the driving alternated sinusoidal electric field (of amplitude = 6 V and frequency = 1 kHz) in lift mode, at a nominal height from the sample surface of ≈ 40 nm, using the substrate as a reference. Brighter areas represent zones of the sample with higher dielectric loss at the selected frequency.

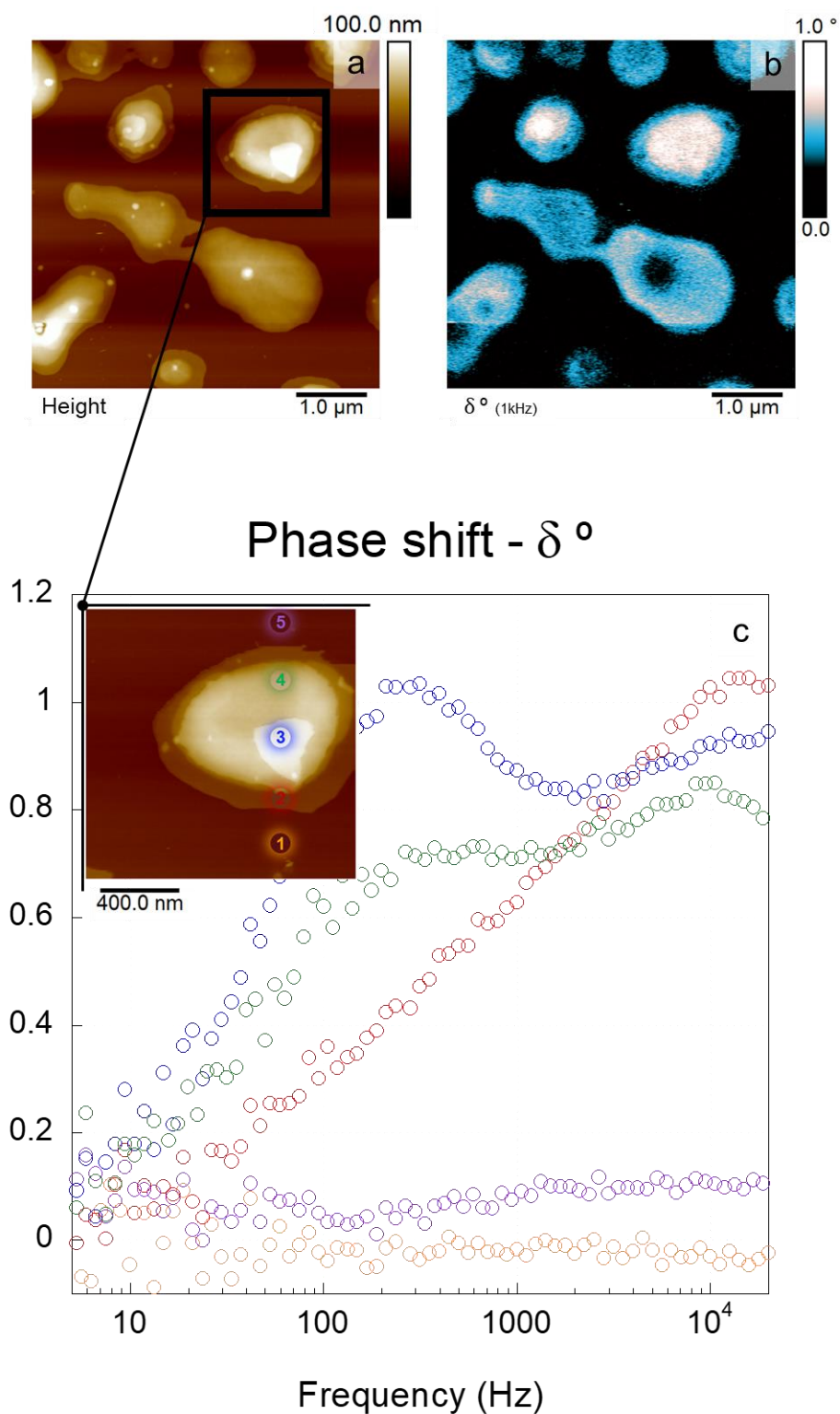


Figure 3.17. Topography image acquired in PFT-AFM (a), phase_{II harmonic} image in $\delta^{1\text{kHz}}$ from lift (b), and *n*DS results (c) of a PEO^{35kDa} microdomain isolated on Si substrate.

As observed from the *n*DS phase image, PEO aggregates always show an *n*DS signal, which increases when increasing the height of the aggregate (at the selected frequency). To further understand the involved dynamics and explain this evidence, we performed local *n*DS experiments on selected areas of the surface. The spectra were collected by subtracting the

phase registered for every frequency from the one collected on a reference sample of PVAc (110 nm thick) with the same settings, known this to have no relaxations occurring at the given experimental conditions¹⁷³. The results of the analysis are shown in Figure 3.17(c). The values of δ in all the explored frequency range is zero on the substrate (spots 1-orange and 5-purple) excluding the occurrence of any dielectric relaxation. The spectrum from one isolated lamella with thickness ≈ 12 nm (spot 2-red) reveals the presence of one main contribution with the maximum of the peak near $\approx 1 \times 10^4$ Hz, the broadened shape of the signal suggests the presence of a second contribution at lower frequencies masked by a more intense one. By increasing the thickness of the sample up to 50 nm (spot 4-green) and 70 nm (spot 3-blue), corresponding respectively to the stack of 3 and 4 lamellae, one can clearly distinguish two peaks, one at $\approx 1 \times 10^4$ Hz and another at $\approx 3 \times 10^2$ Hz. Hence, the sample displays two distinct contributions to the dielectric function well separated in frequency; by increasing the thickness, the low frequency contribution increases in dielectric strength while the second one slightly decreases. We will refer now on to the peak at lower frequency as ζ and to the one at higher frequency as ξ . At room temperature, PEO does not present any relaxation ascribable to segmental motion or molecular contributions, meaning that the given peaks ζ and ξ in δ must be related to polarization phenomena or conductivity contribution to its dielectric function^{141,174,175}.

To have more insights into the influence of conductivity on the dielectric function of PEO a direct investigation of the bulk material is of fundamental importance, as a thick film would present dielectric properties closer to the ones expected for thicker areas on the sample. At this purpose, two different samples of PEO (with $M_w=35$ kDa) in different content of ionic dopant were analyzed by BDS near room temperature, both having thickness of 0.1 mm. One sample is pure PEO while the other is PEO doped with LiClO_4 in a molar ratio between the oxide specie on the polymer chains and cation Li^+ equal to $\text{Ox} : \text{Li}^+ = 100 : 1$. The relative conductivity of the two samples measured by BDS at 1 Hz was found to be 1.6×10^{-8} S/cm and 1.7×10^{-6} S/cm respectively for the pure the doped specimen. The results from the BDS characterization at 30° C are shown in Figure 3.18, where the real and the imaginary part of the complex dielectric modulus M' and M'' are also reported.

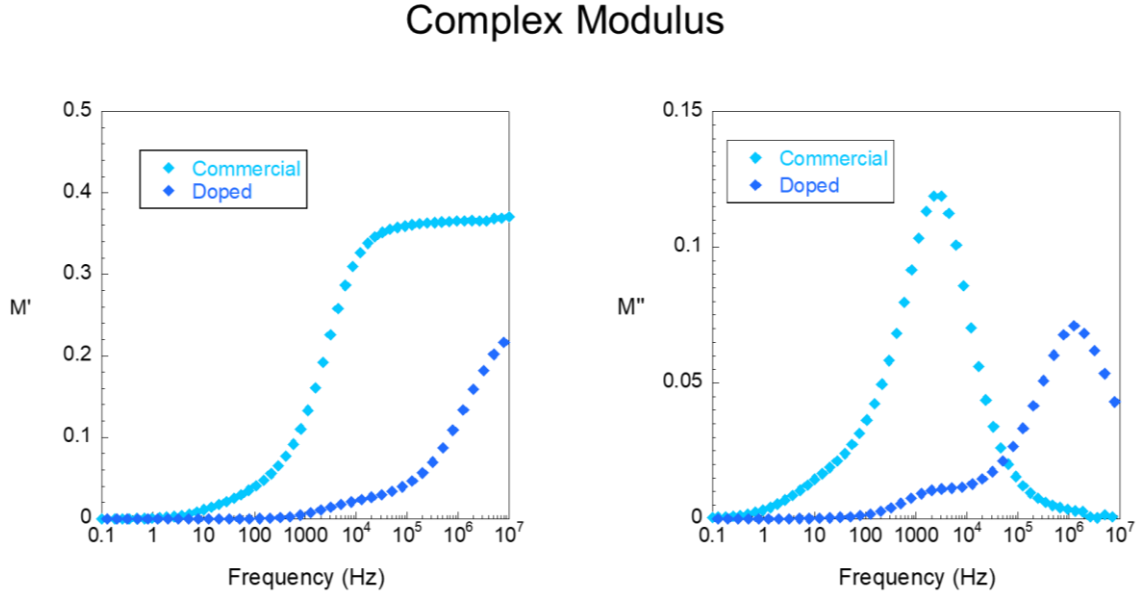


Figure 3.18. Real and imaginary part of the complex modulus in commercial and Li^+ doped PEO on samples with thickness equal to 0.1 mm.

The commercial and the doped precursors both reflect the typical characteristics of PEO for which we can clearly distinguish one peak in M'' ¹⁷⁶. The maximum of the peak is $\approx 2.8 \times 10^3$ Hz for the commercial and $\approx 1.2 \times 10^6$ Hz for the doped one. In the study case, the maximum in the imaginary part of the modulus provides information about the characteristic relaxation time τ_e of the ionic hopping^{177,178}, which is directly linked to the bulk conductivity mechanism following the semi-empirical relation in eq. 1.29 and 1.30, defining the transition region from dc to ac conductivity. From the obtained results we conclude that an increased conductivity leads to a shift toward higher frequencies of the peak in M'' of PEO, meaning that changes in conductivity also should result in a change of δ_{\max} from n DS experiments on ultra-thin films, for which we remember it is valid the approximation $\tan(\delta) \propto M''$ (eq. 3.15).

These outcomes provide an important starting point for the understanding of the results shown in Figure 3.17, where the two signals detected do not undergo any change in δ by changing the sample thickness, but a change in intensity was observed instead. For a fixed ionic conductivity, the contribution of the dielectric function of pure PEO to its n DS response should account for the Maxwell-Wagner-Sillars interfacial polarization process at the amorphous/crystalline interfaces¹⁶². On the other hand, a different ion mobility could be expected from an adsorbed interfacial layer in proximity of the substrate^{178,179}. In this scenario, the total modulus M_{tot} (given in eq. 3.23) can be derived from the reciprocal of the dielectric constant resulting from the $\text{PEO}^{adsorbed}/\text{PEO}^{bulk}$ bilayer once known the volumetric fraction φ of the adsorbed layer (of volume V_a) respect the total volume ($V_{tot} = V_a + V_{bulk}$).

$$\varphi = \frac{V_a}{V_a + V_{bulk}} \quad (3.21)$$

$$\varepsilon_{tot} = \frac{\varepsilon_a \varepsilon_{bulk}}{(1-\varphi)\varepsilon_a + (\varphi)\varepsilon_{bulk}} \quad (3.22)$$

$$M_{tot} = M_a(\varphi) + M_{bulk}(1 - \varphi) \quad (3.23)$$

In this approximation, the total contribution to the spectrum in δ is proportional to M_a'' for a purely adsorbed monolayer of PEO. When the thickness of the sample increases, the contribution of the upmost bulky material increases until reaching the situation in which δ depends on the bulk properties only as $\lim_{\varphi \rightarrow 0} M_{tot} = M_{bulk}$. It follows that the two processes ζ and ξ correspond to distinct relaxation phenomena linked to the ion hopping in different states of the matter: the upturn of ζ above ξ as the number of stacked lamellae increases is a consequence of an increased contribution of a bulk-like ionic transport. Regarding the adsorbed layer at the interface with the substrate and described by the ξ -process, we registered a higher value of τ_e , resulting in an improved conductivity respect to the bulk material. We envisage that such an increase in conductivity can be explained by two assumptions: i) the adsorbed layer does not present crystalline objects obstructing the ionic coordination to amorphous PEO¹⁸⁰, ii) the number of impurities in proximity of the surface is higher, leading to a higher ion concentration in the adsorbed layer¹⁸¹.

To complete the study about the inhomogeneous ion transport in the considered semicrystalline system, an analysis of a pristine continuous thin film of PEO at high molecular weight (thickness $h = 120$ nm) was performed by AFM both in its structural and *nano*-dielectric properties. The sample was obtained by spin coating on Si wafer a 20 mg/mL concentrated solution in Toluene of PEO with molecular weight $M_w = 100$ kDa, the M_w value was selected to allow coherence with the BDS study proposed at the very beginning of the chapter (section 3.1). The AFM characterization was performed by means of an HQ_DPE_XSC11 AFM probe (Table 3.1).

Figure 3.19(a), shows the topography of the sample's surface as acquired by PFT-AFM in proximity of a zone displaying both flat-on (example: green arrow on image) and edge-on (example: blue arrow on image) lamellar disposition respect to the substrate (Si) plane. The topography of the sample returns the classical PEO patterns, with a mean roughness $R_a = 6.6$ nm^{182,183}. In Figure 3.19(b) we reported the n DS amplitude from the second harmonic for an applied electric field of 6 V and 1 kHz with sample-tip separation (z -distane) of 40 nm. Brighter

areas in the image correspond to higher electrical forces $F_{e(2\omega_e)}$, so then higher values of ϵ , that we attribute to higher local ionic conductivity (eq. 1.27) ⁶¹.

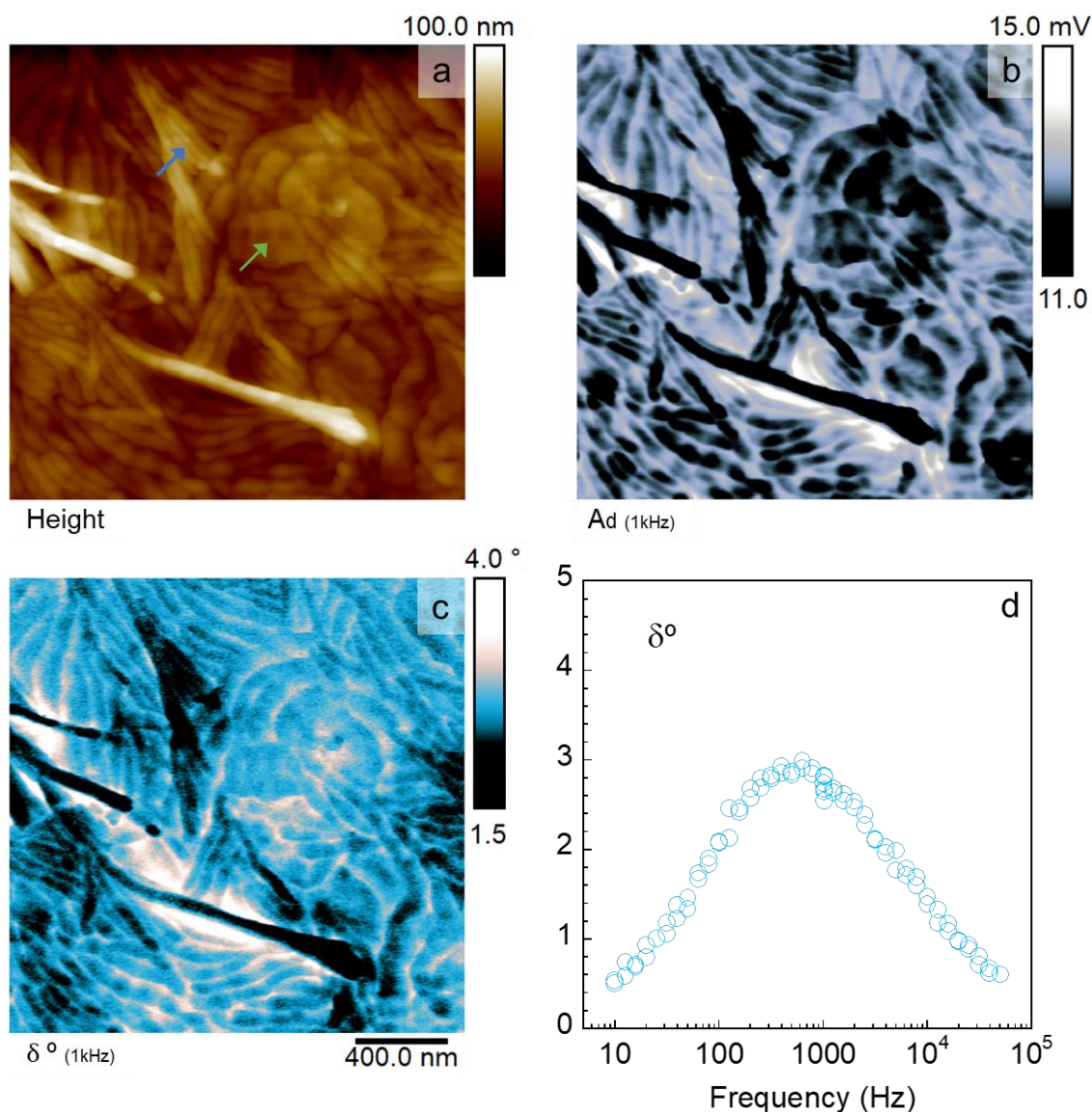


Figure 3.19. AFM characterization of PEO thin film ($h = 120$ nm): images from the height (a), the amplitude^{II_harmonic} (b), and the δ (c) channels. The typical spectrum in δ on a random spot of the surface is also shown (d).

As expected, a higher conductivity was detected in proximity of zones at the border of the crystals boundaries, demonstrating a more effective ion transport in the amorphous fraction of the material. Interestingly, a neat lower value of the electrical force was registered on edge-on lamellae, evidencing an anisotropic transport with respect to the orientation of the crystalline fraction. As already mentioned in section 3.1, the ion transport in PEO is dominated by interfacial polarization at the interphase with the crystalline lamellae (that to say in the presence of amorphous zones), then the lower conductivity in specific zones of the surface can be related

to both a more prominent MWS polarization or a lower effective ionic concentration. To shed light on the possible mechanism responsible for such heterogeneity, we reported in Figure 3.19(c,d) the nDS δ characteristic for the studied surface, acquired in the middle of the image. Firstly, we specify that the dielectric spectra, acquired in the chosen frequency window, did not undergo any important change in shape for different spots probed both upon flat-on or edge-on domains, meaning that the τ_e characterizing the nature of the polarization is not structure-dependent but a bulk parameter¹⁶². An example for a local nDS experiment at tip-sample distance $z = 30$ nm is reported in Figure 3.19(d). As we can appreciate from the spectra, and unlike the previous case (Figure 3.16), only one process manifests; this is in line with our discussion for which by increasing the film thickness up to a certain threshold the contribution to the dielectric function arising from heterogeneity at the sample-substrate interface is neglected, and only ζ is observed. As expected, the ζ -process is more intense in the amorphous domains due to a higher ionic coordination to the PEO segments, generating preferential conducting paths in the material^{180,184}.

At this point, the highlight from the δ image is the higher magnitude of the relaxation on flat-on lamellae respect to the edge-on ones. This fact leads to the conclusion that, if the nature of the relaxation is the same, the results evidenced a less dense charge fluctuation in the parallel direction of the lamella.

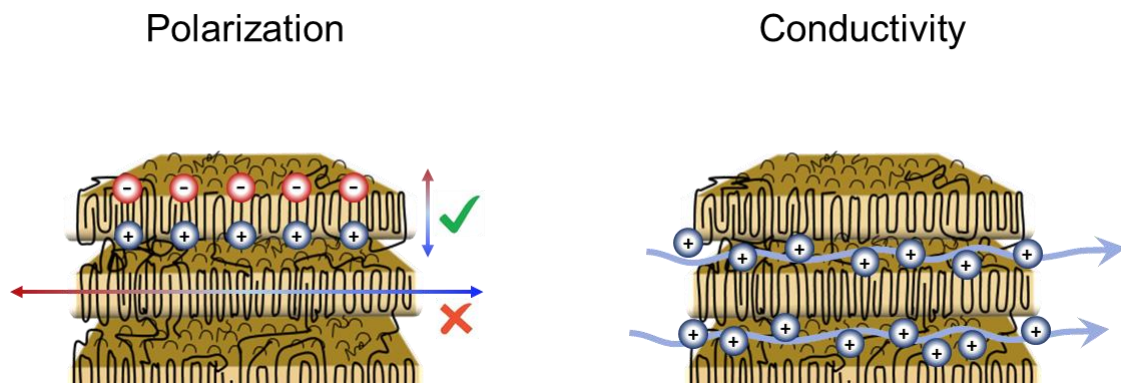


Figure 3.20. A sketch of the interfacial polarizations phenomena and ion channels with respect to the direction of the lamellae in the material in the presence of a hypothetical electric field meant to be in the same direction as the arrows in each independent case.

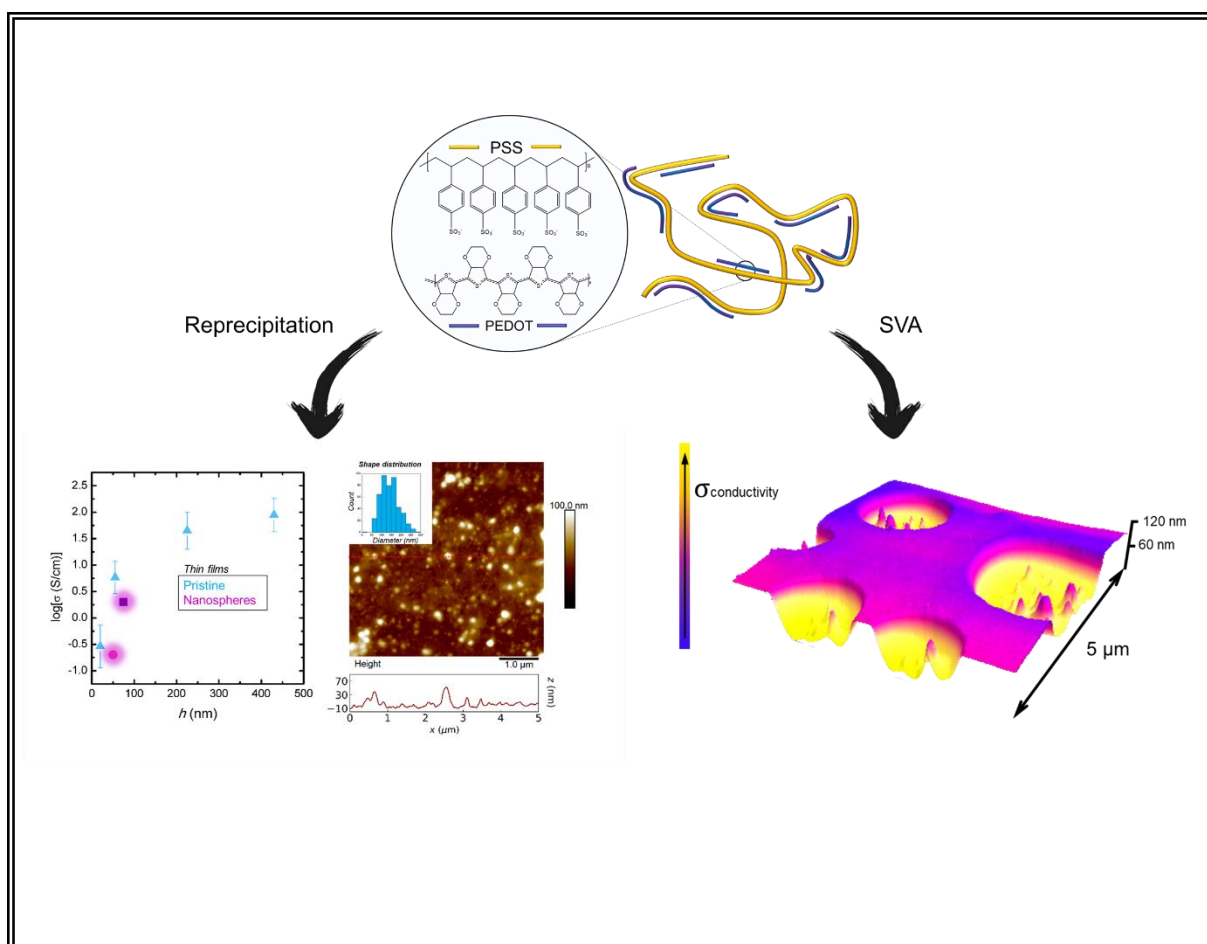
3.4 Summary

In the first part of this chapter, we were able to determine the melting dynamics of semicrystalline polymers starting from the investigation of the dielectric properties of PEO, also revealing the charge transport dynamics in the material both in solid and at the liquid transition. The results revealed a strong dependence of the charge transport regime with the polymer nanostructure, this being mostly determined by the arrangement of amorphous and crystalline domains in it. At this point, we employed *n*DS to directly visualize such domains and to address their specific contribution to the charge transport dynamics; but before processing the *n*DS results, it had been necessary to model the AFM apparatus under the experimental conditions. Then, a model was developed and verified experimentally, enabling the precise characterization of the interfacial polarization processes occurring in PEO as long as the heterogeneous ion conductivity in the semicrystalline polymer. Finally, the results showed the preferential conducting paths as ion channels located in the amorphous part and the preferential orientation of the interfacial polarization processes with respect to the lamellar disposition.

The aim of this thesis is the investigation of the complex nanostructures given by polymeric precursors and the impact they have in determining the resulting physical properties at the base of their final applications. In this sense, we already provided in this chapter a comprehensive understanding of the complex nature of semicrystalline polymers and its impact on charge transport dynamics. In the following chapter, we are going to focus our attention on another transport phenomenon displayed by a certain class of polymers: electronic conduction. In particular, we are going to see how the nanostructure of an intrinsically conducting polymer, PEO:DT:PSS, affects the transport properties of the material, also providing effective methodologies to take advantage of it in order to tune the final electrical response.

Chapter 4

Fabrication and nanoscale properties of tailored PEDOT:PSS nanostructures



4.1 Introduction

PEDOT:PSS is an electrically conductive polymer presenting tailorable transport properties¹⁰², transparency to visible light¹⁸⁵, and physicochemical stability¹⁸⁶. Moreover, it can be readily prepared as a thin film. Figure 4.1 presents the morphology of a PEDOT:PSS thin film, spin-casted onto an ITO substrate. The AFM topography images, at 3 magnification levels, show that the polymer forms a continuous surface, coating the whole support. The resulting film is far from flat, presenting a mean roughness of 3.5 nm. This result is expected due to the intrinsic nanostructured nature of PEDOT:PSS, composed of nanoparticles in the water dispersion, as introduced in section 2.1 and references therein.

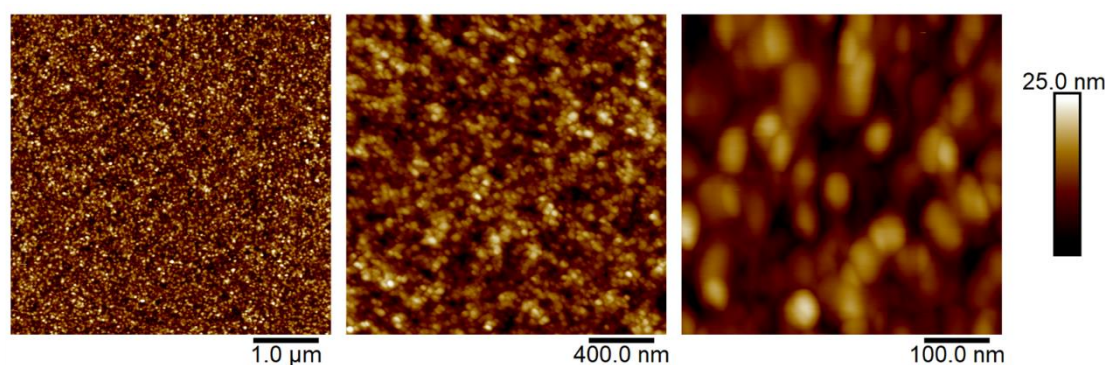


Figure 4.1. AFM topography images of a PEDOT:PSS thin film with different magnifications.

The excellent properties of PEDOT:PSS as well as its ability to form polymer thin films allowed this material to find applications in organic solar cells¹⁸⁷, supercapacitors¹⁸⁸, organic light-emitting diodes¹⁸⁹, and sensors¹⁹⁰. In the recent years, the fabrication of precise PEDOT:PSS nanostructures have permitted the modification and enhancement of the resulting polymer properties^{120,191–193}, in turn, leading to boosted applications^{194–200}. Moreover, the modification of the particles' dimensions and/or shapes could give to the material new bulk properties and extend the possible applications, especially in the field of nanostructured devices, where the conformation of the electrical contact at the nanoscale is fundamental²⁰¹.

The fabrication of precise nanostructures of conducting polymers has been widely studied for both fundamental research and potential applications^{202,203}. In the particular case of PEDOT:PSS, it is crucial to have control over the superficial nanostructure of the polymer for most of its applications, since the hierarchical arrangement of PEDOT and PSS components dictates the resulting properties. Then, an increasing attention in finding reproducible and economic ways to tailor PEDOT:PSS nanostructures has awakened recent interest in the scientific community in order to develop advanced nanostructuring techniques and methodologies. In this

area of research, intrinsically conducting and semiconducting polymeric nanospheres captured the attention of the scientific community in the past few years ^{204–207}. Recently, PEDOT hollowed nanospheres were synthesized by Zhang et al. for applications into electrochromic systems ²⁰⁸. The results showed that, for nanospheres with diameter around 100 nm, the ion transport in the material was promoted, with respect to the denser and more compact bare PEDOT, underling the importance of tuning the dimensions of the particles for in PEDOT-based system. This finding highlighted the importance that the control over the nanoparticle dimensions of the active layer has in systems such as supercapacitors.

On the other hand, several authors have focused on modifying the PEDOT:PSS surface properties, as its work function and electrical/thermoelectrical response, while leaving mostly unchanged its surface morphology. For example, the removal of the free PSS phase that connects the PEDOT:PSS rich grains in the thin film geometry allowed to increase the thin film electrical conductivity ^{209–211}, without important impact on the surface topography. For this purpose, many solvent-based methods have been largely used, mostly employing high boiling point polar molecules as ethylene glycol (EG), dimethyl sulfoxide (DMSO), or dimethylformamide (DMF), as well as other liquids as alcohols, sorbitol and acids ²¹². Also, the use of other molecules has allowed to tune the polymer's work function ^{213–216}.

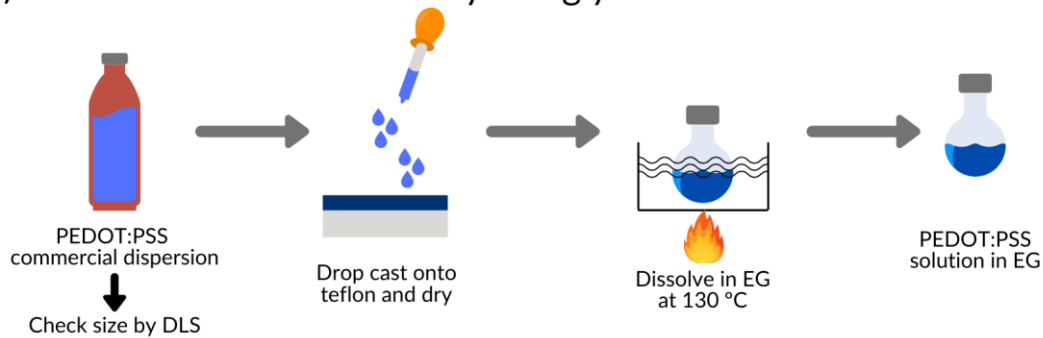
In this Chapter, we propose two different approaches to tune the resulting PEDOT:PSS properties and physical behavior: the modification of the nanoparticles' size and the selective modification of the surficial interface. The two different nanostructuring strategies allowed us to modify the electrical properties of the substrate also providing important insights about the transport properties occurring in the resulting materials.

4.2 Fabrication and local properties of PEDOT:PSS nanostructures

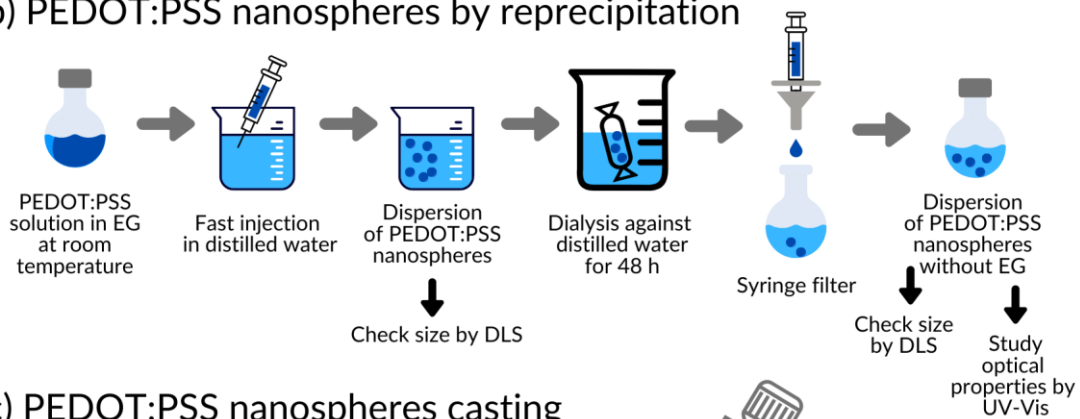
4.2.1 PEDOT:PSS nanospheres

PEDOT:PSS nanospheres were prepared following the reprecipitation method. This method is a solvent-displacement technique that relies on crashing out hydrophobic polymer chains in solution by displacing a solvent with a non-solvent, generally water¹⁰⁶. The polymer solvent and the non-solvent must be miscible with each other, as in the case of water and EG.

(a) PEDOT:PSS solution in ethylene glycol



(b) PEDOT:PSS nanospheres by reprecipitation



(c) PEDOT:PSS nanospheres casting

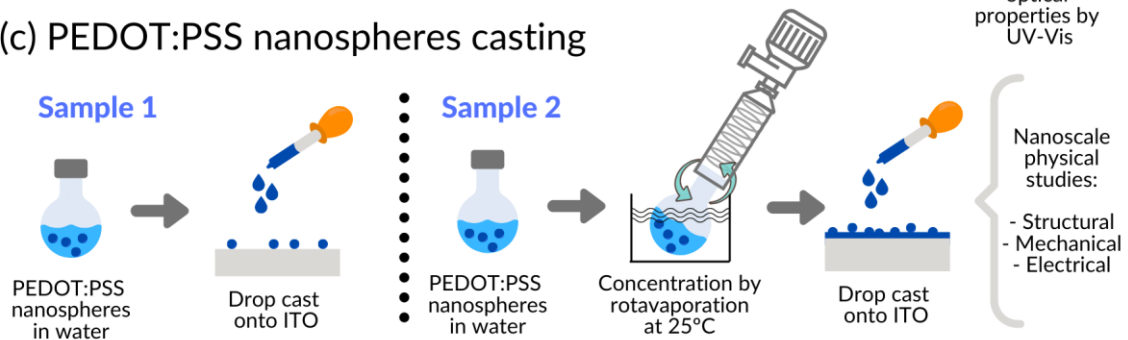


Figure 4.2. Scheme showing the PEDOT:PSS nanospheres' fabrication process. (a) Strategy to dissolve PEDOT:PSS in EG. (b) Fabrication of PEDOT:PSS nanospheres by reprecipitation. (c) Casting of PEDOT:PSS nanospheres for physical studies.

The scheme in Figure 4.2 presents the overall process of PEDOT:PSS nanospheres fabrication. The first step in the fabrication of these nanostructures was the dissolution process of PEDOT:PSS in EG (Figure 4.2(a)). This process was optimized by a solubility test, as detailed in the following lines. 100 μL of the commercial PEDOT:PSS dispersion were drop-casted on a Teflon plate. The dispersion was left in a vacuum oven (pressure < 10⁻¹ bar) for 2 hours at room temperature to allow water evaporation. Then, the sample was transferred to a higher vacuum chamber (pressure < 10⁻⁴ bar) and left overnight (~16 h) at room temperature, in order to evaporate all possible residual water. After this throughout drying process, we obtained a brittle dark blue homogeneous film. 1 mg of solid PEDOT:PSS was obtained from the dried film and re-dispersed in 1 mL of EG by stirring the solution over weekend, at room temperature. Afterwards, the mixture was heated to 130° C, under continuous stirring, and the temperature was kept for different times: 30 minutes, 1 hour, 3 hours, and 5 hours. The PEDOT:PSS dissolution process was followed by eye inspection and DLS measurements (Figure 4.3). Our experiments showed that 3 hours was the optimum dissolution time, as it was the limit before microaggregates in solution started to appear, as observed in the DLS results. The progressive precipitation of the polymer with time can be related to internal PEDOT and PSS dissociation at temperature near 120° C, which can alter the hydrophilicity of the compound²¹⁷.

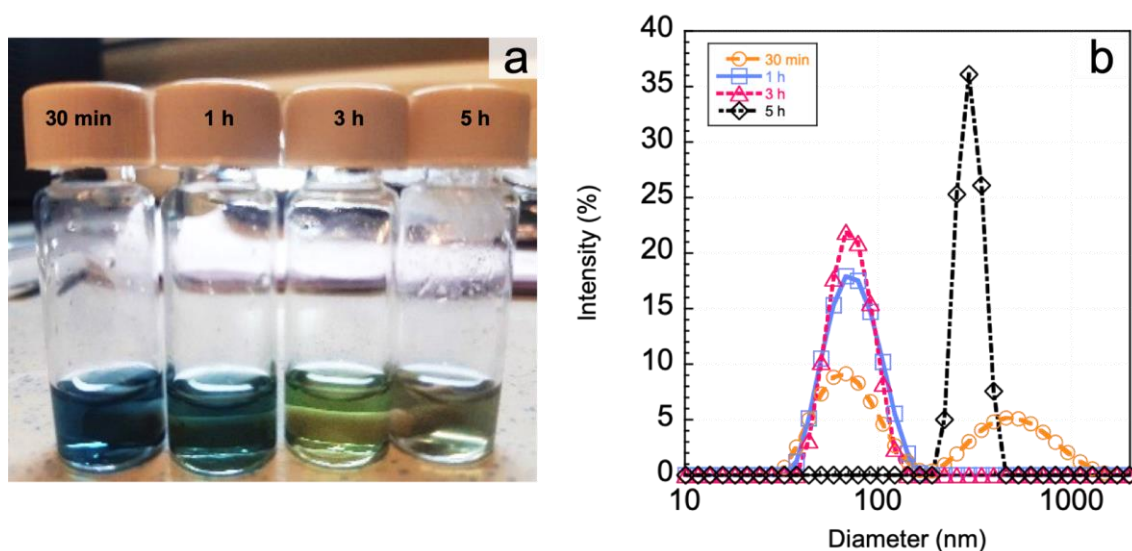


Figure 4.3. (a) Photographs of PEDOT:PSS solutions in EG, after 30 min, 1 hour, 3 hours, and 5 hours. (b) DLS measurements of the PEDOT:PSS solutions as a function of time.

For the nanospheres preparation, the PEDOT:PSS solution in EG was injected into 10 mL of H₂O using a syringe, at room temperature and under stirring (Figure 4.2(b)). Immediately afterwards, we performed a DLS measurement to check the PEDOT:PSS structure in the dispersion (Figure 4.4(a), squares). The results showed that the reprecipitated PEDOT:PSS

dispersion was composed of features reaching a Z-average value of 160 nm in diameter. This result represented an increase in about a factor 3 compared to the diameter of the as received PEDOT:PSS dispersion (Figure 4.4(a), triangles). Also, the relative width of the distribution was narrower for the reprecipitated sample, compared to the commercial PEDOT:PSS. These results showed that the reprecipitation process allowed the fabrication of customizable nanostructures, different in size from the original dispersion with a better size dispersion.

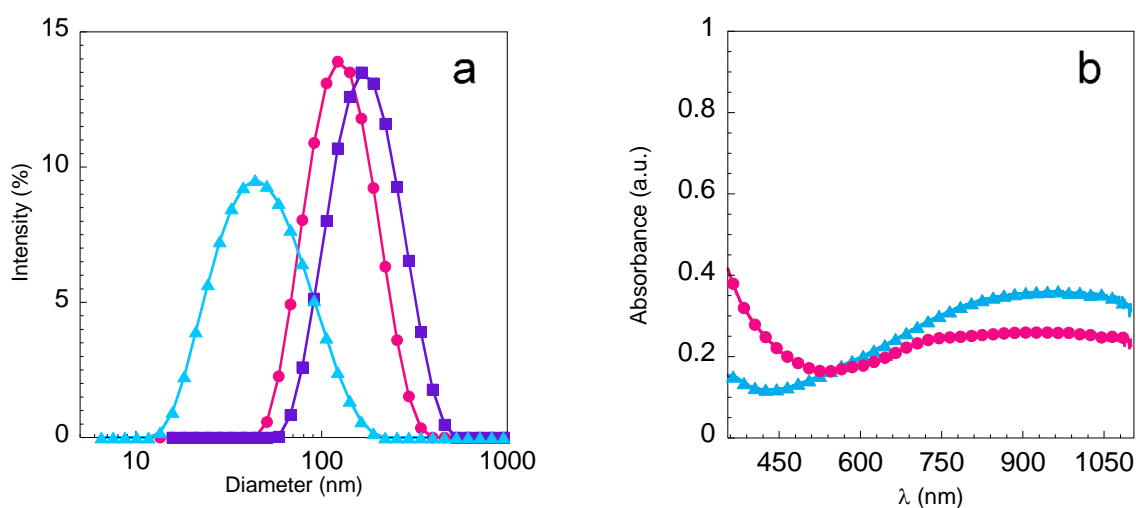


Figure 4.4. (a) DLS results as intensity as a function of feature diameter: commercial PEDOT:PSS (triangles), PEDOT:PSS nanospheres (squares), purified PEDOT:PSS nanospheres (circles). (b) UV-Vis results: commercial PEDOT:PSS (triangles) and the purified nanospheres (circles). The UV-Vis data is shown as 1 point of every 5 measurements.

After reprecipitation, we carried out the following purification process. The EG molecules still present in the resulting aqueous dispersion were removed by dialysis against water. The dialysis process was carried out in a 2 L H₂O reservoir, with continuous water changes throughout 48 h. Then, to remove any possible micrometric aggregates, we filtered the dispersion with a PTFE filter (0.2 μm pore size). The obtained purified dispersion was measured again by DLS (Figure 4.4(a), circles). Now, the observed unimodal distribution of sizes had a Z-average value of 120 nm in diameter, indicating a small decrease when compared to the sample prior dialysis. This decrease could be related to the expel of residual EG, which was previously swelling the polymer. The width of the distribution did not show any changes, remaining narrower than the commercial product. Different tests showed that the final diameter of PEDOT:PSS nanospheres prepared following this protocol ranged between 90 to 130 nm. These diameters were comparable to those reported for other conducting polymer nanospheres²¹⁸, as poly(3-hexylthiophene)^{205,219}, PCDTBT²²⁰, and poly(p-phenylene ethynylene)²²¹.

As recently reviewed by E. Gutiérrez-Fernández et al., one of the most direct strategies for the preparation of nanospheres using functional polymers require the use of polymer solutions in water-miscible solvents, with low boiling points ²⁰⁷. However, in the case of PEDOT:PSS, this approach is limited because of its bad solubility in most of commercial solvents with these requirements. Another option to dissolve this polymer is to exploit the PEDOT:PSS high affinity to polar high boiling point solvents, as EG and DMSO ²²². For example, the interactions between PEDOT:PSS and EG, results in a new molecular conformation of PEDOT and PSS, imposed by the solvent molecules after specific treatments ^{223,224}. This fact has led to a sensitive enhancement of the intrinsic conductivity of the polymer ^{225,226}. Thanks to such polymer/solvent affinity, it was possible to dissolve the PEDOT:PSS in EG, opening the possibility to manufacture nanostructures directly from solution and finding new possible applications.

In order to characterize the optical properties of the purified PEDOT:PSS nanospheres dispersion, we performed UV-Vis measurements. Figure 4.4(b) shows the obtained spectra for the commercial PEDOT:PSS product (triangles) and our prepared nanospheres (circles). We observed that after reprecipitation, the UV-Vis signal showed some changes. For example, the characteristic bipolaron absorption band at around 800 nm was comparable to the one found for the synthesis of PEDOT:PSS using SCNPs ²²⁷ and enzymes ²²⁸, were good electrical transport properties were measured in the obtained solid-state films. Moreover, the lack of UV-Vis absorption peaks around $\lambda = 600$ nm and the plateau observed for $\lambda > 900$ nm, indicated that nanospheres preparation process by reprecipitation did not alter the PEDOT chains oxidation state ²²⁹ nor resulted in pronounced chemical modifications of the PEDOT:PSS complex ^{230,231}.

Film formation and solid-state properties of PEDOT:PSS nanospheres.

Figure 4.5 shows the morphology of solid-state PEDOT:PSS nanospheres, obtained after drying the purified aqueous dispersion following two different deposition processes (Figure 4.2(c)). Figure 4.5(a) shows a representative AFM topography image of the so-called Sample 1, which was obtained directly from the obtained PEDOT:PSS nanospheres dispersion. In this case, we observed well-defined and isolated PEDOT:PSS nanospheres, with a mean diameter of ~140 nm and typical height of ~50 nm. These geometrical differences indicated that possible interactions with the supporting substrate during the drying process affected the final solid-state morphology. The AFM images also showed that the topography of the free surface surrounding the nanospheres matched the expected characteristics of ITO (mean

roughness $\approx 3.8 \text{ nm}^{232}$). This observation indicated that the concentration of the purified aqueous dispersion was not high enough to allow film formation.

Figure 4.5(d) presents the resulting surface morphology of the so-called Sample 2. In this case, prior deposition, the purified nanospheres dispersion was concentrated using a rotary evaporator ($T = 25 \text{ }^\circ\text{C}$) starting with a 10 mL volume, until the content decreased down to ~ 0.5 mL. Afterwards, the obtained concentrated dispersion was drop casted onto an ITO substrate. As presented in Figure 4.5(d), the concentration process allowed to coat the ITO surface, forming a continuous nanostructured film. The surface morphology was characterized by aggregates of solid-state PEDOT:PSS nanospheres, resulting in a surface roughness of $\sim 8 \text{ nm}$. By scratching the obtained film, AFM measurements allowed to determine a typical film thickness of 100 nm.

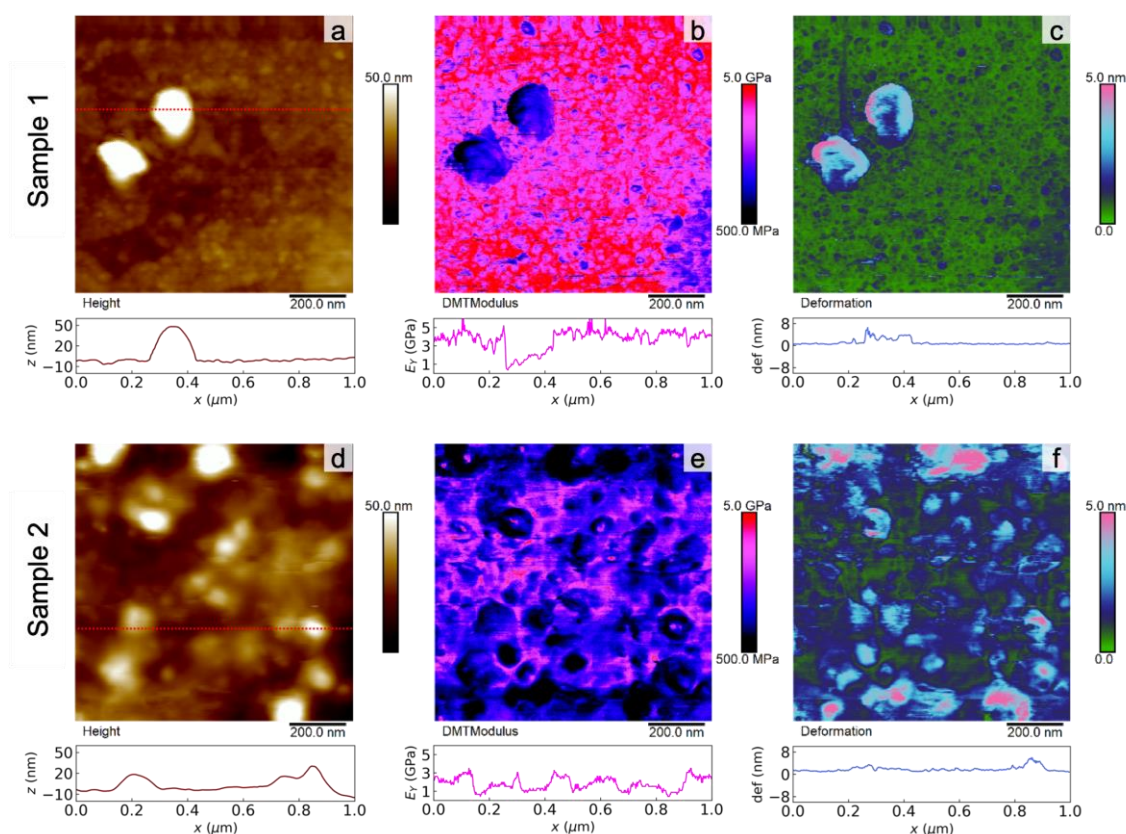


Figure 4.5. $1 \times 1 \mu\text{m}^2$ dynamic nanomechanical properties of solid-state PEDOT:PSS nanospheres determined by AFM. (a,d) Height. (b,e) Young's modulus. (c,f) Surface deformation.

In Sample 1, the nanospheres showed Young's modulus (E) values varying between 1-2 GPa, accompanied by a deformation of 5-6 nm (Figure 4.5(b,c)). Sample 2 (Figure 4.5(e,f)) presented fairly similar Young's modulus and deformation values, comparing to the isolated nanospheres. This result indicates that the film formation process did not alter the PEDOT:PSS nanospheres mechanical properties.

Based on the mechanical contrast maps, comparing the prepared nanospheres with a pristine PEDOT:PSS thin film (see Appendix), we observe a softening of PEDOT:PSS when confined in the spherical geometry. To better support this outcome, we acquired force-separation curves for PEDOT:PSS nanospheres and PEDOT:PSS from the commercial solution, obtained by the force spectroscopy technique. We note to the reader that the force-separation curves were captured on top of the nanospheres, in order to avoid any possible impact of nanostructure geometry on the mechanical properties' determination, as previously discussed in the literature ²³³. The obtained results from this quasi-static approach are summarized in Table 4.1; from these experiments we can observe that Sample 1 and Sample 2 possess similar mechanical response and both samples are softer compared to spun cast thin film. These observations supported the results obtained from the nanomechanical maps. Going into detail, we quantified a stiffness decrease in the PEDOT:PSS nanospheres of over 50%, from 20 N/m to 8 N/m. As expected, this was accompanied by a higher indentation depth, of about a factor 2. Finally, the Young's modulus, was calculated by fitting eq. 1.12 to the retract data in the 10 – 90% total force range. We observed a decrease of E from 3.4 GPa to 2.1 GPa, comparing the thin film with the PEDOT:PSS nanospheres.

Sample	Stiffness (N/m)	δ_i (nm)	E (GPa)
Sample 1	8 ± 1	2 ± 1	2.1 ± 0.3
Sample 2	9 ± 3	2 ± 1	2.1 ± 0.5
PEDOT:PSS thin film	20 ± 5	0.9 ± 0.3	3.4 ± 0.8
PEDOT:PSS _{Baytron P} ²³⁴	-	-	2.6 ± 1.4

Table 4.1. Quantitative nanomechanical results, obtained from force spectroscopy measurements. E indicates the Young's modulus, and δ_i the tip-sample indentation depth. The results are shown as mean value and standard deviation, obtained from at least 6 measurement points. For nanospheres, the force curves were taken at the top of the sphere. A comparison with the E value as found in literature was also reported ²³⁴.

Our nanomechanical results were in line to those previously reported for other PEDOT:PSS nanostructures. For example, different authors reported that PEDOT:PSS ultra-thin films (thickness < 100 nm) presented Young's modulus values ranging between 1 - 2 GPa ^{120,235}; the same range as the one obtained for our PEDOT:PSS nanospheres. Diaz et al. reported a size-dependent stiffness reduction for PEDOT:PSS films, using AFM-based contact resonance measurements ²³⁶. In that work, the authors suggested that the softening was related to a different structural arrangement of the PEDOT and PSS chains in the thinner samples. This

idea was line with the fact that PEDOT has a lower E compared to PSS, as reported by different authors^{237,238} and discussed by us in the Appendix. Following these reports, the observed softening of our PEDOT:PSS nanospheres should relate to a different distribution of PEDOT and PSS in the resulting nanospheres after reprecipitation. In this scenario, the modulus decrease would indicate a PEDOT enriched outer shell in the prepared nanospheres.

Finally, we explored the electric transport properties of the prepared PEDOT:PSS nanospheres. For these studies, we have focused on Sample 2 in view of the following technical limitation. Since the electrical properties determination required scanning in contact mode, we observed that during the scanning of Sample 1 the isolated nanospheres were swept away by the probe. When extremely small forces ($\ll 1$ nN) were used, contact mode scanning was possible without sweeping the structures. However, the probe-sample electrical contact was not adequate to guarantee a proper conductivity measurement, resulting in non-reliable results.

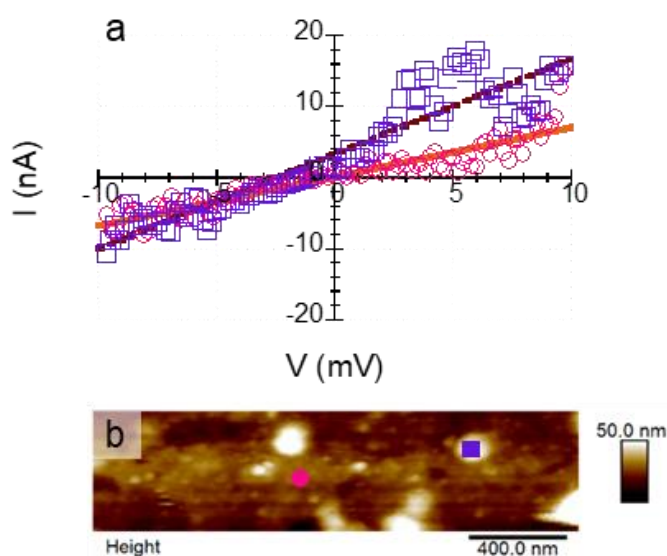


Figure 4.6. C-AFM experiments on PEDOT:PSS nanospheres. (a) Sample 2 topography. (b) Sample 2 I-V curve at the position indicated in panel (a), the electric data is shown as 1 point every 20 measurements. The continuous line represents the linear fit from which the conductivity was calculated. The lines represent the linear fits for the circles (continuous line) and square (dashed line) data.

Figure 4.6(a) shows the I-V response of the PEDOT:PSS nanospheres coating at two different probed areas, indicated by the labels NS1 and NS2 and the distinct symbols on Figure 4.6(b). We emphasize to the reader that, considering the experimental setup and sample preparation procedure, the I-V measurements account for out-of-plane electronic transport phenomena. In Figure 4.6(b), both I-V curves show a linear trend, indicating that Sample 2 presents an Ohmic conductivity behavior; however, the NS1 region shows a clearly steeper slope. From a qualitative point of view, this results indicate that the PEDOT:PSS nanospheres

composing the film preserve the good electronic transport properties of the original material. Going into quantitative details, from the I-V curves we were able to obtain different conductivity values depending on the probed area. In fact, as the measurement point was higher in topography, the higher was the obtained conductivity. For example, the highest probed point of Sample 2 (NS1) presents a conductivity of ~ 2 S/cm, while the lowest one (NS2), results in a ~ 10 times lower conductivity of ~ 0.3 S/cm.

The impact of particles' size on the electric conductivity in PEDOT:PSS thin films

In order to understand how the fabrication process and confinement effects might influence the PEDOT:PSS nanospheres electronic transport, and to contextualize our results, we compared the nanospheres' electrical properties to those shown by PEDOT:PSS. The films resulting from PEDOT:PSS precursors normally provide continuous coating at constant thickness. For these reasons, we compared the nanospheres' electrical properties to those shown by regular PEDOT:PSS thin films at different thickness using the same C-AFM setup. The results and discussion of the analysis on the pristine material is presented in the Appendix. In Table 4.2 we compare the conductivity values of the PEDOT:PSS thin films with the prepared nanospheres. Here, we observe that the NS1 (solid square) and NS2 (solid circle) regions show a lower conductivity, compared to the thin films. For example, by interpolating the results presented in Figure 4.6, the conductivity of NS1 would correspond to that of a thin film of ~ 40 nm, while the NS2 region to a thin film of ~ 20 nm.

Thickness (nm)	Conductance (1/M Ω)	σ (S/cm)
430	10 ± 7	$(9 \pm 6) \cdot 10^1$
225	9 ± 7	$(5 \pm 3) \cdot 10^1$
75 (NS1)	1.1 ± 0.3	1.8 ± 0.5
55	5 ± 3	6 ± 4
50 (NS2)	$(1.4 \pm 0.3) \cdot 10^{-1}$	$(1.5 \pm 0.3) \cdot 10^{-1}$
20	$(7 \pm 6) \cdot 10^{-1}$	$(3 \pm 2) \cdot 10^{-1}$

Table 4.2. Conductance and conductivity values of PEDOT:PSS thin films for different thicknesses.

Since the coordination of EG to PEDOT:PSS normally increases its conductivity^{78,225}, the results shown in Table 4.2 indicate that there were no EG traces still coordinated to the

prepared PEDOT:PSS nanospheres, in an amount big enough to increase their electrical conductivity over those presented by as casted thin films. Then, we envisage that the reduction of the electrical conductivity in Sample 2 should be related to the different particles size respect to the commercial material. Then, for bigger nanoparticles, the 1D confinement has a more pronounced effect on the out-of-plane conductivity. Putting together the nanomechanical and nanoelectrical results, our studies indicated that PEDOT:PSS nanospheres fabricated by a reprecipitation process resulted in good mechanical and electrical properties, yet with a different arrangement of PEDOT and PSS units compared to the one shown by thin films.

4.2.2 Surface nanostructuring of PEDOT:PSS thin films

For the fabrication of solvent-structured PEDOT:PSS surfaces we explored two strategies. First, for fast solvent exposure, we spin casted a drop of THF onto the PEDOT:PSS thin films. Here, a drop of solvent coated the whole material surface, forming a meniscus, and spinning started immediately afterwards. Second, for long solvent exposure, we carried out solvent vapor annealing (SVA) treatments, following the protocol explained in section 2.2. The polymer pristine thin films were subjected to solvent vapors for different times.

Nanostructure formation by exposure to THF

Figure 4.7(a,b) shows the surface topography of a PEDOT:PSS thin film obtained from the commercial PEDOT:PSS water dispersion, without any further treatment (pristine sample, thickness ≈ 400 nm). The surface morphology is in line with those previously reported for PEDOT:PSS thin films^{223,239–241}, where dried PEDOT:PSS has been described as composed by highly conducting PEDOT:PSS grains, each coated with a thin shell of PSS^{241,242}. All the determined structural features for the PEDOT:PSS sample are summarized in Table 4.3.

Sample	t_e	h	$\langle R_a \rangle$	R_{a-up}	h_D	D_i
Pristine	--	400 ± 10 nm	3.4 ± 0.2 nm	--	--	--
PEDOT:PSS-ST	$\ll 1$ min		3.0 ± 0.2 nm	1.0 ± 0.2 nm	18 ± 2 nm	220 ± 50 nm
PEDOT:PSS-LT	10 min		23 ± 1 nm	0.5 ± 0.2 nm	30 ± 10 nm	$0.8 - 3$ μ m

Table 4.3. PEDOT:PSS structural features, as determined by AFM measurements. In this table, t is the exposure time, h the film thickness, $\langle R_a \rangle$ the overall roughness (whole film), R_{a-up} the roughness of the upmost layer, h_D the depth of the inclusions, and D_i the diameter of the inclusions.

Figure 4.7(c-f) shows the surface structure of PEDOT:PSS after two different THF treatments, *i.e.*, *short* and *long* solvent exposure times (t_e). Samples nanostructured by a short exposure to THF ($t_e \ll 1$ min), were prepared by spin casting a drop of THF onto pristine PEDOT:PSS thin films. We found that the surface topography was affected by the fast interaction with the solvent, as shown in Figures 4.7(c,d). In this sample, from now on called PEDOT:PSS-ST, we observed the formation of randomly distributed holes on the PEDOT:PSS surface. These inclusions have a typical diameter of ~ 250 nm, and depths of ~ 18 nm. No changes in the film thickness were detected and the overall film's roughness ($\langle R_a \rangle$) was about 3.0 nm. Moreover, by taking a closer look to the AFM topography images, we observed that the PEDOT:PSS granular structure could not be distinguished anymore on the highest areas of the surface (see green arrows in Figure 4.7(c)). This observation can be further appreciated by comparing Figures 4.7(b and d) and their respective cross-sections. We confirmed the observations by calculating the roughness of the upmost layer (R_{a-up}) of PEDOT:PSS-ST, which resulted in typical values of ~ 1.0 nm, *i.e.*, $\sim 70\%$ lower when compared to the pristine PEDOT:PSS sample (Table 4.3).

Even if a fast exposure of PEDOT:PSS thin films to THF results in a nanostructured surface, we must highlight two observations that hinder its application as structuring strategy. First, the observed changes are not homogeneous throughout the whole film surface, since different areas of the material present different features. This fact can be related to an inhomogeneous distribution of the solvent on the polymer surface during spinning. Second, the resulting structures change dramatically only by small variations of the spin coating process.

Comparing our results with previous works, we found that there are several reports dealing with the use of different solvents to tailor and tune PEDOT:PSS properties^{243–245}. In most cases, the works have used high boiling point solvents, as EG^{244,246,247}, DMF²⁴⁶ and DMSO^{243–246}, or alcohols as ethanol or methanol^{247,248}. In these reports, the authors did not

observed the formation of well-defined nanostructures, as the ones obtained in our current work using THF. However, most authors reported some changes in the surface roughness that, in some cases, allowed a better adhesion of further layers during final device fabrication²⁴³. Moreover, these high boiling points solvents allow tuning the PEDOT:PSS electrical properties, in most cases enhancing the electrical conductivity of the polymer. Nonetheless, an improved electrical conductivity is not the unique factor to consider when tailoring PEDOT:PSS for final applications^{246,249,250}. For example, Liu et al. were able to increase the transport properties of PEDOT:PSS thin films by spin casting EG, DMF, and/or DMSO²⁴⁶. However, the authors observed that the treated films, with enhanced conductivities, lead to poorer device performance in perovskite-based solar cells. In fact, in their work, the authors determined that by inserting a thin layer of non-conducting PSS between the PEDOT:PSS and the perovskite films allowed improving the final device behavior, since PSS allowed a better perovskite adhesion and film formation^{246,249}. In our work, exposure of the PEDOT:PSS thin film to THF vapors also allows its controlled nanostructuring, as presented in the following lines.

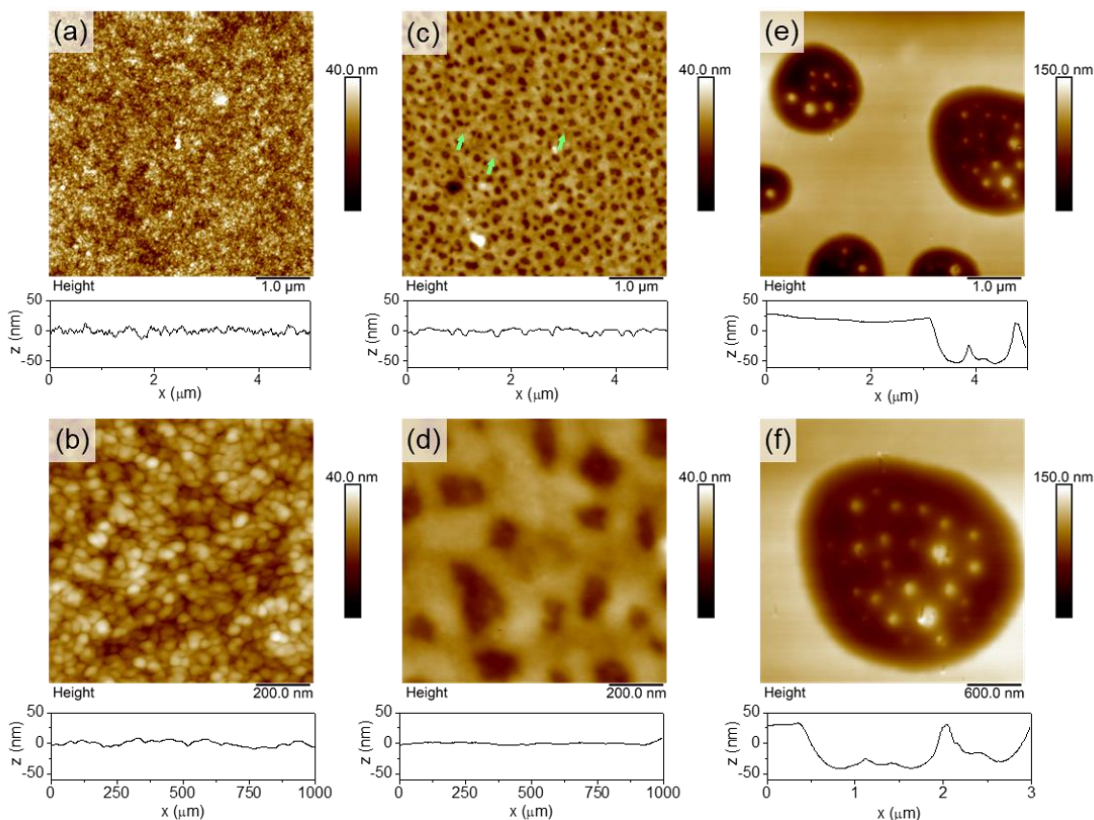


Figure 4.7. AFM topography images of PEDOT:PSS thin films treated with THF: (a,b) pristine sample, (c,d) after short interaction times ($t_e \ll 1$ min), and (e,f) after long interaction times ($t_e = 10$ min). A topography cross-section, taken at the center of each image, is presented below each figure.

Figure 4.7(e,f) shows the topography of a PEDOT:PSS thin film after a long exposure to a saturated THF atmosphere ($t_e = 10$ min). We will refer to this sample as PEDOT:PSS-LT

from now on. Here, the sample was subjected to an SVA treatment that allowed a good control of exposure time (see section 2.2). As shown by the AFM topography images, the long exposure to THF vapors results in a further surface nanostructuring, compared to PEDOT:PSS-ST. Now, the PEDOT:PSS surface is characterized by clearly defined micrometer-sized domains, as if the holes observed for short times keep on increasing due to the influence of the THF vapors. These domains' depth is about 40 nm ($\times 2$ deeper), while their diameter ranges between 0.8 – 3 μm (up to $\times 10$ larger, compared to PEDOT:PSS-ST). The characterization of different samples of PEDOT:PSS-LT, revealed that the domains do not always show a regular circular geometry and they present a typical depth of 30 ± 10 nm. Inside these features, there are other nanometric structures, as islands with typical diameters of 250 nm and varying heights (Figure 4.7(f)). No changes in the film thickness were detected, as measured from the upper layer, indicating that long exposure to THF vapors does not result in film dewetting. Finally, the upmost layer of this sample presents again an extremely low roughness value ($R_{a\text{-up}} = 0.5$ nm), even lower to those found for the flat areas of PEDOT:PSS-ST.

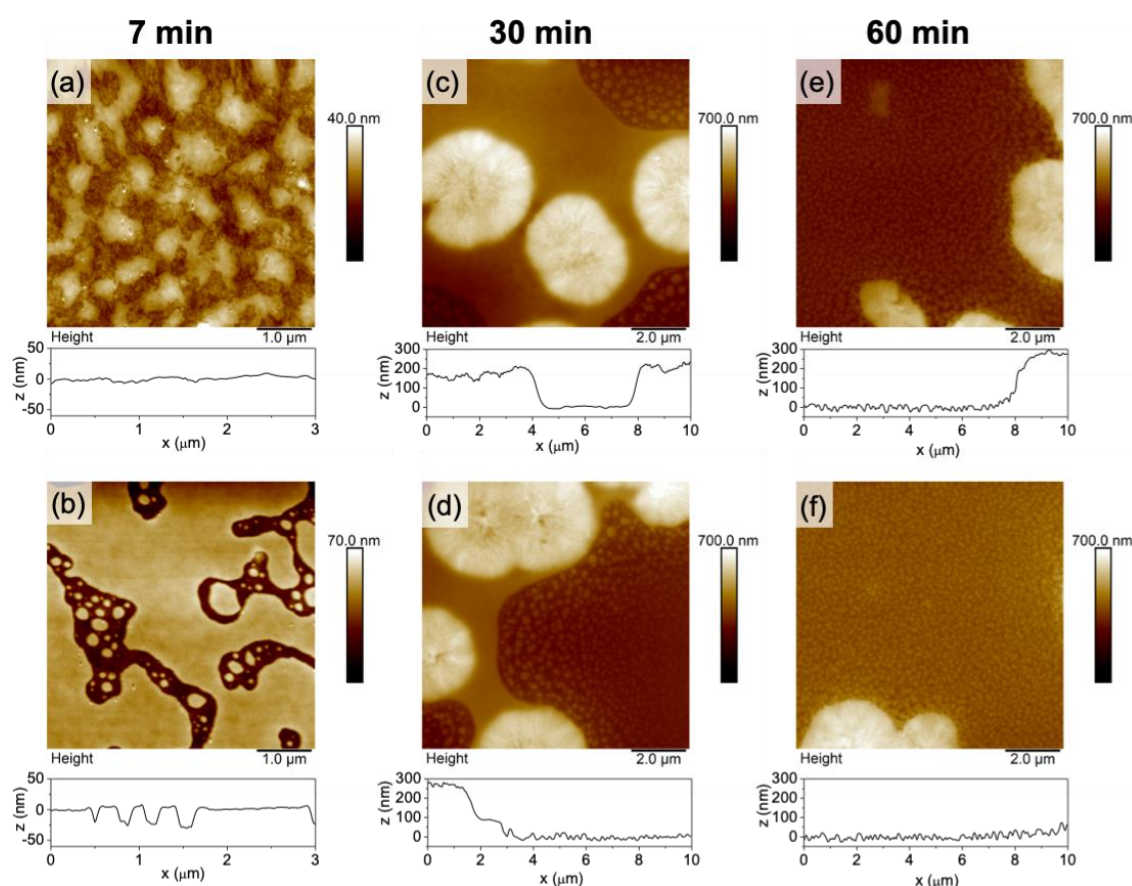


Figure 4.8. AFM topography images of PEDOT:PSS thin films nanostructured by SVA. A topography cross-section, taken at the center of each image, is presented below each figure.

Furthermore, we explored how SVA exposure at different times allows to prepare different nanostructures on the PEDOT:PSS surface. When using $t_e < 10$ min, a similar problem

to that found for spin casting was observed: although surface nanostructuring is possible, the formed features are not reproducible. For example, Figures 4.8(a,b) show two PEDOT:PSS thin film treated by SVA for 7 min where particularly different features were formed. For longer treatment times, $t_e \geq 10$ min, homogeneous surface nanostructuring are achieved. However, for exposure times of 30 and 60 min, the $\langle R_a \rangle$ increases dramatically to values ranging from 30–70 nm. In these two cases, AFM images (Figures 4.8(c-f)) show the breakage of the upper part of the PEDOT:PSS thin film, forming now separated islands of 50 – 300 nm in diameter and ~40 nm of height, for a 30 min treatment. Interestingly enough, after 60 min of solvent exposure these aggregates reach an almost homogeneous size distribution, with diameters and height of 150 nm and 40 nm, respectively. Moreover, for these two cases we observed spherulites in random areas of the films, covering micrometer sized areas of about 4 μm in diameter, and 200 nm of height. Finally, it is worth highlighting that the observed structural rearrangement does not result in film dewetting, but in a thickness reduction. In particular, we were able to quantify a film thickness of ~300 nm for 30 and 60 min SVA treated films, as measured from the homogeneous surface outside the crystalline domains down to the supporting ITO substrate.

Previously, different SVA strategies were used to modify and enhance the behavior of PEDOT:PSS thin films^{251–256}. In most cases, the reported works have focused on tailoring the electric and thermoelectric properties of PEDOT:PSS using DMSO vapors^{251–255}. However, only a few reports have focused on the SVA impact on surface topography and nanostructure formation, where most investigations have pointed out the separation of PEDOT from PSS after solvent exposure. For example, Xu and collaborators observed the formation of smooth and uniform film morphologies after exposing PEDOT:PSS thin films to DMSO vapors for up to 60 min²⁵⁵. The authors associated this structure to the fusion of the PEDOT:PSS grains, which in turn reduced the tunneling distance between molecules and led to enhanced conductivities. Also, Yeo et al.^{245,252} showed that SVA of PEDOT:PSS thin films, using DMSO for up to 120 min, resulted in an homogeneous surface topography with a fairly low roughness of 0.38 nm. This value is comparable to the R_{a-up} calculated for PEDOT:PSS-LT in our present study (0.5 nm). In their work, the authors associated this topography to the formation of an enriched-PSS layer on the top surface of the SVA-treated films, *i.e.*, a vertical PEDOT/PSS phase separation took place due to solvent exposure. This PSS segregation towards the surface allowed preparing PEDOT:PSS anode films with enhanced conductivities and tunable work functions²⁴⁵. However, none of these research works show the possibility of using a SVA strategy to efficiently nanostructure PEDOT:PSS samples, as in our present study. Then, in order to

understand the nature of the different structural phases of the PEDOT:PSS-LT sample, we have investigated its physical properties.

Transport properties of nanostructured PEDOT:PSS thin films

Figure 4.9 shows the nanoscale electrical transport properties of PEDOT:PSS-LT. In particular, Figure 4.9(a) shows the topography of the sample, as obtained from C-AFM experiments. We observed that the scanning process does not result in damage to the surface, under the applied normal force conditions. Figure 4.9(b) presents the electrical current map (electrical current), in a binary color scheme. There, green areas denote electrically conducting areas, while black areas show *non-conducting* areas of the sample. For this binary approach, we selected a current cutoff of 100 pA. This idea allowed highlighting those areas which electrical current values are comparable to those reported for pristine PEDOT:PSS¹²³. The electrical current map of PEDOT:PSS-LT is heterogeneous, *i.e.*, only some parts of the sample present an electrical current flow directly ascribable to the pristine material. In other words, solvent exposure leads to the segregation of conducting domains. As shown in Figure 4.9(b), the electrical conducting regions are composed of a collection of conducting spots, in line with previous reports for PEDOT:PSS thin films^{120,122,257,258}. To link the relations between the formation of surface nanostructures and segregation of conducting domains, in Figure 4.9(c) we present a compound *topography/electrical* map. Here, the green shading over the topography image indicates those areas showing electrical current above 100 pA. By this approach, we were able to determine that the bottom phase of the PEDOT:PSS-LT sample is the only one showing electrical current flow comparable to pristine PEDOT:PSS. On the contrary, both the upper phase and the spherical islands present current values well below our cutoff limit, indicating that these zones do not allow electronic transport under our evaluation conditions. Using the electric current maps, we were able to calculate a typical conductance of ~ 0.5 nS, a value on the same order of magnitude to those found previously for PEDOT:PSS using C-AFM electrical mapping^{193,258}.

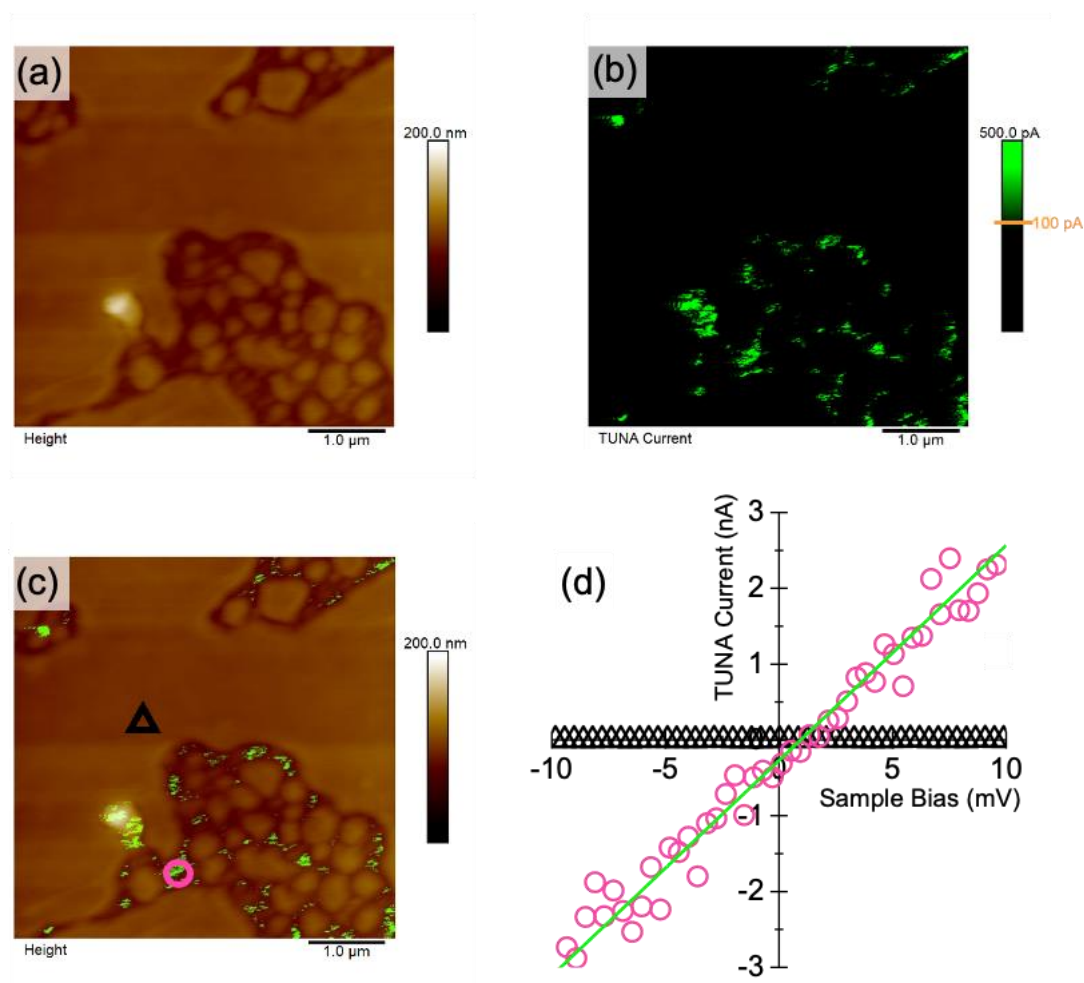


Figure 4.9. Nanoelectrical properties of PEDOT:PSS-LT, as determined by C-AFM experiments. (a) Topography. (b) Electrical current map. Green areas indicate electrical current values above 100 pA. (c) Compound topography/current image. Green shading denotes regions of the sample with current values higher than 100 pA. (d) Current-voltage characteristics (I-V curves) performed by C-AFM experiments on two spots of the PEDOT:PSS-LT sample (see triangle and circle in Figure c). Green continuous line in Figure d is a linear fit to the data (circles only). The data shown for Figure d are presented as 1 point each 200 captured datapoints.

To further prove the preferential disposition of the charge carriers at the bottom phase in PEDOT:PSS-LT, we performed AFM scattering-Scanning Near-field Optical Microscopy (s-SNOM) experiment in collaboration with the group of professor R. Hillenbrand (CIC NanoGUNE BRTA, 20018, Donostia-San Sebastián, Spain). The experimental setup and conditions details can be found in the published version of this work as Sanviti et al., *Polymer*, 246,(2022)²⁵⁹. Interestingly, we observed a strong contrast between the lower and upper phases, indicating that they had distinct infrared reflectivity so then different electrical conductivity. From the contrast maps, it was possible to address a higher charge carriers concentration to the lower phase, confirming and validating the consistency of the C-AFM results.

In order to provide a precise measure of the conductivity of the different phases composing the PEDOT:PSS-LT sample, we performed I-V measurements at the distinct regions. Figure 4.9(d) shows the obtained results at two representative spots of the samples. The top phase of PEDOT:PSS-LT shows a response characteristic of a dielectric material, as observed from the black triangles in Figure 4.9(d). On the contrary, at the bottom phase displays a linear I-V relationship (open circles in Figure 4.9(d)). A conductivity of 3.1 ± 0.1 S/cm for the bottom phase of PEDOT:PSS-LT was calculated. For direct comparison, we measured an I-V curve on a pristine PEDOT:PSS thin film, with the same instrumental setup from which a conductivity of 2.5 ± 0.1 S/cm was calculated. This result evidences that the bottom phase of PEDOT:PSS-LT preserved the good electronic transport properties of the pristine polymer.

Further nanoelectrical experiments allowed to evaluate the disposition of the upper PEDOT:PSS-LT phase and its penetration onto the thin film volume. In this case, we detected the variation of the conductivity along the film thickness by using a controlled penetration of the AFM tip into the sample, as summarized in Figure 4.10.

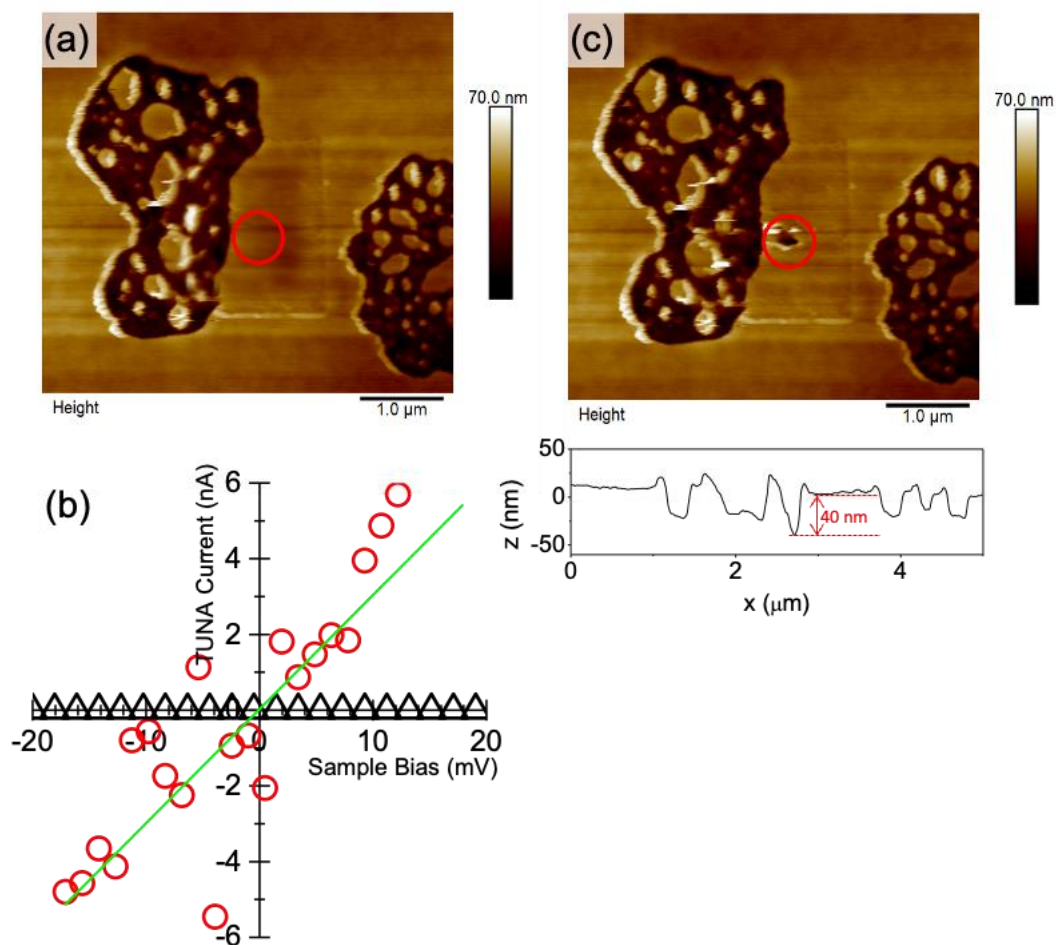


Figure 4.10. (a) AFM topography image of a selected PEDOT:PSS-LT area. (b) I-V curves on the PEDOT:PSS-LT sample before (triangle) and after (circles) nanoindentation. In both cases, data is shown as 1 every 20 points. Green line shows a linear fit to the circles. (c) AFM topography image of the same PEDOT:PSS-LT area after nanoindentation. Below the image, a height cross-section is presented, taken at the center of the print left by nanoindentation.

Going into detail, in an arbitrary spot on the upper layer of the PEDOT:PSS-LT sample, indicated by the red circle in Figure 4.10(a), we measured an I-V curve at the usual conditions. At this initial point, the corresponding I-V spectra showed the non-conducting behavior of the upper phase just discussed. We progressively increased the force setpoint between the tip and the surface, acquiring an I-V curve at every step. When the normal force was increased above ~ 300 nN, an ohmic I-V curve was obtained, with a resistance of $= 2.3$ M Ω (Figure 4.10(b)), indicating that we penetrated the surface deep enough to reach a conductive path. The obtained resistance was fairly similar to that of the bottom phase of PEDOT:PSS-LT, previously presented. After this experiment, a topography image was taken to evaluate the indentation depth necessary to reach the conductive material (Figure 4.10(c)). We found that the imprint

left after the indentation experiment had a depth of 40 nm; a value comparable to the average thickness of the upper phase (see vertical cross-section in Figure 4.10(c)). Our nanoindentation results thus confirmed that the PEDOT:PSS-LT upper phase does not reach the bottom of the film, but only forms a *covering sheet* of a few tens nanometers, leaving a PEDOT:PSS volume below it. In other words, the bulk properties of the PEDOT:PSS thin film below the surface are not affected by the proposed solvent-structuring strategy. The formation of distinct phases, each one presenting particular electrical properties, is not surprising. In fact, the induction of periodic surface structures on semiconducting polymers^{77,260,261}, as well as on PEDOT:PSS¹⁹³, can lead to the segregation of conducting regions.

The zero conductivity of the upper phase of the PEDOT:PSS-LT sample, can be related to different possibilities based on the rearrangement of the PEDOT and PSS phases due to solvent exposure. First, as already discussed, the non-conducting phase could be related to a vertical PEDOT/PSS phase separation. Under this idea, a *pure* PSS layer on the top of the PEDOT:PSS-LT film would provide a “dielectric spacer”, hindering electronic transport. Second, instead of being a *pure* PSS layer, the upper phase could just be a PSS-rich layer where the PEDOT to PSS ratio is below the minimum required to allow the percolation of the conductive polymer grains into the electrolyte matrix, *i.e.*, 1 PEDOT unit for every 6 PSS chains for a Baytron P type²⁶². In fact, the high conductivity of PEDOT:PSS is mostly related to its charge carriers density, which is governed by the PEDOT chains^{263,264}. Then, as a third possibility, the non-conducting behavior of the PEDOT:PSS-LT upper phase could be related to a lower doping level onto the π - π conjugated system along the PEDOT chains, due to differences in the oxidation state of the PEDOT, from its polaron/bipolaron state to a neutral state^{213–216}.

Identification of PEDOT/PSS phases in nanostructured PEDOT:PSS thin films

To further understand the chemical nature of the PEDOT:PSS-LT phases, we performed new experiments. Figure 4.11 shows compound topography/electrical maps for PEDOT:PSS-LT samples, after washing using distilled water. On one hand, Figure 4.11(a) shows the results after spin casting a drop of water onto a PEDOT:PSS-LT sample. On the other hand, Figure 4.11(b) shows the results after immersing a PEDOT:PSS-LT film into a water reservoir, at room temperature, for 10 seconds. We tested these ideas by following the work of DeLongchamp and collaborators, who observed that these protocols would allow removing PSS-rich areas, with negligible PEDOT loss²⁶⁵. As presented in Figure 4.11, our AFM studies show that no

morphological or electrical changes take place after either treatment. This important result indicates that the upper layer of PEDOT:PSS-LT should not be composed by *free* PSS chains exclusively.

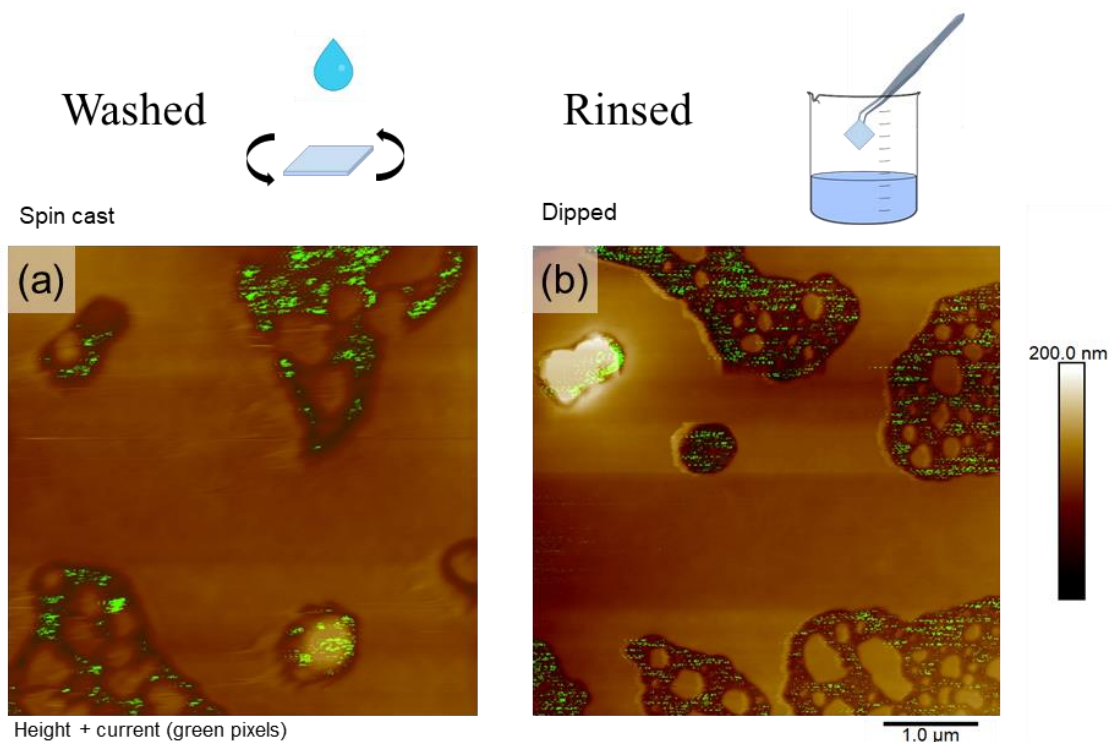


Figure 4.11. Compound topography/electric maps of PEDOT:PSS-LT film after (a) spin casting a H₂O drop, and (b) immersion into a H₂O bath. On both images, green shading indicates regions with current detection above 100 pA.

These facts are furthermore supported by the nanomechanical investigation of PEDOT:PSS-LT. Figure 4.12 shows compound topography/mechanical modulus maps for pristine PEDOT:PSS (Figure 4.12(a)) and PEDOT:PSS-LT (Figure 4.12(b)). The pink areas in these maps denote zones where the Young's modulus values are above 2.7 GPa. This modulus cutoff allowed identifying areas richer in PSS, as previously reported for pristine PEDOT:PSS thin films^{117,237}. In Figure 4.12(a), we observe a homogeneous PSS distribution throughout the pristine thin film. However, the PEDOT:PSS-LT sample shows a distinctive nanomechanical phase separation. In particular, E values above the threshold, indicating PSS presence, are preferentially located at the bottom phase of the film with a disposition comparable in shape and density as in the pristine case. On the contrary, the upper phase is mostly characterized by a slightly lower E , which would be indicative of PEDOT-rich areas, as reported before¹¹⁷.

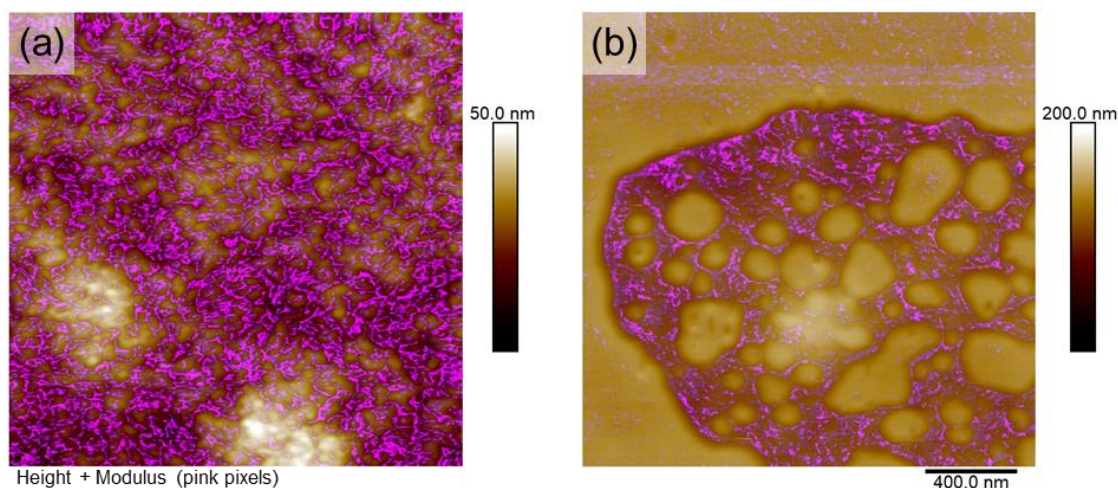


Figure 4.12. Nanomechanical results, as compound topography/modulus maps, for pristine (a) PEDOT:PSS, and (b) PEDOT:PSS-LT. Pink shading refer to zones on the sample where the Young's modulus values were higher than 2.7 GPa.

Our nanoscale studies point out that the upper phase of PEDOT:PSS-LT must be rich in PEDOT chains. However, considering its low conducting properties, the surface chains should be composed by neutral PEDOT chains (PEDOT^0). On the contrary, the nanoscale properties of bottom phase remain fairly similar to those of a pristine PEDOT:PSS thin film. This latter fact indicates that at the conducting areas of PEDOT:PSS-LT, the PEDOT chains remain in the doped polar/bipolaron state ($\text{PEDOT}^{+/2+}$), stabilized by the presence of PSS counterions¹⁰⁰. In other words, our results show that exposure of PEDOT:PSS to THF enhances the mobility of the polymer chains, which allows a vertical phase segregation from the granular PEDOT:PSS; in such a way a PEDOT^0 sheet forms at the surface. A similar vertical phase separation has been observed by Yeo and collaborators, where the segregation of PSS was caused by DMSO exposure²⁴⁵, as already discussed. However, with the use a low boiling point solvent, the PEDOT chains preferentially move towards the surface, forming a discontinuous covering sheet.

The presence of a PEDOT^0 layer at the top of the nanostructured thin films can be interesting for potential applications of the material, for example for tuning its optoelectronic^{266,267} and thermoelectric properties^{215,216}. This is related to the fact that a PEDOT^0 sheet would allow to modify its surficial work function and hole transport properties²⁶⁸. Finally, we point out that our strategy allowed a fast fabrication of nanostructured surface domains on PEDOT:PSS thin films, just by a controlled solvent exposure. The obtained samples showed distinct conducting areas at its upmost surface, while leaving unchanged the nanoelectrical properties of the volume. This result opens the possibility of developing further solvent-based fabrication strategies able to tailor the structure and properties of PEDOT:PSS.

4.3 Summary

By the work presented in this chapter, we were able to quantify the morphological, mechanical, and electrical properties of different nanostructures prepared starting from an intrinsically conducting polymer. We proposed two main methods to act on the nanostructure conformation of the system. On one hand, we changed the nanoparticles' dimensions and the arrangement of the phases defining their composition while, as a second approach, we used a solvent-structuring technique to selectively modify the surface of the thin films, both in conformation and oxidative state.

The nanoscale measurements indicated that the PEDOT:PSS nanospheres fabricated by reprecipitation preserve good mechanical properties. We envisage that there is different arrangement of PEDOT and PSS domains in the nanospheres respect to the commercial precursor, likely related to an enrichment of PEDOT onto the external shell of them. More importantly, out of such characterization we demonstrated that the shape and dimensions of the nanoparticles of PEDOT:PSS does not affect the conductivity as much as the intrinsic formulation of the conductive polymer. In other terms, type and amount of the coordination of PEDOT to PSS in the PEDOT:PSS rich phase, defined by its original synthesis conditions or eventual post treatments, remains the main factor to be considered in order to tune the conductivity of PEDOT:PSS. Finally, the change in size of the particles leads to a change of the finite-size effects in PEDOT:PSS thin films: from the obtained results, for bigger nanoparticles we envisage a more pronounced decrease of the conductivity by reducing the thickness.

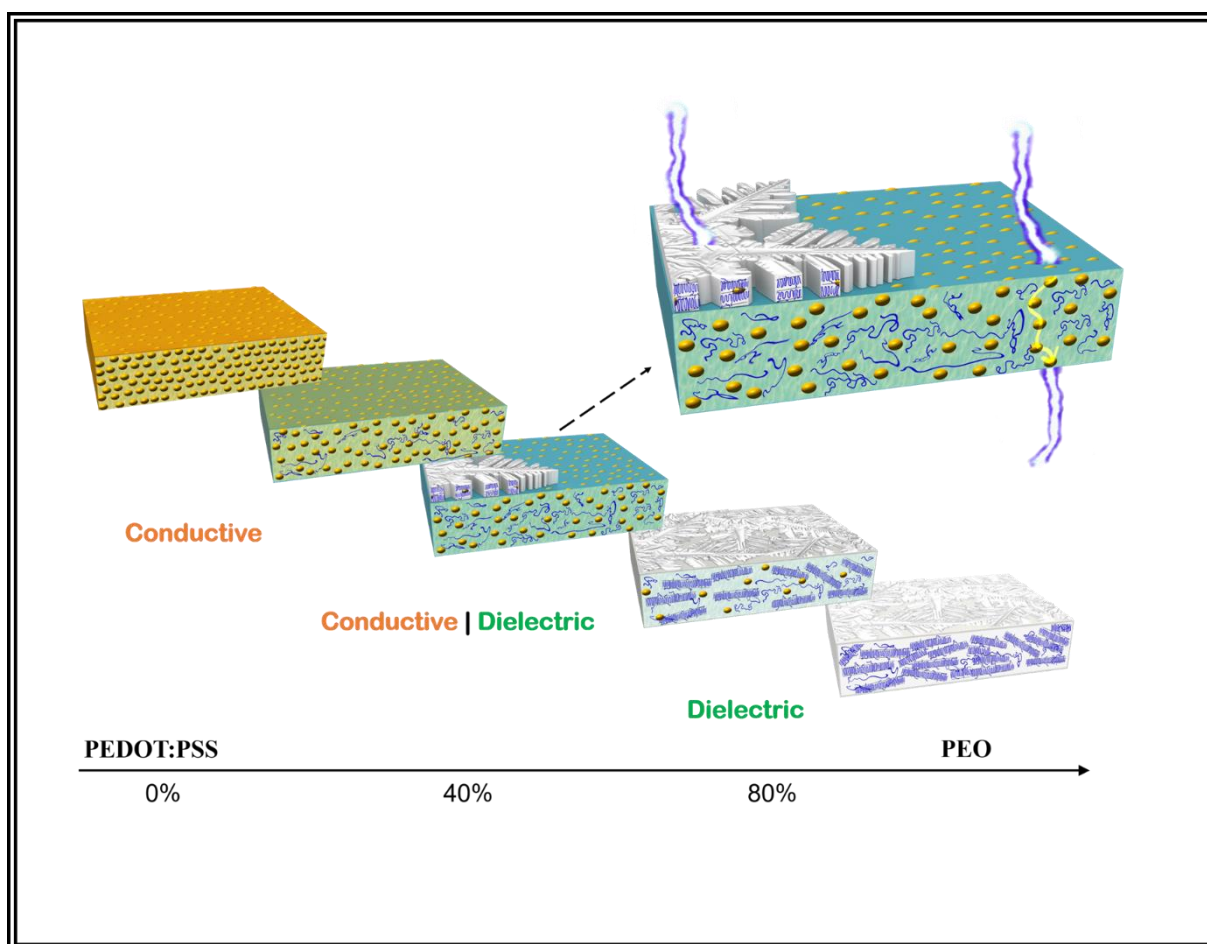
Solvent-structured PEDOT:PSS thin films were fabricated by exposing the material to controlled THF vapors. Spin casting THF onto the polymer thin films allowed a first approach into nanostructure fabrication. However, the method proved to be not reliable to ensure homogeneity and good reproducibility. On the contrary, subjecting the films to a saturated THF atmosphere, by SVA, allowed the fabrication of controlled nanostructured PEDOT:PSS surfaces. The obtained samples showed distinct conducting areas at its upmost surface, while leaving unchanged the nanoelectrical properties of the volume. A combination of nanoscale methods allowed to determine that the exposure of PEDOT:PSS to THF vapors resulted in a vertical phase separation of the PEDOT and PSS components. In particular, we proved that the PEDOT chains moved preferentially towards the material surface, forming a discontinuous covering sheet. This surficial film, of 30 nm in thickness, was preferentially composed of neutral state superficial PEDOT chains. This PEDOT⁰ chains would allow to modify its surface

work function and hole transport properties, opening the possibility of new applications of nanostructured PEDOT:PSS as optoelectronic and thermoelectric material.

Another option adopted in the past few decades to effectively tune the PEDOT:PSS properties has been the blending of the polymer with other non-conducting substrates²⁶⁹. One of the main routes used for this purpose is blending PEDOT:PSS with soft polymers such as poly(acrylic acid) (PAA), PMAA²⁷⁰, poly(vinyl alcohol) (PVA), and PEO^{271–273}, which are able to provide to the final product higher stretchability and, in some cases, improved conductivity. In this scenario, blends of PEDOT:PSS and PEO have been extensively investigated in view of their application to organic mixed ionic-electronic conductors (OMIECs)^{55,274,275}. In chapter 3, we investigated and discussed the ionic conductivity properties of PEO while, in this chapter, we delved into the physical properties of PEDOT:PSS in different conformations and nanostructural arrangements. In order to conclude our study about the charge transport and physical properties in complex polymer thin films, in the following chapter of this thesis we are presenting the characterization of PEDOT:PSS/PEO blends in thin film configuration, trying to put emphasis on their reciprocal influence at the micro- and nano-scale.

Chapter 5

PEDOT:PSS/PEO blend thin films: mechanical and electrical properties at the nanoscale



5.1 Introduction

PEDOT:PSS/PEO blends already showed considerable potential in the panorama of electronic devices not only due to the extremely good stability and compatibility²⁷⁶, but also for their promising electrochemical and electrochromic properties^{274,275}. In fact, the high ionic conductivity of PEO can fasten up the electrochemical turnover kinetics of the couple PEDOT⁰/PEDOT⁺, improving the resulting active electrode efficiency. Therefore, these find several possible applications in flexible electronics, such as electrochemical transistors (ECTs)²⁷⁷, supercapacitors (SCs)²⁷⁸, or electrochromic devices (ECDs)²⁷⁹. However, even if we count several works about the influence of PEO and PEG on PEDOT:PSS^{273,280–282}, in most of them either the PEO concentration is low and used as additive when prepared in thin film geometry by spin-coating or, for higher concentrations, the bulky material is mostly prepared by drop-casting. The fact that PEDOT:PSS derivatives are extensively used in thin film configuration in many of their application fields, makes extremely convenient the study of such materials in thin film configuration^{235,270,283,284}. It is well known that each of the different processing methods has an important impact on the phase separation, crystallinity, and properties of the final system^{285,286}. In this context, the present chapter focuses on the study of structure transition mechanisms (phase separation and crystallization) of spin-coating PEDOT:PSS/PEO blend thin films over the entire range of compositions at different length scales. Special emphasis has been devoted to the influence of structural changes on mechanical and electrical properties at the nanoscale, as well as their dependence on the molecular weight of PEO.

5.2 Topography

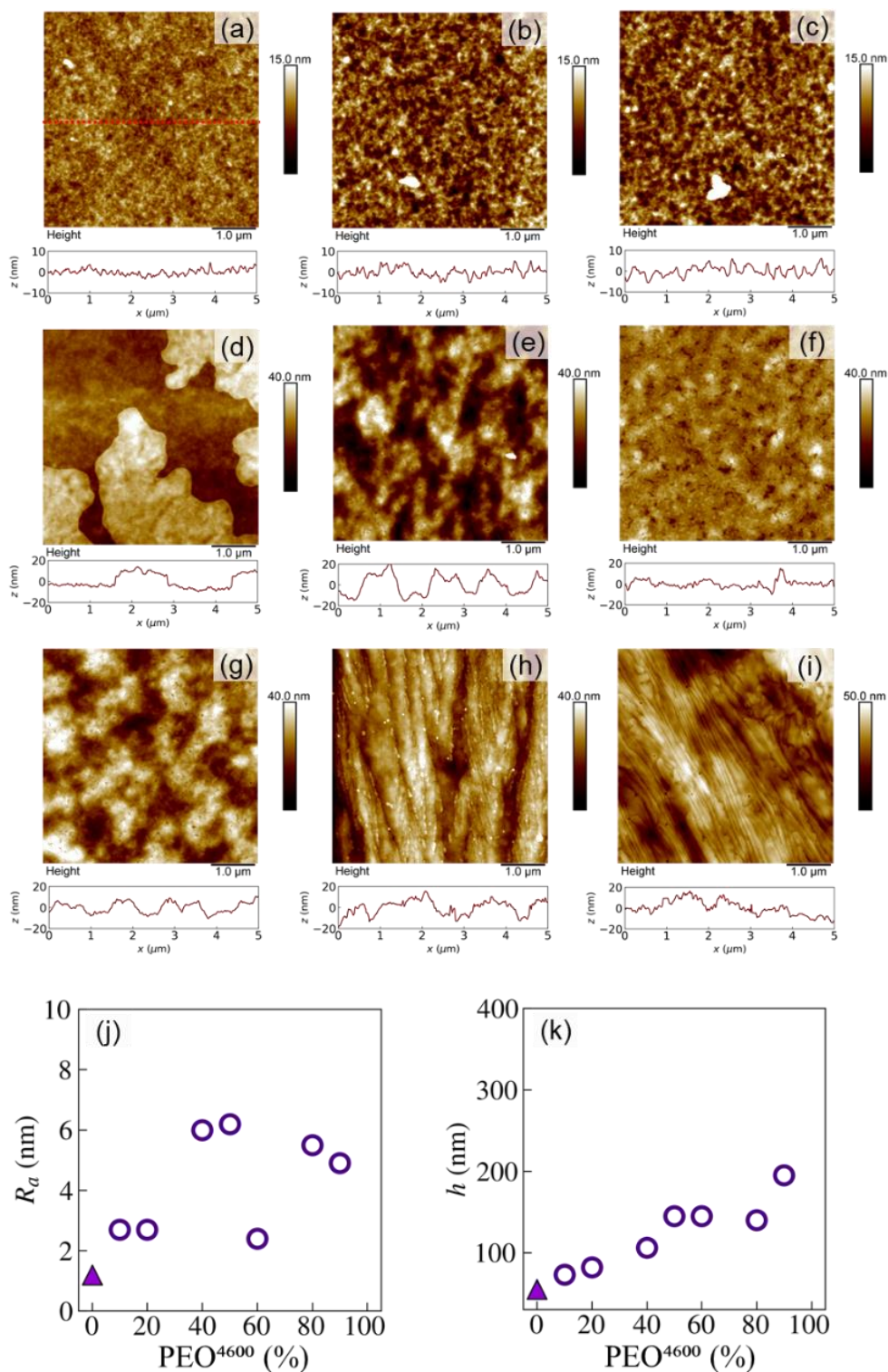


Figure 5.1. AFM topography images of PEDOT:PSS/PEO⁴⁶⁰⁰ blends at different weight ratios of PEO⁴⁶⁰⁰: (a) PEDOT:PSS, (b) PEO⁴⁶⁰⁰-10, (c) PEO⁴⁶⁰⁰-20, (d) PEO⁴⁶⁰⁰-40, (e) PEO⁴⁶⁰⁰-50, (f) PEO⁴⁶⁰⁰-60, (g) PEO⁴⁶⁰⁰-80, (h) PEO⁴⁶⁰⁰-90, (i) PEO⁴⁶⁰⁰ (250 mg/mL). Below each image, a height cross-section is presented. These z vs x plots were calculated at the center of each topography image, as exemplified by the dashed line in panel (a). Below:

graphical representation of the surface roughness (j) and the thickness (k) of the PEDOT:PSS/ PEO⁴⁶⁰⁰ blends as a function of PEO⁴⁶⁰⁰ content. The triangle corresponds to the pristine PEDOT:PSS.

Figure 5.1 shows AFM topography images of PEDOT:PSS/PEO⁴⁶⁰⁰ blends, with different compositions (X/Y). The samples are labeled by PEO^{Mn}-Y wt%, where Y is the PEO content in the blend, expressed as the percentage in weight. The same nomenclature applies for PEO²⁰⁰⁰⁰⁰-based blends, discussed in the following sections.

For all the investigated samples except for the PEO⁴⁶⁰⁰, we observed continuous polymer thin films, with varying roughness and thicknesses. In general, as PEO⁴⁶⁰⁰ content was increased, the film thickness and roughness values increased as well, as shown in Figures 5.1(j and k). Going into detail, the thin films' thicknesses increased almost linearly from 55 nm for pure PEDOT:PSS (Figure 5.1(a)) to 195 nm for PEO⁴⁶⁰⁰-90 (Figure 5.1(h)). The pure PEO⁴⁶⁰⁰ (18 mg/mL) sample presented a heterogeneous thickness with partially dewetted zones, for this reason a sample with higher concentration (250 mg/mL) was prepared in order to obtain a continuous coating with a thickness of ~500 nm (Figure 5.1(i)). It is interesting to point out that an important feature of these blends is their coating properties. As we have shown, the composition of the aqueous mixture precursor strongly affects the resulting thickness of the deposited film. In fact, from these results, we can assume that the addition of a small amount of PEDOT:PSS to pure PEO⁴⁶⁰⁰ importantly improves its coating efficiency from water solutions.

The typical surface topography of pristine PEDOT:PSS is presented in Figure 5.1(a)^{259,287,288}, where we can recognize a regular surface composed of homogeneously distributed PEDOT:PSS nanoparticles of relatively small dimensions (~ 50 nm). As we can see in Figures 5.1(b,c), PEO⁴⁶⁰⁰-10 and PEO⁴⁶⁰⁰-20 also show regular surfaces but, compared with pristine PEDOT:PSS, the roughness of the thin films containing 10% and 20% of PEO⁴⁶⁰⁰ is significantly higher (almost doubled, see Figure 5.1(j)). This behavior has been already reported for systems where PEDOT:PSS was doped by small amounts of high-boiling-point additives or PEO with different molecular weights^{281,288}. Increasing the amount of PEO⁴⁶⁰⁰ in the investigated blends leads to a bilayer morphology. This is the case of PEO⁴⁶⁰⁰-40, where a top layer with dendritic morphology and a thickness of about 15 nm is clearly discernable at the surface of a bottom layer (Figure 5.1(d)). As described in section 1.5, the formation of such dendritic domains is typical of semicrystalline ultra-thin films⁸⁸, also observed in PEO blended with amorphous polymers^{289,290}. For a concentration up to 50% (Figure 5.1(e)) an almost continuous surface is observed. Samples with PEO⁴⁶⁰⁰ content higher than 50% present

homogeneous surfaces with different morphologies as shown in Figure 5.1(f, g, h, and i). PEO⁴⁶⁰⁰ (Figure 5.1(i)) shows the characteristic crystalline lamellae morphology mainly perpendicular to the sample surface. In sample PEO⁴⁶⁰⁰-90, a coarser crystalline lamellae is also observed at the surface and PEDOT:PSS appears as interspersed particulate among them (Figure 5.1(h)).

5.3 Internal structure and phase separation

In order to investigate the internal structure and the possible phase separation of the two components in the PEDOT:PSS/PEO⁴⁶⁰⁰ blend thin films with different compositions, we report the results from GIWAXS experiments. Figure 5.2 shows the 2D GIWAXS patterns of blend thin films at different weight ratios of PEO⁴⁶⁰⁰. Samples PEO⁴⁶⁰⁰-10 and PEO⁴⁶⁰⁰-20 (Figure 5.2(b, c)) present an amorphous halo superposed to the PEDOT:PSS scattered intensity while all the other patterns present PEO reflections²⁹¹ indicating that samples with a PEO⁴⁶⁰⁰ content of 40% and higher are semicrystalline. As indicated by the weak reflections of Figure 5.2(d), the degree of crystallinity is very low for sample PEO⁴⁶⁰⁰-40. Nevertheless, the result confirms the presence of a certain degree of crystallinity at the surface of PEO⁴⁶⁰⁰-40, even though the intensity in the GIWAXS pattern resulted poor due to the discontinuity and the extremely low thickness of the superficial dendritic layer. Exceeding a concentration threshold in PEO⁴⁶⁰⁰ up to 40%, the crystallinity of the blends increases with increasing PEO⁴⁶⁰⁰ content (Figure 5.2(e, f, g and h)). It should be pointed out that the pure PEO⁴⁶⁰⁰ (obtained from a solution with concentration 18 mg/mL) shows a pattern with very weak reflections (Figure 5.2(i)) due to its reduced thickness and the presence of dewetted regions, as it was observed by AFM measurements. It is also interesting to mention that the 2D patterns of PEO⁴⁶⁰⁰ and PEO⁴⁶⁰⁰-90 (Figure 5.2(i, h)) are composed of several ring-like reflections. This indicates a powder-like arrangement of crystallites, in good agreement with the typical spherulitic morphology of bulk samples²⁹¹ and in agreement also with the AFM topography observed in Figure 5.1(h and i), corresponding mainly to edge-on lamella. The 2D GIWAXS patterns for samples PEO⁴⁶⁰⁰-50, PEO⁴⁶⁰⁰-60 and PEO⁴⁶⁰⁰-80 (Figure 5.2(e, f and g)) are quite different compared to those for PEO⁴⁶⁰⁰ and PEO⁴⁶⁰⁰-90. In particular, the pattern corresponding to PEO⁴⁶⁰⁰-60 displays several localized thin reflections with reduced angular distribution. These results would reveal a preferred orientation of crystalline domains induced by a templating effect of PEDOT:PSS, suggesting crystallites with high aspect ratio and flat-on orientation²⁹². Our discussion, along with previous studies²⁹³, attribute the presence of this preferential lamellar orientation to the formation of semicrystalline ultra-thin films at the surface. The flat-on lamella configuration in sample PEO⁴⁶⁰⁰-60 is also supported by the morphology observed in Figure 5.1(f) and by the low surface roughness measured (Figure 5.1(j)).

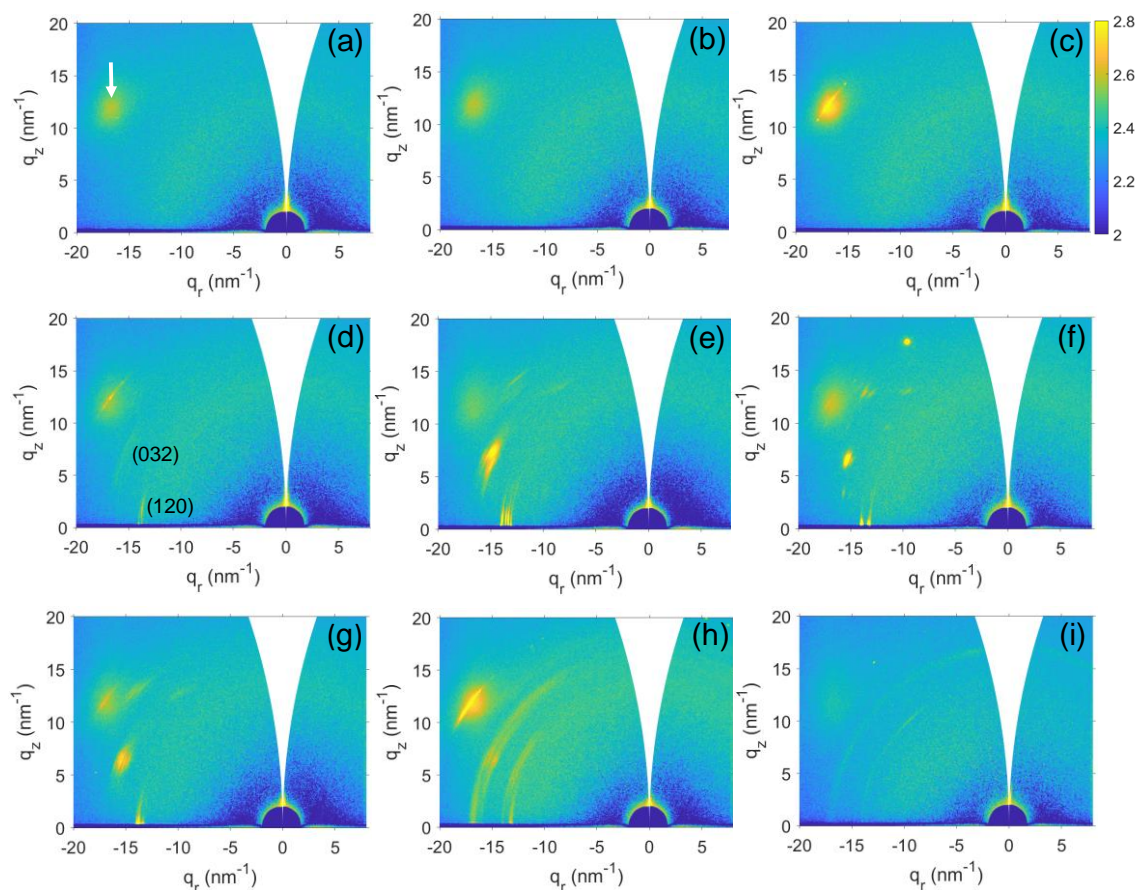


Figure 5.2. 2D GIWAXS patterns of PEDOT:PSS/PEO⁴⁶⁰⁰ blends at different weight ratios of PEO⁴⁶⁰⁰, obtained with an incident angle $\alpha_i=0.2^\circ$: (a) PEDOT:PSS, (b) PEO⁴⁶⁰⁰-10, (c) PEO⁴⁶⁰⁰-20, (d) PEO⁴⁶⁰⁰-40, (e) PEO⁴⁶⁰⁰-50, (f) PEO⁴⁶⁰⁰-60, (g) PEO⁴⁶⁰⁰-80, (h) PEO⁴⁶⁰⁰-90, (i) PEO⁴⁶⁰⁰ (18 mg/mL). Main reflections are indicated in panel (d). The white arrow in pattern (a) indicates a scattering intensity coming from the Silicon substrate and present in all the patterns.

To examine the nature of the two layers observed for sample PEO⁴⁶⁰⁰-40 (Figure 5.1(d)), GIWAXS patterns with different incident angles, $\alpha_i=0.1^\circ$, 0.2° and 0.3° , were obtained. Figure 5.3 shows the 1D GIWAXS intensity profiles obtained azimuthally integrating the 2D patterns through a broad q range avoiding the Silicon reflection (white arrow in Figure 5.2(a)), after the subtraction of a blank containing contribution from the air. While the intensity profile obtained with $\alpha_i=0.1^\circ$ presents the two main reflections of PEO^{291,294}, the one obtained with $\alpha_i=0.3^\circ$ does not present those reflections. This result could be explained considering that for $\alpha_i=0.1^\circ$ we are probing the surface of the sample and increasing the incident angle ($\alpha_i=0.3^\circ$) we are probing the complete thickness of the sample. Moreover, it could suggest that the sample is composed by two different layers due to phase separation, a PEO⁴⁶⁰⁰ upper layer growing on top of a PEDOT:PSS layer. In order to corroborate this hypothesis, we have performed C-AFM and Quantitative Nanomechanical Mapping (QNM) for probing the different electrical and mechanical properties of both materials respectively.

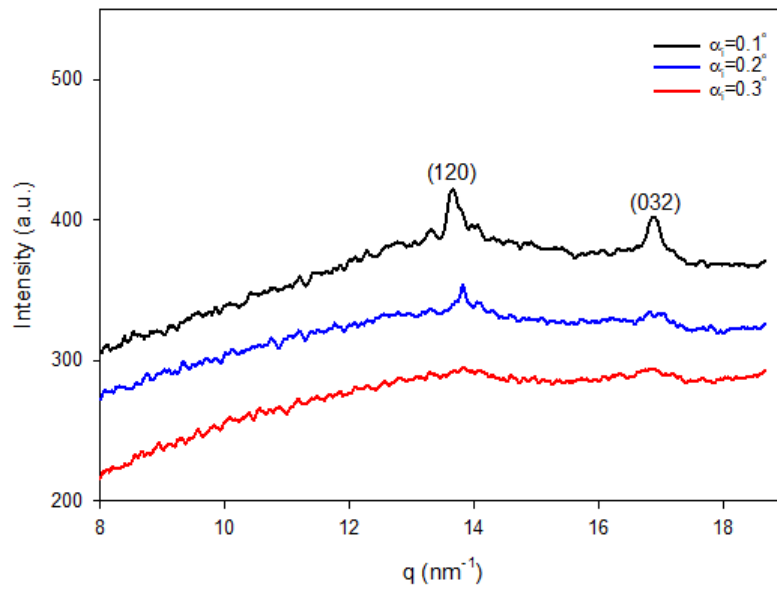


Figure 5.3. 1D GIWAXS intensity profiles as a function of the modulus of the scattering vector q , for sample PEO⁴⁶⁰⁰-40. The profiles were obtained at different incidence angles, as indicated. The main PEO⁴⁶⁰⁰ reflections are labeled.

5.4 Mechanical properties

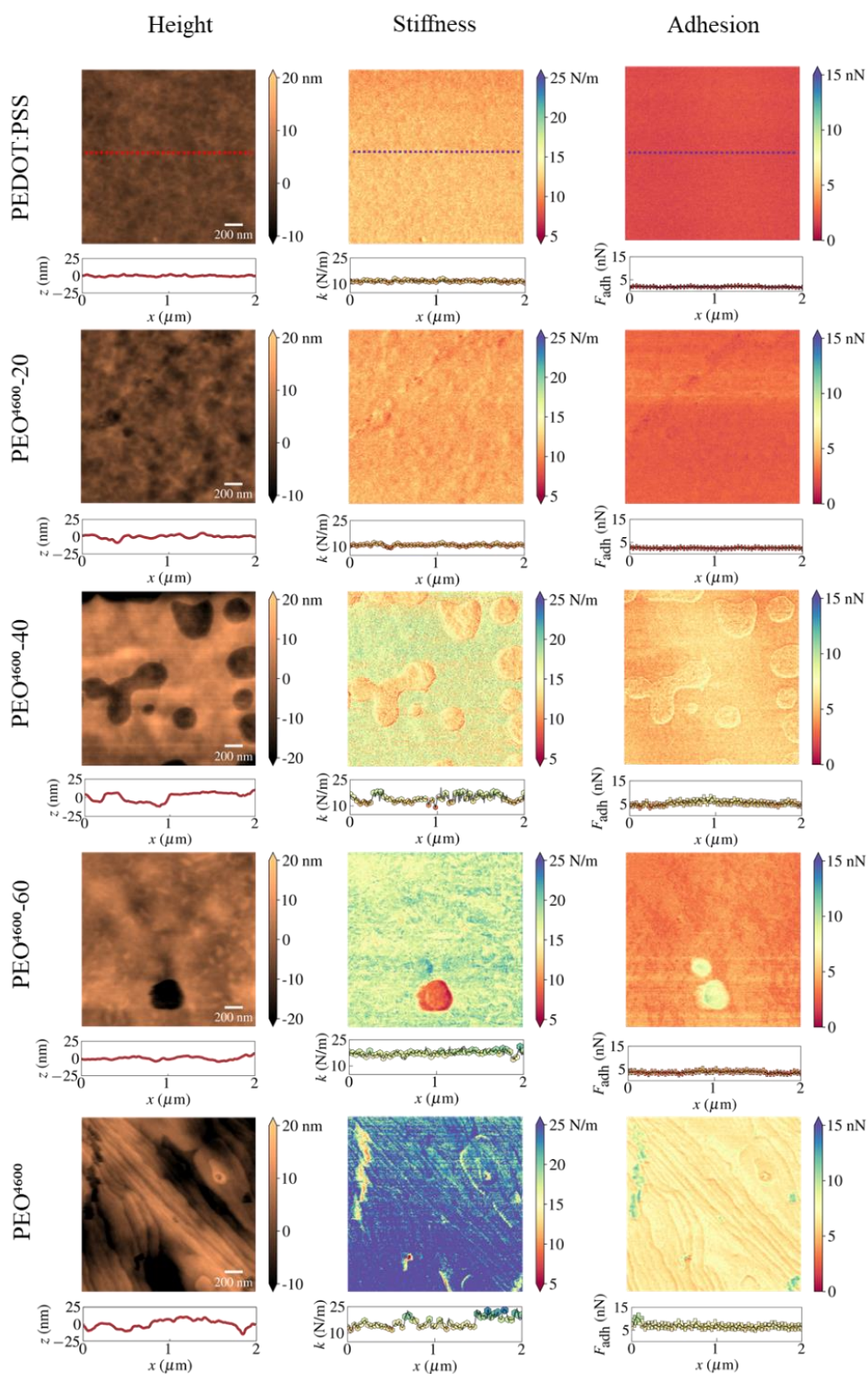


Figure 5.4. Nanomechanical maps for PEDOT:PSS, PEO⁴⁶⁰⁰-20, PEO⁴⁶⁰⁰-40, PEO⁴⁶⁰⁰-60 and PEO⁴⁶⁰⁰ (250 mg/mL): Height (z), stiffness (k), and tip-sample adhesion force (F_{adh}). Below each image, a height cross-section is presented. The dotted lines presented for PEDOT:PSS maps exemplify the cross-section direction.

Figure 5.4 reports stiffness and adhesion maps as well as the characteristic topography of some representative samples (PEDOT:PSS, PEO⁴⁶⁰⁰-20, PEO⁴⁶⁰⁰-40, PEO⁴⁶⁰⁰-60, and PEO⁴⁶⁰⁰). First, we observe a higher stiffness and adhesion for pure PEO⁴⁶⁰⁰ compared to PEDOT:PSS thin film. Also, for PEO⁴⁶⁰⁰, we can recognize the crystalline lamellae frontiers as elongated thin stepped lines in its topography profile. In the same sample, similar features are visible from the stiffness and the adhesion contrast maps matching with the topography profile. We ascribe the contrast in mechanical properties in such zones to the different properties of amorphous and crystalline PEO²⁹⁵. The magnitude of such a difference can be only qualitatively appreciated due to the coincidence with topography steps in proximity of the amorphous domains, that can alter the apparent mechanical response in AFM³².

Samples with a PEO⁴⁶⁰⁰ content up to 20 % show homogeneous and very similar mechanical properties, with a stiffness slightly lower, to that quantified for pure PEDOT:PSS (Figure 5.4). On the other hand, as previously introduced in the topography characterization, for the intermediate concentration case of PEO⁴⁶⁰⁰-40 a more heterogeneous surface was observed. Taking advantage of the AFM topography image in Figure 5.4(PEO⁴⁶⁰⁰-40), and of its relative cross section, it is possible to distinguish an upper layer with a step ~ 15 nm, which is in agreement with the result shown in Figure 5.1(d). By comparing the height image and the stiffness image in Figure 5.4(PEO⁴⁶⁰⁰-40), we can clearly distinguish zones with different mechanical properties at the surface of the sample. More specifically, we were able to distinguish two populations with different stiffness distributions corresponding to an upper layer and a lower one. The difference in stiffness between the upper and the bottom layer is ~ 4-5 N/m, which is about the 30% of the mean value obtained from the whole image (15 N/m). As we know that in this study PEO⁴⁶⁰⁰ is stiffer than PEDOT:PSS, from a first evaluation, the QNM analysis suggests that the upper layer is PEO⁴⁶⁰⁰ rich while the lower one is PEDOT:PSS rich. The GIWAXS and AFM mechanical mapping both point towards the fact that a semicrystalline PEO⁴⁶⁰⁰ upper layer is growing on top of a PEDOT:PSS layer.

Even though it has been reported that in drop cast PEDOT:PSS/PEO films with microns of thickness, the stiffness decreases with increasing the PEO content up to a 10%^{282,296}, relying on the obtained nanomechanical results, we envisage an increase in stiffness with the PEO⁴⁶⁰⁰ content. We believe that the decrease in stiffness at low concentrations is due to the miscibility of components in the blend at these compositions, which inhibits PEO crystallization. At the same time, the trend in the mechanical properties of the system taking into account a wider concentration window, points out an increase in stiffness as the crystallinity of the blend increases.

5.5 Electrical properties

Conductive-AFM was used to characterize the electrical response and the configuration of the conducting paths in PEDOT:PSS/PEO⁴⁶⁰⁰ blend thin films. By this technique, it was possible to acquire the electrical conductivity perpendicular to the film surface, which is of particular relevance to reveal the electrical properties of conductive thin films in view of their applications in electronic devices²⁹⁷.

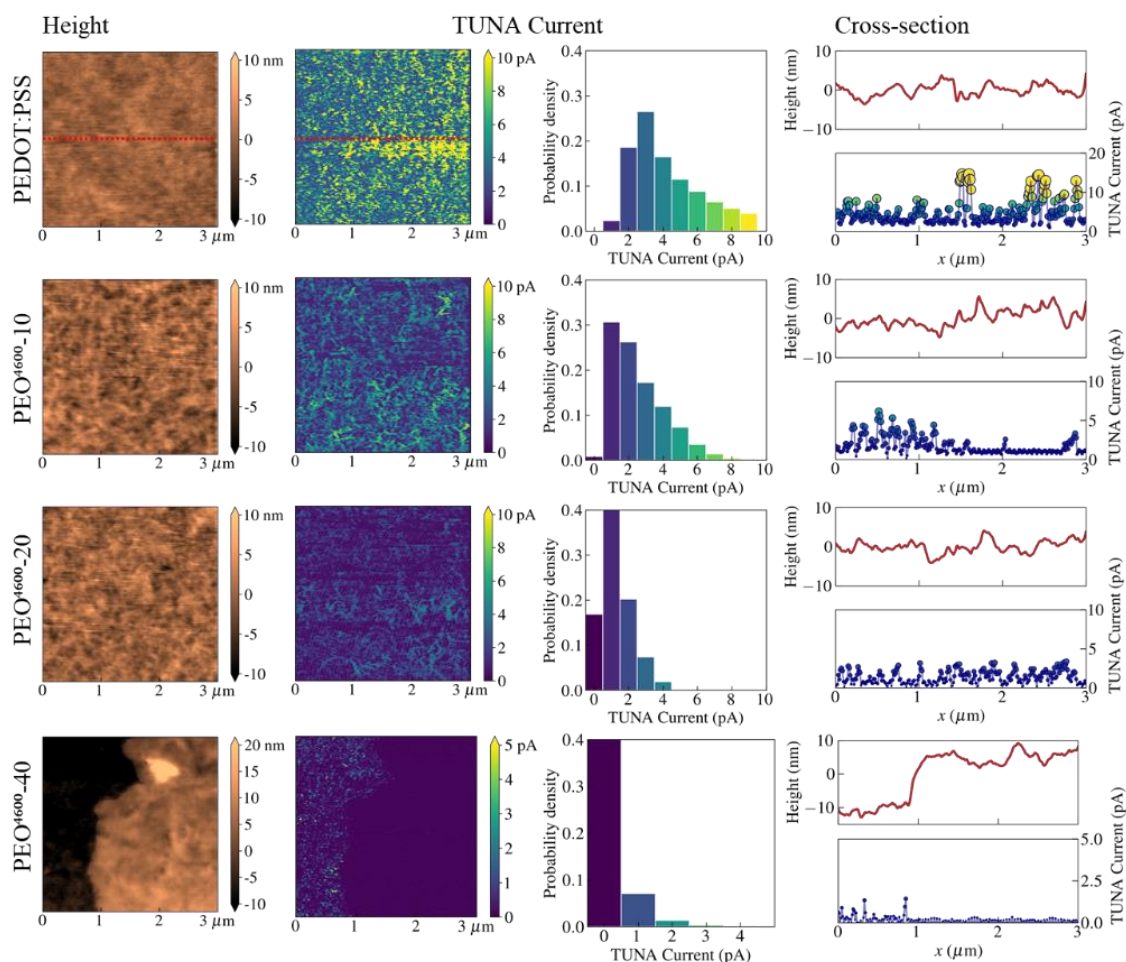


Figure 5.5. Nanoelectrical maps (height and electric current) for PEDOT:PSS, PEO⁴⁶⁰⁰-10, PEO⁴⁶⁰⁰-20 and PEO⁴⁶⁰⁰-40. Histograms were calculated using all data points presented in the current maps (>65000 points). Cross-sections were taken at the middle of the maps (see example for PEDOT:PSS).

Figure 5.5 shows contact mode AFM topography and current images recorded simultaneously by applying a constant sample bias of 500 mV. Histograms and cross-sections of the electrical current are also presented. Among the analyzed PEDOT:PSS/PEO⁴⁶⁰⁰ blends thin films, we were able to detect an electrical signal only in samples with a PEO⁴⁶⁰⁰ content lower or equal to 40%: the conductivity lowers by increasing the amount of PEO⁴⁶⁰⁰, until finally reaching values below our detection limit. Therefore, PEO⁴⁶⁰⁰-40 shows the lowest

conductivity that we could estimate from the conductive thin films in the here discussed set of samples. The current map of pristine PEDOT:PSS thin film shows homogeneously distributed PEDOT-rich and PSS-rich nanodomains. In particular, the bright areas on the images represent the conductive domains attributed to the PEDOT-rich regions, while the dark areas the insulating domains attributed to the PSS-rich zones, this pattern is in accord with previously reported for this material ^{122,242,257}. The current maps of PEO⁴⁶⁰⁰-10 and PEO⁴⁶⁰⁰-20 thin films present a similar scenario compared to pristine PEDOT:PSS, having a homogeneous distribution of conductive and insulating nanodomains, but the average electrical conductivity decreases by increasing PEO⁴⁶⁰⁰ content. This behavior indicates that PEDOT:PSS/PEO⁴⁶⁰⁰ blend is miscible in this range of compositions, and PEO⁴⁶⁰⁰ molecules distort the conducting paths of pristine PEDOT:PSS, resulting in lower conductivity ²⁷¹. The current map of PEO⁴⁶⁰⁰-40 presents two well defined regions: a dielectric upper layer on top of a conductive layer. Combining QNM, GIWAXS and C-AFM results, we can assume that for PEO⁴⁶⁰⁰ content at least in the range 40% to 60% we obtain bilayer samples with an almost continuous semicrystalline PEO⁴⁶⁰⁰-rich layer grown on top of a PEDOT:PSS-rich layer.

5.6 Influence of molecular weight on morphology and structure

The topography images of PEDOT:PSS/PEO²⁰⁰⁰⁰⁰ blends with different PEO²⁰⁰⁰⁰⁰ content (PEO²⁰⁰⁰⁰⁰-Y) are reported in Figure 5.6. All the samples showed continuous polymer thin films with varying roughness, thickness, as well as morphological features. Unlike PEO⁴⁶⁰⁰, pure PEO²⁰⁰⁰⁰⁰ (18 mg/mL) resulted in a regular thin film, with a constant thickness value of ~100 nm. Such outcome is normally associated with the solution used for the fabrication of the sample, for which polymer precursors with higher molecular weight usually provide better coating properties from diluted solutions²⁹⁸. In general, as PEO²⁰⁰⁰⁰⁰ content was increased, the thickness of PEDOT:PSS/PEO²⁰⁰⁰⁰⁰ blends increased as well, as shown in Figure 5.6(k). Going into detail, the thin films' thicknesses increased almost linearly from 55 nm for pure PEDOT:PSS to 358 nm for PEO²⁰⁰⁰⁰⁰-90, while pure PEO²⁰⁰⁰⁰⁰ thickness is about 100 nm. PEDOT:PSS/PEO²⁰⁰⁰⁰⁰ blends (Figure 5.6(k)) almost doubled the thickness of PEDOT:PSS/PEO⁴⁶⁰⁰ blends counterparts (Figure 5.1(k)). Concerning the roughness of the blends, Figure 5.6(j) shows that the measured values range between 3.5 nm and 7.5 nm, generally constituting rougher surfaces compared to pristine PEDOT:PSS ($R_a = 1.2$ nm). In Figure 5.6(b,c) we can see that PEO²⁰⁰⁰⁰⁰-10 and PEO²⁰⁰⁰⁰⁰-20 show regular surfaces, similar to PEO⁴⁶⁰⁰-10 and PEO⁴⁶⁰⁰-20 but with a coarser morphology and with the highest roughness of all measured samples, more than twice the roughness of PEO⁴⁶⁰⁰-10 and PEO⁴⁶⁰⁰-20. Increasing the amount of PEO²⁰⁰⁰⁰⁰, films with a bilayer nature and a dendritic morphology for the top layer is observed for PEO²⁰⁰⁰⁰⁰-40 and PEO²⁰⁰⁰⁰⁰-50 (Figure 5.6(d, e)), while a homogeneous surface with reduced roughness is observed for PEO²⁰⁰⁰⁰⁰-60 (Figure 5.6(f)). Samples PEO²⁰⁰⁰⁰⁰-80 and PEO²⁰⁰⁰⁰⁰-90 (Figure 5.6(g and h)), develop heterogeneous surface topographies suggesting the coexistence of edge-on and flat-on lamella domains. Finally, PEO²⁰⁰⁰⁰⁰ (Figure 5.6(i)) presents the characteristic randomly oriented lamellar structure of spherulitic superstructures.

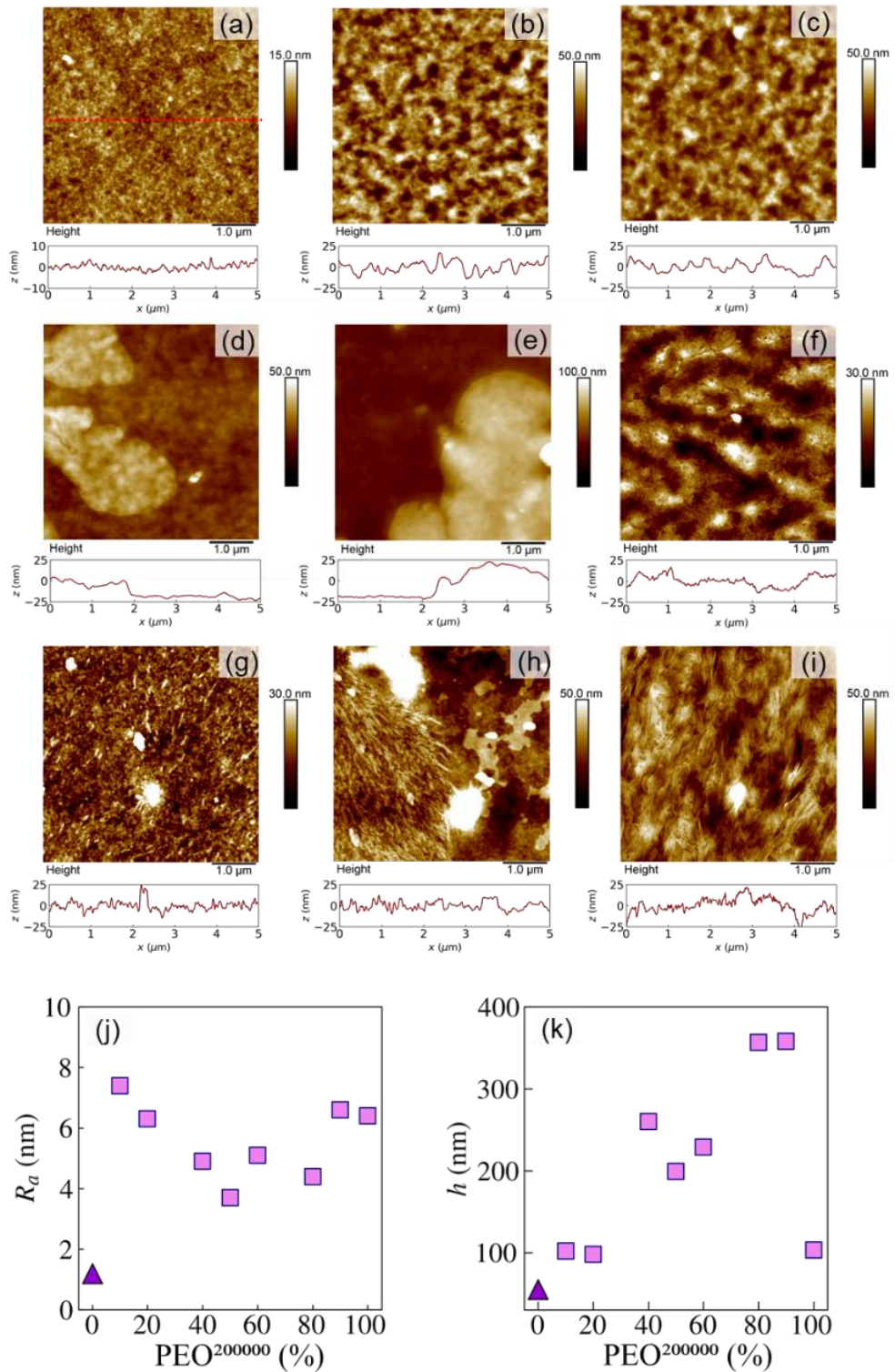


Figure 5.6. AFM height images for (a) PEDOT:PSS, (b) PEO²⁰⁰⁰⁰⁰-10, (c) PEO²⁰⁰⁰⁰⁰-20, (d) PEO²⁰⁰⁰⁰⁰-40, (e) PEO²⁰⁰⁰⁰⁰-50, (f) PEO²⁰⁰⁰⁰⁰-60, (g) PEO²⁰⁰⁰⁰⁰-80, (h) PEO²⁰⁰⁰⁰⁰-90, (i) PEO²⁰⁰⁰⁰⁰. Below each image, a height cross-section is presented, where z refers to the out-of-plane axis and x the direction at which the cross-section was obtained. The dotted line presented in panel (a) exemplifies the cross-section direction. Below: graphical representation of the surface roughness (j) and the thickness (k) of the PEDOT:PSS/PEO²⁰⁰⁰⁰⁰ blends as a function of PEO²⁰⁰⁰⁰⁰ content. The triangle corresponds to the pristine PEDOT:PSS.

The GIWAXS experiments on the PEDOT:PSS/PEO²⁰⁰⁰⁰⁰ are shown in Figure 5.7. From the reported data, the semicrystalline nature of PEO²⁰⁰⁰⁰⁰ is only observed for blends with a content of 50% and higher. A very weak crystalline reflection appears for PEO²⁰⁰⁰⁰⁰-50 (Figure 5.7(e)) indicating a very low degree of crystallinity which increases with increasing PEO²⁰⁰⁰⁰⁰ content (Figure 5.7(f, g and h)). Polarized optical microscopy (POM) (Figure 5.8) allows exploring the morphology at a larger length scale. The POM images of PEO²⁰⁰⁰⁰⁰-40 and PEO²⁰⁰⁰⁰⁰-50 show dendritic structures growing on the surface of the samples but not completely filling it, corresponding to the dendritic lamella polymer crystals of ultra-thin PEO films^{299,300}. The reason why the GIWAXS pattern of PEO²⁰⁰⁰⁰⁰-40 does not show crystal reflections may be that the X-ray beam did not impinge on the dendritic structures, since these structures do not cover the sample completely.

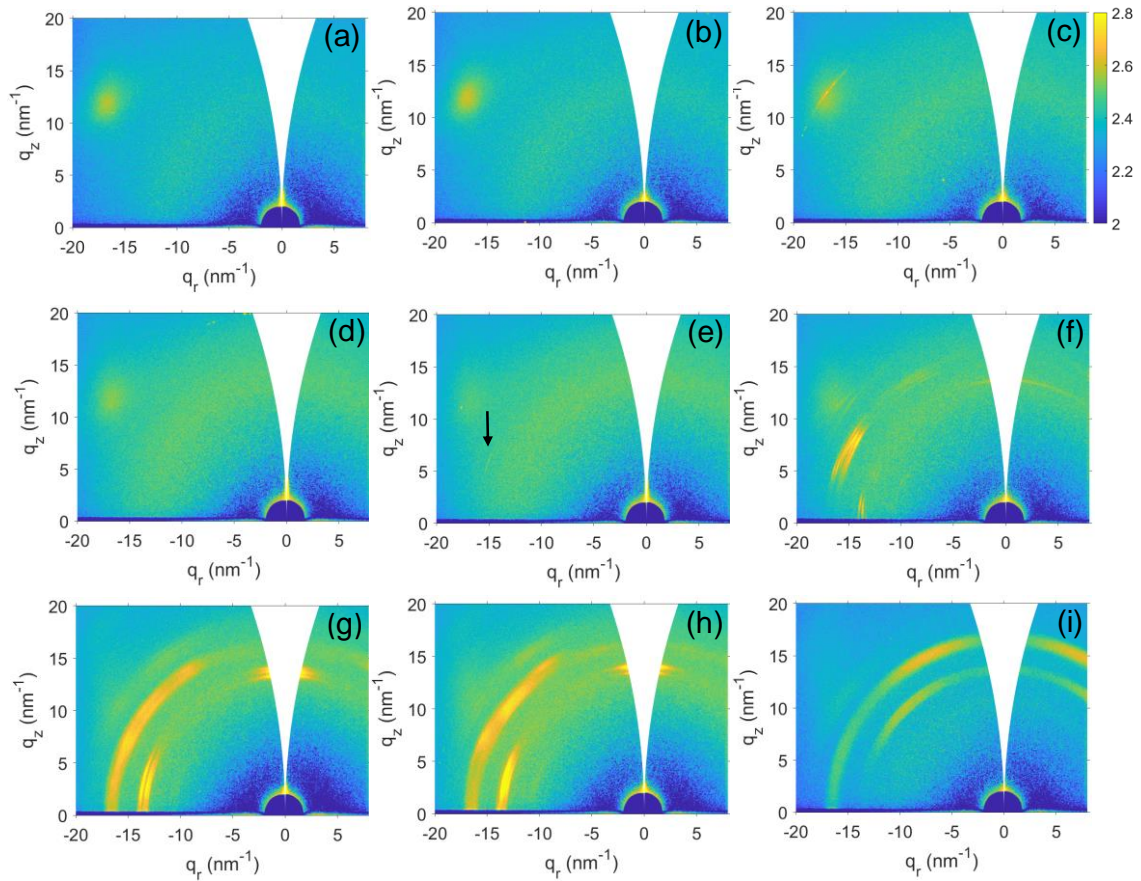


Figure 5.7. 2D GIWAXS patterns of PEDOT:PSS/PEO²⁰⁰⁰⁰⁰ blends at different weight ratios of PEO²⁰⁰⁰⁰⁰, obtained with an incident angle $\alpha_i=0.2^\circ$: (a) PEDOT:PSS, (b) PEO²⁰⁰⁰⁰⁰-10, (c) PEO²⁰⁰⁰⁰⁰-20, (d) PEO²⁰⁰⁰⁰⁰-40, (e) PEO²⁰⁰⁰⁰⁰-50, (f) PEO²⁰⁰⁰⁰⁰-60, (g) PEO²⁰⁰⁰⁰⁰-80, (h) PEO²⁰⁰⁰⁰⁰-90, (i) PEO²⁰⁰⁰⁰⁰. The black arrow in pattern (e) indicates a weak PEO²⁰⁰⁰⁰⁰ reflection.

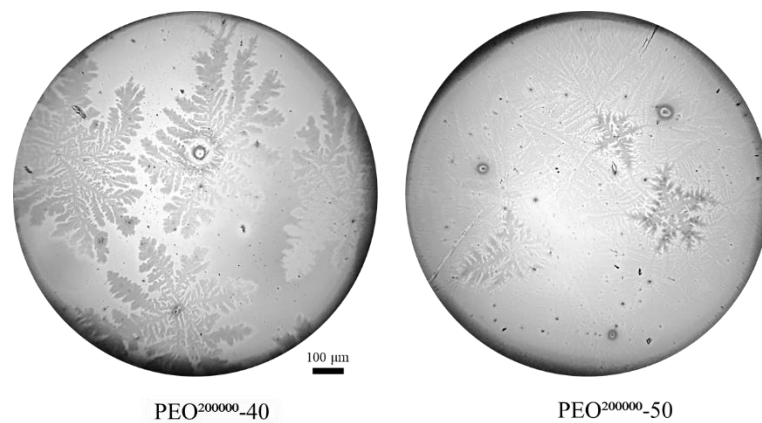


Figure 5.8. Polarized Optical Microscope images of PEO²⁰⁰⁰⁰⁰-40 and PEO²⁰⁰⁰⁰⁰-50.

5.7 Influence of molecular weight on mechanical and electrical properties

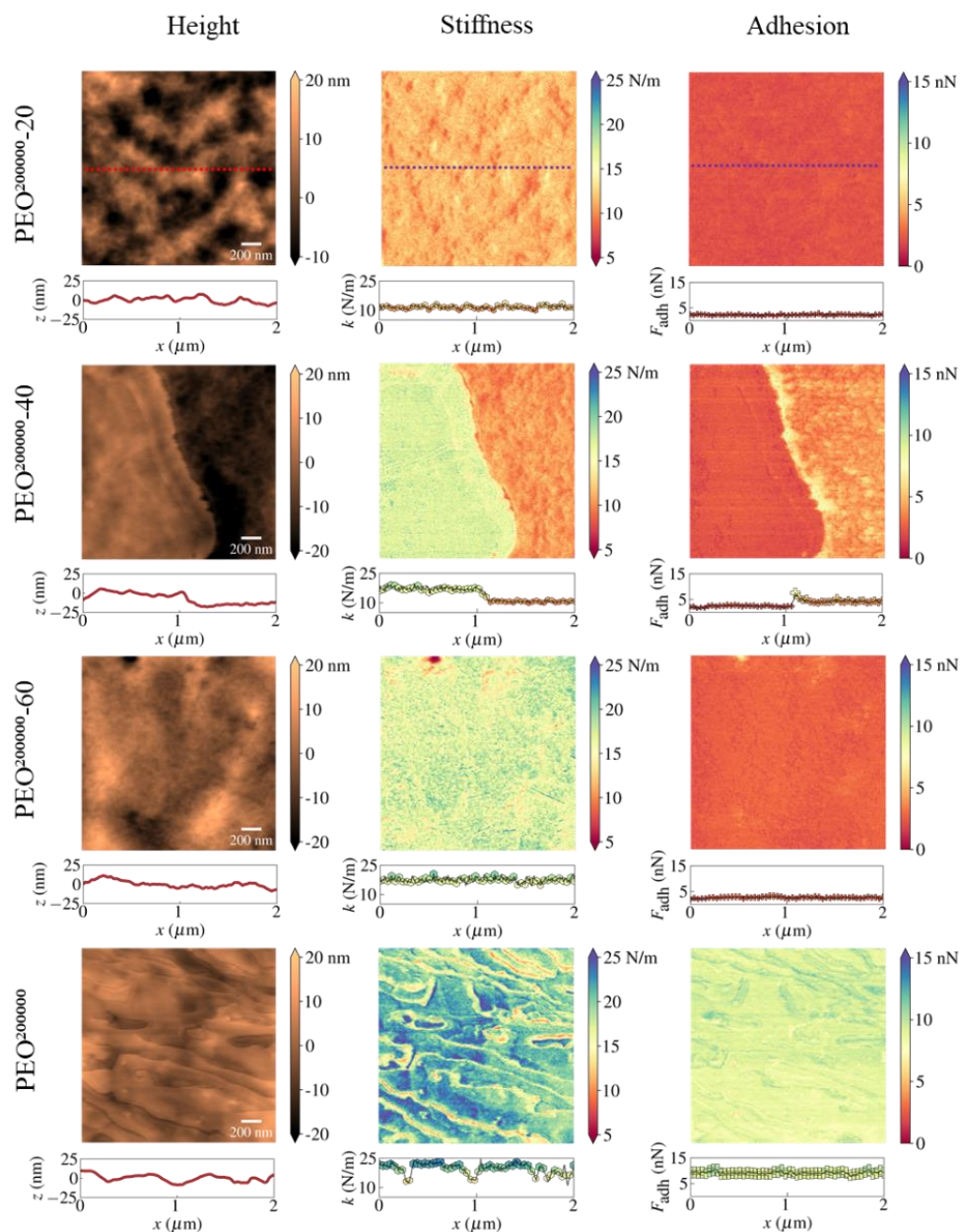


Figure 5.9. Nanomechanical maps for PEO²⁰⁰⁰⁰⁰-20, PEO²⁰⁰⁰⁰⁰-40 (at the edge of a dendritic domain), PEO²⁰⁰⁰⁰⁰-60 and PEO²⁰⁰⁰⁰⁰: Height (z), stiffness (k), and tip-sample adhesion force (F_{adh}). Below each image, a height cross-section is presented. The dotted lines presented for PEO²⁰⁰⁰⁰⁰-20 maps exemplify the cross-section direction.

In Figure 5.9 we report the stiffness and the adhesion maps of representative samples PEO²⁰⁰⁰⁰⁰-20, PEO²⁰⁰⁰⁰⁰-40, PEO²⁰⁰⁰⁰⁰-60 and PEO²⁰⁰⁰⁰⁰, as well as the corresponding height images. PEDOT:PSS, PEO²⁰⁰⁰⁰⁰-10, and PEO²⁰⁰⁰⁰⁰-20 present comparable and homogeneous mechanical properties which indicate the miscibility of the two components for PEO²⁰⁰⁰⁰⁰ fraction lower or equal to 20% (wt%). Images of PEO²⁰⁰⁰⁰⁰-40 were acquired at the boundary

of dendritic domains in order to provide a comprehensive description of all the phases composing the sample surface. By comparing the height images and the stiffness images in Figure 5.9 (PEO²⁰⁰⁰⁰⁰-40), we observe zones with different mechanical properties at the surface of the sample that match with the two different phases under investigation (PEO²⁰⁰⁰⁰⁰-40_{stiffness}: *upper layer* = 17 N/m; *lower layer* = 10 N/m). Combining QNM and POM results, as well as the previous discussion about the low molecular weight case (PEO²⁰⁰⁰⁰⁰-40), we can consider that for PEO²⁰⁰⁰⁰⁰-40 and PEO²⁰⁰⁰⁰⁰-50 a dendritic crystalline PEO²⁰⁰⁰⁰⁰-rich upper layer is growing on top of a PEDOT:PSS-rich layer. Increasing the PEO²⁰⁰⁰⁰⁰ content up to 60% and higher, the samples show homogeneous mechanical properties with stiffness comparable to PEO²⁰⁰⁰⁰⁰. On the other hand, PEO²⁰⁰⁰⁰⁰ presents the highest adhesion value, which can be explained by its semicrystalline character and the random lamellae disposition: amorphous layers in a rubbery state ($T_g < \text{room temperature}$) are intercalated between crystal lamellae, when the disposition is edge-on the AFM tip is accessible to these stickier amorphous regions. But for samples PEO²⁰⁰⁰⁰⁰-40 and PEO²⁰⁰⁰⁰⁰-60 with flat-on lamella disposition, the AFM tip is not accessible to the amorphous regions, explaining the nanomechanical behavior of such samples.

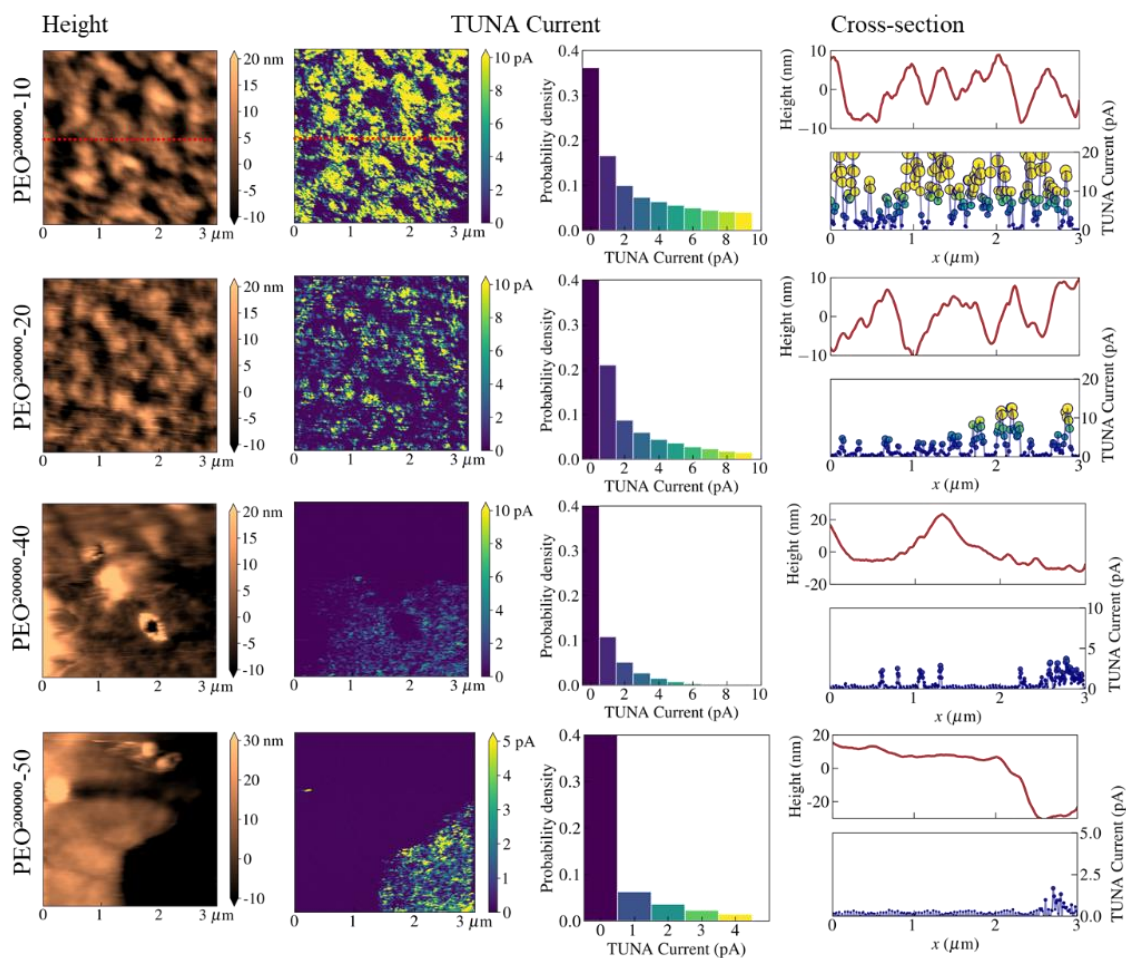


Figure 5.10. Nanoelectrical maps (height and electric current) for PEO²⁰⁰⁰⁰⁰-10, PEO²⁰⁰⁰⁰⁰-20, PEO²⁰⁰⁰⁰⁰-40, and PEO²⁰⁰⁰⁰⁰-50. Histograms were calculated using all data points presented in the current maps (>65000 points). For samples PEO²⁰⁰⁰⁰⁰-40 and PEO²⁰⁰⁰⁰⁰-50, the images refer to the edge of a dendritic domain. Cross-sections were taken at the middle of the maps (see example for PEO²⁰⁰⁰⁰⁰-10).

The electrical contrast maps of PEDOT:PSS/PEO²⁰⁰⁰⁰⁰ blend thin films were acquired in the same conditions used for the low molecular weight samples, and evenly reported in Figure 5.10. Starting from PEO²⁰⁰⁰⁰⁰-10, we can distinguish highly conducting microdomains homogeneously distributed at the surface (bright areas in the electrical map of PEO²⁰⁰⁰⁰⁰-10, Figure 5.10). Such domains are uniformly fused with the less conducting zones, as we can better appreciate in the histogram scheme related to the discussed image. This result suggests a different arrangement of the PEO²⁰⁰⁰⁰⁰ intercalation in the PEDOT:PSS matrix with respect to the low molecular weight case, where the electrical maps showed a more random distribution of the conducting nanodomains at the surface of the samples (Figure 5.5). PEO²⁰⁰⁰⁰⁰-20 shows an electrical map similar to PEO²⁰⁰⁰⁰⁰-10, but with lower conductivity. Compared with PEO⁴⁶⁰⁰-10 and PEO⁴⁶⁰⁰-20, the high molecular weight counterparts present coarser conducting paths. As previously commented, the two systems have a comparable degree of miscibility. PEO²⁰⁰⁰⁰⁰-40 maintains a certain conductivity exclusively outside the dendritic domains in a way similar

to PEO⁴⁶⁰⁰-40. On the other hand, contrary to PEO⁴⁶⁰⁰-50, some regions of PEO²⁰⁰⁰⁰⁰-50 can conduct electricity. This fact constitutes one of the main differences between PEO²⁰⁰⁰⁰⁰ and PEO⁴⁶⁰⁰ blends as, for the low molecular weight system, no contrast in conductivity was observed among the whole surface. In the case of PEO⁴⁶⁰⁰-50 a continuous semicrystalline covering layer was obtained, while for PEO²⁰⁰⁰⁰⁰-50 it was discontinuous, leaving access to the AFM tip to probe the lower PEDOT:PSS-rich conducting layer. We attribute this behavior to the conditions of the film formation by considering that, for longer PEO macromolecular chains, the coordination is obstructed as a consequence of the reduction in the mixing entropic term (accordingly to the Flory-Huggins theory). For this reason, the diffusivity of PEO²⁰⁰⁰⁰⁰ into the PEDOT:PSS-rich domains is less promoted²⁸¹, leading to a more effective phase segregation than in the case of the low molecular weight counterpart. This results in an enhanced mobility of the PEO-rich phase, which can more likely arrange in dendritic domains, providing a discontinuous coating³⁰¹.

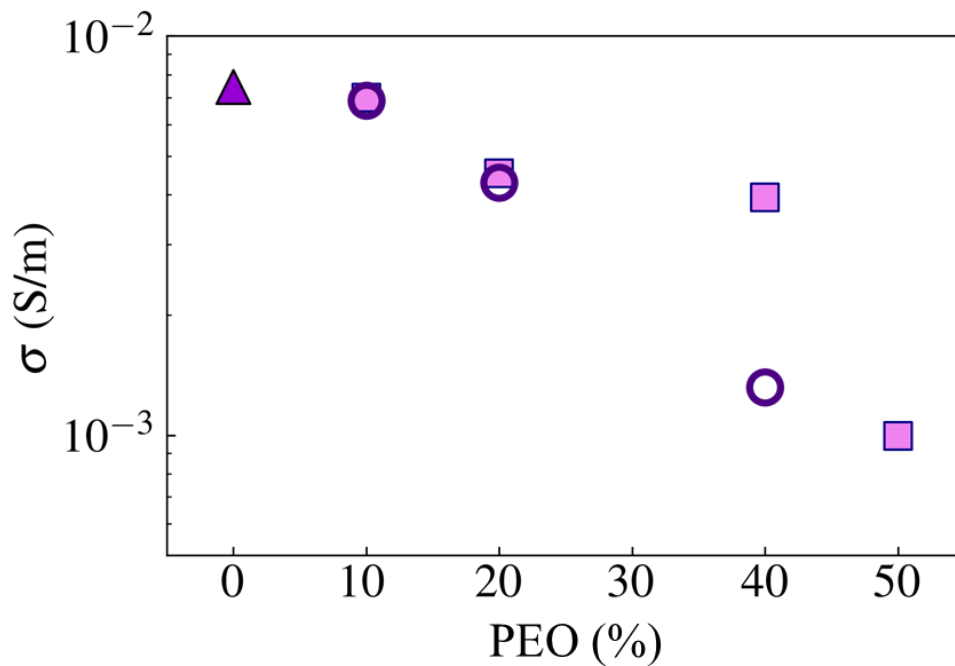


Figure 5.11. Conductivity of blend thin films as a function of: PEO⁴⁶⁰⁰ content (open circles) and PEO²⁰⁰⁰⁰⁰ content (filled squares). The filled triangle corresponds to pristine PEDOT:PSS.

Finally, in Figure 5.11 we present the electrical conductivity of PEDOT:PSS/PEO⁴⁶⁰⁰ and PEDOT:PSS/PEO²⁰⁰⁰⁰⁰ blend thin films. The electrical conductivity was calculated from I-V curves acquired in C-AFM. The I-V curves have been measured in representative regions for both set of samples, these being zones on the samples' surface where electrical signal was detected. Both systems with a 10% of either PEO⁴⁶⁰⁰ or PEO²⁰⁰⁰⁰⁰ show the same conductivity

and very close to that of the pure PEDOT:PSS. With increasing the content of the non-conducting component the conductivity decreases being slightly higher for PEO²⁰⁰⁰⁰⁰-20 than for PEO⁴⁶⁰⁰-20. The main difference arises for samples with a bilayer morphology, while the PEO²⁰⁰⁰⁰⁰-40 bottom layer shows a conductivity similar to that of PEO²⁰⁰⁰⁰⁰-20, the conductivity of PEO⁴⁶⁰⁰-40 bottom layer drops considerably. This behavior could be explained considering that the phase segregation in PEDOT:PSS/PEO²⁰⁰⁰⁰⁰ blends is more efficient than in PEDOT:PSS/PEO⁴⁶⁰⁰ blends, as it is seen in the electrical contrast maps of Figure 5.10 compared to those of Figure 5.5. It means that the PEDOT:PSS bottom layer in PEDOT:PSS/PEO²⁰⁰⁰⁰⁰ blend thin films is purer than in PEDOT:PSS/PEO⁴⁶⁰⁰ blends.

5.8 Summary

Blends of PEDOT:PSS/PEO have been investigated in thin film geometry by AFM and GIWAXS: through a precise analysis of the different phases and domains constituting the resulting thin films, we were able to identify the reciprocal influence of the two polymers according to the different concentrations and molecular weights.

For concentrations of PEO⁴⁶⁰⁰ up to 20%, the PEDOT:PSS matrix can host highly-amorphous PEO⁴⁶⁰⁰ nanodomains providing continuous thin films with homogeneous electrical and mechanical properties. At a concentration of 40% we observed a phase segregation of PEO⁴⁶⁰⁰ towards the surface of the film, forming insulator crystalline dendritic structures on top of a conducting PEDOT:PSS-rich bottom layer. The bilayer structure is kept for the intermediate concentrations, while a spherulitic morphology is developed for blends with high PEO⁴⁶⁰⁰ concentration. As a general trend, the stiffness and adhesion of blends with PEO⁴⁶⁰⁰ concentrations up to 20% are very similar to those of the pure PEDOT:PSS and both magnitudes increase with increasing PEO⁴⁶⁰⁰ content. On the other hand, the conductivity of films with 10% of PEO⁴⁶⁰⁰ is very close to the conductivity measured for pure PEDOT:PSS, while for 20% it drops considerably and it is almost negligible for 40% of PEO⁴⁶⁰⁰. Concerning the impact of the molecular weight of on the structure and properties of the resulting thin films, both families of blends follow a similar trend but with some differences: in the low range concentration, up to 20%, the PEO²⁰⁰⁰⁰⁰ blends present coarser conducting paths than the low molecular weight counterparts; and for intermediate concentrations, a more effective segregation of PEDOT:PSS and PEO²⁰⁰⁰⁰⁰ is achieved, leading to purer conductive and dielectric layers in the bilayer structure. It is interesting to point out that these differences have direct impact on the final electrical conductivity of the blend, which is higher for higher molecular weight of PEO at the given concentration.

Chapter 6

Conclusions

6.1 Final remarks

The effect of the nanostructure conformation on the physical properties of several polymer systems was systematically investigated under the 1D confinement imposed by thin film configuration. In this work, we focused on the study of the charge transport properties of the complex nanostructures under investigation. The evaluation of the nanoelectrical and nanomechanical properties was carried out by AFM-based techniques while the dielectric properties were investigated by both BDS and AFM.

As a first example, we discussed the dielectric properties of semicrystalline PEO through the BDS characterization of its relative solid and melt state, in such a way as to understand the kinetics governing the solid-melt transition, as long as the dynamics of the melt and the role played by heterogeneity in the equilibration of the supported thin films. To study the relaxation phenomena near the melting and crystallization temperatures, we investigated the dielectric response of the samples in thin film configuration in order to neglect any polarization contribution which may mask other intrinsic relaxation processes.

By doing so, we were able to identify the melting temperature and the crystallization one following the values of the dielectric constant respectively in heating and in cooling scans. Observing the relaxation phenomena taking place in the samples, we also addressed the role of heterogeneity in the dynamics of the melt which, depending on the interpretation, may come from the bulk liquid or from the adsorbed interfaces at the electrodes. In the same case study, information concerning the charge-induced dielectric polarization at the interfaces of semicrystalline objects is also provided, showing the role that crystallinity has on the evolution of the ionic displacement before and after the melting point. More specifically, in solid state the charges in the matrix can provide a strong interfacial polarization at the interface of the lamellae under the applied electric field. Interestingly, we observed that the electrode polarization taking place after melt transition is the very same process observed in the solid, which evolves toward interfacial polarization between the two electrodes once the lamellae configuration breaks as a consequence of melting.

With the intention of visualizing the phase arrangement involved in such interfacial polarization, we presented the nano-dielectric characterization of the films by coupling the BDS concept with AFM, then performing nano-Dielectric Spectroscopy (*n*DS) experiments. The setup and operating conditions of the *n*DS were described in detail and a faithful model to interpret the output signal was provided complete with theoretical discussion and validating

experimental data. Based on the assumptions imposed by the model, we were able to image the disposition of the ion transport channels and the orientation of the interfacial polarization in semicrystalline thin films by *n*DS AFM characterization.

Following the AFM characterization approach for the study of complex polymer thin films, we proposed the investigation of an organic conducting material, which also exhibits its own intrinsic nanostructure: PEDOT:PSS. PEDOT:PSS is a well-known intrinsically conducting polymer extensively used in the fabrication of electronic devices due to its high electrical conductivity. PEDOT:PSS thin films are composed of nanograins stacked together in a hierarchical structure whose conformation strongly influences the conductivity in the material. In order to improve or modify the properties of the pristine thin films, we discussed the use of two nanostructuring techniques: reprecipitation and solvent vapor annealing. By reprecipitation we could obtain conductive polymeric nanospheres, while by solvent vapor annealing it was possible to selectively modify at the surface both morphology and conductivity of the material. The nanostructures obtained were composed of several phases each characterized by different mechanical and/or electrical properties. To address the compositional characteristics and the physical properties corresponding to each element constituting the nanostructured thin films, a detailed study in nanomechanical and nanoelectrical AFM was presented and discussed.

The nanospheres obtained by reprecipitation method displayed similar mechanical and electrical properties compared to pristine PEDOT:PSS, yet resulting in a different arrangement in the core-shell distribution of PSS and PEDOT:PSS phases. Our nanoelectrical study revealed that the obtained nanospheres, which doubled in size the original diameter of the commercial precursor, more likely suffer the influence of 1D confinement on the final electrical response compared to the commercial product. This means that the size of the nanoparticles directly affects the grains aggregation when constrained in thin film geometry.

The thin film structured by solvent vapor annealing provided modified surfaces while leaving unchanged the underlying material. The nanostructured superficial layer possessed a thickness of a few tens of nanometers. Again, it was possible to characterize the composition of the obtained nanostructures by nanoelectrical and nanomechanical analysis through AFM-based techniques. It was found that the composition of the upper phase was richer in PEDOT, mostly uncoordinated to the sulphonic groups of PSS, and less conducting respect with the pristine thin films. This upmost phase did not cover homogeneously the thin film, presenting micrometer sized domains where the bottom conducting layer is exposed at the surface. We

were able to prove that the PEDOT-rich layer only superficially covered the thin films by means of nano-indentation experiments in conductive AFM mode, also verifying that the bottom phase preserved the good conductivity properties typical of the raw material.

Finally, the properties at the nanoscale of thin films obtained by blending together PEO and PEDOT:PSS were studied. The blends were prepared by varying the concentration of the two components over the entire range of compositions. Phase separation and crystallization have been studied at different length scales by combining AFM and GIWAXS. GIWAXS analysis provided fundamental information about the internal structure and phase separation in the studied blends. In addition to that, we were able to estimate quantitative nanomechanical and nanoelectrical properties via AFM, finally revealing the dependence of the thin films' physical properties on their composition and structure. From the obtained blends, we achieved different coating capabilities, mechanical properties, and electrical conductivity.

Several different arrangements in the thin films of the two polymers constituting the blend were observed: for low concentration of PEO, the PEDOT:PSS matrix can host the poly oxide in a mostly amorphous state; when reaching intermediate concentration, PEO starts segregating at the surface in a discontinuous, ultra-thin, semicrystalline superficial layer; finally, at low content of PEDOT:PSS, we observed a highly crystalline system intercalated by conducting nanograins. From our mechanical characterization, we registered an overall increase of the stiffness by increasing the concentration of PEO also, in those samples where more than one phase was discernable, the PEO-rich one always possessed higher stiffness. On the other hand, the electrical characterization pointed out a decrease of the conductivity by decreasing the amount of PEDOT:PSS in the blend; in those samples where more than one phase was present, we were able to detect the electrical current signal in PEDOT:PSS-rich domains only.

We completed the study on the reciprocal influence of PEO and PEDOT:PSS in their blends by varying the molecular weight of PEO in the blend composition. Depending on the PEO molecular weight, the electrical response of the resulting thin films shows some differences. In the low concentration range, the blend thin films with high molecular weight PEO present coarser conducting paths than in those with the low molecular weight counterparts. For intermediate concentrations, a more effective phase segregation of PEDOT:PSS and PEO is achieved for high molecular weight PEO. These differences are also translated to different electrical conductivity.

6.2 Perspectives

By the study of semicrystalline polymer thin films in BDS we obtained information about the complex dynamics involved in the melting of the polymeric thin films yet leaving open the discussion about the reason behind the heterogeneity displayed by the resulting supported melt. Depending on the solution to such questions, this issue would enable: i) a better understanding of polymer heterogeneous melt or ii) to clarify the dynamics involved in the equilibration of polymer adsorbed interfaces.

Different strategies for the nanostructural manipulation of a conducting polymer were provided and the resulting materials possessed new and tailored properties, expanding its possible applications in electronics and optoelectronic devices. Similar perspectives can be given to the presented polymer blends, as they space a wide set of mechanical and electrical properties depending on the concentration and molecular weight of their components. Hence, an interesting continuation of this work would be the implementation of the obtained systems in the engineering of electronic devices, if and where convenient.

From a purely technical point of view, with the work presented in this elaborate we hope to have opened new perspectives in the nanocharacterization of polymeric and nanostructured materials by BDS and AFM. First, the developed model for nanodielectric characterization of thin films provides an interesting tool which can be used for the imaging and the quantitative estimation of the dielectric features on whichever unknown dielectric surface. Secondly, we have shown how a rigorous nanomechanical investigation can address important insights into a given microstructure. Thirdly, we have demonstrated the high potential of nanoelectrical characterization in describing the distribution of conducting domains in complex surfaces, also presenting the possibility of obtaining valuable subsurface information when employed in nanoindentation experiments.

Appendix

Nanoscale properties of pristine PEDOT:PSS thin films

Figure A.1 shows the nanomechanical maps of a PEDOT:PSS thin film of 430 nm in thickness. These maps were obtained using the PF-QNM technique presented in section 2.3.1. The topography image (Figure A.1(a)) shows that the PEDOT:PSS film is composed of nanometric grains, as expected. The nanomechanical maps (Figures A.1(b) and (c)) present a well-defined contrast, indicating two distinctive regions. In particular, zones on the maps corresponding the PEDOT:PSS grains revealed higher deformation and lower Young's modulus with respect to the intergranular regions.

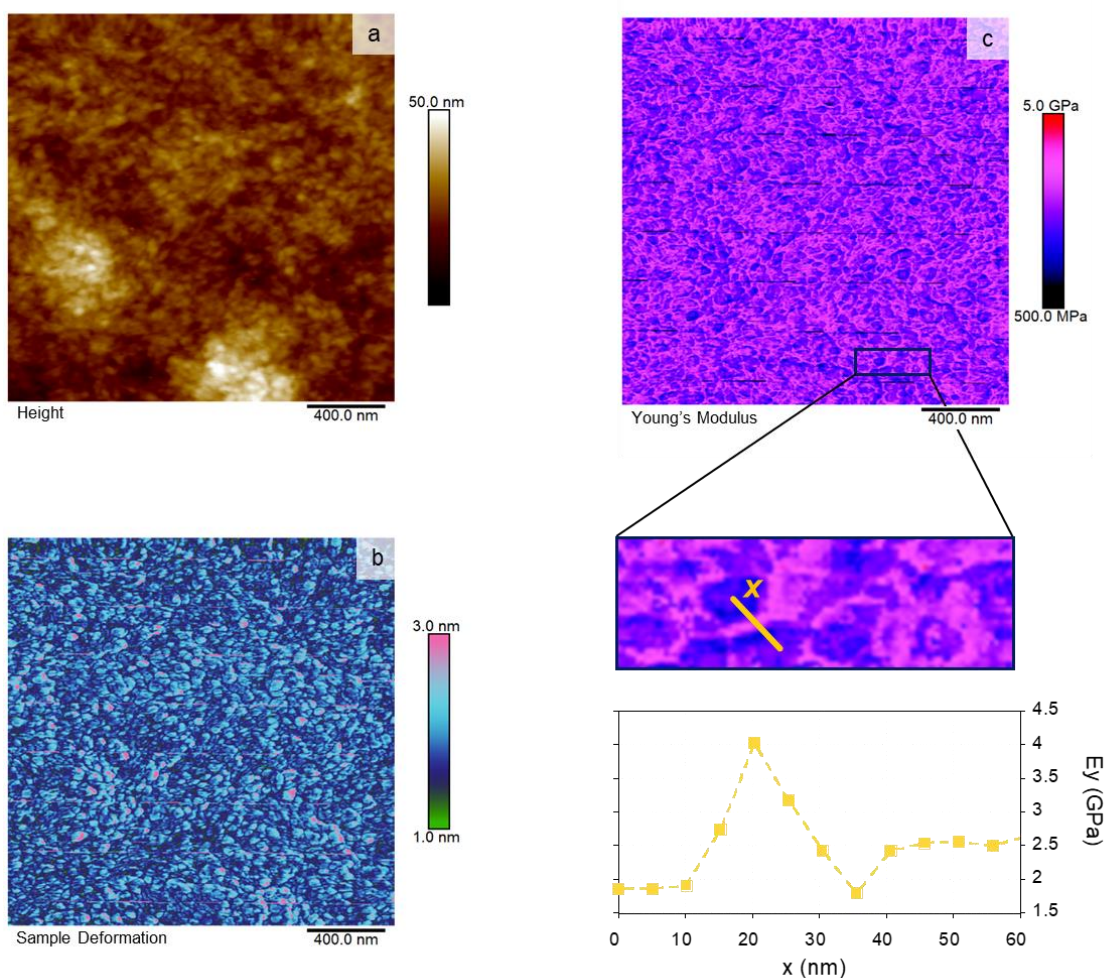


Figure A.1. Nanomechanical results for pristine PEDOT:PSS. (a) Topography, (b) Sample Deformation, (c) Young's modulus (with relative zoom-in and cross-section).

A cross-section of the Young's modulus map is also shown (see zoom-in region in Figure A.1(c)), where we can appreciate the difference in modulus between the distinct zones of the sample surface. The AFM images associate different mechanical properties to the grains with respect to the matrix; however, a further analysis has been carried out to quantify the mechanical properties associated to the observed nanomechanical contrast. In this way, we calculated the distribution of Young's modulus values for Figure A.1(c). The obtained results

are presented as a histogram in Figure A.2, fitted by a sum of two Gaussian functions (fitting curve $R^2 = 0.99$, red line in Figure A.2). We were able to ascribe these functions to the representation of two distinct populations (blue and violet lines). The mean value (μ) for these populations was $\mu_1 = 2.6$ GPa and $\mu_2 = 3.3$ GPa, respectively, with comparable standard deviations of $\sigma = 0.4$. These results were in line with the data presented by Qu et al. in a PF-QNM study on PEDOT thin films (~ 2.5 GPa)²³⁴. By comparing with the nanomechanical maps, we observed that the granular objects were the ones presenting the lower modulus and higher sample deformation, while the interconnecting layer was characterized by a higher modulus and lower deformation. We believe that the presence of these two distinct populations can be ascribed to local mechanical differences between PEDOT:PSS rich grains and a PSS interconnecting layer. Following this idea, we were able to calculate the width of the PSS interconnecting layer between the grains and the diameter of the grains, measuring ~ 15 nm and ~ 60 nm, respectively. The obtained values were in line with those reported previously for PEDOT:PSS by TEM and Energy Dispersive X-ray (EDX) methods²⁴¹. Moreover, the distribution of mechanical phases shown in our study is in line with a previous report. There E. S. Muckley et al. showed that the PSS rich phase in PEDOT:PSS was characterized by higher modulus than the granules constituting the material, as studied by nano-mechanical mapping in AFM²³⁸.

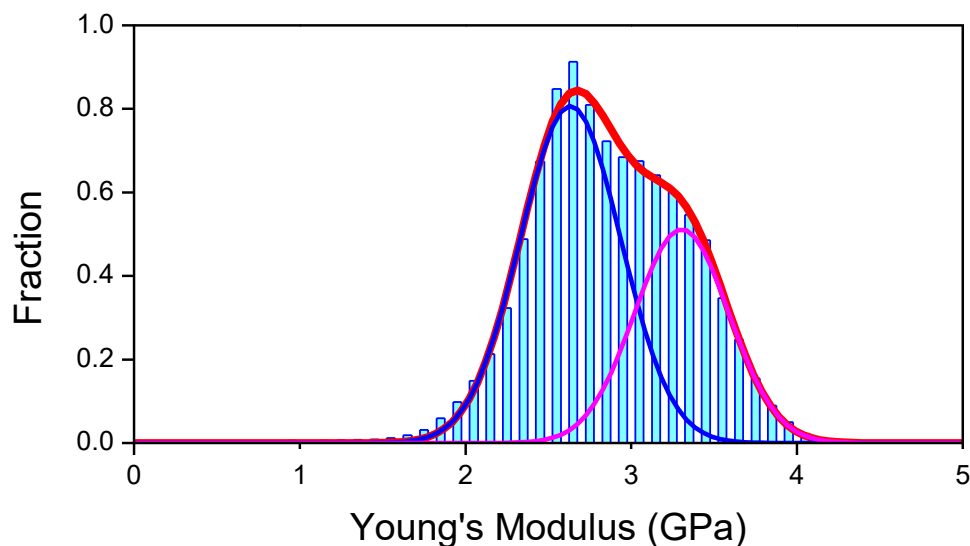


Figure A.2. Young's modulus distribution from the nanomechanical map presented in Figure A.1(c). The fitting curve (—) represents the sum of a low modulus contribution (—) and a high modulus one (—).

As observed from the PF-QNM analysis, the complex structure of PEDOT:PSS gives rise to several distinct domains, each presenting peculiar composition and properties. Being the

conductivity of PEDOT:PSS intimately related to the distribution of such domains, these first evidences provide the basis to understand the electrical conduction regime in the material.

As we may know, the electronic properties of conducting polymers are related to the conjugated nature of their backbones and to the formation of *polarons* able to move along them, which constitute the charge carriers providing the electrical conductivity. The movement of the charge carriers along and between the chains usually provides itself a good model to understand the nature of conductivity in polymers, but in presence of complex nanostructures we might need to integrate other factors. As we showed, PEDOT:PSS constitutes itself an intrinsically nanostructured material, with alternated insulating PSS interfaces among PEDOT:PSS-rich nano-grains. For this reason, we describe the charge transport in it by the nearest-neighbor hopping model, considering the hopping between the grains the limiting factor contributing to the activation energy of single charge displacement¹⁰¹. If this is true, the stack morphology of the conducting grains must have direct impact on the final conductivity. To prove this evidence we considered 1D thin film confinement, where we expect a different disposition of the nanoparticles by varying the thickness. The characterization of the thin films was carried out by C-AFM, which enabled obtaining the *out-of-plane* conductivity as a function of thickness.

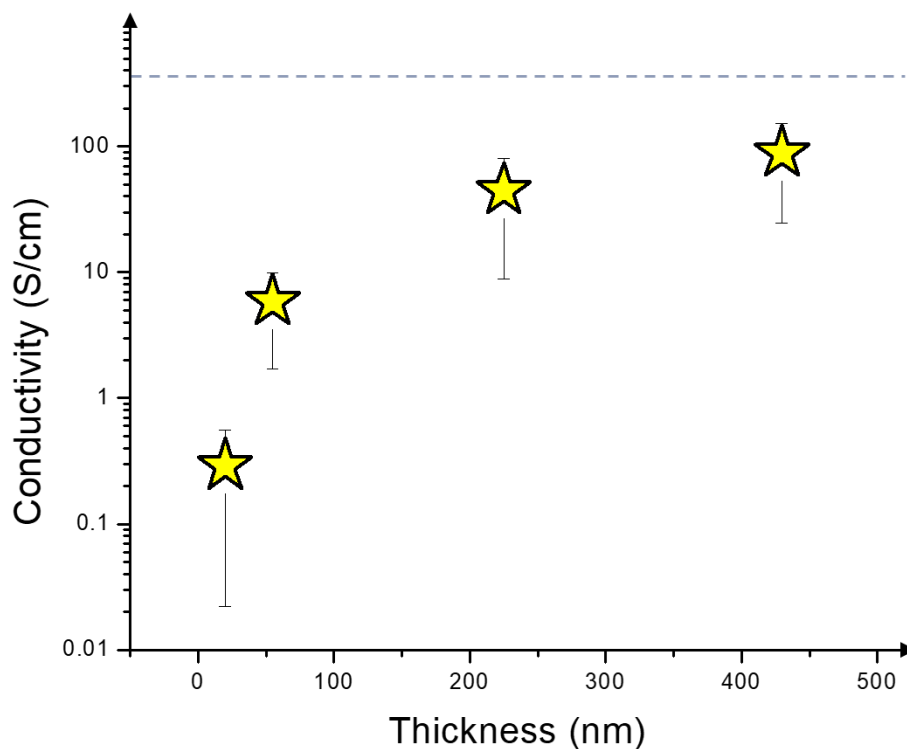


Figure A.3. Logarithm of the conductivity of PEDOT:PSS as a function of thin film thickness. The values correspond to the mean over 5 measured points on different locations, reported in Table 4.2 and plotted as star points. The conductivity of the in-plane conductivity of PEDOT:PSS was also plotted (dashed line).

The obtained results are shown in Figure A.3. The thicker analyzed sample (430 nm) showed the highest conductivity, this equal to ~ 90 S/cm. For all the studied samples, we observed that as the thin film thickness decreases so does the conductivity. More specifically, the conductivity decreases by lowering the thickness in about 2 orders of magnitude. All the values obtained by C-AFM were lower with respect the *in-plane* conductivity measured by four-point-probe, this latter estimated to be $\sigma_{\text{PEDOT:PSS}} = 3.6 \times 10^3$ S/cm for a film of thickness ≈ 0.5 μm . Interestingly, similar findings were also pointed out in previous reports^{91,235}. In these works, the authors explained that the conductivity reduction is related to an anisotropy in the disposition of the PEDOT:PSS grains during film formation, where the conducting granules would tend to preferentially arrange coaxially and perpendicular to the substrate plane. For the thin film geometrical constrain, the out-of-plane conductivity strongly depends on the thickness due to a less packed disposition of the conducting grains as the film thickness decreases, which argues our previous statements demonstrating how the electric conductivity mechanism of PEDOT:PSS is intimately related to its nanostructured nature²⁴².

List of publications

- Sanviti M., Mester L, Hillenbrand R., Alegría A., Martínez-Tong D. E., Solvent-structured PEDOT:PSS surfaces: Fabrication strategies and nanoscale properties, *Polymer*, **2022**, 246, <https://doi.org/10.1016/j.polymer.2022.124723>.
- Sanviti M., Alegría A., Martínez-Tong D. E., Fabrication and nanoscale properties of PEDOT:PSS conducting polymer nanospheres, *Soft Matter*, **2022**, 18, DOI: 10.1039/D1SM01712H.
- Sanviti M., Martínez-Tong D. E., Rebollar E., Ezquerra T. A., García-Gutiérrez M. C., Crystallization and phase separation in PEDOT:PSS/PEO blend thin films: Influence on mechanical and electrical properties at the nanoscale, *Polymer*, **2022**, 262, <https://doi.org/10.1016/j.polymer.2022.125475>.
- Wang B., Sanviti M., Alegría A., Napolitano S., Molecular mobility of polymers at the melting transition, *submitted to a scientific journal*.

References

- (1) Cooper, A. R. The Influence of Molecular Weight and Molecular Weight Distribution on Mechanical Properties of Polymers. *J. Macromol. Sci. Part C* **1972**, 8 (1), 57–199. <https://doi.org/10.1080/15321797208068169>.
- (2) Henson, Z. B.; Müllen, K.; Bazan, G. C. Design Strategies for Organic Semiconductors beyond the Molecular Formula. *Nat. Chem.* **2012**, 4 (9), 699–704. <https://doi.org/10.1038/nchem.1422>.
- (3) Gedde, U. L. F. *Polymer Physics*; Springer Science & Business Media, 1995.
- (4) Namazi, H. Polymers in Our Daily Life. *BioImpacts* **2017**, 7 (2), 73–74. <https://doi.org/10.15171/bi.2017.09>.
- (5) Donth, E.-J. *The Glass Transition: Relaxation Dynamics in Liquids and Disordered Materials*; Springer Science & Business Media, **2001**.
- (6) Debenedetti, P. G.; Stillinger, F. H. *Supercooled Liquids and the Glass Transition*; **2001**.
- (7) Schmelzer, J. W. P. Kinetic Criteria of Glass Formation and the Pressure Dependence of the Glass Transition Temperature. *J. Chem. Phys.* **2012**, 136 (7). <https://doi.org/10.1063/1.3685510>.
- (8) Clark, J. B.; Hastie, J. W.; Kihlberg, L. H. E.; Metselaar, R.; Thackeray, M. M. Definitions of Terms Relating to Phase Transitions of the Solid State, UPAC. *Pure Appl. Chem.* **1994**, 66 (3), 577–594. <https://doi.org/10.1351/pac199466030577>.
- (9) Rahman, M. S.; Al-Marhubi, I. M.; Al-Mahrouqi, A. Measurement of Glass Transition Temperature by Mechanical (DMTA), Thermal (DSC and MDSC), Water Diffusion and Density Methods: A Comparison Study. *Chem. Phys. Lett.* **2007**, 440 (4–6), 372–377. <https://doi.org/10.1016/j.cplett.2007.04.067>.
- (10) Hutchinson, J. M. Studying the Glass Transition by DSC and TMDSC. *J. Therm. Anal. Calorim.* **2003**, 72 (2), 619–629. <https://doi.org/10.1023/A:1024542103314>.
- (11) Rault, J. Origin of the Vogel-Fulcher-Tammann Law in Glass-Forming Materials: The β Bifurcation. *J. Non. Cryst. Solids* **2000**, 271 (3), 177–217. [https://doi.org/10.1016/S0022-3093\(00\)00099-5](https://doi.org/10.1016/S0022-3093(00)00099-5).
- (12) Morthomas, J.; Fusco, C.; Zhai, Z.; Lame, O.; Perez, M. Crystallization of Finite-Extensible Nonlinear Elastic Lennard-Jones Coarse-Grained Polymers. *Phys. Rev. E* **2017**, 96 (5), 1–10. <https://doi.org/10.1103/PhysRevE.96.052502>.
- (13) Li, C. Y. The Rise of Semicrystalline Polymers and Why Are They Still Interesting. *Polymer (Guildf)*. **2020**, 211 (August), 123150. <https://doi.org/10.1016/j.polymer.2020.123150>.
- (14) Zhu, L.; Li, J.; Li, H.; Liu, B.; Chen, J.; Jiang, S. End Groups Affected Crystallization Behavior of Unentangled Poly(ϵ -Caprolactone)S. *Polymer (Guildf)*. **2022**, 241 (January), 124534. <https://doi.org/10.1016/j.polymer.2022.124534>.
- (15) Cheng, B.; Qian, L.; Qian, H. J.; Lu, Z. Y.; Cui, S. Effects of Stereo-Regularity on the Single-Chain Mechanics of Polylactic Acid and Its Implications on the Physical

- Properties of Bulk Materials. *Nanoscale* **2017**, *9* (38), 14312–14316. <https://doi.org/10.1039/c7nr06483g>.
- (16) Young, R. J.; Lovel, P. A. The Crystalline State. In *Introduction to Polymers*; **2011**; 405–408. <https://doi.org/10.1201/b15405-5>.
- (17) Nejabat, G. A Theoretical Reasoning on Why Coordination Catalysts Supported on Mesoporous Supports Can Produce HDPE Crystalline Nanofibers but Not IPP Crystalline Nanofibers. *Polyolefins J.* **2018**, *5* (2), 3–6. <https://doi.org/10.22063/poj.2018.2122.1111>.
- (18) Cheng, S. Z. D.; Lotz, B. Enthalpic and Entropic Origins of Nucleation Barriers during Polymer Crystallization: The Hoffman-Lauritzen Theory and Beyond. *Polymer (Guildf)*. **2005**, *46* (20), 8662–8681. <https://doi.org/10.1016/j.polymer.2005.03.125>.
- (19) Ma, Q.; Georgiev, G.; Cebe, P. Constraints in Semicrystalline Polymers: Using Quasi-Isothermal Analysis to Investigate the Mechanisms of Formation and Loss of the Rigid Amorphous Fraction. *Polymer (Guildf)*. **2011**, *52* (20), 4562–4570. <https://doi.org/10.1016/j.polymer.2011.08.006>.
- (20) Špitalský, Z.; Bleha, T. Elastic Moduli of Highly Stretched Tie Molecules in Solid Polyethylene. *Polymer (Guildf)*. **2003**, *44* (5), 1603–1611. [https://doi.org/10.1016/S0032-3861\(02\)00908-4](https://doi.org/10.1016/S0032-3861(02)00908-4).
- (21) Chanda, M.; Roy, S. K. *Industrial Polymers, Specialty Polymers, and Their Applications*, CRC Press.; **2009**.
- (22) Chakraborty, B. C.; Ratna, D. *Polymers for Vibration Damping Applications*; Elsevier, **2020**. <https://doi.org/10.1016/B978-0-12-819252-8.00003-3>.
- (23) Suresh, G.; Jatav, S.; Mallikarjunachari, G.; Rao, M. S. R.; Ghosh, P.; Satapathy, D. K. Influence of Microstructure on the Nanomechanical Properties of Polymorphic Phases of Poly(Vinylidene Fluoride). *J. Phys. Chem. B* **2018**, *122* (36), 8591–8600. <https://doi.org/10.1021/acs.jpcc.8b05972>.
- (24) Li, L.; Xu, X.; Liu, L.; Song, P.; Cao, Q.; Xu, Z.; Fang, Z.; Wang, H. Water Governs the Mechanical Properties of Poly(Vinyl Alcohol). *Polymer (Guildf)*. **2021**, *213* (August 2020), 123330. <https://doi.org/10.1016/j.polymer.2020.123330>.
- (25) Ishiyama, C.; Higo, Y. Effects of Humidity on Young's Modulus in Poly(Methyl Methacrylate). *J. Polym. Sci. Part B Polym. Phys.* **2002**, *40* (5), 460–465. <https://doi.org/10.1002/polb.10107>.
- (26) Brydson, J. A. *Plastics Materials*; Elsevier, **1999**.
- (27) Tobolsky, A. V.; Callinan, T. D. *Properties and Structure of Polymers*; John Wiley & Sons, New York. Reprinted by permission of John Wiley & Sons, Inc., **1960**.
- (28) Codou, A.; Moncel, M.; Van Berkel, J. G.; Guigo, N.; Sbirrazzuoli, N. Glass Transition Dynamics and Cooperativity Length of Poly(Ethylene 2,5-Furandicarboxylate) Compared to Poly(Ethylene Terephthalate). *Phys. Chem. Chem. Phys.* **2016**, *18* (25), 16647–16658. <https://doi.org/10.1039/c6cp01227b>.
- (29) Deshmukh, K.; Kovářik, T.; Muzaffar, A.; Basheer Ahamed, M.; Khadheer Pasha, S. K. *Mechanical Analysis of Polymers*; **2020**. <https://doi.org/10.1016/b978-0-12-816808-0.00004-4>.
- (30) VanLandingham, M. R. Review of Instrumented Indentation. *J. Res. Natl. Inst. Stand. Technol.* **2003**, *108* (4), 249–265. <https://doi.org/10.6028/jres.108.024>.

- (31) Lucca, D. A.; Herrmann, K.; Klopstein, M. J. Nanoindentation: Measuring Methods and Applications. *CIRP Ann. - Manuf. Technol.* **2010**, *59* (2), 803–819. <https://doi.org/10.1016/j.cirp.2010.05.009>.
- (32) Germanicus, C. R.; Mercier, D.; Agrebi, F.; Febvre, M.; Mariolles, D.; Descamps, P.; Leclere, P. Quantitative Mapping of High Modulus Materials at the Nanoscale: Comparative Study between Atomic Force Microscopy and Nanoindentation. *J. Microsc.* **2020**, *280*, 51–62. <https://doi.org/10.1111/jmi.12935>.
- (33) Cappella, B.; Dietler, G. Force-Distance Curves by Atomic Force Microscopy. *Surf. Sci. Rep.* **1999**, *34* (1–3), 1–3. [https://doi.org/10.1016/S0167-5729\(99\)00003-5](https://doi.org/10.1016/S0167-5729(99)00003-5).
- (34) Kontomaris, S. V.; Stylianou, A. Atomic Force Microscopy for University Students: Applications in Biomaterials. *Eur. J. Phys.* **2017**, *38* (3). <https://doi.org/10.1088/1361-6404/aa5cd6>.
- (35) Bahrami, A.; Bailly, C.; Nysten, B. Spatial Resolution and Property Contrast in Local Mechanical Mapping of Polymer Blends Using AFM Dynamic Force Spectroscopy. *Polymer (Guildf)*. **2019**, *165*, 180–190. <https://doi.org/10.1016/J.POLYMER.2019.01.023>.
- (36) Theiler, P. M.; Ritz, C.; Stemmer, A. Shortcomings of the Derjaguin–Muller–Toporov Model in Dynamic Atomic Force Microscopy. *J. Appl. Phys.* **2021**, *130* (24), 244304. <https://doi.org/10.1063/5.0073933>.
- (37) Pandey, J. C.; Singh, M. Dielectric Polymer Nanocomposites: Past Advances and Future Prospects in Electrical Insulation Perspective. *SPE Polym.* **2021**, *2* (4), 236–256. <https://doi.org/10.1002/pls2.10059>.
- (38) Young, R.; Lovel, P. Electrical Properties. In *Introduction to Polymers*; **2011**; 623–630.
- (39) Böttcher, C. J. F.; van Belle, O. C.; Bordewijk, P.; Rip, A.; Yue, D. D. Theory of Electric Polarization. *J. Electrochem. Soc.* **1974**, *121* (6), 211C. <https://doi.org/10.1149/1.2402382>.
- (40) Kremer F., Schönhals A., *Broadband Dielectric Spectroscopy*, Eds.; **2003**. <https://doi.org/10.1016/b978-0-12-823518-8.00001-3>.
- (41) Rouse, P. E. A Theory of the Linear Viscoelastic Properties of Dilute Solutions of Coiling Polymers. *J. Chem. Phys.* **1953**, *21* (7), 1272–1280. <https://doi.org/10.1063/1.1699180>.
- (42) Baumgaertel, M.; Schausberger, A.; Winter, H. H. The Relaxation of Polymers with Linear Flexible Chains of Uniform Length. *Rheol. Acta* **1990**, *29* (5), 400–408. <https://doi.org/10.1007/BF01376790>.
- (43) Song, Z.; Zhou, H. Towards Sustainable and Versatile Energy Storage Devices: An Overview of Organic Electrode Materials. *Energy Environ. Sci.* **2013**, *6* (8), 2280–2301. <https://doi.org/10.1039/c3ee40709h>.
- (44) Namsheer, K.; Rout, C. S. Conducting Polymers: A Comprehensive Review on Recent Advances in Synthesis, Properties and Applications. *RSC Adv.* **2021**, *11* (10), 5659–5697. <https://doi.org/10.1039/D0RA07800J>.
- (45) Xue, Q.; Sun, J.; Huang, Y.; Zhu, M.; Pei, Z.; Li, H.; Wang, Y.; Li, N.; Zhang, H.; Zhi, C. Recent Progress on Flexible and Wearable Supercapacitors. *Small* **2017**, *13* (45), 1–11. <https://doi.org/10.1002/sml.201701827>.
- (46) Ong, B. S.; Wu, Y.; Liu, P.; Gardner, S. High-Performance Semiconducting

- Polythiophenes for Organic Thin-Film Transistors Scheme 1. *J. AM. CHEM. SOC* **2004**, *126* (100), 3378–3379. <https://doi.org/10.1021/ja039772w>.
- (47) Kushto, G. P.; Kim, W.; Kafafi, Z. H. Flexible Organic Photovoltaics Using Conducting Polymer Electrodes. *Appl. Phys. Lett* **2005**, *86*, 93502. <https://doi.org/10.1063/1.1867568>.
- (48) Sekine, C.; Tsubata, Y.; Yamada, T.; Kitano, M.; Doi, S. Recent Progress of High Performance Polymer OLED and OPV Materials for Organic Printed Electronics. *Sci. Technol. Adv. Mater.* **2014**, *15* (3). <https://doi.org/10.1088/1468-6996/15/3/034203>.
- (49) Heydari Gharahcheshmeh, M.; Gleason, K. K. Texture and Nanostructural Engineering of Conjugated Conducting and Semiconducting Polymers. *Mater. Today Adv.* **2020**, *8*, 100086. <https://doi.org/10.1016/j.mtadv.2020.100086>.
- (50) Bisquert, J.; Garcia-Belmonte, G. Interpretation of AC Conductivity of Lightly Doped Conducting Polymers in Terms of Hopping Conduction. *Russ. J. Electrochem.* **2004**, *40* (3), 352–358. <https://doi.org/10.1023/B:RUEL.0000019676.99599.bc>.
- (51) Blythe, A. R. *Electrical Properties of Polymers*; Cambridge University Press, **1979**.
- (52) Kaiser, A. B.; Skakalova, V. Electronic Conduction in Polymers, Carbon Nanotubes and Graphene. *Chem. Soc. Rev* **2011**, *40*, 3786–3801. <https://doi.org/10.1039/c0cs00103a>.
- (53) Mott, N. F.; Davis, E. A. *Electronic Processes in Non-Crystalline Materials*, Second ed.; Clarendon Press: Oxford, **1979**.
- (54) Cendra, C.; Giovannitti, A.; Savva, A.; Venkatraman, V.; McCulloch, I.; Salleo, A.; Inal, S.; Rivnay, J. Role of the Anion on the Transport and Structure of Organic Mixed Conductors. *Adv. Funct. Mater.* **2019**, *29* (5), 1–11. <https://doi.org/10.1002/adfm.201807034>.
- (55) Paulsen, B. D.; Tybrandt, K.; Stavrinidou, E.; Rivnay, J. Organic Mixed Ionic–Electronic Conductors. *Nat. Mater.* **2020**, *19* (1), 13–26. <https://doi.org/10.1038/s41563-019-0435-z>.
- (56) Kirchmeyer, S.; Reuter, K. Scientific Importance, Properties and Growing Applications of Poly(3,4-Ethylenedioxythiophene). *J. Mater. Chem.* **2005**, *15* (21), 2077–2088. <https://doi.org/10.1039/b417803n>.
- (57) Fan, X.; Nie, W.; Tsai, H.; Wang, N.; Huang, H.; Cheng, Y.; Wen, R.; Ma, L.; Yan, F.; Xia, Y. PEDOT:PSS for Flexible and Stretchable Electronics: Modifications, Strategies, and Applications. *Adv. Sci.* **2019**, *6* (19), 1900813. <https://doi.org/10.1002/advs.201900813>.
- (58) Angell, C. A.; Liu, C.; Sanchez, E. Rubbery Solid Electrolytes with Dominant Cationic Transport and High Ambient Conductivity. *Nature* **1993**, *362* (6416), 137–139. <https://doi.org/10.1038/362137a0>.
- (59) Di Noto, V.; Lavina, S.; Giffin, G. A.; Negro, E.; Scrosati, B. Polymer Electrolytes: Present, Past and Future. *Electrochim. Acta* **2011**, *57* (1), 4–13. <https://doi.org/10.1016/j.electacta.2011.08.048>.
- (60) Wang, Y. Ionic Transport and Dielectric Relaxation in Polymer Electrolytes. *Dielectric Properties of Ionic Liquids*; **2016**; 131–156. https://doi.org/10.1007/978-3-319-32489-0_6.
- (61) Pal, P.; Ghosh, A. Investigation of Ionic Conductivity and Relaxation in Plasticized PMMA-LiClO₄ Solid Polymer Electrolytes. *Solid State Ionics* **2018**, *319* (November

- 2017), 117–124. <https://doi.org/10.1016/j.ssi.2018.02.009>.
- (62) Roling, B. Modeling of Ion Transport Processes in Disordered Solids: Monte Carlo Simulations of the Low-Temperature Particle Dynamics in the Random Barrier Model. *Phys. Chem. Chem. Phys.* **2001**, *3*, 5093–5098 <https://doi.org/10.1039/b105094j>.
- (63) Aziz, S. B.; Marif, R. B.; Brza, M. A.; Hamsan, M. H.; Kadir, M. F. Z. Employing of Trukhan Model to Estimate Ion Transport Parameters in PVA Based Solid Polymer Electrolyte. *Polymers (Basel)*. **2019**, *11* (10). <https://doi.org/10.3390/polym11101694>.
- (64) Utracki, L. A. Development of Polymer Blends. In *Commercial Polymer Blends*; **1998**; pp 117–135. <https://doi.org/10.1007/978-1-4615-5789-0>.
- (65) Ajitha, A. R.; Thomas, S. Introduction: Polymer Blends, Thermodynamics, Miscibility, Phase Separation, and Compatibilization. In *Compatibilization of Polymer Blends*; Elsevier Inc., **2019**; 1–29. <https://doi.org/10.1016/B978-0-12-816006-0.00001-3>.
- (66) Utracki, L. A.; Mukhopadhyay, P.; Gupta, R. K. Polymer Blends: Introduction. In *Polymer Blends Handbook*; **2014**; pp 19–36.
- (67) Utracki, L. A.; Shi, H. During Compounding in a Twin-Screw Extruder . Part I : Droplet Dispersion and Coalescence-A Review. *Polym. Eng. Sci.* **1992**, *32* (24), 1824–1833.
- (68) Thomas, S.; Shanks, R.; Chandran, S. Nano/Micro and Hierarchical Structured Surfaces in Polymer Blends. In *Nanostructured polymer blends*; Elsevier, **2014**; pp 358–407.
- (69) Casuscelli, S.; Crivello, M.; Eimer, G. Nanostructured Materials. *Mol. Catal.* **2020**, *481*. <https://doi.org/10.1016/j.mcat.2019.110646>.
- (70) Martin-Martinez, F. J.; Jin, K.; López, D.; Barreiro, L.; Buehler, M. J. The Rise of Hierarchical Nanostructured Materials from Renewable Sources: Learning from Nature. *ACS Nano* **2018**, *12*, 7425–7433. <https://doi.org/10.1021/acsnano.8b04379>.
- (71) Serghei, A.; Tress, M.; Kremer, F. Confinement Effects on the Relaxation Time Distribution of the Dynamic Glass Transition in Ultrathin Polymer Films. *Macromolecules* **2006**, *39* (26), 9385–9387. <https://doi.org/10.1021/ma061290s>.
- (72) Roth, C. B. Polymers under Nanoconfinement: Where Are We Now in Understanding Local Property Changes? *Chem. Soc. Rev.* **2021**, *50* (14), 8050–8066. <https://doi.org/10.1039/d1cs00054c>.
- (73) Roth, C. B.; Mcnerny, K. L.; Jager, W. F.; Torkelson, J. M. Eliminating the Enhanced Mobility at the Free Surface of Polystyrene: Fluorescence Studies of the Glass Transition Temperature in Thin Bilayer Films of Immiscible Polymers. *Macromolecules* **2007**, *40*, 7, 2568–2574. <https://doi.org/10.1021/ma062864w>.
- (74) Zhang, C.; Boucher, V. M.; Cangialosi, D.; Priestley, R. D. Mobility and Glass Transition Temperature of Polymer Nanospheres. *Polymer (Guildf)*. **2013**, *54* (1), 230–235. <https://doi.org/10.1016/j.polymer.2012.11.036>.
- (75) Liu, G.; Mü, A. J.; Wang, D. Confined Crystallization of Polymers within Nanopores. *Acc. Chem. Res* **2021**, *54*, 28. <https://doi.org/10.1021/acs.accounts.1c00242>.
- (76) Massa, M. V.; Carvalho, J. L.; Dalnoki-Veress, K. Confinement Effects in Polymer Crystal Nucleation from the Bulk to Few-Chain Systems. *Phys. Rev. Lett.* **2006**, *97* (24), 1–4. <https://doi.org/10.1103/PhysRevLett.97.247802>.
- (77) Rodríguez-Rodríguez, A.; Rebollar, E.; Ezquerro, T. A.; Castillejo, M.; Garcia-Ramos, J. V; García-Gutiérrezgutiérrez, M.-C. Patterning Conjugated Polymers by Laser:

- Synergy of Nanostructure Formation in the All-Polymer Heterojunction P3HT/PCDTBT. *Langmuir* **2018**, *34*, 115–125. <https://doi.org/10.1021/acs.langmuir.7b03761>.
- (78) Yabu, H. Self-Organized Precipitation: An Emerging Method for Preparation of Unique Polymer Particles. *Polym. J.* **2013**, *45*, 261–268. <https://doi.org/10.1038/pj.2012.151>.
- (79) Sinturel, C.; Vayer, M.; Morris, M.; Hillmyer, M. A. Solvent Vapor Annealing of Block Polymer Thin Films. *Macromolecules* **2013**, *46* (14), 5399–5415. <https://doi.org/10.1021/ma400735a>.
- (80) Higgins, A. M.; Sferrazza, M.; Jones, R. A. L.; Jukes, P. C.; Sharp, J. S.; Dryden, L. E.; Webster, J. The Timescale of Spinodal Dewetting at a Polymer/Polymer Interface. *Eur. Phys. J. E* **2002**, *8* (2), 137–143. <https://doi.org/10.1140/epje/i2001-10061-3>.
- (81) Keddie, J. L.; Jones, R. A. L.; Cory, R. A. *Size-Dependent Depression of the Glass Transition Temperature in Polymer Films*; **1994**; Vol. 27.
- (82) Zuo, B.; Zhou, H.; Davis, M. J. B.; Wang, X.; Priestley, R. D. Effect of Local Chain Conformation in Adsorbed Nanolayers on Confined Polymer Molecular Mobility. *Phys. Rev. Lett.* **2019**, *122* (21), 217801. <https://doi.org/10.1103/PhysRevLett.122.217801>.
- (83) Song, Z.; Rodríguez-tinoco, C.; Mathew, A.; Napolitano, S. Fast Equilibration Mechanisms in Disordered Materials Mediated by Slow Liquid Dynamics. *Sci. Adv.* **2022**, 1–8.
- (84) Monnier, X.; Napolitano, S.; Cangialosi, D. Direct Observation of Desorption of a Melt of Long Polymer Chains. *Nature Communications* **2020**, *11*, 4354. <https://doi.org/10.1038/s41467-020-18216-y>.
- (85) Vignaud, G.; Chebil, M. S.; Bal, J. K.; Delorme, N.; Beuvier, T.; Grohens, Y.; Gibaud, A. Densification and Depression in Glass Transition Temperature in Polystyrene Thin Films. *Langmuir* **2014**, *30* (39), 11599–11608. <https://doi.org/10.1021/la501639z>.
- (86) Wang, H.; Keum, J. K.; Hiltner, A.; Baer, E.; Freeman, B.; Rozanski, A.; Galeski, A. Confined Crystallization of Polyethylene Oxide in Nanolayer Assemblies. *Science* (80-). **2009**, *323* (5915), 757–760. <https://doi.org/10.1126/science.1164601>.
- (87) Keller, A.; Waring, J. R. S. The Spherulitic Structure of Crystalline Polymers. Part III. Geometrical Factors in Spherulitic Growth and the Fine-Structure. *J. Polym. Sci.* **1955**, *17* (86), 447–472. <https://doi.org/10.1002/pol.1955.120178601>.
- (88) Taguchi, K.; Miyaji, H.; Izumi, K.; Hoshino, A.; Miyamoto, Y.; Kokawa, R. Crystal Growth of Isotactic Polystyrene in Ultrathin Films: Thickness and Temperature Dependence. *J. Macromol. Sci. Part B Phys.* **2006**, *45*, 1141–1147. <https://doi.org/10.1081/MB-120013081>.
- (89) Schönherr, H.; Frank, C. W. Ultrathin Films of Poly(Ethylene Oxides) on Oxidized Silicon. 2. In Situ Study of Crystallization and Melting by Hot Stage AFM. *Macromolecules* **2003**, *36* (4), 1199–1208. <https://doi.org/10.1021/ma020686a>.
- (90) Stafford, C. M.; Vogt, B. D.; Harrison, C.; Julthongpiput, D.; Huang, R. Elastic Moduli of Ultrathin Amorphous Polymer Films. *Macromolecules* **2006**, *39*, 15, 5095–5099. <https://doi.org/10.1021/ma060790i>.
- (91) Nardes, A. M.; Kemerink, M.; Janssen, R. A. J.; Bastiaansen, J. A. M.; Kiggen, N. M. M.; Langeveld, B. M. W.; Van Breemen, A. J. J. M.; De Kok, M. M. Microscopic Understanding of the Anisotropic Conductivity of PEDOT:PSS Thin Films. *Adv. Mater.*

- 2007, 19 (9), 1196–1200. <https://doi.org/10.1002/adma.200602575>.
- (92) Rao, C. N. R.; Biswas, K. Characterization of Nanomaterials by Physical Methods. *Annu. Rev. Anal. Chem.* **2009**, 2, 435–462. <https://doi.org/10.1146/annurev-anchem-060908-155236>.
- (93) Knop, K.; Hoogenboom, R.; Fischer, D.; Schubert, U. S. Poly(Ethylene Glycol) in Drug Delivery: Pros and Cons as Well as Potential Alternatives. *Angew. Chemie - Int. Ed.* **2010**, 49 (36), 6288–6308. <https://doi.org/10.1002/anie.200902672>.
- (94) Xue, Z.; He, D.; Xie, X. Poly(Ethylene Oxide)-Based Electrolytes for Lithium-Ion Batteries. *J. Mater. Chem. A* **2015**, 3 (38), 19218–19253. <https://doi.org/10.1039/c5ta03471j>.
- (95) Karan, N. K.; Pradhan, O. K.; Thomas, R.; Natesan, B.; Katiyar, R. S. Solid Polymer Electrolytes Based on Polyethylene Oxide and Lithium Trifluoro- Methane Sulfonate (PEO-LiCF₃so₃): Ionic Conductivity and Dielectric Relaxation. *Solid State Ionics* **2008**, 179 (19–20), 689–696. <https://doi.org/10.1016/j.ssi.2008.04.034>.
- (96) Wu, C. Simulated Glass Transition of Poly(Ethylene Oxide) Bulk and Film: A Comparative Study. *J. Phys. Chem. B* **2011**, 115 (38), 11044–11052. <https://doi.org/10.1021/JP205205X>.
- (97) Devaux, D.; Bouchet, R.; Glé, D.; Denoyel, R. Mechanism of Ion Transport in PEO/LiTFSI Complexes: Effect of Temperature, Molecular Weight and End Groups. *Solid State Ionics* **2012**, 227, 119–127. <https://doi.org/10.1016/j.ssi.2012.09.020>.
- (98) Laskarakis, A.; Karagkiozaki, V.; Georgiou, D.; Gravalidis, C.; Logothetidis, S. Insights on the Optical Properties of Poly(3,4-Ethylenedioxythiophene): Poly(Styrenesulfonate) Formulations by Optical Metrology. *Materials (Basel)*. **2017**, 10 (8), 16–20. <https://doi.org/10.3390/ma10080959>.
- (99) Elschner, A.; Lovenich, W. Solution-Deposited PEDOT for Transparent Conductive Applications. *MRS Bull.* **2011**, 36 (10), 794–798. <https://doi.org/10.1557/mrs.2011.232>.
- (100) Modarresi, M.; Mehandzhiyski, A.; Fahlman, M.; Tybrandt, K.; Zozoulenko, I. Microscopic Understanding of the Granular Structure and the Swelling of PEDOT:PSS. *Macromolecules* **2020**, 53, 6267–6278. <https://doi.org/10.1021/acs.macromol.0c00877>.
- (101) Horii, T.; Li, Y.; Mori, Y.; Okuzaki, H. Correlation between the Hierarchical Structure and Electrical Conductivity of PEDOT/PSS. *Polym. J.* **2015**, 47 (10), 695–699. <https://doi.org/10.1038/pj.2015.48>.
- (102) Fan, Z.; Du, D.; Yao, H.; Ouyang, J. Higher PEDOT Molecular Weight Giving Rise to Higher Thermoelectric Property of PEDOT:PSS: A Comparative Study of Clevios P and Clevios PH1000. *ACS Appl. Mater. Interfaces* **2017**, 9 (13), 11732–11738. <https://doi.org/10.1021/acsami.6b15158>.
- (103) Dossi, M.; Liang, K.; Hutchinson, R. A.; Moscatelli, D. Investigation of Free-Radical Copolymerization Propagation Kinetics of Vinyl Acetate and Methyl Methacrylate. *J. Phys. Chem. B* **2010**, 114, 4213–4222.
- (104) Örs, Y.; Atar, M.; Özçifçi, A. Bonding Strength of Poly(Vinyl Acetate)-Based Adhesives in Some Wood Materials Treated with Impregnation. *J. Appl. Polym. Sci.* **2000**, 76 (9), 1472–1479. [https://doi.org/10.1002/\(SICI\)1097-4628\(20000531\)76:9<1472::AID-APP11>3.0.CO;2-O](https://doi.org/10.1002/(SICI)1097-4628(20000531)76:9<1472::AID-APP11>3.0.CO;2-O).
- (105) Ali, U.; Karim, K. J. B. A.; Buang, N. A. A Review of the Properties and Applications

- of Poly (Methyl Methacrylate) (PMMA). *Polym. Rev.* **2015**, *55* (4), 678–705. <https://doi.org/10.1080/15583724.2015.1031377>.
- (106) Shimuzu, H.; Yamada, M. Ã.; Wada, R.; Okabe, M. Preparation and Characterization of Water Self-Dispersible Poly(3-Hexylthiophene) Particles. *Polym. J.* **2008**, *40* (1), 33–36. <https://doi.org/10.1295/polymj.PJ2007043>.
- (107) Limayem, I.; Charcosset, C.; Fessi, H. Purification of Nanoparticle Suspensions by a Concentration/Diafiltration Process. *Sep. Purif. Technol.* **2004**, *38* (1), 1–9. <https://doi.org/10.1016/j.seppur.2003.10.002>.
- (108) Martínez-Tong, D. E.; Ruzié, C.; Geerts, Y. H.; Sferrazza, M. Structural Evolution of an Organic Semiconducting Molecule onto a Soft Substrate. *ChemPhysChem* **2016**, *17* (8), 1174–1179. <https://doi.org/10.1002/cphc.201501144>.
- (109) Chapman, D. V.; Du, H.; Lee, W. Y.; Wiesner, U. B. Optical Super-Resolution Microscopy in Polymer Science. *Prog. Polym. Sci.* **2020**, *111*. <https://doi.org/10.1016/j.progpolymsci.2020.101312>.
- (110) Hobbs, J. K.; Farrance, O. E.; Kailas, L. How Atomic Force Microscopy Has Contributed to Our Understanding of Polymer Crystallization. *Polymer (Guildf)*. **2009**, *50* (18), 4281–4292. <https://doi.org/10.1016/j.polymer.2009.06.021>.
- (111) Kaemmar, S. B. Introduction to Bruker’s ScanAsyst and PeakForce Tapping AFM Technology. *Appl. note* **2011**, *133* (Rev. A0), 12.
- (112) Magonov, S. N.; Elings, V.; Whangbo, M. H. Phase Imaging and Stiffness in Tapping-Mode Atomic Force Microscopy. *Surface Science*. **1997**. [https://doi.org/10.1016/S0039-6028\(96\)01591-9](https://doi.org/10.1016/S0039-6028(96)01591-9).
- (113) Xu, K.; Sun, W.; Shao, Y.; Wei, F.; Zhang, X.; Wang, W.; Li, P. Recent Development of PeakForce Tapping Mode Atomic Force Microscopy and Its Applications on Nanoscience. *Nanotechnol. Rev.* **2018**, *7* (6), 605–621. <https://doi.org/10.1515/ntrev-2018-0086>.
- (114) Zhang, S.; Weng, Y.; Ma, C. Quantitative Nanomechanical Mapping of Polyolefin Elastomer at Nanoscale with Atomic Force Microscopy. *Nanoscale Res Lett* **2021**, *16*, 113. <https://doi.org/10.1186/s11671-021-03568-1>.
- (115) Stan, G.; Gates, R. S.; Rosenberger, M. R.; Chen, S.; Prater, C. B. The Use of the PeakForce TM Quantitative Nanomechanical Mapping AFM-Based Method for High-Resolution Young’s Modulus Measurement of Polymers. *Meas. Sci. Technol* **2011**, *22*, 125703. <https://doi.org/10.1088/0957-0233/22/12/125703>.
- (116) Sahin, O.; Erina, N.; Wagner, R.; Moon, R.; Pratt, J.; Shaw, G.; Raman, A. Uncertainty Quantification in Nanomechanical Measurements Using the Atomic Force Microscope *. *Nanotechnology* **2011**, *22*, 455703–455712. <https://doi.org/10.1088/0957-4484/22/45/455703>.
- (117) Sanviti, M.; Alegria, A.; Martínez-Tong, D. E. Fabrication and Nanoscale Properties of PEDOT:PSS Conducting Polymer Nanospheres. *ChemRxiv* **2021**, 1–29. <https://doi.org/10.26434/chemrxiv.14135315>.
- (118) Sader, J. E.; Chon, J. W. M.; Mulvaney, P. Calibration of Rectangular Atomic Force Microscope Cantilevers. *Rev. Sci. Instrum.* **1999**, *70*, 3967. <https://doi.org/10.1063/1.1150021>.
- (119) Sader, J. E.; Borgani, R.; Gibson, C. T.; Haviland, D. B.; Higgins, M. J.; Kilpatrick, J.

- I.; Lu, J.; Mulvaney, P.; Shearer, C. J.; Slattery, A. D.; Thorén, A.; Tran, J.; Zhang, H.; Zhang, H.; Zheng, T. A Virtual Instrument to Standardise the Calibration of Atomic Force Microscope Cantilevers. *Rev. Sci. Instrum.* **2016**, *87*, 093711. <https://doi.org/10.1063/1.4962866>.
- (120) Gutiérrez-Fernández, E.; Gabaldón-Saucedo, I. A.; García-Gutiérrez, M. C.; Varea, A.; Nogales, A.; Rebollar, E.; Vilà, A.; Ezquerra, T. A.; Cirera, A. Quantitative Assessment by Local Probe Methods of the Mechanical and Electrical Properties of Inkjet-Printed PEDOT:PSS Thin Films over Indium Tin Oxide Substrates. *Org. Electron.* **2019**, *70* (February), 258–263. <https://doi.org/10.1016/j.orgel.2019.04.020>.
- (121) Saadi, M. A. S. R.; Uluutku, B.; Parvini, C. H.; Solares, S. D. Soft Sample Deformation, Damage and Induced Electromechanical Property Changes in Contact- A Nd Tapping-Mode Atomic Force Microscopy. *Surf. Topogr. Metrol. Prop.* **2020**, *8* (4). <https://doi.org/10.1088/2051-672X/abb888>.
- (122) Lee, H. J.; Lee, J.; Park, S. M. Electrochemistry of Conductive Polymers. 45. Nanoscale Conductivity of PEDOT and PEDOT:PSS Composite Films Studied by Current-Sensing AFM. *J. Phys. Chem. B* **2010**, *114* (8), 2660–2666. <https://doi.org/10.1021/jp9113859>.
- (123) Castagnola, V.; Bayon, C.; Descamps, E.; Bergaud, C. Morphology and Conductivity of PEDOT Layers Produced by Different Electrochemical Routes. *Synth. Met.* **2014**, *189*, 7–16. <https://doi.org/10.1016/j.synthmet.2013.12.013>.
- (124) Butt, H. J.; Cappella, B.; Kappl, M. Force Measurements with the Atomic Force Microscope: Technique, Interpretation and Applications. *Surf. Sci. Rep.* **2005**, *59* (1–6), 1–152. <https://doi.org/10.1016/j.surfrep.2005.08.003>.
- (125) Miccio, L. A.; Kummali, M. M.; Schwartz, G. A.; Alegría, Á.; Colmenero, J. Dielectric Spectroscopy at the Nanoscale by Atomic Force Microscopy: A Simple Model Linking Materials Properties and Experimental Response. *J. Appl. Phys.* **2014**, *115* (18). <https://doi.org/10.1063/1.4875836>.
- (126) Fumagalli, L.; Gramse, G.; Esteban-Ferrer, D.; Edwards, M. A.; Gomila, G. Quantifying the Dielectric Constant of Thick Insulators Using Electrostatic Force Microscopy. *Appl. Phys. Lett.* **2010**, *96* (18), 2008–2011. <https://doi.org/10.1063/1.3427362>.
- (127) Riedel, C.; Sweeney, R.; Israeloff, N. E.; Arinero, R.; Schwartz, G. A.; Alegria, A.; Tordjeman, P.; Colmenero, J. Imaging Dielectric Relaxation in Nanostructured Polymers by Frequency Modulation Electrostatic Force Microscopy. *Appl. Phys. Lett.* **2010**, *96* (21). <https://doi.org/10.1063/1.3431288>.
- (128) Riedel, C.; Alegría, A.; Schwartz, G. A.; Colmenero, J.; Senz, J. J. Numerical Study of the Lateral Resolution in Electrostatic Force Microscopy for Dielectric Samples. *Nanotechnology* **2011**, *22* (28). <https://doi.org/10.1088/0957-4484/22/28/285705>.
- (129) Verdonck, E.; Schaap, K.; Thomas, L. C. A Discussion of the Principles and Applications of Modulated Temperature DSC (MTDSC). *Int. J. Pharm.* **1999**, *192* (1), 3–20. [https://doi.org/10.1016/S0378-5173\(99\)00267-7](https://doi.org/10.1016/S0378-5173(99)00267-7).
- (130) Schuetze, A. P.; Lewis, W.; Brown, C.; Geerts, W. J. A Laboratory on the Four-Point Probe Technique. *Am. J. Phys.* **2004**, *72* (2), 149–153. <https://doi.org/10.1119/1.1629085>.
- (131) Hernández, J. J.; Rueda, D. R.; García-Gutiérrez, M. C.; Nogales, A.; Ezquerra, T. A.; Soccio, M.; Lotti, N.; Munari, A. Structure and Morphology of Thin Films of Linear Aliphatic Polyesters Prepared by Spin-Coating. *Langmuir* **2010**, *26* (13), 10731–10737.

<https://doi.org/10.1021/la100959j>.

- (132) Nogales, A.; Gutiérrez-Fernández, E. 2D Representation of a Wide Angle X Ray Scattering Pattern as a Function of Q Vector Components. *MathWorks File Exchange* **2019**.
- (133) Gutiérrez-Fernández, E.; Rebollar, E.; Cui, J.; Ezquerra, T. A.; Nogales, A. Morphology and Ferroelectric Properties of Semiconducting/ Ferroelectric Polymer Bilayers. *Macromolecules* **2019**, *52*, 7396–7402. <https://doi.org/10.1021/acs.macromol.9b00859>.
- (134) Sergeï, A.; Tress, M.; Sangoro, J. R.; Kremer, F. Electrode Polarization and Charge Transport at Solid Interfaces. *Phys. Rev. B - Condens. Matter Mater. Phys.* **2009**, *80* (18), 1–5. <https://doi.org/10.1103/PhysRevB.80.184301>.
- (135) Gainaru, C.; Stacy, E. W.; Bocharova, V.; Gobet, M.; Holt, A. P.; Saito, T.; Greenbaum, S.; Sokolov, A. P. Mechanism of Conductivity Relaxation in Liquid and Polymeric Electrolytes: Direct Link between Conductivity and Diffusivity. *J. Phys. Chem. B* **2016**, *120* (42), 11074–11083. <https://doi.org/10.1021/acs.jpcc.6b08567>.
- (136) Wang, Y.; Sun, C. N.; Fan, F.; Sangoro, J. R.; Berman, M. B.; Greenbaum, S. G.; Zawodzinski, T. A.; Sokolov, A. P. Examination of Methods to Determine Free-Ion Diffusivity and Number Density from Analysis of Electrode Polarization. *Phys. Rev. E - Stat. Nonlinear, Soft Matter Phys.* **2013**, *87* (4), 1–9. <https://doi.org/10.1103/PhysRevE.87.042308>.
- (137) Klein, R. J.; Zhang, S.; Dou, S.; Jones, B. H.; Colby, R. H.; Runt, J. Modeling Electrode Polarization in Dielectric Spectroscopy: Ion Mobility and Mobile Ion Concentration of Single-Ion Polymer Electrolytes. *Altern. Curr. Charact. J. Chem. Phys.* **2006**, *124*, 341. <https://doi.org/10.1063/1.2186638>.
- (138) Lu, H.; Zhang, X.; Zhang, H. Influence of the Relaxation of Maxwell-Wagner-Sillars Polarization and Dc Conductivity on the Dielectric Behaviors of Nylon 1010. *J. Appl. Phys.* **2006**, *100* (5), 0–7. <https://doi.org/10.1063/1.2336494>.
- (139) Arous, M.; Amor, I. Ben; Kallel, A.; Fakhfakh, Z.; Perrier, G. Crystallinity and Dielectric Relaxations in Semi-Crystalline Poly(Ether Ether Ketone). *J. Phys. Chem. Solids* **2007**, *68* (7), 1405–1414. <https://doi.org/10.1016/j.jpcs.2007.02.046>.
- (140) Alig, I.; Dudkin, S. M.; Jenninger, W.; Marzantowicz, M. Ac Conductivity and Dielectric Permittivity of Poly(Ethylene Glycol) during Crystallization: Percolation Picture. *Polymer (Guildf)*. **2006**, *47* (5), 1722–1731. <https://doi.org/10.1016/j.polymer.2005.12.026>.
- (141) Barroso-Bujans, F.; Cervený, S.; Palomino, P.; Enciso, E.; Rudić, S.; Fernandez-Alonso, F.; Alegria, A.; Colmenero, J. Dynamics and Structure of Poly(Ethylene Oxide) Intercalated in the Nanopores of Resorcinol-Formaldehyde Resin Nanoparticles. *Macromolecules* **2016**, *49* (15), 5704–5713. <https://doi.org/10.1021/acs.macromol.6b01285>.
- (142) Roy, D.; Roland, C. M. Reentanglement Kinetics in Polyisobutylene. *Macromolecules* **2013**, *46*, 5. <https://doi.org/10.1021/ma402074b>.
- (143) Frantz, P.; Granick, S. Exchange-Kinetics of Adsorbed Polymer and the Achievement of Conformational Equilibrium. *Society* **1994**, 2553–2558.
- (144) Zhang, Q.; Archer, L. A. Effect of Surface Confinement on Chain Relaxation of Entangled Cis-Polyisoprene. *Langmuir* **2003**, *19*, 8094–8101. <https://doi.org/10.1021/la0346649>.

- (145) Yamazaki, S.; Gu, F.; Watanabe, K.; Okada, K.; Toda, A.; Hikosaka, M. Two-Step Formation of Entanglement from Disentangled Polymer Melt Detected by Using Nucleation Rate. *Polymer (Guildf)*. **2006**, *47* (18), 6422–6428. <https://doi.org/10.1016/j.polymer.2006.07.010>.
- (146) Sangroniz, L.; Alamo, R. G.; Cavallo, D.; Santamaría, A.; Müller, A. J.; Alegría, A. Differences between Isotropic and Self-Nucleated PCL Melts Detected by Dielectric Experiments. *Macromolecules* **2018**, *51* (10), 3663–3671. <https://doi.org/10.1021/acs.macromol.8b00708>.
- (147) Rastogi, S.; Lippits, D. R.; Peters, G. W. M.; Graf, R.; Yao, Y.; Spiess, H. W. Heterogeneity in Polymer Melts from Melting of Polymer Crystals. *Nat. Mater.* **2005**, *4*, 635–641. <https://doi.org/10.1038/nmat1437>.
- (148) Chu, L.; Xu, K.; Graf, R.; Yan, Z. C.; Li, J.; Yao, Y. F. Dynamic Heterogeneity in Homogeneous Polymer Melts. *Soft Matter* **2021**, *17* (25), 6081–6087. <https://doi.org/10.1039/d1sm00017a>.
- (149) Mcleish, T. C. B. A Theory for Heterogeneous States of Polymer Melts Produced by Single Chain Crystal Melting. **2006**. <https://doi.org/10.1039/b611620e>.
- (150) Wang, X.; Yi, J.; Wang, L.; Yuan, Y.; Feng, J. Thermorheological Evidence and Structure of Heterogeneity in Syndiotactic Polypropylene Melts with Strong Memory Effects. *Polymer (Guildf)*. **2021**, *218* (February), 123484. <https://doi.org/10.1016/j.polymer.2021.123484>.
- (151) Martins, J. A.; Zhang, W.; Brito, A. M. Origin of the Melt Memory Effect in Polymer Crystallization. *Polymer (Guildf)*. **2010**, *51* (18), 4185–4194. <https://doi.org/10.1016/j.polymer.2010.07.010>.
- (152) Tang, X.; Chen, W.; Li, L. The Tough Journey of Polymer Crystallization: Battling with Chain Flexibility and Connectivity. *Macromolecules* **2019**, *52* (10), 3575–3591. <https://doi.org/10.1021/acs.macromol.8b02725>.
- (153) Hu, W.; Cai, T. Regime Transitions of Polymer Crystal Growth Rates: Molecular Simulations and Interpretation beyond Lauritzen-Hoffman Model. *Macromolecules* **2008**, *41* (6), 2049–2061. <https://doi.org/10.1021/ma702636g>.
- (154) Long, Y.; Shanks, R. A.; Stachurski, Z. H. Kinetics of Polymer Crystallisation. *Prog. Polym. Sci.* **1995**, *20* (4), 651–701. [https://doi.org/10.1016/0079-6700\(95\)00002-W](https://doi.org/10.1016/0079-6700(95)00002-W).
- (155) Avrami, M. Kinetics of Phase Change. I General Theory. *Heterog. Nucleation J. Chem. Phys.* **1939**, *7*, 64901. <https://doi.org/10.1063/1.1750380>.
- (156) Wang, B.; Mathew, A.; Napolitano, S. Temperature and Thickness Dependence of the Time Scale of Crystallization of Polymers under 1D Confinement. *ACS Macro Lett.* **2021**. <https://doi.org/10.1021/acsmacrolett.1c00123>.
- (157) Yoshida, K.; Manabe, H.; Takahashi, Y.; Furukawa, T. Correlation between Ionic and Molecular Dynamics in the Liquid State of Polyethylene Oxide/Lithium Perchlorate Complexes. *Electrochim. Acta* **2011**, *57* (1), 139–146. <https://doi.org/10.1016/j.electacta.2011.06.099>.
- (158) Murphy, J. G.; Raybin, J. G.; Sibener, S. J. Correlating Polymer Structure, Dynamics, and Function with Atomic Force Microscopy. *J. Polym. Sci.* **2021**, No. April, 1–17. <https://doi.org/10.1002/pol.20210321>.
- (159) Cook, A. B.; Barrett, Z.; Lyon, S. B.; McMurray, H. N.; Walton, J.; Williams, G.

- Calibration of the Scanning Kelvin Probe Force Microscope under Controlled Environmental Conditions. *Electrochim. Acta* **2012**, *66*, 100–105. <https://doi.org/10.1016/j.electacta.2012.01.054>.
- (160) Dazzi, A.; Prater, C. B. AFM-IR: Technology and Applications in Nanoscale Infrared Spectroscopy and Chemical Imaging. *Chem. Rev.* **2017**, *117* (7), 5146–5173. <https://doi.org/10.1021/acs.chemrev.6b00448>.
- (161) Markus, P.; Martínez-Tong, D. E.; Papastavrou, G.; Alegria, A. Effect of Environmental Humidity on the Ionic Transport of Poly(Ethylene Oxide) Thin Films, Investigated by Local Dielectric Spectroscopy. *Soft Matter* **2020**, *16* (13), 3203–3208. <https://doi.org/10.1039/c9sm02471a>.
- (162) Martínez-Tong, D. E.; Miccio, L. A.; Alegria, A. Ionic Transport in the Amorphous Phase of Semicrystalline Polyethylene Oxide Thin Films. *Soft Matter* **2017**, *13* (33), 5597–5603. <https://doi.org/10.1039/c7sm00651a>.
- (163) Schwartz, G. A.; Riedel, C.; Arinero, R.; Tordjeman, P.; Alegría, A.; Colmenero, J. Broadband Nanodielectric Spectroscopy by Means of Amplitude Modulation Electrostatic Force Microscopy (AM-EFM). *Ultramicroscopy* **2011**, *111* (8), 1366–1369. <https://doi.org/10.1016/j.ultramic.2011.05.001>.
- (164) Fumagalli, L.; Ferrari, G.; Sampietro, M.; Gomila, G. Dielectric-Constant Measurement of Thin Insulating Films at Low Frequency by Nanoscale Capacitance Microscopy. *Appl. Phys. Lett.* **2007**, *91* (24). <https://doi.org/10.1063/1.2821119>.
- (165) Hudlet, S.; Saint Jean, M.; Guthmann, C.; Berger, J. Evaluation of the Capacitive Force between an Atomic Force Microscopy Tip and a Metallic Surface. *Eur. Phys. J. B* **1998**, *2* (1), 5–10. <https://doi.org/10.1007/s100510050219>.
- (166) Nakamura, M. Form And Capacitance of Parallel-Plate Capacitors. *IEEE Trans. Components Packag. Manuf. Technol. Part A* **1994**, *17* (3), 477–484. <https://doi.org/10.1109/95.311759>.
- (167) Law, B. M.; Rieutord, F. Electrostatic Forces in Atomic Force Microscopy. *Phys. Rev. B - Condens. Matter Mater. Phys.* **2002**, *66* (3), 354021–354026. <https://doi.org/10.1103/PhysRevB.66.035402>.
- (168) Sometani, T. Image Method for a Dielectric Plate and a Point Charge. *Eur. J. Phys.* **2000**, *21* (6), 549–554. <https://doi.org/10.1088/0143-0807/21/6/305>.
- (169) Lacava, F. *Classical Electrodynamics From Image Charges to the Photon Mass and Magnetic Monopoles*; **2016**.
- (170) Kummali, M. M.; Miccio, L. A.; Schwartz, G. A.; Alegría, A.; Colmenero, J.; Otegui, J.; Petzold, A.; Westermann, S. Local Mechanical and Dielectric Behavior of the Interacting Polymer Layer in Silica Nano-Particles Filled SBR by Means of AFM-Based Methods. *Polymer (Guildf)*. **2013**, *54* (18), 4980–4986. <https://doi.org/10.1016/j.polymer.2013.07.032>.
- (171) Gomila, G.; Toset, J.; Fumagalli, L. Nanoscale Capacitance Microscopy of Thin Dielectric Films. *J. Appl. Phys.* **2008**, *104* (2). <https://doi.org/10.1063/1.2957069>.
- (172) Jin, T.; Niu, X.; Xiao, G.; Wang, Z.; Zhou, Z.; Yuan, G.; Shu, X. Effects of Experimental Variables on PMMA Nano-Indentation Measurements. *Polym. Test.* **2015**, *41*, 1–6. <https://doi.org/10.1016/j.polymertesting.2014.09.015>.
- (173) Tyagi, M.; Alegría, A.; Colmenero, J. Broadband Dielectric Study of Oligomer of

- Poly(Vinyl Acetate): A Detailed Comparison of Dynamics with Its Polymer Analog. *Phys. Rev. E - Stat. Nonlinear, Soft Matter Phys.* **2007**, *75* (6), 1–9. <https://doi.org/10.1103/PhysRevE.75.061805>.
- (174) Do, C.; Lunkenheimer, P.; Diddens, D.; Götz, M.; Weiß, M.; Loidl, A.; Sun, X. G.; Allgaier, J.; Ohl, M. Li⁺ Transport in Poly(Ethylene Oxide) Based Electrolytes: Neutron Scattering, Dielectric Spectroscopy, and Molecular Dynamics Simulations. *Phys. Rev. Lett.* **2013**, *111* (1), 1–5. <https://doi.org/10.1103/PhysRevLett.111.018301>.
- (175) Natesan, B.; Karan, N. K.; Rivera, M. B.; Aliev, F. M.; Katiyar, R. S. Segmental Relaxation and Ion Transport in Polymer Electrolyte Films by Dielectric Spectroscopy. *J. Non. Cryst. Solids* **2006**, *352* (42-49 SPEC. ISS.), 5205–5209. <https://doi.org/10.1016/j.jnoncrysol.2006.01.138>.
- (176) Karmakar, A.; Ghosh, A. Dielectric Permittivity and Electric Modulus of Polyethylene Oxide (PEO)-LiClO₄ Composite Electrolytes. *Curr. Appl. Phys.* **2012**, *12* (2), 539–543. <https://doi.org/10.1016/j.cap.2011.08.017>.
- (177) Tripathi, N.; Shukla, A.; Thakur, A. K.; Marx, D. T. Dielectric Modulus and Conductivity Scaling Approach to the Analysis of Ion Transport in Solid Polymer Electrolytes. *Polym. Eng. Sci.* **2020**, *60* (2), 297–305. <https://doi.org/10.1002/pen.25283>.
- (178) Elmahdy, M. M.; Chrissopoulou, K.; Afratis, A.; Floudas, G.; Anastasiadis, S. H. Effect of Confinement on Polymer Segmental Motion and Ion Mobility in PEO/Layered Silicate Nanocomposites. *Macromolecules* **2006**, *39* (16), 5170–5173. <https://doi.org/10.1021/ma0608368>.
- (179) Tu, C. H.; Veith, L.; Butt, H. J.; Floudas, G. Ionic Conductivity of a Solid Polymer Electrolyte Confined in Nanopores. *Macromolecules* **2022**, *55* (4), 1332–1341. <https://doi.org/10.1021/acs.macromol.1c02490>.
- (180) Das, D.; Chandrasekaran, A.; Venkatram, S.; Ramprasad, R. Effect of Crystallinity on Li Adsorption in Polyethylene Oxide. *Chem. Mater.* **2018**, *30* (24), 8804–8810. <https://doi.org/10.1021/acs.chemmater.8b03434>.
- (181) Hourai, M.; Naridomi, T.; Oka, Y.; Murakami, K.; Sumita, S.; Fujino, N.; Shiraiwa, T. A Method of Quantitative Contamination with Metallic Impurities of the Surface of a Silicon Wafer. *Jpn. J. Appl. Phys.* **1988**, *27* (12A), L2361–L2363. <https://doi.org/10.1143/JJAP.27.L2361>.
- (182) Hobbs, J. K.; Vasilev, C.; Humphris, A. D. L. Real Time Observation of Crystallization in Polyethylene Oxide with Video Rate Atomic Force Microscopy. *Polymer (Guildf)*. **2005**, *46* (23), 10226–10236. <https://doi.org/10.1016/j.polymer.2005.08.042>.
- (183) Zhao, J.; Yin, X.; Shi, J.; Zhao, X.; Gutmann, J. S. Melting and Crystallization of Poly(Ethylene Oxide) Nanofilms Studied by Micromechanical Cantilevers. *J. Phys. Chem. C* **2011**, *115* (45), 22347–22353. <https://doi.org/10.1021/jp205381b>.
- (184) Fullerton-Shirey, S. K.; Maranas, J. K. Effect of LiClO₄ on the Structure and Mobility of PEO-Based Solid Polymer Electrolytes. *Macromolecules* **2009**, *42* (6), 2142–2156. <https://doi.org/10.1021/ma802502u>.
- (185) Singh, R.; Tharion, J.; Murugan, S.; Kumar, A. ITO-Free Solution-Processed Flexible Electrochromic Devices Based on PEDOT:PSS as Transparent Conducting Electrode. *ACS Appl. Mater. Interfaces* **2017**, *9* (23), 19427–19435. <https://doi.org/10.1021/acsami.6b09476>.
- (186) Vitoratos, E.; Sakkopoulos, S.; Poliatsas, N.; Emmanouil, K.; Choulis, S. A.

- Conductivity Degradation Study of PEDOT: PSS Films under Heat Treatment in Helium and Atmospheric Air. *Open J. Org. Polym. Mater.* **2012**, *02* (01), 7–11. <https://doi.org/10.4236/ojopm.2012.21004>.
- (187) Hu, L.; Song, J.; Yin, X.; Su, Z.; Li, Z. Research Progress on Polymer Solar Cells Based on PEDOT:PSS Electrodes. *Polymer (Guildf)*. **2020**, *12* (145), 1–19.
- (188) Song, J.; Ma, G.; Qin, F.; Hu, L.; Lou, B.; Liu, T.; Yin, X.; Su, Z.; Zeng, Z.; Jiang, Y.; Wang, G.; Li, Z. High-Conductivity, Flexible and Transparent PEDOT:PSS Electrodes for High Performance Semi-Transparent Supercapacitors. *Polymers (Basel)*. **2020**, *12*, 450. <https://doi.org/doi:10.3390/polym12020450>.
- (189) Lee, J.; Kim, Y. H. High Performance ITO-Free White Organic Light-Emitting Diodes Using Highly Conductive PEDOT:PSS Transparent Electrodes. *Synth. Met.* **2018**, *242* (March), 99–102. <https://doi.org/10.1016/j.synthmet.2018.05.009>.
- (190) Beccatelli, M.; Villani, M.; Gentile, F.; Bruno, L.; Seletti, D.; Maria Nikolaidou, D.; Culiolo, M.; Zappettini, A.; Coppede, N. All-Polymeric Pressure Sensors Based on PEDOT:PSS-Modified Polyurethane Foam. *Cite This ACS Appl. Polym. Mater* **2021**, *3*, 1563–1572. <https://doi.org/10.1021/acsapm.0c01389>.
- (191) Hu, X.; Chen, G.; Wang, X.; Wang, H. Tuning Thermoelectric Performance by Nanostructure Evolution of a Conducting Polymer †. *J. Mater. Chem. A* **2015**, No. 3, 20896–20902. <https://doi.org/10.1039/c5ta07381b>.
- (192) Radivo, A.; Enrico Sovrnigo, A.; Marco Caputo, A.; Dal Zilio, S.; Endale, T.; Pozzato, A.; Goldoni, A.; Tormen, M. Patterning PEDOT:PSS and Tailoring Its Electronic Properties by Water-Vapour-Assisted Nanoimprint Lithography †. *RSC Adv.* **2014**, *4*, 34014–34025. <https://doi.org/10.1039/c4ra04807e>.
- (193) Gutiérrez-Fernández, E.; Gabaldón-Saucedo, I. A.; Rodríguez-Rodríguez, Á.; Solano, E.; García-Gutiérrez, M. C.; Nogales, A.; Cirera, A.; Ezquerra, T. A.; Rebollar, E. Laser Nanostructuring of Thin Films of PEDOT:PSS on ITO: Morphology, Molecular Structure and Electrical Properties. *Appl. Surf. Sci.* **2020**, *509* (September 2019). <https://doi.org/10.1016/j.apsusc.2020.145350>.
- (194) Tseng, S. F.; Hsiao, W. T.; Huang, K. C.; Chiang, D. Electrode Patterning on PEDOT:PSS Thin Films by Pulsed Ultraviolet Laser for Touch Panel Screens. *Appl. Phys. A Mater. Sci. Process.* **2013**, *112* (1), 41–47. <https://doi.org/10.1007/s00339-012-7172-3>.
- (195) Choi, J. H.; Choi, H. J.; Shin, J. H.; Kim, H. P.; Jang, J.; Lee, H. Enhancement of Organic Solar Cell Efficiency by Patterning the PEDOT:PSS Hole Transport Layer Using Nanoimprint Lithography. *Org. Electron.* **2013**, *14* (12), 3180–3185. <https://doi.org/10.1016/j.orgel.2013.09.020>.
- (196) Tang, F.-C.; Wu, F.-C.; Yen, C.-T.; Chang, J.; Chou, W.-Y.; Chang, S.-H. G.; Cheng, H.-L. A Nanoscale Study of Charge Extraction in Organic Solar Cells: The Impact of Interfacial Molecular Configuration. *Nanoscale* **2014**, *7*, 104. <https://doi.org/10.1039/c4nr03176h>.
- (197) Moyen, E.; Hama, A.; Ismailova, E.; Assaud, L.; Malliaras, G. G.; Hanbuchen, M.; Owens, R. M. Nanostructured Conducting Polymers for Stiffness Controlled Cell Adhesion. *Nanotechnology* **2016**, *27*, 074001. <https://doi.org/10.1088/0957-4484/27/7/074001>.
- (198) Mirsafaei, M.; Hossein Fallahpour, A.; Lugli, P.; Rubahn, H.-G.; Adam, J.; Madsen, M.

- The Influence of Electrical Effects on Device Performance of Organic Solar Cells with Nano-Structured Electrodes. *Sci. Rep.* **2017**, *7*, 5300. <https://doi.org/10.1038/s41598-017-05591-8>.
- (199) Ohayon, D.; Pitsalidis, C.; Pappa, A.-M.; Hama, A.; Zhang, Y.; Gallais, L.; Owens, R. M. Laser Patterning of Self-Assembled Monolayers on PEDOT:PSS Films for Controlled Cell Adhesion. *Adv. Mater. Interfaces* **2017**, *4*, 1700191. <https://doi.org/10.1002/admi.201700191>.
- (200) Li, J.; Chang, X.; Li, S.; Shrestha, K.; Tan, E. K. W.; Chu, D. High-Resolution Electrochemical Transistors Defined by Mold-Guided Drying of PEDOT:PSS Liquid Suspension. *ACS Appl. Electron. Mater.* **2020**, *2*, 2611–2618. <https://doi.org/10.1021/acsaelm.0c00491>.
- (201) Snaith, H. J.; Kenrick, H.; Chiesa, M.; Friend, R. H. Morphological and Electronic Consequences of Modifications to the Polymer Anode “PEDOT:PSS.” *Polymer (Guildf)*. **2005**, *46* (8), 2573–2578. <https://doi.org/10.1016/j.polymer.2005.01.077>.
- (202) Zhang, L.; Du, W.; Nautiyal, A.; Liu, Z.; Zhang, X. Recent Progress on Nanostructured Conducting Polymers and Composites: Synthesis, Application and Future Aspects. **2018**, *61* (3), 303–352. <https://doi.org/10.1007/s40843-017-9206-4>.
- (203) Wang, B.; Zhang, B.; Shen, C.; Chen, J.; Nter Reiter, G. Generating Nanoscopic Patterns in Conductivity within a Poly(3-Hexylthiophene) Crystal via Bias-Controlled Scanning Probe Nanolithography. *Macromolecules* **2018**, *51*, 7692–7698. <https://doi.org/10.1021/acs.macromol.8b01465>.
- (204) Jaworska, E.; Michalska, A.; Maksymiuk, K. Polypyrrole Nanospheres-Electrochemical Properties and Application as a Solid Contact in Ion-Selective Electrodes. *Electroanalysis* **2017**, *29*, 123–130. <https://doi.org/10.1002/elan.201600554>.
- (205) Schwarz, K. N.; Farley, S. B.; Smith, T. A.; Ghiggino, K. P. Charge Generation and Morphology in P3HT:PCBM Nanoparticles Prepared by Mini-Emulsion and Reprecipitation Methods †. *Nanoscale* **2015**, *7*, 19899–19904. <https://doi.org/10.1039/c5nr06244f>.
- (206) Pecher, J.; Mecking, S. Nanoparticles of Conjugated Polymers Contents 1. *Chem. Rev.* **2010**, *110*, 6260–6279. <https://doi.org/10.1021/cr100132y>.
- (207) Gutiérrez-Fernández, E.; Cui, J.; Martínez-Tong, D. E.; Nogales, A. Preparation, Physical Properties, and Applications of Water-Based Functional Polymer Inks. *Polymers (Basel)*. **2021**, *13* (9), 1–17. <https://doi.org/10.3390/polym13091419>.
- (208) Zhang, S.; Ren, J.; Zhang, Y.; Peng, H.; Chen, S.; Yang, F.; Cao, Y. PEDOT Hollow Nanospheres for Integrated Bifunctional Electrochromic Supercapacitors. *Org. Electron.* **2020**, *77* (August 2019), 105497. <https://doi.org/10.1016/j.orgel.2019.105497>.
- (209) Shi, H.; Liu, C.; Jiang, Q.; Xu, J. Effective Approaches to Improve the Electrical Conductivity of PEDOT:PSS: A Review. *Adv. Electron. Mater.* **2015**, *1* (4), 1–16. <https://doi.org/10.1002/aelm.201500017>.
- (210) Zhao, Z.; Richardson, G. F.; Meng, Q. Effect of Liquid Immersion of PEDOT: PSS-Coated Polyester Fabric on Surface Resistance and Wettability. *Smart Mater. Struct.* **2017**, *26*, 065016. <https://doi.org/10.1088/1361-665X/aa6f25>.
- (211) Lee, S. H.; Sohn, J. S.; Kulkarni, S. B.; Patil, U. M.; Jun, S. C.; Kim, J. H. Modified Physico-Chemical Properties and Supercapacitive Performance via DMSO Inducement to PEDOT:PSS Active Layer. *Org. Electron.* **2014**, *15* (12), 3423–3430.

<https://doi.org/10.1016/j.orgel.2014.09.020>.

- (212) Fallahzadeh, A.; Saghaei, J.; Yousefi, M. H. Effect of Alcohol Vapor Treatment on Electrical and Optical Properties of Poly(3,4-Ethylene Dioxothiophene):Poly(Styrene Sulfonate) Films for Indium Tin Oxide-Free Organic Light-Emitting Diodes. *Appl. Surf. Sci.* **2014**, *320*, 895–900. <https://doi.org/10.1016/j.apsusc.2014.09.143>.
- (213) Jakobsson, F. L. E.; Crispin, X.; Lindell, L.; Kancierzewska, A.; Fahlman, M.; Salaneck, W. R.; Berggren, M. Towards All-Plastic Flexible Light Emitting Diodes. *Chem. Phys. Lett.* **2006**, *433* (1–3), 110–114. <https://doi.org/10.1016/j.cplett.2006.11.007>.
- (214) Reyes-Reyes, M.; López-Sandoval, R.; Tovar-Martínez, E.; Cabrera-Salazar, J. V.; Martínez-Ponce, G. Tuning the Dedoping Process of PEDOT:PSS Films Using DBU-Solvent Complexes. *Synth. Met.* **2018**, *243*, 25–33. <https://doi.org/10.1016/j.synthmet.2018.05.004>.
- (215) Li, Q.; Zhou, Q.; Wen, L.; Liu, W. Enhanced Thermoelectric Performances of Flexible PEDOT:PSS Film by Synergistically Tuning the Ordering Structure and Oxidation State. *J. Mater.* **2020**, *6* (1), 119–127. <https://doi.org/10.1016/j.jmat.2020.01.001>.
- (216) Tsai, T. C.; Chang, H. C.; Chen, C. H.; Huang, Y. C.; Whang, W. T. A Facile Dedoping Approach for Effectively Tuning Thermoelectricity and Acidity of PEDOT:PSS Films. *Org. Electron.* **2014**, *15* (3), 641–645. <https://doi.org/10.1016/j.orgel.2013.12.023>.
- (217) Vitoratos, E.; Sakkopoulos, S.; Dalas, E.; Paliatsas, N.; Karageorgopoulos, D.; Petraki, F.; Kennou, S.; Choulis, S. A. Thermal Degradation Mechanisms of PEDOT:PSS. *Org. Electron.* **2009**, *10* (1), 61–66. <https://doi.org/10.1016/j.orgel.2008.10.008>.
- (218) Huang, W.; Zhang, C. Tuning the Size of Poly(Lactic-Co-Glycolic Acid) (PLGA) Nanoparticles Fabricated by Nanoprecipitation. **2017**. <https://doi.org/10.1002/biot.201700203>.
- (219) Gutiérrez-Fernández, E.; Ezquerro, T. A.; Rebollar, E.; Cui, J.; Marina, S.; Martín, J.; Nogales, A. Photophysical and Structural Modulation of Poly(3-Hexylthiophene) Nanoparticles via Surfactant-Polymer Interaction. *Polymer (Guildf)*. **2021**, *218* (February). <https://doi.org/10.1016/j.polymer.2021.123515>.
- (220) Cheruku, S.; D’olieslaeger, L.; Smisdrom, N.; Smits, J.; Vanderzande, D.; Maes, W.; Ameloot, M.; Ethirajan, A. Fluorescent PCDTBT Nanoparticles with Tunable Size for Versatile Bioimaging. *Materials (Basel)*. **2019**, *12*, 2497. <https://doi.org/10.3390/ma12152497>.
- (221) D’Olieslaeger, L.; Braeken, Y.; Cheruku, S.; Smits, J.; Ameloot, M.; Vanderzande, D.; Maes, W.; Ethirajan, A. Tuning the Optical Properties of Poly(p-Phenylene Ethynylene) Nanoparticles as Bio-Imaging Probes by Side Chain Functionalization. *J. Colloid Interface Sci.* **2017**, *504*, 527–537. <https://doi.org/10.1016/J.JCIS.2017.05.072>.
- (222) Ouyang, J.; Chu, C.-W.; Chen, F.-C.; Xu, Q.; Yang, Y. High-Conductivity Poly(3,4-Ethylenedioxythiophene):Poly(Styrene Sulfonate) Film and Its Application in Polymer Optoelectronic Devices. *Adv. Funct. Mater.* **2005**, *15* (2), 203–208. <https://doi.org/10.1002/adfm.200400016>.
- (223) Yan, H.; Okuzaki, H. Effect of Solvent on PEDOT/PSS Nanometer-Scaled Thin Films: XPS and STEM/AFM Studies. *Synth. Met.* **2009**, *159* (21–22), 2225–2228. <https://doi.org/10.1016/j.synthmet.2009.07.032>.
- (224) Itoh, K.; Kato, Y.; Honma, Y.; Masunaga, H.; Fujiwara, A.; Iguchi, S.; Sasaki, T. Structural Alternation Correlated to the Conductivity Enhancement of PEDOT:PSS

- Films by Secondary Doping. *J. Phys. Chem. C* **2019**, *123*, 13467–13471. <https://doi.org/10.1021/acs.jpcc.9b02475>.
- (225) Dimitriev, O. P.; Grinko, D. A.; Noskov, Y. V.; Ogurtsov, N. A.; Pud, A. A. PEDOT:PSS Films-Effect of Organic Solvent Additives and Annealing on the Film Conductivity. *Synth. Met.* **2009**, *159* (21–22), 2237–2239. <https://doi.org/10.1016/j.synthmet.2009.08.022>.
- (226) Kim, Y. H.; Sachse, C.; MacHala, M. L.; May, C.; Müller-Meskamp, L.; Leo, K. Highly Conductive PEDOT:PSS Electrode with Optimized Solvent and Thermal Post-Treatment for ITO-Free Organic Solar Cells. *Adv. Funct. Mater.* **2011**, *21* (6), 1076–1081. <https://doi.org/10.1002/adfm.201002290>.
- (227) De-La-Cuesta, J.; Asenjo-Sanz, I.; Latorre-Sánchez, A.; González, E.; Martínez-Tong, D. E.; Pomposo, J. A. Enzyme-Mimetic Synthesis of PEDOT from Self-Folded Iron-Containing Single-Chain Nanoparticles. *Eur. Polym. J.* **2018**, *109*, 447–452. <https://doi.org/10.1016/J.EURPOLYMJ.2018.09.012>.
- (228) Wang, J.; Fang, B. S.; Chou, K. Y.; Chen, C. C.; Gu, Y. A Two-Stage Enzymatic Synthesis of Conductive Poly(3,4-Ethylenedioxythiophene). *Enzyme Microb. Technol.* **2014**, *54* (1), 45–50. <https://doi.org/10.1016/J.ENZMICTEC.2013.10.002>.
- (229) Heuer, H. W.; Wehrmann, R.; Kirchmeyer, S. Electrochromic Window Based on Conducting Poly(3,4-Ethylenedioxythiophene)- Poly(Styrene Sulfonate). *Adv. Funct. Mater.* **2002**, *12* (2), 89–94. [https://doi.org/10.1002/1616-3028\(20020201\)12:2<89::AID-ADFM89>3.0.CO;2-1](https://doi.org/10.1002/1616-3028(20020201)12:2<89::AID-ADFM89>3.0.CO;2-1).
- (230) Sakunpongpitorn, P.; Phasuksom, K.; Paradee, N.; Sirivat, A. Facile Synthesis of Highly Conductive PEDOT:PSS via Surfactant Templates. *RSC Adv.* **2019**, *9*, 6363–6378. <https://doi.org/10.1039/c8ra08801b>.
- (231) Khan, S.; Narula, A. K. Bio-Hybrid Blended Transparent and Conductive Films PEDOT:PSS:Chitosan Exhibiting Electro-Active and Antibacterial Properties. *Eur. Polym. J.* **2016**, *81*, 161–172. <https://doi.org/10.1016/J.EURPOLYMJ.2016.06.005>.
- (232) You, Z. Z. Combined AFM, XPS, and Contact Angle Studies on Treated Indium–Tin-Oxide Films for Organic Light-Emitting Devices. *Mater. Lett.* **2007**, *61* (18), 3809–3814. <https://doi.org/10.1016/J.MATLET.2006.12.063>.
- (233) Soccio, M.; Lotti, N.; Munari, A.; Rebollar, E.; Martínez-Tong, D. E. Wrinkling Poly(Trimethylene 2,5-Furanoate) Free-Standing Films: Nanostructure Formation and Physical Properties. *Polymer (Guildf)*. **2020**, *202*, 122666. <https://doi.org/10.1016/J.POLYMER.2020.122666>.
- (234) Qu, J.; Ouyang, L.; Kuo, C. C.; Martin, D. C. Stiffness, Strength and Adhesion Characterization of Electrochemically Deposited Conjugated Polymer Films. *Acta Biomater.* **2016**, *31* (November), 114–121. <https://doi.org/10.1016/j.actbio.2015.11.018>.
- (235) Greco, F.; Zucca, A.; Taccola, S.; Menciassi, A.; Fujie, T.; Haniuda, H.; Takeoka, S.; Dario, P.; Mattoli, V. Ultra-Thin Conductive Free-Standing PEDOT/PSS Nanofilms. *Soft Matter* **2011**, *7* (22), 10642–10650. <https://doi.org/10.1039/c1sm06174g>.
- (236) Diaz, A. J.; Noh, H.; Meier, T.; Solares, S. D. High-Stress Study of Bioinspired Multifunctional PEDOT: PSS/Nanoclay Nanocomposites Using AFM, SEM and Numerical Simulation. *Beilstein J. Nanotechnol.* **2017**, *8* (1), 2069–2082. <https://doi.org/10.3762/bjnano.8.207>.
- (237) Tank, D.; Lee, H. H.; Khang, D. Y. Elastic Moduli of Organic Electronic Materials by

- the Buckling Method. *Macromolecules* **2009**, *42* (18), 7079–7083. <https://doi.org/10.1021/ma900137k>.
- (238) Muckley, E. S.; Collins, L.; Srijanto, B. R.; Ivanov, I. N. Machine Learning-Enabled Correlation and Modeling of Multimodal Response of Thin Film to Environment on Macro and Nanoscale Using “Lab-on-a-Crystal.” *Adv. Funct. Mater.* **2020**, *30*, 1908010. <https://doi.org/10.1002/adfm.201908010>.
- (239) Cho, H.; Cho, W.; Kim, Y.; Lee, J. G.; Kim, J. H. Influence of Residual Sodium Ions on the Structure and Properties of Poly(3,4-Ethylenedioxythiophene):Poly(Styrenesulfonate). *RSC Adv.* **2018**, *8* (51), 29044–29050. <https://doi.org/10.1039/c8ra05150j>.
- (240) Pasha, A.; Khasim, S.; Al-Hartomy, O. A.; Lakshmi, M.; Manjunatha, K. G. Highly Sensitive Ethylene Glycol-Doped PEDOT-PSS Organic Thin Films for LPG Sensing. *RSC Adv.* **2018**, *8* (32), 18074–18083. <https://doi.org/10.1039/c8ra01061g>.
- (241) Lang, U.; Muller, E.; Naujoks, N.; Dual, J. Microscopical Investigations of PEDOT:PSS Thin Films. *Adv. Funct. Mater.* **2009**, *19* (8), 1215–1220. <https://doi.org/10.1002/adfm.200801258>.
- (242) Horii, T.; Hikawa, H.; Katsunuma, M.; Okuzaki, H. Synthesis of Highly Conductive PEDOT:PSS and Correlation with Hierarchical Structure. *Polymer (Guildf)*. **2018**, *140*, 33–38. <https://doi.org/10.1016/j.polymer.2018.02.034>.
- (243) Niu, Q.; Huang, W.; Tong, J.; Lv, H.; Deng, Y.; Ma, Y.; Zhao, Z.; Xia, R.; Zeng, W.; Min, Y.; Huang, W. Understanding the Mechanism of PEDOT: PSS Modification via Solvent on the Morphology of Perovskite Films for Efficient Solar Cells. *Synth. Met.* **2018**, *243*, 17–24. <https://doi.org/10.1016/j.synthmet.2018.05.012>.
- (244) Girtan, M.; Mallet, R.; Socol, M.; Stanculescu, A. On the Physical Properties PEDOT:PSS Thin Films. *Mater. Today Commun.* **2020**, *22*, 100735. <https://doi.org/10.1016/j.mtcomm.2019.100735>.
- (245) Yeo, J.-S.; Yun, J.-M.; Kim, D.-Y.; Park, S.; Kim, S.-S.; Yoon, M.-H.; Kim, T.-W.; Na, S.-I. Significant Vertical Phase Separation in Solvent-Vapor-Annealed Poly(3,4-Ethylenedioxythiophene):Poly(Styrene Sulfonate) Composite Films Leading to Better Conductivity and Work Function for High-Performance Indium Tin Oxide-Free Optoelectronics. *ACS Appl. Mater. Interfaces* **2012**, *4*, 2551–2560. <https://doi.org/10.1021/am300231v>.
- (246) Liu, H.; Li, X.; Zhang, L.; Hong, Q.; Tang, J.; Zhang, A.; Ma, C. Q. Influence of the Surface Treatment of PEDOT:PSS Layer with High Boiling Point Solvent on the Performance of Inverted Planar Perovskite Solar Cells. *Org. Electron.* **2017**, *47*, 220–227. <https://doi.org/10.1016/j.orgel.2017.05.025>.
- (247) Reza, K. M.; Gurung, A.; Bahrami, B.; Mabrouk, S.; Elbohy, H.; Pathak, R.; Chen, K.; Chowdhury, A. H.; Rahman, M. T.; Letourneau, S.; Yang, H. C.; Saianand, G.; Elam, J. W.; Darling, S. B.; Qiao, Q. Tailored PEDOT:PSS Hole Transport Layer for Higher Performance in Perovskite Solar Cells: Enhancement of Electrical and Optical Properties with Improved Morphology. *J. Energy Chem.* **2020**, *44*, 41–50. <https://doi.org/10.1016/j.jechem.2019.09.014>.
- (248) Rwei, S. P.; Lee, Y. H.; Shiu, J. W.; Sasikumar, R.; Shyr, U. T. Characterization of Solvent-Treated PEDOT:PSS Thin Films with Enhanced Conductivities. *Polymers (Basel)*. **2019**, *11* (1). <https://doi.org/10.3390/polym11010134>.

- (249) Li, X.-Y.; Zhang, L.-P.; Tang, F.; Bao, Z.-M.; Lin, J.; Li, Y.-Q.; Chen, L.; Ma, C.-Q. The Solvent Treatment Effect of the PEDOT:PSS Anode Interlayer in Inverted Planar Perovskite Solar Cells †. *RSC Adv.* **2016**, *6*, 24501–24507. <https://doi.org/10.1039/c5ra25787e>.
- (250) Misael Vedovatte, R.; Matheus, ·; Saccardo, C.; Lima Costa, · Eduardo; Cava, C. E. PEDOT:PSS Post-Treated by DMSO Using Spin Coating, Roll-to-Roll and Immersion: A Comparative Study. *J. Mater. Sci. Mater. Electron.* **2020**, *31*, 317–323. <https://doi.org/10.1007/s10854-019-02524-1>.
- (251) Jiang, Q.; Liu, C.; Song, H.; Shi, H.; Yao, Y.; Xu, J.; Zhang, G.; Lu, B. Improved Thermoelectric Performance of PEDOT:PSS Films Prepared by Polar-Solvent Vapor Annealing Method. *J Mater Sci Mater Electron* **2013**, *24*, 4240–4246. <https://doi.org/10.1007/s10854-013-1391-z>.
- (252) Yeo, J. S.; Yun, J. M.; Kim, D. Y.; Kim, S. S.; Na, S. I. Successive Solvent-Treated PEDOT:PSS Electrodes for Flexible ITO-Free Organic Photovoltaics. *Sol. Energy Mater. Sol. Cells* **2013**, *114*, 104–109. <https://doi.org/10.1016/j.solmat.2013.02.031>.
- (253) Lingstedt, L. V; Ghittorelli, M.; Lu, H.; Koutsouras, D. A.; Marszalek, T.; Torricelli, F.; Cra, N. I.; Gkoupidenis, P.; Blom, P. W. M. Effect of DMSO Solvent Treatments on the Performance of PEDOT:PSS Based Organic Electrochemical Transistors. *Adv. Electron. Mater* **2019**, *5*, 1800804. <https://doi.org/10.1002/aelm.201800804>.
- (254) Wang, X.; Liu, P.; Jiang, Q.; Zhou, W.; Xu, J.; Liu, J.; Jia, Y.; Duan, X.; Liu, Y.; Du, Y.; Jiang, F. Efficient DMSO-Vapor Annealing for Enhancing Thermoelectric Performance of PEDOT:PSS-Based Aerogel. *ACS Appl. Mater. Interfaces* **2019**, *11*, 2408–2417. <https://doi.org/10.1021/acsami.8b19168>.
- (255) Xu, Y.; Liu, Z.; Wei, X.; Wu, J.; Guo, J.; Zhao, B.; Wang, H.; Chen, S.; Dou, Y. Morphological Modulation to Improve Thermoelectric Performances of PEDOT:PSS Films by DMSO Vapor Post-Treatment. *Synth. Met.* **2021**, *271*, 116628. <https://doi.org/10.1016/j.synthmet.2020.116628>.
- (256) Liu, G.; Xie, X.; Liu, Z.; Cheng, G.; Lee, E.-C. Alcohol Based Vapor Annealing of a Poly(3,4-Ethylenedioxythiophene):Poly(Styrenesulfonate) Layer for Performance Improvement of Inverted Perovskite Solar Cells †. *Nanoscale* **2018**, *10*, 11043. <https://doi.org/10.1039/c8nr02146e>.
- (257) Pingree, L. S. C.; Macleod, B. A.; Ginger, D. S. The Changing Face of PEDOT:PSS Films: Substrate, Bias, and Processing Effects on Vertical Charge Transport. *J. Phys. Chem. C* **2008**, *112*, 7922–7927. <https://doi.org/10.1021/jp711838h>.
- (258) Mativetsky, J. M.; Tarver, J.; Yang, X.; Koel, B. E.; Loo, Y. L. Structural Origin of Anisotropic Transport in Electrically Conducting Dichloroacetic Acid-Treated Polymers. *Org. Electron.* **2014**, *15* (2), 631–638. <https://doi.org/10.1016/j.orgel.2013.12.019>.
- (259) Sanviti, M.; Mester, L.; Hillenbrand, R.; Alegría, A.; Martínez-Tong, D. E. Solvent-Structured PEDOT:PSS Surfaces: Fabrication Strategies and Nanoscale Properties. *Polymer (Guildf)*. **2022**, *246* (February), 124723. <https://doi.org/10.1016/j.polymer.2022.124723>.
- (260) Gutiérrez-Fernández, E.; Rodríguez-Rodríguez, Á.; García-Gutiérrez, M. C.; Nogales, A.; Ezquerro, T. A.; Rebollar, E. Functional Nanostructured Surfaces Induced by Laser on Fullerene Thin Films. *Appl. Surf. Sci.* **2019**, *476*, 668–675. <https://doi.org/10.1016/j.apsusc.2019.01.141>.

- (261) Rodríguez-Rodríguez, A.; Rebollar, E.; Soccio, M.; Ezquerro, T. A.; Rueda, D. R.; Vicente Garcia-Ramos, J.; Castillejo, M.; Garcia-Gutierrez, M.-C. Laser-Induced Periodic Surface Structures on Conjugated Polymers: Poly(3-Hexylthiophene). *Macromolecules* **2015**, *48*, 4024–4031. <https://doi.org/10.1021/acs.macromol.5b00804>.
- (262) Stoker, T.; Kohler, A.; Moos, R. Why Does the Electrical Conductivity in PEDOT:PSS Decrease with PSS Content? A Study Combining Thermoelectric Measurements with Impedance Spectroscopy. *J Polym Sci Part B Polym Phys* **2012**, *50*, 976–983. <https://doi.org/10.1002/polb.23089>.
- (263) Stepien, L.; Roch, A.; Schlaier, S.; Dani, I.; Kiriy, A.; Simon, F.; Lukowicz, M. v.; Leyens, C. Investigation of the Thermoelectric Power Factor of KOH-Treated PEDOT:PSS Dispersions for Printing Applications. *Energy Harvest. Syst.* **2016**, *3* (1), 101–111. <https://doi.org/10.1515/ehs-2014-0060>.
- (264) Zhang, L.; Yang, K.; Chen, R.; Zhou, Y.; Chen, S.; Zheng, Y.; Li, M.; Xu, C.; Tang, X.; Zang, Z.; Sun, K. The Role of Mineral Acid Doping of PEDOT:PSS and Its Application in Organic Photovoltaics. *Adv. Electron. Mater.* **2020**, *6*, 1900648. <https://doi.org/10.1002/aelm.201900648>.
- (265) DeLongchamp, D. M.; Vogt, B. D.; Brooks, C. M.; Kano, K.; Obrzut, J.; Richter, C. A.; Kirillov, O. A.; Lin, E. K. Influence of a Water Rinse on the Structure and Properties of Poly(3,4-Ethylene Dioxythiophene):Poly(Styrene Sulfonate) Films. *Langmuir* **2005**, *21* (24), 11480–11483. <https://doi.org/10.1021/la051403l>.
- (266) Li, Z.; Liang, Y.; Zhong, Z.; Qian, J.; Liang, G.; Zhao, K.; Shi, H.; Zhong, S.; Yin, Y.; Tian, W. A Low-Work-Function, High-Conductivity PEDOT:PSS Electrode for Organic Solar Cells with a Simple Structure. *Synth. Met.* **2015**, *210*, 363–366. <https://doi.org/10.1016/j.synthmet.2015.11.006>.
- (267) Wang, Z.; Gao, L.; Wei, X.; Zhao, M.; Miao, Y.; Zhang, X.; Zhang, H.; Wang, H.; Hao, Y.; Xu, B.; Guo, J. Energy Level Engineering of PEDOT:PSS by Antimonene Quantum Sheet Doping for Highly Efficient OLEDs. *J. Mater. Chem. C* **2020**, *8*, 1796. <https://doi.org/10.1039/c9tc06049a>.
- (268) Kim, N.; Petsagkourakis, I.; Chen, S.; Berggren, M.; Crispin, X.; Jonsson, M. P.; Zozoulenko, I. *Electric Transport Properties in PEDOT Thin Films*; **2019**. <https://doi.org/10.1201/9780429190520-3>.
- (269) Yang, Y.; Deng, H.; Fu, Q. Recent Progress on PEDOT:PSS Based Polymer Blends and Composites for Flexible Electronics and Thermoelectric Devices. *Mater. Chem. Front.* **2020**, *4* (11), 3130–3152. <https://doi.org/10.1039/d0qm00308e>.
- (270) Tseng, Y. T.; Lin, Y. C.; Shih, C. C.; Hsieh, H. C.; Lee, W. Y.; Chiu, Y. C.; Chen, W. C. Morphology and Properties of PEDOT:PSS/Soft Polymer Blends through Hydrogen Bonding Interaction and Their Pressure Sensor Application. *J. Mater. Chem. C* **2020**, *8* (18), 6013–6024. <https://doi.org/10.1039/d0tc00559b>.
- (271) Li, P.; Sun, K.; Ouyang, J. Stretchable and Conductive Polymer Films Prepared by Solution Blending. *ACS Appl. Mater. Interfaces* **2015**, *7* (33), 18415–18423. <https://doi.org/10.1021/acsami.5b04492>.
- (272) Li, H.; Mao, P.; Davis, M.; Yu, Z. PEDOT:PSS-Polyethylene Oxide Composites for Stretchable and 3D-Printed Thermoelectric Devices. *Compos. Commun.* **2021**, *23* (October 2020), 100599. <https://doi.org/10.1016/j.coco.2020.100599>.
- (273) Duc, C.; Stoclet, G.; Soulestin, J.; Samuel, C. Poly(Ethylene Oxide)/Poly(3,4-

- Ethylendioxythiophene):Poly(Styrene Sulfonate) (PEDOT:PSS) Blends: An Efficient Route to Highly Conductive Thermoplastic Materials for Melt-State Extrusion Processing? *ACS Appl. Polym. Mater.* **2020**, *2* (6), 2366–2379. <https://doi.org/10.1021/acsapm.0c00303>.
- (274) McDonald, M. B.; Hammond, P. T. Efficient Transport Networks in a Dual Electron/Lithium-Conducting Polymeric Composite for Electrochemical Applications. *ACS Appl. Mater. Interfaces* **2018**, *10* (18), 15681–15690. <https://doi.org/10.1021/acsami.8b01519>.
- (275) Fu, K.; Lv, R.; Na, B.; Zou, S.; Zeng, R.; Wang, B.; Liu, H. Mixed Ion-Electron Conducting PEO/PEDOT: PSS Miscible Blends with Intense Electrochromic Response. *Polymer (Guildf)*. **2019**, *184* (October), 121900. <https://doi.org/10.1016/j.polymer.2019.121900>.
- (276) Vempati, S.; Ertas, Y.; Celebioglu, A.; Uyar, T. Tuning the Degree of Oxidation and Electron Delocalization of Poly(3,4-Ethylendioxythiophene):Poly(Styrenesulfonate) with Solid-Electrolyte. *Appl. Surf. Sci.* **2017**, *419*, 770–777. <https://doi.org/10.1016/j.apsusc.2017.05.049>.
- (277) Li, Y.; Zhang, S.; Li, X.; Unnava, V. R. N.; Cicoira, F. Highly Stretchable PEDOT:PSS Organic Electrochemical Transistors Achieved via Polyethylene Glycol Addition. *Flex. Print. Electron.* **2019**, *4* (4), 044004. <https://doi.org/10.1088/2058-8585/ab5202>.
- (278) Ghosh, S.; Inganäs, O. Networks of Electron-Conducting Polymer in Matrices of Ion-Conducting Polymers. Applications to Fast Electrodes. *Electrochem. Solid-State Lett.* **2000**, *3* (5), 213–215. <https://doi.org/10.1149/1.1391005>.
- (279) Gavim, A. E. X.; Santos, G. H.; de Souza, E. H.; Rodrigues, P. C.; Floriano, J. B.; Kamikawachi, R. C.; de Deus, J. F.; Macedo, A. G. Influence of Electrolyte Distribution in PEDOT:PSS Based Flexible Electrochromic Devices. *Chem. Phys. Lett.* **2017**, *689*, 212–218. <https://doi.org/10.1016/j.cplett.2017.10.022>.
- (280) Wang, T.; Qi, Y.; Xu, J.; Hu, X.; Chen, P. Effects of Poly(Ethylene Glycol) on Electrical Conductivity of Poly(3,4-Ethylendioxythiophene)–Poly(Styrenesulfonic Acid) Film. *Appl. Surf. Sci.* **2005**, *250* (1), 188–194. <https://doi.org/10.1016/j.apsusc.2004.12.051>.
- (281) Alemu Mengistie, D.; Wang, P. C.; Chu, C. W. Effect of Molecular Weight of Additives on the Conductivity of PEDOT:PSS and Efficiency for ITO-Free Organic Solar Cells. *J. Mater. Chem. A* **2013**, *1* (34), 9907–9915. <https://doi.org/10.1039/c3ta11726j>.
- (282) Li, Y.; Li, X.; Zhang, S.; Liu, L.; Hamad, N.; Rao Bobbara, S.; Pasini, D.; Cicoira, F. Autonomic Self-Healing of PEDOT:PSS Achieved Via Polyethylene Glycol Addition. *Adv. Funct. Mater.* **2020**, *30*, 2002853. <https://doi.org/10.1002/adfm.202002853>.
- (283) Zabihi, F.; Xie, Y.; Gao, S.; Eslamian, M. Morphology, Conductivity, and Wetting Characteristics of PEDOT:PSS Thin Films Deposited by Spin and Spray Coating. *Appl. Surf. Sci.* **2015**, *338*, 163–177. <https://doi.org/10.1016/j.apsusc.2015.02.128>.
- (284) Hong, K.; Yang, S. Y.; Yang, C.; Kim, S. H.; Choi, D.; Park, C. E. Reducing the Contact Resistance in Organic Thin-Film Transistors by Introducing a PEDOT:PSS Hole-Injection Layer. *Org. Electron.* **2008**, *9* (5), 864–868. <https://doi.org/10.1016/j.orgel.2008.06.008>.
- (285) Toolan, D. T. W.; Pullan, N.; Harvey, M. J.; Topham, P. D.; Howse, J. R. In Situ Studies of Phase Separation and Crystallization Directed by Marangoni Instabilities During

- Spin-Coating. *Adv. Mater.* **2013**, *25* (48), 7033–7037. <https://doi.org/https://doi.org/10.1002/adma.201302657>.
- (286) Wang, Z.; Gao, K.; Kan, Y.; Zhang, M.; Qiu, C.; Zhu, L.; Zhao, Z.; Peng, X.; Feng, W.; Qian, Z.; Gu, X.; Jen, A. K.-Y.; Tang, B. Z.; Cao, Y.; Zhang, Y.; Liu, F. The Coupling and Competition of Crystallization and Phase Separation, Correlating Thermodynamics and Kinetics in OPV Morphology and Performances. *Nat. Commun.* **2021**, *12* (1), 332. <https://doi.org/10.1038/s41467-020-20515-3>.
- (287) Modarresi, M.; Franco-Gonzalez, J. F.; Zozoulenko, I. Computational Microscopy Study of the Granular Structure and PH Dependence of PEDOT:PSS. *Phys. Chem. Chem. Phys.* **2019**, *21* (12), 6699–6711. <https://doi.org/10.1039/c8cp07141a>.
- (288) Gutierrez-Fernandez, E.; Ezquerro, T. A.; García-Gutiérrez, M.-C. Additive Effect on the Structure of PEDOT:PSS Dispersions and Its Correlation with the Structure and Morphology of Thin Films. *Polymers (Basel)*. **2022**, *14* (1), 141. <https://doi.org/10.3390/polym14010141>.
- (289) Okerberg, B. C.; Marand, H. Crystal Morphologies in Thin Films of PEO/PMMA Blends. *J. Mater. Sci.* **2007**, *42* (12), 4521–4529. <https://doi.org/10.1007/s10853-006-0471-3>.
- (290) Zhu, J.; Wang, M. Temperature-Induced Pattern Transition in Crystallizing Ultrathin Polymer Films. *J. Macromol. Sci. Part B Phys.* **2008**, *47* (2), 401–408. <https://doi.org/10.1080/00222340701849541>.
- (291) Gbabode, G.; Delvaux, M.; Schweicher, G.; Andreasen, J. W.; Nielsen, M. M.; Geerts, Y. H. Unique Crystal Orientation of Poly(Ethylene Oxide) Thin Films by Crystallization Using a Thermal Gradient. *Macromolecules* **2017**, *50* (15), 5877–5891. <https://doi.org/10.1021/acs.macromol.7b00441>.
- (292) Cheng, S.; Smith, D. M.; Li, C. Y. How Does Nanoscale Crystalline Structure Affect Ion Transport in Solid Polymer Electrolytes? *Macromolecules* **2014**, *47* (12), 3978–3986. <https://doi.org/10.1021/ma500734q>.
- (293) Schönherr, H.; Frank, C. W. Ultrathin Films of Poly(Ethylene Oxides) on Oxidized Silicon. 1. Spectroscopic Characterization of Film Structure and Crystallization Kinetics. *Macromolecules* **2003**, *36* (4), 1188–1198. <https://doi.org/10.1021/ma020685i>.
- (294) Zardalidis, G.; Mars, J.; Allgaier, J.; Mezger, M.; Richter, D.; Floudas, G. Influence of Chain Topology on Polymer Crystallization: Poly(Ethylene Oxide) (PEO) Rings vs. Linear Chains. *Soft Matter* **2016**, *12* (39), 8124–8134. <https://doi.org/10.1039/C6SM01622G>.
- (295) Polińska, M.; Rozanski, A.; Galeski, A.; Bojda, J. The Modulus of the Amorphous Phase of Semicrystalline Polymers. *Macromolecules* **2021**, *54* (19), 9113–9123. <https://doi.org/10.1021/ACS.MACROMOL.1C01576>.
- (296) Dauton, E.; Lin, Y.; Faber, H.; Yengel, E.; Sallenave, X.; Plesse, C.; Goubard, F.; Amassian, A.; Anthopoulos, T. D.; Dauton, E.; Lin, Y.; Faber, H.; Yengel, E.; Anthopoulos, T. D.; Sallenave, X.; Plesse, C.; Goubard, F.; Amassian, A. Stretchable and Transparent Conductive PEDOT:PSS-Based Electrodes for Organic Photovoltaics and Strain Sensors Applications. *Adv. Funct. Mater.* **2020**, *30*, 2001251. <https://doi.org/10.1002/adfm.202001251>.
- (297) Mativetsky, J. M.; Loo, Y. L.; Samorì, P. Elucidating the Nanoscale Origins of Organic Electronic Function by Conductive Atomic Force Microscopy. *J. Mater. Chem. C* **2014**,

- 2 (17), 3118–3128. <https://doi.org/10.1039/C3TC32050B>.
- (298) Yeong Na, J.; Kang, B.; Don Park, Y. Influence of Molecular Weight on the Solidification of a Semiconducting Polymer during Time-Controlled Spin-Coating. *J. Phys. Chem. C* **2019**, *123*, 17102–17111. <https://doi.org/10.1021/acs.jpcc.9b03203>.
- (299) Reiter, G.; Sommer, J.-U. Polymer Crystallization in Quasi-Two Dimensions. I. Experimental Results. *J. Chem. Phys.* **2000**, *112* (9), 4376–4383. <https://doi.org/10.1063/1.480984>.
- (300) Braun, H.-G.; Meyer, E. Structure Formation of Ultrathin PEO Films at Solid Interfaces—Complex Pattern Formation by Dewetting and Crystallization. *International Journal of Molecular Sciences* . **2013**. <https://doi.org/10.3390/ijms14023254>.
- (301) Petri, D. F. S. Characterization of Spin-Coated Polymer Films. *J. Braz. Chem. Soc.* **2002**, *13* (5), 695–699. <https://doi.org/10.1590/S0103-50532002000500027>.

Acknowledgements

The dissertation offered by this recollection of results, ideas and scientific contents, is not an outcome that I could have achieved without the effort and the dedication of many people who I personally retain the major contributors to the thesis, which inevitably pushes a sincere necessity to communicate my gratitude.

To Simone Napolitano. He supervised my internship in Brussels, offering me a safe working environment and teaching me the core concepts of his research as well as the key notions to be able to handle the work in the most productive possible way. But the most remarkable thing he gave me during the time spent together is the freedom to guess, the freedom to follow the investigation lines that my own perspective, accompanied by his way more experienced point of view, could bring. For this and for much more, thank you Simone.

To the collaborators who have made possible what would have been impossible alone. To Lars Mester, with whom a beautiful joined work started from the simplicity of a talk about our common scientific interests. To Mari Cruz García-Gutiérrez, whose dedication and reliability provided a solid and durable professional correspondence by which it was possible to see through several research topics. She admirably supported our investigation work, also providing critical supervision at every stage of the collaboration. Thank you sincerely Mari Cruz for believing in our work.

To Angel Alegría, my supervisor and thesis director. I thank him for being always there whenever a theoretical or technical issue arose day by day. It was thanks to his experience and organizational skills that my Ph.D. could progress in the most positive way. Due to his kindness, patience, and know how, I must admit that I could not imagine any better person to be in charge of the role of supervisor during this predoctoral academic path.

To Daniel Enrique Martínez-Tong, my supervisor and most valuable teacher. I learned kind of everything from Daniel: investigation methods, experimental routine, data processing, or whatever being a “researcher” could possibly mean. My deepest gratitude goes to him for being so much more than just a supervisor. He helped me valuating the proportional weight of joys and troubles that accompanied the entire thesis work, always supporting with incredible efficiency and remarkable persistence.

I acknowledge the University of the Basque Country (UPV/EHU) and the Material Physics Centre (CFM, MPC) for the financial support, without which nothing of the reported

work would have ever been done. Moreover, I want to acknowledge all the group of Polymers and Soft Matter, full of talented people with good brains and good hearts.